Interactions of Environmentally-Responsive Nanoparticles with Synthetic and Biological Membranes

by

Reid Chi Van Lehn

B.S., Massachusetts Institute of Technology (2009)

Submitted to the Department of Materials Science and Engineering
in partial fulfillment of the requirements for the degree of

Doctor of Philosophy in Materials Science and Engineering

at the

MASSACHUSETTS INSTITUTE OF TECHNOLOGY

September 2014

Author .....
Department of Materials Science and Engineering
August 6, 2014

Certified by .....
Alfredo Alexander-Katz
Walter Henry Gale Associate Professor of Materials Science and Engineering
Thesis Supervisor

Accepted by .....
Gerbrand Ceder
Chair, Departmental Committee on Graduate Students

Interactions of Environmentally-Responsive Nanoparticles with Synthetic and Biological Membranes

by

Reid Chi Van Lehn

Submitted to the Department of Materials Science and Engineering
on August 6, 2014, in partial fulfillment of the
requirements for the degree of
Doctor of Philosophy in Materials Science and Engineering

Abstract

Nanoparticles (NPs) have recently emerged as a versatile new materials platform for biomedical applications. By tuning their surface functionality, NPs can be engineered to resemble proteins in terms of size, shape, and chemistry, making them ideal for use *in vivo*. However, a theoretical understanding of how NPs interact with the biological milieu has lagged far behind experiments. In particular, it is critical to gain physical insight into the behavior of NPs at cell surfaces in order to minimize cytotoxic side effects while maximizing NP efficacy.

In this thesis, I use several biomolecular simulation techniques to model the interactions of amphiphilic, monolayer-protected NPs with lipid bilayers. This work is motivated by the recent experimental finding that certain gold NPs can penetrate into cells via an unexplained non-endocytic, non-disruptive mechanism. I propose that such a penetration process is possible if the surface properties of the NP can effectively reorganize in the presence of the lipid bilayer. I show that such *environmentally-responsive* NPs can stably insert into lipid bilayers as a precursor to cell penetration. The thesis divides this study into three Parts.

In Part I, I study the thermodynamics of NP-bilayer interactions using both a coarse-grained methodology and a novel implicit bilayer, implicit solvent model. I show that NPs with flexible ligands can fuse with lipid bilayers by "snorkeling" charged end groups out of the bilayer core and into solution. Several experimental studies confirm aspects of this fusion hypothesis and indicate that fusion may be a precursor to cellular internalization. In Part II, I use atomistic molecular dynamics simulations to uncover the kinetic pathway for NP-bilayer fusion. Fusion occurs spontaneously if the NP comes into contact with lipid tail protrusions which occur stochastically over long timescales. In Part III I perform initial studies on cooperative NP behavior. I first show that NPs must be carefully engineering to avoid aggregation in solution prior to contact with the bilayer. I then show that embedded NPs induce membrane deformations similar to those around transmembrane proteins, a finding that implies thats NPs may aggregate due to membrane-mediated forces. On the basis of these results, I propose several examples of cooperative interactions that bear future investigation.

The findings of this thesis are a comprehensive study of novel nano-bio interactions that reveal a previously unknown pathway for NP-bilayer fusion. Moreover, the physicochemical similarity between the NPs studied here and both other NP formulations and proteins implies that the results may generalize to a large variety of other synthetic and biological systems. This work will be essential in guiding the design of novel biomaterial systems for bioimaging, biosensing, and drug delivery applications and provides significant physical insight into behavior at the cell surface.

Thesis Supervisor: Alfredo Alexander-Katz
Title: Walter Henry Gale Associate Professor of Materials Science and Engineering

Acknowledgments

This thesis is the culmination of years of work that would have been impossible without the dedication and support of so many colleagues, family members, and friends. While I only have space to thank a small fraction of the people who made this possible, I truly appreciate everyone who guided me on this path and I could have not made it this far without you.

I am endlessly grateful to my adviser, Prof. Alfredo Alexander-Katz, whose infectious enthusiasm for science, incredible creativity, and constant dedication to his students has been inspirational. Under Alfredo's guidance I have grown immeasurably as a scientist and I thank him for giving me the confidence to continue pursuing my academic dreams. I am also thankful to my lab mates, especially the original Alexander-Katz group pioneers (Charles, YJ, and Hsieh). It has been a pleasure watching us all grow as researchers and friends, and I will always remember starting out with you in the basement of Building 12. I also want to thank the more recent additions to the Alexander-Katz group - Josh, Juan, Yi, Karim, Mukarram, Ric, and Jiaqi - for nurturing an engaging, collaborative atmosphere that has made every day a joy. The group is in excellent hands and I look forward to seeing what you all accomplish in the future.

Beyond my group members, I have been very fortunate to have had the privilege of working with an incredibly talented set of collaborators around the world. I want to first thank Prof. Francesco Stellacci who introduced me to Alfredo's work when I was still a confused undergraduate, then continued on as an experimental collaborator for the years to come. Similarly, I am indebted to Prof. Darrell J. Irvine whose enthusiasm, ideas, and support for our collaboration has been invaluable. I also thank Darrell and Francesco's students, Prabhani Atukorale, Sabrina Yang, Randy Carney, and Maria Ricci, who are all brilliant and dedicated scientists, creative collaborators, and wonderful friends. Finally, I want to thank my thesis committee, Prof. Michael Rubner and Prof. Krystyn Van Vliet, not only for their feedback and guidance on this project but also for inspiring me to continue in research after introducing me to biomaterials during my undergraduate classes at MIT.

Finally, I would never have made it this far without the encouragement and guidance of my family and friends. My parents, sisters, grandmother, and extended family have always been amazing motivators, advisers, and cheerleaders, and I thank them for their unwavering confidence in me and for setting the bar so high. I also want to thank Nicole for standing by my side for these last few years. Graduate school would not have been the same without you, and I am so glad that we could do it together. Lastly, I want to thank all of my friends who have made my time at MIT so wonderful. While the names are too many to list, I want to thank especially all of my friends in DMSE, the men of Phi Delta Theta, the members of DT over the years, and the staff over at the Thirsty Ear. It has been an honor and privilege knowing you all.

Table of Contents

List of Figures

List of Tables

Chapter 1
Introduction

In recent years, nanoparticles (NPs) have emerged as an exciting new class of material with diverse applications in biology. A NP can be simply defined as a particle with a diameter ranging from 1-100 nanometers [1]. Given this broad definition, the generic term nanoparticle has been applied to a large set of materials of varying core chemistry, surface properties, size, and shape. As a result of this design flexibility, an enormous variety of NPs have been engineered for use in targeted drug delivery, bioimaging, and biosensing applications, often inspired by examples from biology. However, physical insight into the interactions of NPs with biological materials is still largely lacking despite these engineering achievements. In particular, many applications require NPs to either interact with the cell membrane directly or bypass the membrane to reach the cell interior. Designing NPs for this goal requires a detailed molecular understanding of NP-membrane interactions to design NPs for efficient cellular entry with minimal toxic side effects.

In this thesis, I will use molecular simulation techniques to show that NPs protected by amphiphilic, environmentally-responsive surface monolayers can stably fuse with lipid bilayers via a novel mechanism. Inspired by previous experimental studies, I will demonstrate that experimental observations of non-disruptive, non-endocytic cellular penetration may be related to favorable interactions between the NP surface and the hydrophobic core of the lipid bilayer. Such interactions require that the surface properties of the NP dynamically rearrange to minimize the exposure of charges to the bilayer core while maximizing hydrophobic driving forces. This thesis presents a physical understanding of this novel interaction pathway between NPs and both synthetic and biological membranes that will be invaluable for guiding the design of NPs for future biomedical applications.

1.1 Biological applications of nanoparticles

NPs have become prominent materials for bioengineering applications in part because NPs can mimic typical globular proteins in terms of solubility, surface chemistry, and size. The most common current biological applications of NPs can be largely be divided into three categories: imaging, sensing, and the targeted delivery of small molecules such as drugs or DNA. In imaging applications, the NP is designed to emit a detectable signal in the presence of a target molecule or cell [2, 3, 4]. For example, a NP might fluoresce only in the presence of an acidic tumor microenvironment. Similarly, NPs used in sensing applications are typically engineered to exhibit a modified signal upon the adsorption of specific molecules [5, 6]. In this case, the emission intensity of the NP might be altered upon the binding of an analyte to the NP surface. In targeted delivery applications, the NP acts as a vehicle to release desired molecules at specific sites within the body [7, 8]. For instance, in drug delivery applications NPs might bind with cancer cells in order to release drugs

locally and minimize harmful side effects.

Several classes of NPs have already been developed for these applications and can be categorized on the basis of their composition and structure. One possible classification is to broadly describe NPs as being either "soft" or "hard". Soft nanoparticles are self-assembled from molecular constituents such as lipids or polymers. For example, polymeric NPs are cross-linked polymeric capsules frequently used in drug delivery by having crosslinks degrade at a target site to release encapsulated cargo [9, 10, 11]. Liposomes are hollow spheres composed of an outer lipid bilayer self-assembled synthetically as an analogue to biological vesicles. Like polymeric NPs, liposomes are often designed to encapsulate materials for targeted delivery applications [12, 13, 14]. The second class of NP is hard NPs with cores composed of metal, silica, semiconductor materials, or combinations of these components. The surface properties of these NPs are determined by molecules grafted to the core. Several different metal substrates have been used in the literature with the most common choices being either gold or silver in part due to the availability of well-established synthetic techniques [3]. Gold NPs are particularly useful for imaging and sensing applications due to their surface plasmon resonant properties which can be used to identify molecular contact at nanometer resolution [2, 15, 16]. NPs made of semiconductor materials, more commonly referred to as quantum dots, are typically engineered to exhibit size-dependent fluorescence properties for imaging applications [17, 18]. In addition to these materials, magnetic NPs that incorporate iron into the core have also been used for imaging applications [19] or to induce cell death by local heating [20]. Finally, carbon-based NPs, such as fullerenes or carbon nanotubes, have been increasingly used in biological applications [21]. However, these NPs are less likely to be water-soluble due to their hydrophobicity which may be limiting in some applications. These examples represent only a very small fraction of the many types of NPs currently in development and several NP designs are already in clinical trials [22].

Regardless of the exact application or NP composition, the desired NP must possess a few general characteristics. The most important property is biocompatibility, which means that the NP must be able to achieve its desired goal without inducing toxic side effects or eliciting an adverse immune response [24]. A second requirement useful for most applications is the ability for the NP to be targeted to specific areas of the body, a feature particularly important for delivery applications [25]. NPs might be directed to a variety of targets, both extracellular (such as the surface of a cancer cell) or intracelluar (such as the cytosol or nucleus). A final property is the ability of the NP to achieve its purpose without being rapidly eliminated by the immune system, although this issue might be circumvented by local injections [26]. All of these requirements can be achieved by carefully tuning NP surface properties that determine interactions with the biological milieu [27, 28]. For example, biocompatibility can be achieved by tuning the charge and hydrophobicity of the NP surface to avoid inducing cell death, targeting is often facilitated by incorporating ligands that bind to overexpressed receptors on desired cell surfaces, and protein resistance is achievable by grafting a dense polymer layer to act as a steric barrier to adsorption. It is possible to engineer the surface properties of a NP to achieve these general design goals regardless of the functional purpose or exact

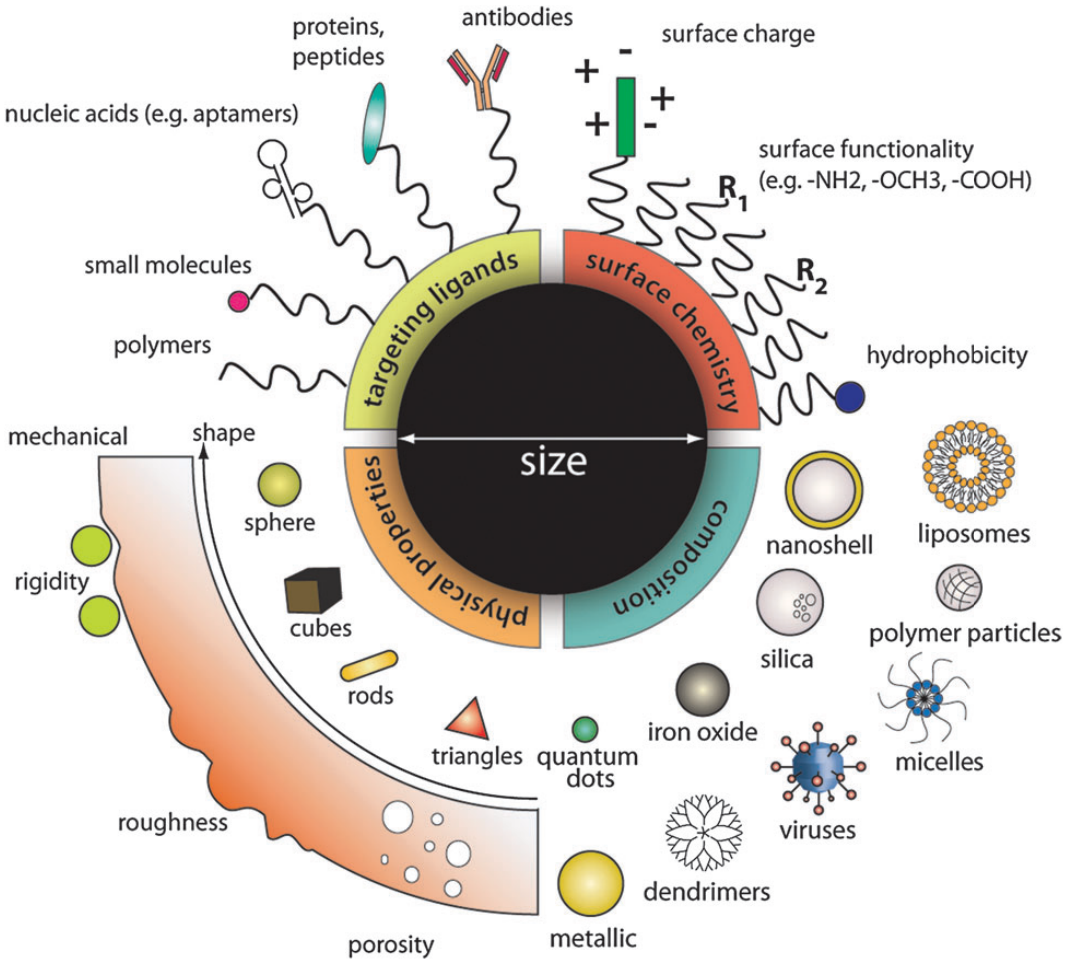

Figure 1-1: Summary of synthetic toolbox for nanoparticle design. Reproduced from Ref. [23] with permission of The Royal Society of Chemistry.

composition of the NP. For example, it is common to protect the surface of NPs with a polymer layer by either grafting the polymer to the core of a hard NP or incorporating it into the outer surface of a self-assembled soft NP [29, 30]. Functional molecules such as dyes, drugs, or targeting ligands can also be grafted to the surface, in which case the core serves primarily as a substrate [31]. While adding multiple surface components can lead to both spatial and compositional heterogeneities on the surface, increasingly complex multicomponent surface monolayers have been developed to fulfill multiple functional roles simultaneously [32]. The design process for choosing a NP system thus consists of a identifying a suitable core material, core size, and potentially core shape, and then optionally adding one or more surface components to impart biological stability or additional function. Fig. 1-1 illustrates the major tuning parameters involved in NP design along with particular examples currently in use. This large set of possible NP formulations necessitates the development of rational design rules to aid in engineering NPs for specific applications.

Despite the success of some current NPs, there are still a vast number of open questions regarding the exact interactions of NPs in biological environments. In particular, it is critical to gain a detailed

understanding of how NPs interact with cells, as ultimately the cell surface or interior is the final destination of many NPs for all three applications listed above. Moreover, toxic side effects related to NPs can often be attributed to disruptive interactions with the cell surface that trigger cell death [27]. The interface dividing the extracellular region of the cell from the intracellular compartment is called the cell membrane and is the surface of interest in understanding NP-cell interactions. Depending on the application, the NP must be able to at minimum avoid disrupting the membrane sufficiently to induce cell death, but also may need to penetrate through the membrane to deliver target molecules to the cell interior. However, finding a method to reliably penetrate into cells non-disruptively and efficiently is difficult due to the barrier properties of the membrane.

1.2 Properties of the cell membrane

The cell membrane is a complex, multicomponent soft material that regulates transport into and out of the cell. In eukaryotes, the cell membrane is composed primarily of lipids and a wide variety of membrane proteins [33]. Lipids are biological amphiphilies composed of a charged, hydrophilic head group and one or more hydrophobic tail groups. The most prominent lipids in biological membranes are phospholipids that contain a head group composed of an anionic phosphate group and possibly other charged moieties along with two aliphatic tails of varying length and saturation. The charge of biological phospholipids is always either negative or zwitterionic, leading to an overall negative net charge of biological membranes due to the uncompensated fraction of anionic lipids. In water, lipids self-assemble into a variety of structures to minimize the unfavorable solvation of the hydrophobic tails. One such structure is a bilayer in which two water-exposed hydrophilic head group regions sandwich a hydrophobic tail group region. The lipid bilayer forms the structural backbone of the cell membrane and maintains a thickness of approximately 5 nm [34]. Membrane proteins, which occupy roughly 50% of the membrane by volume, interact with the bilayer by either binding to the surface (peripheral membrane proteins) or embedding within the bilayer (integral membrane proteins) [33]. Integral membrane proteins can insert into one monolayer or fully span the entire lipid bilayer in which case the protein is classified as a transmembrane protein. Fig. 1-2a schematically shows the structure of the membrane and a typical phospholipid, DOPC. In order to stably embed within the bilayer, transmembrane proteins must have physicochemical properties that match the amphiphilic nature of the bilayer. As a result, most transmembrane proteins express hydrophobic amino acid side chains that preferentially interact with the hydrophobic core of the bilayer while hydrophilic side chains are exposed to the surrounding solvent [35]. Finally, in addition to the phospholipids and transmembrane proteins, there are several other classes of carbohydrates and other lipid species found within the membrane in smaller quantities. For example, cholesterol and sphingomyelin are single tail lipids that are found in significant proportions while membrane-bound sugars represent a large component of the extracellular matrix [33].

In additional to the compositional complexity of the membrane, the soft, fluid-like nature of the lipid bilayer allows the constant diffusion of membrane components throughout the lipid ma-

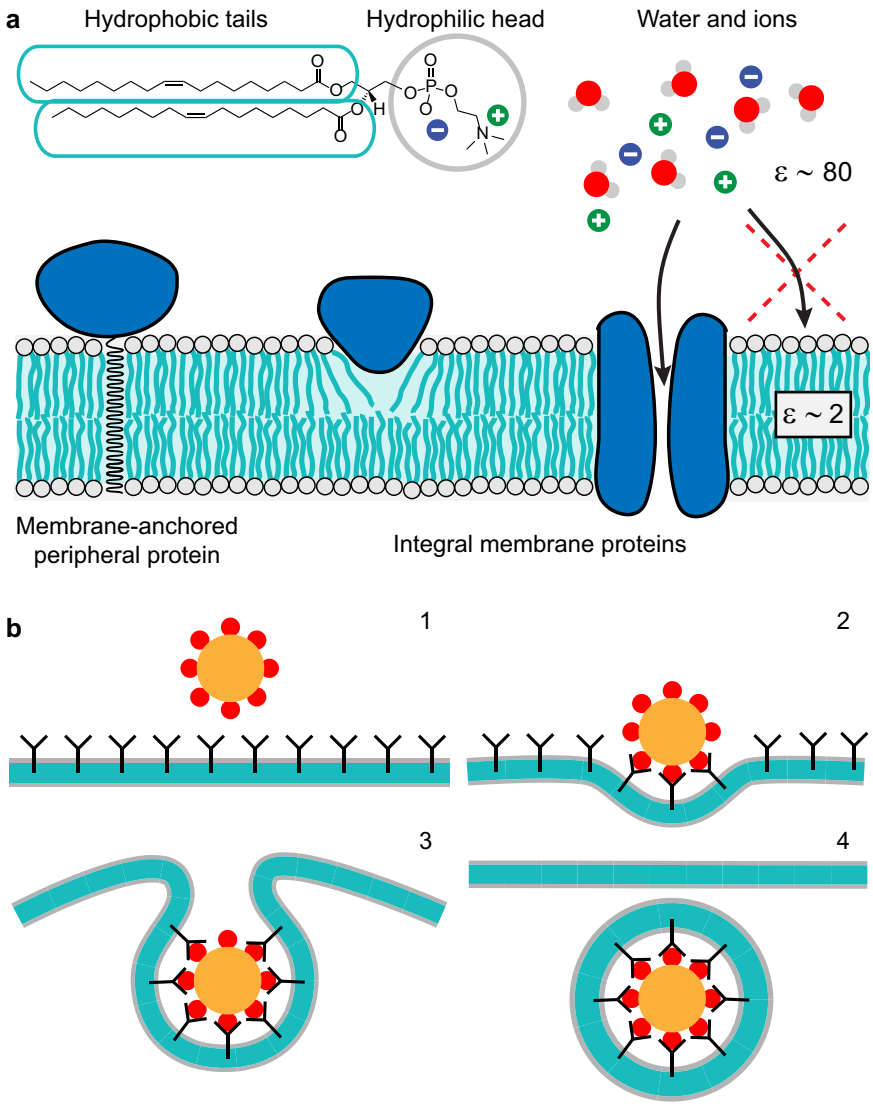

Figure 1-2: Overview of cell membrane properties. **a** The membrane consists primarily of amphiphilic lipids self-assembled into a bilayer that contains a variety of embedded proteins. The low dielectric constant bilayer core inhibits the translocation of ions and water which instead pass through channel or transporter proteins. **b** Overview of receptor-mediated endocytosis. Binding of receptors (black) to ligands on a molecule's surface (red) triggers membrane wrapping.

trix. The most common depiction of the membrane as a "fluid mosaic", a description originally attributed to Singer and Nicholson, captures the dynamic nature of the membrane [36]. The many different species of lipids and proteins can be pictured as constantly being in motion, and as a result the membrane can be imagined as an approximately 2D soup of different species diffusing freely. However, it is also important to recognize that as a soft material, fluctuations in the bilayer occur simply from thermal energy, leading to large out-of-plane undulations and even microscopic protrusions of lipids into solvent [37]. Moreover, the soft nature of the bilayer allows for local bilayer deformations in response to perturbations from membrane proteins or other biological

molecules [38]. The membrane thus has dynamically changing properties driven by thermal energy or modifications to the local environment.

Both the properties of the lipid bilayer and transmembrane proteins are critical for regulating transport across the membrane. Because of the low dielectric constant of the hydrophobic core region (≈ 2) compared to water (≈ 80), the lipid bilayer acts as a passive filter by imposing a large free energy barrier to prevent the diffusion of water, ions, and other hydrophilic molecules across the membrane [37]. While some limited passive diffusion is possible, this transport occurs over timescales on the order of hours to days [39], far too slow for biological processes that require rapid transport such as the propagation of neural signals. Instead, ions and water primarily cross the membrane through transmembrane channels either by an active transport process (e.g. voltage-gated ion channels) or through passive diffusion (e.g. water transport by aquaporins) [33]. For larger molecules, such as NPs, intracellular transport is usually achieved by a process called endocytosis. Endocytosis involves the wrapping of a portion of the cell membrane around a particular molecule (or volume of fluid) mediated by attraction to the membrane [40]. The attractive interactions can involve the binding of the substrate to particular protein receptors in the membrane or can involve non-specific interactions that bind the target molecule to lipids or other species directly. In either case, the bilayer plays a critical role in determining whether endocytosis proceeds as the wrapping process requires an input of energy to compensate for the mechanical deformation of the bilayer and thus the size, curvature, and shape of the transported substrate can determine endocytic efficiency [41, 42]. As wrapping proceeds, the substrate buds into the intracellular region until cytosolic proteins are eventually recruited to pinch off the bud, creating an intracellular endosome. The endosome, still containing the substrate, is then trafficked into the cell where receptors in the endosomal membrane allow the transport of protons that acidify the endosomal interior. If the substrate does not escape the endosome by some means and is not transported to other intracellular compartments, it will eventually be transported to a lysozyme to be degraded [40]. Fig. 1-2 shows a diagram illustrating receptor-mediated endocytosis as one possible endocytic mechanism.

Given the barrier properties of the bilayer, finding a method to transport NPs into the cell such that they can deliver molecules to the cytosol, act as imaging agents, or sense cytosolic material is a significant challenge. For example, charged NPs in principle are excluded from crossing the bilayer in the same manner as ions, but are too large to travel via existing channel proteins. Similarly, NPs that are targeted to the cell surface via interactions with particularly receptors will likely be endocytosed and may be trapped in endosomes without ever accessing the cytosol. One seemingly feasible solution might be to design uncharged, hydrophobic NPs that can bypass the hydrophobic core of the membrane, but ensuring the solubility of such NPs prior to cell interactions would be a significant challenge. Developing general methods to reliably penetrate into the cytosol without NP degradation would thus be extremely valuable for biomedical applications, but doing so requires circumventing the membrane's barrier properties.

1.3 Synthetic and biological mechanisms for membrane translocation

Several biological and synthetic systems can bypass the membrane via varying mechanisms despite its barrier properties. The most prominent biological peptides to achieve cellular internalization are called cell-penetrating peptides, or CPPs. CPPs are typically short ($\approx$ 20 amino acid) arginine-rich alpha helices that bear a net positive charge and contain a series of hydrophobic side chains to impart amphiphilic surface properties [43]. The mechanism by which CPPs enter the cell is still unknown and likely varies depending on the exact CPP structure, but several studies have hypothesized that CPPs either directly penetrate through the membrane due to electrostatic interactions between the cationic peptides and the anionic membrane [44, 45] or undergo endocytosis prior to escaping from endosomes [46, 47, 48]. Another possibility is that CPPs bind to the bilayer so strongly that they induce significant membrane curvature that facilitates internalization, perhaps with lipids forming an inverse micelle around the CPP [49, 50, 51]. Regardless of the exact mechanism, however, a downside of CPPs is that they may have toxic side effects [52]. Cytotoxicity may be related to the poration of the membrane, allowing the escape of cytosolic material (i.e. cytosolic leakage) that contributes to cell death. Such a mechanism may occur for CPPs that open pores during translocation [53, 54, 55]. Fig. 1-3a schematically shows several possible methods for CPP translocation.

A similar mechanism is responsible for cell death triggered by antimicrobial peptides (AMPs). AMPS, like CPPs, are typically small, $\approx$ 20 residue alpha helices rich in cationic and hydrophobic residues [56]. Unlike CPPs, AMPs typically organize their side chains such that the helix has a cationic face and a hydrophobic face, generating a "Janus" like morphology. AMPs first bind to the surface of the membrane driven by electrostatics until a sufficiently high AMP concentration drives the creation of a membrane pore to reduce the lateral surface pressure created by AMP-AMP interactions. The pore can be stabilized either by strong interactions with the charged AMPs (in the "carpet model" of pore formation) or by the insertion of the hydrophobic face of the AMPs into the hydrophobic region of the bilayer (in the "barrel-stave model" of pore formation) [57, 58]. Cytosolic leakage through the pore then kills the cell. Fig. 1-3b summarizes both models for pore formation. Given the physicochemical similarities between AMPs and CPPs, such pore formation may be induced by CPPs as well.

Another important class of membrane-active peptides are fusion peptides, which as their name suggests facilitate vesicle-vesicle fusion or fusion between viruses and membranes. Fusion peptides are typically hydrophobic and insert into the membrane where they are believed to promote membrane curvature [59, 60, 61]. While fusion peptides biologically facilitate the formation of curved intermediates in order to stabilize a highly curved stalk-like intermediate in the vesicle fusion pathway [62], the incorporation of fusion peptides alone into vesicles is sufficient to cause the leakage of vesicle contents into solution [63]. This finding thus suggests again that some property of the peptide alone is sufficient to disrupt the membrane, and again may lead to cytotoxic effects.

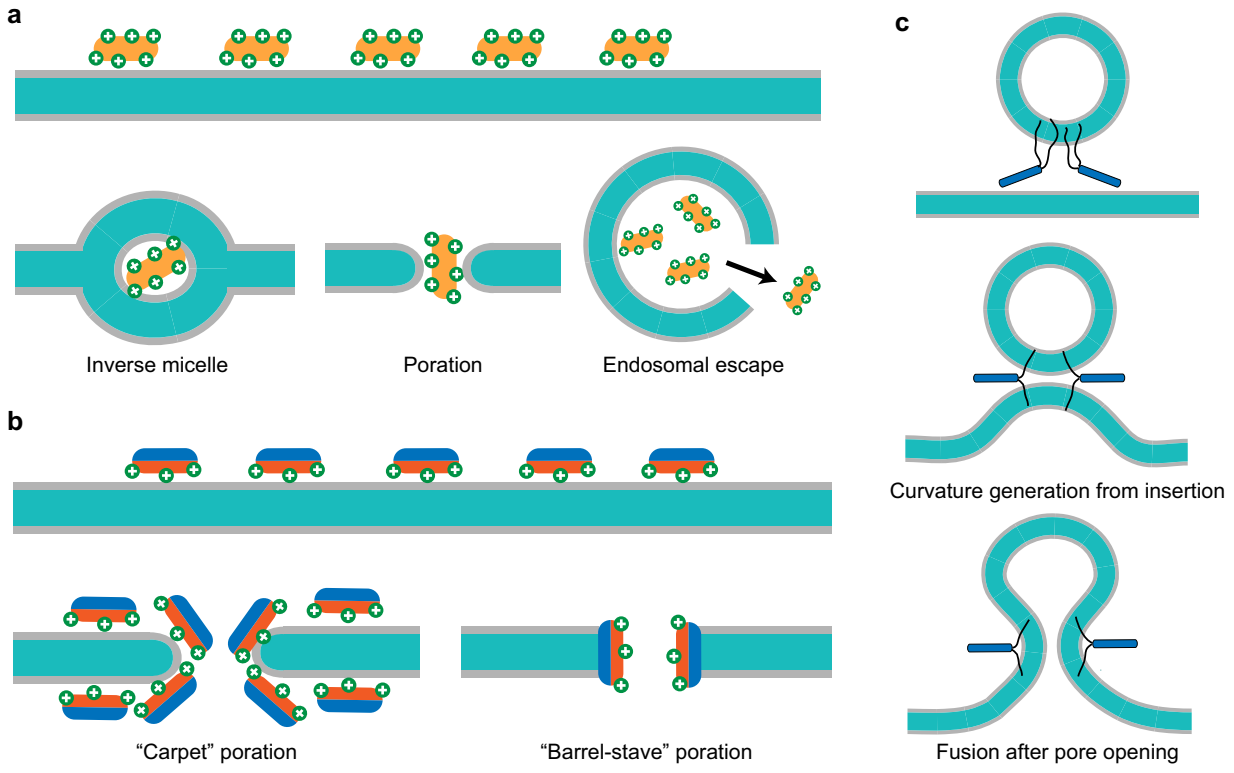

Figure 1-3: Schematic of several biological protein-membrane interactions. **a** Charged, cationic cell-penetrating peptides first bind to the membrane surface before forming inverse micelle structures, directly penetrating into the cell via porating the membrane, or triggering endocytosis and eventual endosomal escape. **b** Antimicrobial peptides form pores in the membrane at high concentration by either inducing a hydrophilic pore stabilized by electrostatic interactions (carpet model) or inserting hydrophobic moieties into the bilayer core (barrel-stave model). **c** Fusion peptides facilitate membrane fusion by binding to a target membrane and inducing curvature that destabilizes the membrane and lowers the barrier for fusion intermediates.

Finally, both peripheral and integral membrane proteins have favorable interactions with the bilayer as noted previously, although they may not directly achieve cytosolic entry. Peripheral proteins are able to bind to the bilayer via a combination of electrostatic and hydrophobic interactions [64]. One possible method is by inserting amphipathic helices into the bilayer to initially anchor the protein before lipids are recruited to further stabilize binding electrostatically [65]. As previously noted, transmembrane proteins generally have amphiphilic surfaces that match the amphiphilic structure of the bilayer, leading to hydrophobic amino acids primarily exposed to the hydrophobic core of the bilayer. However, recent biophysical studies on the free energy cost associated with mutating amino acids on transmembrane proteins have shown a surprisingly low barrier for incorporating hydrophilic side chains into the hydrophobic core region of the bilayer [66, 67, 68, 69]. These "biological hydrophobicity" scales suggest that the favorable driving force for incorporating hydrophobic residues in the bilayer can overcome the relatively low penalty for inserting charged side chains. While the reason the penalty for inserting hydrophilic residues is so low is still un-

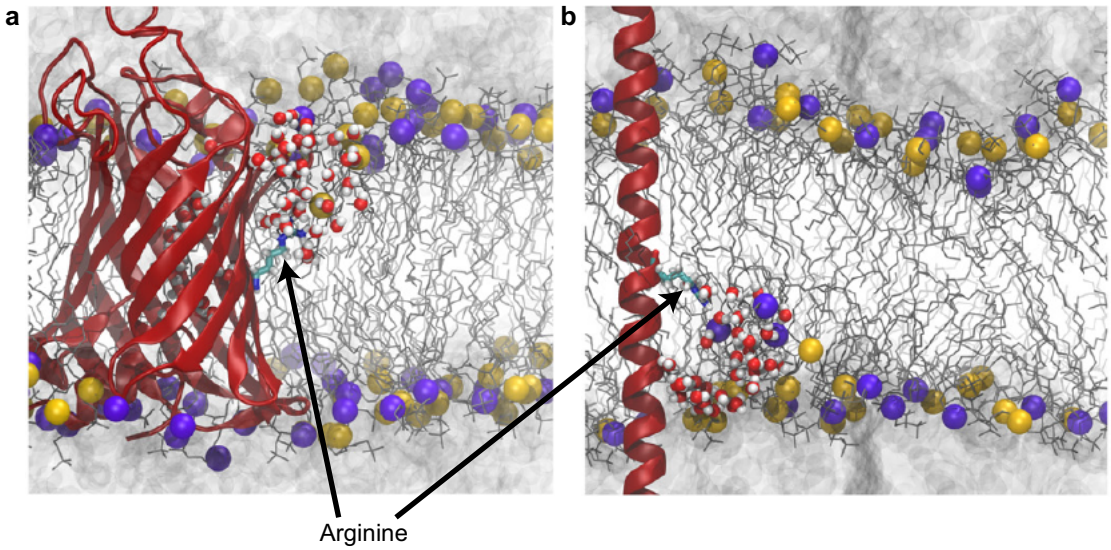

Figure 1-4: Simulation snapshots of arginine snorkeling from molecular dynamics simulations. The arginine is positioned at the center of the bilayer and is attached to either a OmpLA β-barrel backbone (a) or a polyleucine helix backbone (b). The protein is drawn in red, the arginine in teal, water as red/white balls, hydrophilic lipid head groups as blue/yellow, and lipid tails as grey lines. Reprinted from *Biophysical Journal*, vol 102, J. C. Gumbart and B. Roux, "Determination of membrane-insertion free energies by molecular dynamics simulations", 795-801, ©2012, DOI: 10.1016/j.bpj.2012.01.021 with permission from Elsevier (Ref. [75]).

der debate, several theoretical studies have concluded that the "snorkeling" of charged groups can explain the lowered penalty [70, 71]. During snorkeling, the charged group of the amino acid fluctuates toward the nearest fluid interface while the membrane locally deforms, allowing the charge to be solvated by water while the residue still resides within the membrane region [72, 73, 74, 75]. These coupled fluctuations are essentially a response of the arginine to its local environment, and emphasize the soft nature of the bilayer to allow such deformations to occur. Fig. 1-4 shows examples of arginine snorkeling from recent molecular dynamics simulations [75]. The ability of side chains to snorkel implies that transmembrane proteins may contain more hydrophilic side chains than would be expected.

Inspired in part by these biological examples, there have been several NP formulations that seek to achieve cytosolic entry. In practice, NPs have largely sought to mimic the structure of CPPs in terms of mixing hydrophobic and cationic surface properties in order to achieve direct penetration into the cytosol. Unfortunately, most examples of cationic NPs in the literature induce cell disruption and cytotoxicity, perhaps in part due to the similarity between CPPs and AMPs, indicating that small changes in surface properties can lead to membrane disruption [76, 77, 78, 79]. Another synthetic strategy is to target NPs to the cell surface for internalization by endocytosis, and then incorporate a mechanism to encourage endosomal escape to allow cytosolic access. Typically, this strategy relies on the change in pH upon endosomal uptake to trigger the release of osmolytes (or adsorb protons to induce the influx of osmolytes from the cytosol) that osmotically stress the

membrane, allowing for leakage into the cytosol [80]. However, this approach suffers from the possibility that the NP and its cargo are degraded before endosomal escape occurs, hampering delivery efficiency. While other diverse strategies exist, such as incorporating fusion peptides, grafting CPPs directly to a NP surface, etc., nearly all approaches have serious concerns regarding toxicity or the ability to actually achieve cytosolic access [23]. There is a significant need for new approaches to NP design to maximize favorable bilayer interactions and avoid cytotoxic side effects.

1.4 Amphiphilic, monolayer-protected gold nanoparticles

The several biological and synthetic approaches to achieving cytosolic penetration all come with significant drawbacks, particularly due to the likelihood of pore formation and cell death, which significantly hampers the biomedical applications of NPs as well as underscoring the difficulty of bilayer penetration. An ideal approach would be to achieve direct cell penetration without any bilayer disruption or endosomal trapping, facilitating cytosolic access without toxic side effects. In 2008, a joint study by the Irvine and Stellacci groups at MIT demonstrated such behavior by a new class of amphiphilic, monolayer-protected gold NPs [81]. In their work, the authors used NPs with gold core diameters of approximately 4.5 nm that were protected by a mixed-monolayer of two oligomeric ligands. The first ligand, 11-mercapto-1-undecane sulfonate (MUS), has a sulfur head group, hydrophobic backbone with eleven alkyl groups, and is end-functionalized with a hydrophilic sulfonate group. The sulfonate head group has a pKa of approximately 2 and is nearly 99% dissociated at physiological pH, bearing a single negative charge. The second ligand, 1-octanethiol (OT), consists of a sulfur head group and eight hydrophobic alkyl groups and is purely hydrophobic. Both ligands were grafted to the gold core via thiol chemistry where the sulfur groups bond with the gold atoms leaving the backbones free to fluctuate in the surrounding volume [82]. The combination of the purely hydrophobic OT ligand and the amphiphilic MUS ligand makes the entire NP monolayer amphiphilic and water-soluble [83]. Moreover, by adjusting the relative ratio of MUS:OT, the relative hydrophobicity of the monolayer can be tuned. Fig. 1-5 shows the structures of the ligands used and a representation of the amphiphilic NP monolayer.

By incorporating multiple ligand species into a mixed monolayer, the relative nanoscale positions of the two ligand species on the NP surface becomes another potential tuning parameter. The Stellacci group demonstrated that if two grafted ligand species have different lengths, the ligands will preferentially segregate into a "striped" pattern with a domain size on the order of a single molecule [84, 85, 86, 87, 88, 89, 90]. The origin of this ordering is hypothesized to be due to entropic effects - the longer ligands prefer to reside next to shorter ligands in order to maximize the free volume accessible to the long ligands and thus maximize their conformational entropy [91]. Several theoretical studies have shown that such a driving force can induce stripe formation for sufficient ligand length mismatches and correct ratios of the two components [91, 92, 93, 94]; Appendix B presents one such approach that achieves stripe formation. Furthermore, Verma et al. found that stripe formation could be inhibited by introducing branched points in the OT

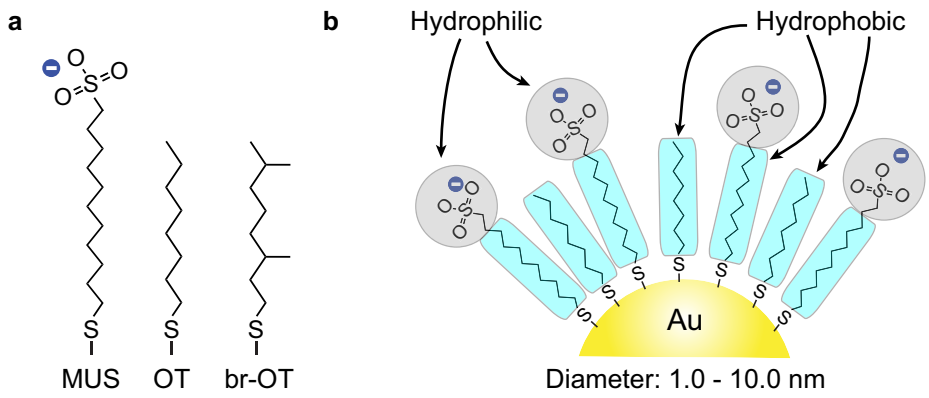

Figure 1-5: Chemical structure of amphiphilic NPs. **a** Structures of the three ligands used in original experiments. **b** Representation of amphiphilic monolayers with both hydrophobic alkane backbones and hydrophilic sulfonate groups.

ligands, creating branched-octanethiol (br-OT) ligands that preferentially formed uniformly mixed monolayers, possibly due to steric effects [81]. The structure of br-OT is shown in Fig. 1-5.

Several key aspects of these NPs distinguish them from previous designs, making them potentially ideal for cellular interactions. First, a novel one-phase synthesis method was used to incorporate the water-soluble MUS ligands into the surface monolayer [83]. This approach allowed for the incorporation of MUS ligands into monolayers that possessed a large number of hydrophobic ligands. The use of MUS itself was critical, as this ligand was found to be extremely water-soluble; indeed, NPs with ratios of MUS:OT in ratios as high as 1:4 MUS:OT were found to be highly soluble in aqueous solution. Incorporating large numbers of hydrophobic ligands could maximize favorable interactions with the hydrophobic core of the bilayer as previously illustrated by the biological hydrophobicity scales discussed above [66, 67, 68, 69]. In contrast, swapping the sulfonate end group for a carboxylic acid group (i.e. switching from mercaptoundecane sulfonate to mercaptoundecanoic acid) dramatically reduced the solubility such that only all-MUA compositions were soluble [83]. Incorporating MUS thus allowed for highly water-soluble NPs that contained much larger amounts of hydrophobic material than previously possible. Another major distinction between these NPs and previous formulations was the anionic surface charge, again due to the use of MUS. As noted above, cationic NPs are often associated with cytotoxic side effects and are much more cytotoxic than anionic NPs [95, 76, 77, 96, 78, 79], likely due to strong electrostatic interactions between the anionic membrane and cationic ligands. While modulating the hydrophobicity of cationic NPs can reduce membrane disruption, this was again previously limited by the solubility of previous NPs [97, 15, 30]. Finally, the size of the 4.5 nm NPs, even with a 3 nm ligand layer, was close to the thickness of the bilayer ($\approx$ 5 nm). This size range is also similar to the size of the membrane-active proteins discussed above. Moreover, the NPs are also small enough that they are taken up inefficiently by endocytosis, maximizing residence time at the bilayer surface without internalization and may be useful for achieving direct penetration prior to endocytosis [98, 99]. The amphiphilic NPs thus possessed a unique combination of ideal size, solubility, surface charge, and

surface hydrophobicity that could maximize favorable interactions with cell membranes.

Using multiple different NP surface compositions, Verma et al. showed that the amphiphilic NPs could spontaneously penetrate into the cytosol via a non-endocytic pathway with no signs of membrane disruption or toxicity [81]. The efficacy of this direct penetration strongly depended on both NP composition and monolayer morphology. Three NP compositions were tested: all-MUS NPs, which contained only the amphiphilic MUS ligands; 2:1 MUS:OT NPs, which were more hydrophobic than all-MUS NPs and contained ligands in a striped pattern as discussed above; and 2:1 MUS:br-OT NPs, which were of similar zeta potential and hydrophobicity as the 2:1 MUS:OT NPs but but with a uniform rather than striped surface morphology. The NPs were labeled with the fluorescent dye BODIPY, incubated with mouse dendritic cells at both 37°C and 4°C, and visualized using confocal fluorescence microscopy after 3 hours. Confocal images showed that all-MUS and 2:1 MUS:br-OT NPs largely exhibited small sharp punctate fluorescence patterns that would be consistent with entrapment in endosomes (reproduced in Fig. 1-6). In comparison, the MUS:OT NPs exhibited a diffuse pattern of fluorescence indicative of cytosolic access rather than endosomal trapping. Moreover, at 4°C, a temperature sufficiently low that endocytic processes should be inhibited, the MUS:OT NPs still showed significant cellular uptake in comparison to both the all-MUS and MUS:br-OT NPs. Quantification of the fluorescence signal indicated an approximate 8x increase in fluorescence relative to cells lacking NPs for MUS:OT compared to a 1.5-2x increase for all-MUS and MUS:br-OT NPs respectively. To confirm non-endocytic entry, uptake was also shown to occur at 37°C but in the presence of drugs designed to inhibit endocytosis; again uptake was observed primarily by MUS:OT NPs. The results were found to not depend on the presence of extracellular serum implying that internalization was not mediated by the non-specific attachment of serum proteins. Transmission electron microscopy (TEM) images further confirmed that direct cytosolic access was achieved by the NPs with the extent of internalization again following the pattern of 2:1 MUS:OT > 2:1 MUS:br-OT > all-MUS. Finally, the penetration process was shown to be non-disruptive by monitoring either the influx or efflux of membrane-impermeable dyes during the penetration process. While cationic control NPs triggered dye leakage, the amphiphilic, anionic NPs did not. Similarly, only 34% of cells grown for 24 hours after incubation with cationic control NPs survived compared to nearly 90% of NPs incubated with the amphiphilic NPs. This extensive set of experiments thus confirmed a new non-endocytic, non-disruptive membrane penetration pathway seemingly related to both monolayer composition and morphology [81].

The finding that these amphiphilic NPs could directly access the cytosol with negligible toxicity, while still being water-soluble, could be extremely powerful for the applications discussed previously. Indeed, these NPs have already been used for oligonucleotide delivery [100] and intracellular imaging [101]. However, a major issue in maximizing the utility of the NPs is the lack of understanding of the mechanism by which direct penetration occurs. The experimental results suggest that the mechanism does not involve transient pore formation when compared to cationic NPs. The results also provide evidence that both the ratio of hydrophilic:hydrophobic components and the ligand organization are critical parameters. However, there is a potentially large set of other unexplored

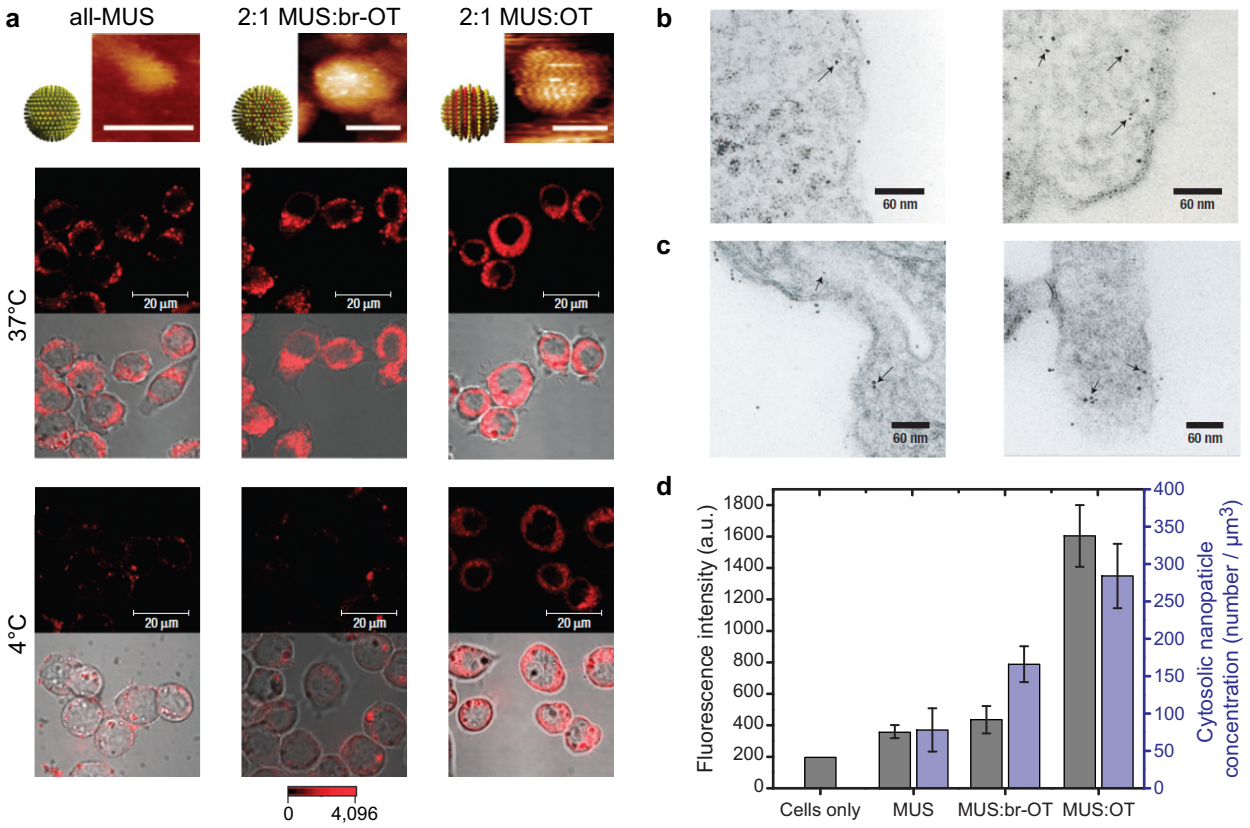

Figure 1-6: Summary of experimental findings on non-disruptive cell penetration by amphiphilic nanoparticles. Adapted with permission from Macmillan Publishers Ltd: *Nature Materials*, Vol 7, A. Verma et al, "Surface-structure-regulated cell-membrane penetration by monolayer-protected nanoparticles", 588-595, ©2008, DOI: 10.1038/nmat2202 (Ref. [81]). **a** Confocal fluorescence microscopy images of three NP compositions being taken up by cells at both 37°C and 4°C. **b** TEM images of 2:1 MUS:OT NPs in the process of cytosolic entry. Arrows point out particular examples. **c** TEM images of 1:2 MUS:OT NPs during direct penetration. **d** Summary of composition-dependent uptake from both fluorescence measurements (black) and TEM images (blue), showing similar trends for both measurement techniques.

tuning parameters, including NP size, ligand lengths, and ligand grafting densities that could be optimized to facilitate (or hinder) cellular entry. Achieving a detailed understanding of the translocation mechanism could thus enable such optimization and expand the use of these NPs in clinical applications. Moreover, given the ability to tune NP surface properties independent of exact core composition or NP function, understanding the mechanism of cellular entry could lead to general design guidelines applicable to a wide range of NP architectures. Gaining such a molecular-level understanding of this novel membrane interaction is the goal of this thesis.

1.5 Molecular simulation provides means to study NP-bilayer interactions

Experimental methods for probing molecular mechanisms for NP-bilayer interactions are limited due to the difficulty in reaching short length- and time-scales of relevance. Instead, molecular simulations have emerged as a valuable method for gaining physical insight into these processes. Molecular simulations are capable of resolving behavior at length scales far smaller than achievable experimentally; for example, molecular dynamics simulations can predict membrane deformations at atomistic resolutions [102]. Such simulations can act as a "computational microscope" to identify nanoscale behavior that can be used to predict macroscopic behavior [103]. However, molecular simulations are limited by available computational power, which effectively limits the maximum size and time able to be modeled. In recent years, a large number of studies have begun to examine interactions between various types of NPs and lipid bilayers [104, 105, 106, 107, 108, 42, 109, 110, 54, 111, 112]. The study of NP-bilayer translocation has been of particular interest as computational resources have become sufficiently powerful to model this process. However, previous simulation approaches have largely been limited by the use of unphysical forces to bias NP translocation or by the use of highly coarse-grained simulation techniques that may underestimate repulsive forces in the system.

Several initial simulation studies of NP-bilayer interactions used the coarse-grained (CG) MARTINI model. The MARTINI model is parameterized to group four heavy atoms into single effective atoms, sacrificing some accuracy in the representation of atomic fluctuations and physicochemical forces for enhanced computational efficiency. In the original MARTINI model, all water molecules were coarse-grained into uncharged water beads. The lack of solvent polarity thus eliminated the effective dielectric constant of water which was instead globally set to 15 (instead of 80) to partially compensate for this effect [113]. As a result, electrostatic interactions in this model were unphysically enhanced by a factor for 4. Despite this deficiency, multiple simulations used this model to probe NP-bilayer interactions driven primarily by electrostatics. For example, multiple studies have examined interactions between cationic NPs and anionic membranes, often demonstrating rapid pore formation from single NPs [106, 114, 115, 116, 107]. The lack of accurate ligand fluctuations may also impact CG results as often the ligands were represented as single effective beads which may underestimate fluctuations considerably. This may play a significant role especially in modeling relative ligand arrangements [110, 107, 117]. Another popular method is dissipative particle dynamics (DPD) which uses a similar coarse-grained description of particles but models all intermolecular interactions using soft harmonic springs to speed up system dynamics by allowing unphysical overlap between beads. This method often also lacks explicit electrostatic interactions as well, often with a biasing force. DPD simulations have been used to model membrane penetration by NPs, but require fine-tuning of parameters without necessarily establishing their physical basis to achieve penetration behavior [105, 110, 108]. Field-based modeling strategies, such as self-consistent field theory or single-chain in mean field theory, have also been applied to membrane

systems, but these methods are primarily suited for studying thermodynamics and cannot capture system dynamics [118, 119]. While these methods are the most common, there are other examples of CG methods that again may not adequately model the steep penalty associated with exposing charged end groups to the bilayer core [120, 109]. While these CG methods may have benefits in terms of computational efficiency, their physical accuracy for modeling NP-bilayer interactions may be questionable.

Recently, the use of a polarizable water model in the MARTINI force field has improved the CG model's treatment of electrostatic effects [121], leading to its use in a recent study of pore formation by cationic NPs [54]. Similarly, a first atomistic model of NP-bilayer interactions was recently published, with its focus again on pore formation by cationic NPs [112]. These studies represent the first efforts to make more detailed models of interactions at this important interface, but there is still significant room for improved simulation techniques to aid in modeling the translocation of amphiphilic NPs.

1.6 Hypothesis: Environmentally-responsive behavior mediates NP-bilayer interactions

The finding of non-endocytic, non-disruptive membrane penetration strongly suggests that the anionic, amphiphilic NPs are able to favorably interact with the membrane via a completely different mechanism from cationic CPPs or NPs. It should be noted that in the hypothesized pore-formation process associated with CPPs or cationic NPs, the NPs never directly cross the hydrophobic core of the membrane. One possibility is that the amphiphilic NPs are able to directly cross the membrane to achieve intracellular entry. Such a process seems contrary to the known barrier properties of the membrane, particularly the inability for charges to directly cross the hydrophobic core. However, the low free energy cost associated with snorkeling might imply that similar dynamic changes to the arrangement of charge on the NP surface could minimize the penalty for charge insertion into the membrane. Similarly, the properties of membrane proteins demonstrate that incorporating hydrophobic material into the NP monolayer can maximize favorable interactions with the bilayer. The difference in internalization efficiency between all-MUS and more hydrophobic MUS:OT NPs suggests that the additional hydrophobic ligands, while presumably shielded from water in solution, might be able to drive favorable interactions when instead exposed to the bilayer environment [81].

Inspired by these biological examples, the central hypothesis of this thesis is that favorable NP-membrane interactions if the NP surface properties are environmentally-responsive. Specifically, I propose that the surface properties of a NP can effectively reorganize when in contact with the hydrophobic core of the bilayer in comparison to the properties in solution. Such reorganization would maximize favorable hydrophobic interactions between the NP surface and hydrophobic core of the bilayer while allowing charges to snorkel to the aqueous interface as in the case of amino acid side chains. By interacting with the hydrophobic core directly, the NP could access the cytosol without triggering the opening of membrane pores, and moreover without inducing membrane wrapping as

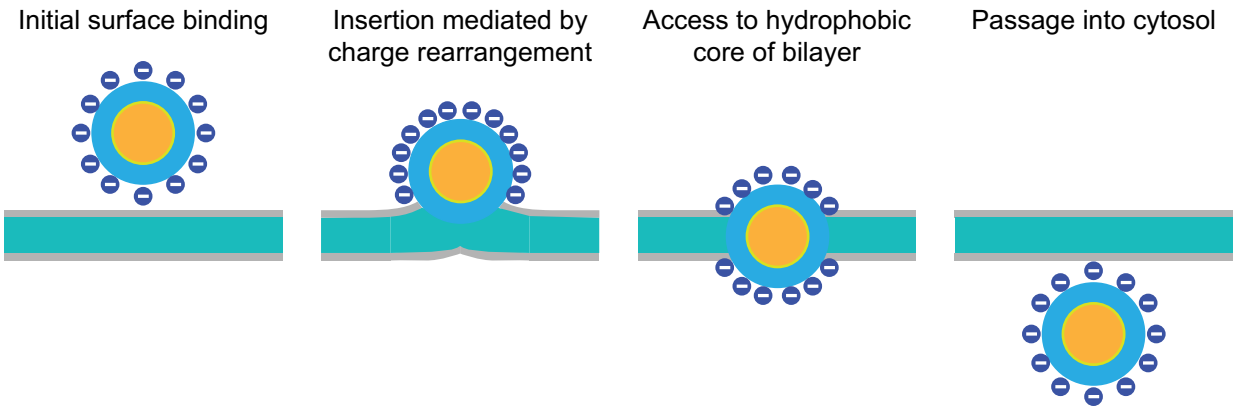

Figure 1-7: Proposed mechanism of environmentally-responsive NP-bilayer interaction. Charge rearrangement on the NP surface allows maximal exposure of hydrophobic NP ligands (blue) to hydrophobic bilayer core (teal) during insertion process, allowing NP to access cytosol non-disruptively.

in endocytosis. Given the physicochemical similarities between the NPs and protein analogues, it seems possible that the NPs could also exhibit similar properties as membrane-active proteins such as the transmembrane proteins or fusion peptides discussed previously, allowing further inspiration to be drawn from biological materials. Fig. 1-7 schematically shows the proposed process and specifically the rearrangement of charge necessary to facilitate direct interactions with hydrophobic lipid tails.

To evaluate this hypothesis, I will employ novel molecular simulation techniques in order to gain detailed physical insight into interactions at the NP-membrane interface. A key assumption made throughout this thesis is that NP-membrane interactions depend primarily on interactions with the lipid bilayer as it is the lipids that confer the barrier properties important to cellular penetration. The full compositional complexity of the membrane can then be minimized by only examining interactions between NPs and single-component bilayers as model cell membranes, allowing such behavior to be modeled over reasonable timescales. While this approximation clearly overlooks several important features, such as the presence of a transmembrane potential, the charge asymmetry between bilayer leaflets, and the compositional fluctuations that may impact bilayer permeability, the accuracy of the simulation predictions can still be compared to experiments on similar single-component lipid systems. Furthermore, by studying lipid bilayers as a general soft material, the exact biological composition is ignored and thus the findings can be generalized to a wide variety of NP-lipid interactions independent of the exact cell type.

I will explore two possible extremes of environmentally-responsive behavior. First, I will determine membrane interactions in the limit that the NP surface can globally rearrange the position of all surface ligands over a very fast timescale, effectively leading to optimal surface properties. Next, I will take the opposite extreme and treat the ligands as permanently grafted to a single point on the NP core, but able to fluctuate due to the flexible backbones of the ligands and extremely small NP

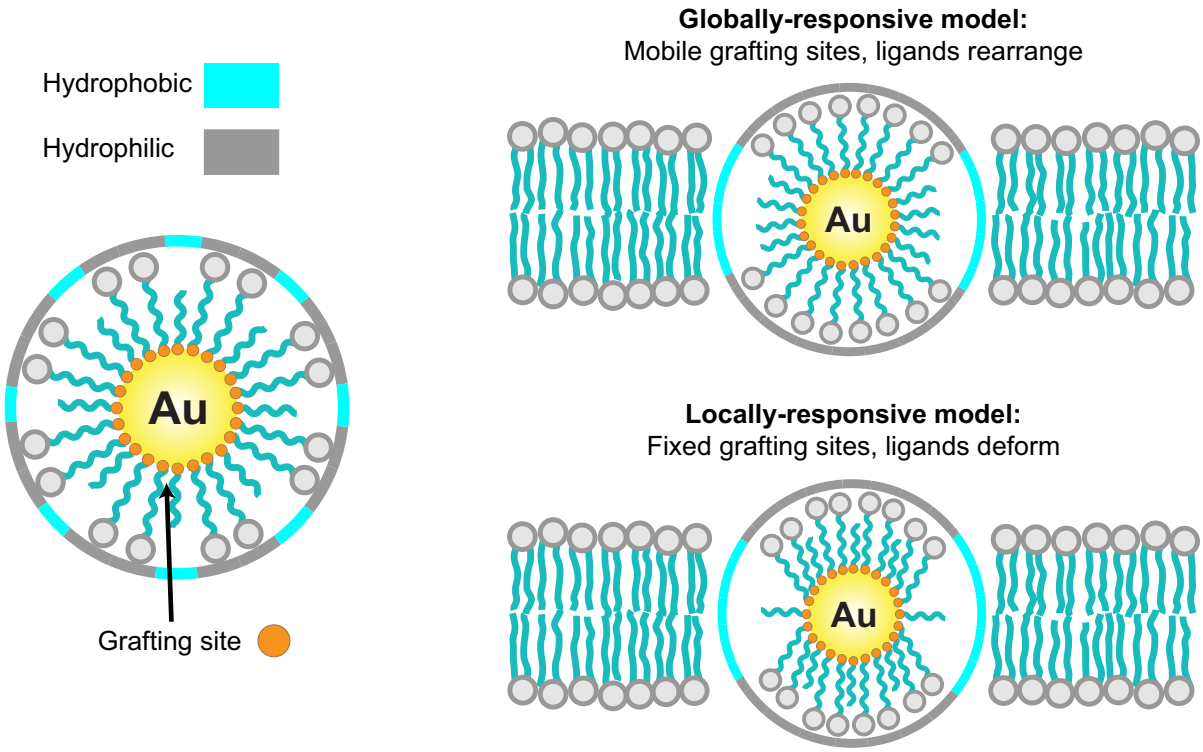

Figure 1-8: Schematic of globally- vs locally-responsive models. The hydrophobic and hydrophilic surface properties can adjust either due to the mobility of ligands on the surface (globally-responsive model) or due to ligand backbone deformations (locally-responsive model).

core diameters. Fig. 1-8 illustrates both of these models for environmental-responsiveness. In Part I, I will show that for either model, there is a thermodynamic driving force that prefers the fusion of the NP with the biological core into a final state resembling a transmembrane protein. In Part II, I will investigate the kinetics of this fusion process and show that it mechanistically resembles the first stages of vesicle-vesicle fusion. In Part III, I will show that cooperative interactions between NPs are critical to both their behavior in solution and their post-fusion behavior when embedded in the bilayer. Using these findings, I will discuss guidelines for designing NPs to optimally fuse with membranes, and also suggest mechanisms from which cytosolic access could occur. I expect that the findings of this thesis will be critical in developing both an enhanced molecular understanding NP-membrane interactions for both this NP system and others in the literature as well as providing rules to guide the development of future NPs for biomedical applications.

Part I

Thermodynamics of NP-bilayer interactions

Chapter 2

Environmentally-Responsive NPs: Global Rearrangement

Work in this chapter was published in:

R. C. Van Lehn and A. Alexander-Katz, "Penetration of lipid bilayers by nanoparticles with environmentally-responsive surfaces: simulations and theory" *Soft Matter*, **7**, pp. 11392-11404, 2011, DOI: 10.1039/c1sm06405c.

One hypothesis of this thesis is that there must be some physicochemical similarity between the surface of the NPs and the lipid bilayer to allow NPs to enter cells non-disruptively. However, for soluble, charged NPs, the expectation is that the charged ligands in their protecting monolayer will try to uniformly coat the particle surface to minimize electrostatic interactions. To have favorable interactions with the hydrophobic core, the surface of the particle must effectively rearrange its surface properties to display hydrophobic regions that can stably sequester within the bilayer interior. In other words, the NP surface must be environmentally-responsive in order to rearrange its properties in the presence of the bilayer.

In this Chapter, we will consider one limit of such responsive behavior by assuming that the NP surface is capable of *global rearrangement* - that is, the positions of ligands on the surface are completely unrestrained and can diffuse to maximize favorable interactions with the bilayer core. The ability for such rearrangement is supported by some experimental evidence. For example, studies of monolayer-protected NPs similar to the ones that inspired this work have analyzed the phase characteristics of the monolayer as a function of chain length [122, 91], composition [123, 124], and temperature [125], studies that suggest the ability of the monolayer to rearrange in response to changes in environmental conditions. It also has been suggested that these systems exhibit lateral surface mobility, providing a mechanism for rearrangement consistent with this approach [126, 127, 128]. The strongest evidence of such rearrangement occurs when these (or similar NPs) are positioned at the air-water interface where they can assume Janus-like morphologies within minutes to preferentially expose only hydrophilic ligands to water [129, 130, 131]. This work cumulatively suggests that surface rearrangement is possible within experimental timescales and may influence NP-bilayer interactions. Here, we will propose a new coarse-grained simulation model that couples a Monte Carlo model for surface rearrangement to a Brownian dynamics method for capturing molecular motion. Using this model, we will determine the effect of surface rearrangement on the interactions between a single NP and a lipid bilayer.

2.1 Model for globally-responsive NPs

In the globally-responsive model, ligands can rearrange to any position on the surface independent of their starting positions. It is assumed that all ligands are either hydrophobic or hydrophilic such that exposure to the hydrophobic core is energetically favorable for the former and unfavorable for the latter. To put the model in the most general terms possible, the physical mechanism of rearrangement is not explicitly defined and instead the surface is rearranged to minimize an effective surface energy which is a function of the surface composition, ligand positions, and interactions with the surrounding environment. Because ligands are able to rearrange without any constraints, the surface exhibits phase behavior that is biased by contact with the hydrophobic bilayer core.

A simple Ising model is used to represent interactions between the ligands. Interactions with the bilayer are included by treating the hydrophobic core as an effective field that contributes a term to each ligand's energy. The energy of ligand i is then defined as:

$$E_i = B_i - \lambda \sum_{j \in n(i)} \sigma_i \sigma_j \tag{2.1}$$

where B_i is the energy of the ligand interacting with the hydrophobic core of the bilayer, $n(i)$ is the set of nearest-neighbors for ligand i, λ is a parameter defining the strength of the interaction between near-neighbor ligands, and σ is the "spin" of the ligand, defined as $+1$ if the ligand is hydrophilic and -1 if the ligand is hydrophobic. B_i is defined as 0 for all ligands that do not interact with the hydrophobic core, positive for hydrophilic ligands exposed to the core, and negative for hydrophobic ligands exposed to the core. The total energy of the surface is equal to the sum over all ligands.

The critical parameter in the Ising model is λ which determines interactions between neighboring ligands and gives rise to surface phase behavior when the NP is not in contact with the bilayer ($B_i = 0$ for all i). If $\lambda < 0$, the surface energy is minimized by mixing different ligand types while if $\lambda > 0$ phase separation is energetically preferred leading to macrophase-separated Janus particles. Because the rearrangement process permits many states of the surface that have an identical surface energy but distinct ligand positions, there is also a configurational entropy contribution to the total free energy of the surface that favors the homogeneous state. Due to this entropy term, the order-disorder transition (ODT) between the homogeneous and heterogeneous state occurs for a critical value $\lambda_c > 0$. Fig. 2-1 shows simulation snapshots of the two initial surface morphologies expected for NPs prior to exposure to the bilayer. It should also be emphasized that upon contact with the bilayer, the parameter B_i in eq. (2.1) will no longer be 0 and as a result the NP will not necessarily maintain one of these two morphologies.

2.1.1 Coarse-grained model of NP-bilayer system

A coarse-grained, implicit solvent model first developed by Cooke et al [132, 133] was chosen to represent the interaction of the NP with a bilayer. This model has been previously used to simulate

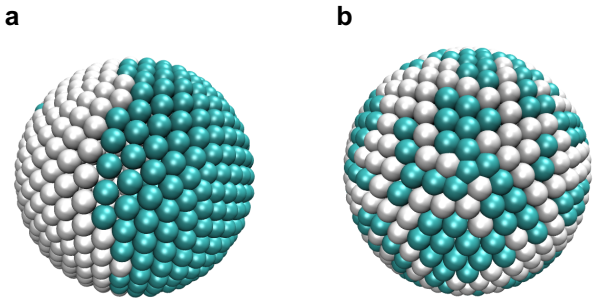

Figure 2-1: Simulation snapshots of NPs with their initial surface configurations prior to bilayer interactions. The two ligand types are mixed in a 1:1 ratio. **a** Phase separated state, corresponding to $\lambda > \lambda_c$. **b** Mixed state, corresponding to $\lambda < \lambda_c$.

bilayer interactions with cell penetrating peptides [134] and viruses [135]. Each lipid was modeled as a hydrophilic head bead and two hydrophobic tail beads joined by harmonic springs with an additional spring potential between the first and third bead to limit bending. Spring constants were set to 200 kT/δ^2 and 10 kT/δ^2 for the two potentials respectively. The diameter of all beads was set by a repulsive Weeks-Chandler-Anderson potential,

$$U_{rep}(r) = \begin{cases} 4\epsilon[(b/r)^{12} - (b/r)^6 + 1/4] & r \leq r_c \\ 0 & r > r_c \end{cases} \tag{2.2}$$

This potential defines r_c as the diameter of the beads, with $r_c = 2^{1/6}b$. The length b was set such that $b_{head,head} = b_{head,tail} = 0.95\delta$ and $b_{tail,tail} = 1.0\delta$ to represent a larger volume for tail beads. δ and ϵ set the length and energy scales of the simulation respectively. In the absence of water molecules, the bilayer is instead maintained by long-range attractive potentials between all tail beads. This potential has been identified as sufficient to self-assemble free lipids into a bilayer that displays physical parameters (e.g. area per lipid, bending modulus, etc.) equivalent to those found in biological membranes [132, 133]. The chief advantage of the solvent-free approach is computational efficiency, even compared to other coarse-grained models [136]. We used a modified Lennard-Jones potential,

$$U_{attr}(r) = \begin{cases} -\epsilon & r < r_c + w_f \\ 4\epsilon\left[\left(\frac{b}{r-w_f}\right)^{12} - \left(\frac{b}{r-w_f}\right)^{6}\right] & r_c + w_f \leq r \leq 3.0\delta \\ 0 & r > 3.0\delta \end{cases} \tag{2.3}$$

Together, the combination of eq. (2.2) and eq. (2.3) yield a Lennard-Jones potential modified by the addition of a flat plateau inserted at the energy minimum, ϵ, with a width w_f. Changing the value of w_f shifts the bilayer state from fluid to gel phase and is a critical tuning parameter in this model. In this work, w_f was set to 0.35δ, corresponding to a fluid bilayer [132]. The length scale of the system was set as $\delta = 0.7$ nm in order to reproduce experimental measurements for the average

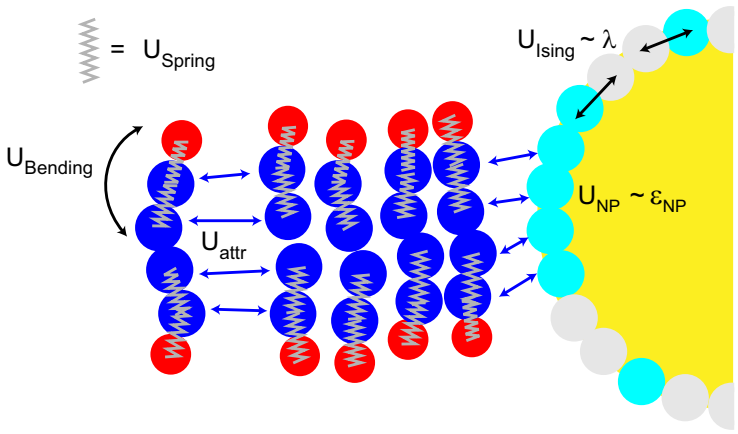

Figure 2-2: Schematic illustrating different potentials acting on the system in the coarse-grained, implicit solvent representation.

area per lipid in the fluid phase. Finally, the energy scale was set by $\epsilon = 1.3\ kT$, again consistent with literature phase diagrams [132]. With this set of potentials, the bilayer self-assembled from a random initial lipid configuration. Fig. 2-2 presents a schematic of the potentials present in the system.

The NP was constructed as a uniformly spherical, hollow shell of beads, assembled by defining an initial icosahedron and iteratively bisecting sides of each face then scaling each bead to the appropriate radius to yield a spherical surface. All surface beads had six nearest neighbors except for the initial twelve beads which had five nearest neighbors, creating a well-defined lattice. All beads on the NP surface had a diameter of δ and the diameter of the assembled particle was set to 14.0δ, or 9.8 nm, with 642 total beads. The spherical surface was maintained by joining all beads together with harmonic springs to maintain their initial positions. Finally, each bead on the surface was defined as either hydrophobic or hydrophilic with a set phase fraction ϕ defining the relative proportions of each type.

Interactions between the NP and bilayer were modeled using a combination of long- and short-ranged potentials. The long-range potential described in eq. (2.3) was applied between hydrophobic beads on the NP surface and the lipid hydrophobic tails; however, this potential was only applied when the NP beads were not within the core of the bilayer (defined as the z-coordinate of the NP bead being within the z-coordinates of the upper and lower head beads of the closest lipids). A repulsive short-ranged potential was applied between embedded hydrophilic NP beads and the bilayer core while an attractive short-ranged potential was applied between hydrophobic NP beads and the bilayer core. The short-ranged potentials were given by

$$U^{np}_{attr}(r) = -\epsilon_{np} e^{-r/\xi} \tag{2.4}$$

$$U^{np}_{rep}(r) = \kappa_{np} e^{-r/\xi} \tag{2.5}$$

where ϵ_{np} and κ_{np} are prefactors giving the strength of the attractive and repulsive potentials, respectively, and ξ is the decay length. The short-range potentials were necessary to realistically model the system because the long-range potential alone presented no barrier for moving hydrophilic NP beads into the bilayer core, biasing lipids toward completely wrapping around the NP. Using the short-range potentials encouraged strong hydrophobic matching between hydrophobic beads on the NP and the lipid tails while penalizing exposure of hydrophilic beads to the hydrophobic environment. The long-range attractive potential modeled the driving force for hydrophobic attraction (i.e. the hydrophobic effect [137]) and provided an initial driving force for NP-bilayer interaction until the NP came into contact with the bilayer core. For all simulations κ_{np} was fixed at 1.0 kT, while ϵ_{np} was varied as a primary tuning parameter. The value of κ_{np} was sufficient to ensure favorable rearrangement of the surface to avoid hydrophilic NP-hydrophobic tail bead contacts for all observed simulations and higher values of κ_{np} made no appreciable difference. ξ was set such that the attractive potential dropped to a value of 0.1 kT at a distance of two bead diameters. Finally, it should be noted that no interactions with the hydrophilic lipid head beads were included; while in principle the NP could interact with the lipid heads (as is observed in biological systems, including cell-penetrating peptides [44]), these interactions would likely have a highly specific form depending on the structure of the NP surface that cannot be captured with this simple model.

Two separate simulation methodologies were employed to simultaneously model the evolution of bead positions in the system and the dynamic rearrangement of the NP surface. A Brownian dynamics algorithm was used to simulate the motion of beads in the bilayer system subject to the potentials described above. Brownian dynamics is a simulation technique developed to implicitly model the effect of solvent by incorporating random forces to account for friction with the missing solvent as described in Appendix A. Eq. (A.35) was used to model bead motions in the system with dimensionless step size $\Delta\tilde{t} = \sqrt{\frac{2D}{\Delta t}} = 10^{-4}$ defined from the diffusion coefficient, D, of the system.

To model the rearrangement of the NP surface, a Monte Carlo algorithm was used to switch adjacent beads on the NP surface to maintain an optimal configuration. For each Monte Carlo timestep, two near-neighbor beads of opposite type (hydrophobic/hydrophilic) were chosen and randomly switched with a probability

$$P_{ij} = \begin{cases} 1 & \Delta U_{ij}^{ising} < 0 \\ e^{-\Delta U_{ij}^{ising}/kT} & \Delta U_{ij}^{ising} \geq 0 \end{cases} \tag{2.6}$$

where ΔU_{ij}^{ising} is the change in energy of beads i and j and their neighbors from the Ising model defined in eq. (2.1). The external field B_i in this equation was determined for each ligand from the pair-potentials defined in equations (2.3), (2.4) and (2.5). By switching beads, the total number of each type of ligand on the NP surface was conserved throughout the entire simulation run. The timescale for rearrangement was assumed to be faster than the diffusion time of lipids, so 1,000 Monte Carlo timesteps were taken per Brownian dynamics timestep allowing the surface energy to locally equilibrate as bead positions evolve. From this equation and the potentials that

determine B_i, rearrangement was dependent on the parameter λ, the cost for neighbor interactions on the surface, κ_{np}, the cost for exposing hydrophilic NP beads to lipid tails, and ϵ_{np}, the gain in energy for bringing hydrophobic NP beads in contact with lipid tails. The effectively instantaneous, unconstrained response of the ligands to the bilayer is the hallmark of the globally-responsive assumption; the opposite regime, in which ligand positions are fixed to a grafting site, will be considered in the following Chapters. Given the simplifications of the model and the assumption of near-instantaneous rearrangement, we cannot use this model to determine any information about the kinetics of bilayer interactions, but we can gain an understanding of the thermodynamics of any interactions that are identified after simulations converge to equilibrium.

To calculate the critical value λ_c for the ODT, Monte Carlo simulations of the rearrangement process were run in the absence of a bilayer with steadily increasing values of λ. The total system energy was calculated from eq. (2.1) with B_i set to 0 for all beads. The heat capacity of the system is proportional to the fluctuations in the surface energy and was calculated as a function of λ [138]. λ_c was identified as the value of λ where a maximum in the heat capacity was observed, which occurred for a value of 0.32 for a phase fraction of $\phi = 0.5$ and 0.38 for $\phi = 0.4$ and $\phi = 0.6$.

Full simulations were run by introducing NPs very close to the surface of pre-equilibrated bilayers in the fluid state containing 7,200 lipids. The bilayer was maintained with zero surface tension by using large free bilayers (i.e. no periodic boundary conditions). No additional driving force for aggregation was introduced. Simulations were run for 40,000,000 Brownian dynamics timesteps. Three parameters were varied between simulations: λ, ϵ_{np}, and ϕ.

2.2 Phase diagram for NP-bilayer interactions

Fig. 2-3 presents simulation snapshots of the observed NP-bilayer interactions and corresponding "phase diagrams" for the system, depicting values of λ and ϵ_{np} for which the different behaviors were observed. Three diagrams are shown for different phase fractions ϕ of NP hydrophilic beads. λ is normalized by the critical value λ_c for each ϕ. If $\lambda/\lambda_c < 1$, the NP surface preferred a homogeneous state when not in contact with the bilayer while if $\lambda/\lambda_c > 1$ the NP surface preferred a phase separated state.

Varying λ and ϵ_{np} gave rise to five distinct behaviors that are illustrated in Fig. 2-3a. The first behavior (black diamonds in Fig. 2-3) was trivial. For low values of ϵ_{np} and λ, the surface of the NP maintained an homogeneous morphology since the value of ϵ_{np} was too small to induce surface reconstruction on the NP - that is, even when in contact with the bilayer the morphology was dominated by the parameter λ rather than the field B_i. The repulsive interactions between the hydrophobic bilayer core and the hydrophilic ligands in the homogeneous morphology thus prevented any NP-bilayer complexation. In the case of $\lambda/\lambda_c > 1$, where the NP assumed a Janus morphology, if ϵ_{np} was too low there would be an insufficient driving force for penetration to compensate for the cost in deforming the bilayer. The other four regimes all involved perturbation of the bilayer, and were distinguished largely by the NP's ability to rearrange its surface to maximize

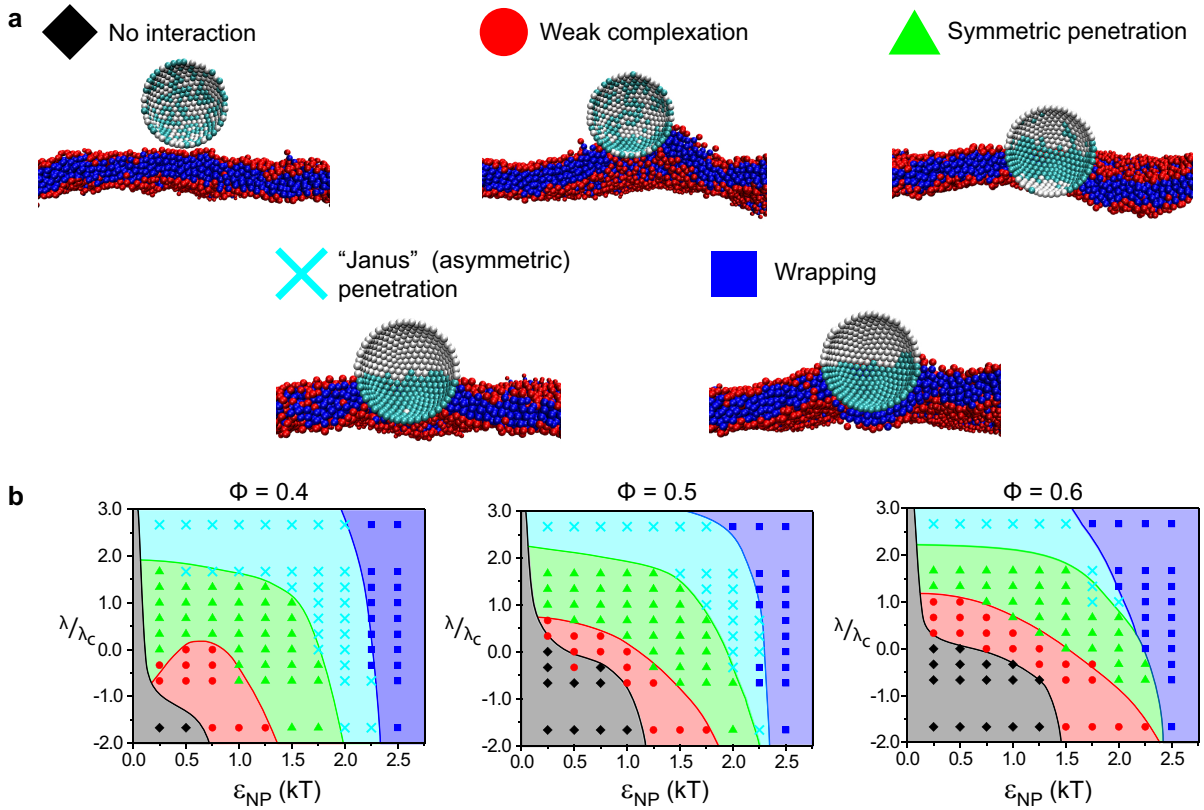

Figure 2-3: Results from coarse-grained Brownian dynamics simulations with NP of diameter $2R \approx 14.0\delta$. Values of the Ising parameter λ are shown scaled by the critical value λ_c. **a** Simulation snapshots of the five observed behaviors, including the case when no interaction between NP and bilayer was observed. Hydrophobic beads are teal/blue in the NP/bilayer respectively while hydrophilic beads are white/red. **b** Phase diagrams illustrating when each different behavior was observed as a function of the key parameters λ, ϵ_{np}, and ϕ.

favorable interactions between the surface and the bilayer core. Note that in all cases, NP-bilayer interactions occurred spontaneously since no additional force was applied to push the NP into the bilayer.

For values of $\lambda < \lambda_c$ and low values of ϵ_{np}, a weak complexation behavior was observed (red circles in Fig. 2-3). The NP was unable to translocate to the bilayer midplane but instead induced significant curvature of the bilayer, similar to the curvature induced by wedge-like proteins [139]. This behavior resulted from the strong tendency for the NP to maintain a homogeneous surface when $\lambda < \lambda_c$, and the relatively weak interaction with the bilayer was insufficient to induce surface reconstruction. The overall driving force for penetration was thus insufficient to allow complete penetration to the midplane and the bilayer instead curved to maximize matching with the curved surface of the sphere. It is possible also that this an effect of kinetic trapping and that the energy barrier for complete penetration is too high for the NP to bypass during these simulations.

When λ or ϵ_{np} was increased, the NP surface was able to rearrange to form a characteristic three-region symmetric morphology and the NP penetrated fully to the bilayer midplane (green

triangles in Fig. 2-3). The region of the NP that was embedded in the bilayer core was primarily hydrophobic and the two protruding spherical caps were hydrophilic, resembling transmembrane proteins. The formation of this surface resulted from both a low barrier to rearrangement and strong perturbation from the bilayer (high ϵ_{np}). The barrier for formation of this surface morphology was lowest when λ was near the critical value λ_c for an ODT on the particle surface. Near this transition, the energy cost for an initially homogeneous surface to phase separate was low, and the cost for an initially heterogeneous surface to create a third phase (and resulting line tension) was also low. The perturbing effect of the bilayer due to ϵ_{np} was thus able to induce the rearrangement of hydrophobic ligands into contact with the bilayer core while displacing hydrophilic ligands at the same time, leading to a strongly preferred transmembrane morphology. A simulation snapshot of this three-region symmetric morphology is shown in Fig. 2-3a.

If λ was further increased well above λ_c, the NP surface preferred a phase separated, Janus morphology (shown in Fig. 2-1a) in the absence of the bilayer. As a result, contact with the bilayer was insufficient to induce the three-region symmetric morphology characteristic of penetration due to the high line tension between phases on the surface. There were two separate behaviors that were observed in this case. For low values of ϵ_{np}, the favorable interaction between lipids and the hydrophobic region of the NP surface led to some anchoring of lipids to the surface (teal crosses in Fig. 2-3). However, the bilayer did not show noticeable deformation, with the lipids preferring to maintain coordination by other lipids. In this case, the NP exposed the hydrophobic ligands not in contact with the bilayer core to the implicit solvent while still penetrating toward the bilayer midplane, a mechanism we refer to as "Janus" penetration. It is likely that strongly Janus particles of this type would have induced pore formation in order to minimize this hydrophobic exposure if multiple NPs were present in the simulation [140, 134]. For large values of ϵ_{np}, lipids instead adhered strongly to the NP surface and wrapped around the entire hydrophobic region of the NP (blue squares in Fig. 2-3). The favorable gain in energy due to a high ϵ_{np} from these NP-lipid contacts was sufficient to overcome the considerable strain energy associated with this bilayer disruption. NP adhesion of this type has been observed in simulation studies previously [141].

The phase diagrams for different hydrophilic phase fractions showed the same five behaviors though under different parameters. As ϕ increased from 0.4 to 0.6, symmetric penetration behavior was observed for a smaller range of λ and ϵ_{np} values, consistent with a smaller number of hydrophobic ligands and resulting decrease in attractive interactions with the bilayer. Most notable, however, is that symmetric penetration behavior was consistently observed for the lowest values of ϵ_{np} when the NP surface was near an ODT ($\lambda/\lambda_c \approx 1.0$), implying that even if the gain in interfacial energy was minimal the NP was still able to penetrate. This result can be again understood due to the low cost of forming the three-region symmetric morphology exhibited by NPs that penetrate.

These phase diagrams present several options for manipulating NP-bilayer interactions depending on the ease of modifying the key parameters λ, ϵ_{np}, and ϕ. In principle, λ is dependent on the physical system under consideration. Since ϵ_{np} is effectively an interfacial energy, this parameter may be more difficult to modify chemically and hence NP-bilayer behaviors should be tuned by

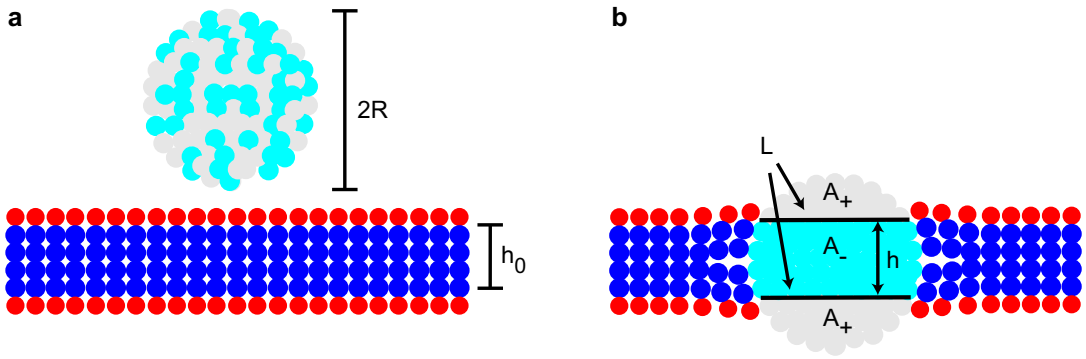

Figure 2-4: Schematic illustrating the different geometric variables considered in the mean field theory. **a** The initial state. **b** The final state.

modifying λ and ϕ.

2.3 Mean field theory for globally responsive NPs

While the coarse-grained simulations established the variety of interactions possible between the NP and bilayer, the thermodynamics of NP penetration are of particular interest to identify long-timescale behavior. The simulation results indicated that two primary types of penetration were possible: symmetric penetration, where the NP translocated to a stable position at the bilayer midplane and all hydrophobic surface area was exposed to the bilayer core; and Janus penetration, where the NP maintained a phase separated Janus morphology and exposed some hydrophobic area to solvent upon penetration into the bilayer. To fully understand the penetration of NPs, the free energy change for achieving either of these two states can be calculated.

The change in free energy of the system for both cases will be derived using a continuum approximation for the NP and bilayer in place of the discretized approach used in simulations. In the continuum approximation, the key parameter ϵ_{np}, which acted as a pair-potential in simulations, is replaced instead by γ, a parameter giving the attractive interfacial energy per hydrophobic ligand. Similarly, κ_{np}, the prefactor for the repulsive interaction that was fixed in the simulations is now replaced by μ, the repulsive interfacial energy per hydrophilic ligand. The free energy is thus a function of γ, μ, and λ. Finally, while λ in this continuum approximation is qualitatively the same as in the discretized simulations, treating the NP as a continuum rather than discrete lattice leads to a quantitatively different λ_c than in simulations; however, the effect of λ on the system remains the same.

Fig. 2-4 shows a schematic outlining the system under consideration in the case of symmetric penetration. The initial state of the system is an unperturbed bilayer of height h_0 and a NP of radius R, with a surface morphology dependent on the neighbor interaction energy λ. It is assumed that in the final state the NP penetrates exactly to the bilayer midplane, and there is complete symmetry around the bilayer center. It is further assumed that the NP surface will divide into

two distinct regions, representing one area exposed to the bilayer core and one area (divided into two spherical caps) exposed to aqueous solvent. These regions are labeled as A_+ and A_- in Fig. 2-4, and can be calculated from R and h, the deformed thickness of the bilayer. In general, the region labeled as A_+ will tend to be more hydrophilic due to solvent exposure while the region labeled as A_- will tend to be more hydrophobic providing favorable hydrophobic matching. This morphology is identical to that in simulations (shown in Fig. 2-3) when penetration occurs. Finally, the boundary between the external and internal regions on the surface has length L, and gives rise to a line tension between these two phases.

Based on the system described, four terms are included in the overall free energy change: $\Delta G_{int}(h, R, \gamma, \mu)$, the interfacial energy change for the NP surface; $\Delta G_{line}(h, R, \lambda)$, the line tension between regions on the NP surface; $\Delta G_{surf}(h, R, \lambda)$, the change in surface energy due to neighbor interactions; and $\Delta G_{bilayer}(h, h_0)$, the change in bilayer elastic energy from deformation induced by the particle. The total change in free energy is then:

$$\Delta G = \Delta G_{int} + \Delta G_{line} + \Delta G_{surf} + \Delta G_{bilayer} \tag{2.7}$$

The driving force behind penetration is the change in interfacial energy as all the other terms are positive.

2.3.1 Surface (Ising) energy

The energy of the NP surface can be determined from the Ising model defined in eq. (2.1) using a mean field approximation. It is assumed that all the ligands in a given region have the same average "hydrophilicity." The two different regions, A_+ and A_- will generally have different average hydrophilicities, denoted by $\langle\sigma\rangle_+$ and $\langle\sigma\rangle_-$ respectively. Recall that in eq. (2.1), hydrophilic ligands are given a spin of +1 and hydrophobic ligands are given a spin of -1, so that the names of the two areas reflect the sign of the average hydrophilicity in each. In this mean field approximation, the summation in eq. (2.1) is replaced by

$$E_i = -\lambda\langle\sigma(\lambda)\rangle^2 \tag{2.8}$$

There is no reference to the number of neighbors for molecule i as it is assumed that the number of near-neighbors is incorporated in the effective parameter λ. The external field B_i is also set to zero and the effect of the external field from the bilayer core is instead included in the ΔG_{int} term described below. Given these assumptions, a complete expression for the surface energy is written as

$$E_{surf} = -\rho\lambda\left(A_+\langle\sigma\rangle_+^2 + A_-\langle\sigma\rangle_-^2\right) \tag{2.9}$$

where ρ is the grafting density of ligands on the surface. In addition to the surface energy, it is also necessary to include the Bragg-Williams entropy of mixing in each region to account for the

configurational entropy associated with rearrangement:

$$S_- = -k\rho A_- \left[\phi_- \ln(\phi_-) + (1-\phi_-)\ln(1-\phi_-)\right] \tag{2.10}$$

$$S_+ = -k\rho A_+ \left[\phi_+ \ln(\phi_+) + (1-\phi_+)\ln(1-\phi_+)\right] \tag{2.11}$$

where $\phi_- = \frac{1+\langle\sigma\rangle_-}{2}$ and $\phi_+ = \frac{1+\langle\sigma\rangle_+}{2}$, representing the phase fractions of hydrophilic ligands in each region, rather than the average hydrophilicity. Note that the entropy of either region is set to 0 if either ϕ is 0 as this is the limit of complete phase separation.

The total surface free energy is then given as the sum of the energetic and entropic components, giving:

$$G_{surf}^{final} = E_{surf} - T(S_- + S_+) \tag{2.12}$$

While this is the final surface free energy, the free energy change ΔG_{surf} is the quantity of interest so the baseline free energy must also be calculated as described below.

2.3.2 Line tension

If the average hydrophilicities of A_+ and A_- are different, as is expected in general, a line tension will arise due to unfavorable interactions along the boundary between regions. This term can be calculated from the Ising model and eq. (2.8) by assuming that ligands on the border between the regions have an environment where half of the neighbors are from one region and half are from the other. Along the boundary, the surface energy of the ligands inside the bilayer will be given by $-\frac{\lambda}{2}\left[\langle\sigma\rangle_-\langle\sigma\rangle_+ + \langle\sigma\rangle_-^2\right]$, while the energy of the ligands outside the bilayer will be given by $-\frac{\lambda}{2}\left[\langle\sigma\rangle_-\langle\sigma\rangle_+ + \langle\sigma\rangle_+^2\right]$. However, in the previous section it was assumed that all ligands had the same surface energy, so to avoid overcounting $-\lambda\langle\sigma\rangle_-^2$ must be subtracted for each ligand along the boundary internal to the bilayer and $-\lambda\langle\sigma\rangle_+^2$ must be subtracted for each ligand external to the bilayer since these energies would have been already been included in the previous calculation. Finally, it is necessary to account for the number of ligands affected, which is approximately given by the product of the boundary length L and $\sqrt{\rho}$. The total line tension (doubled to account for the two boundaries) is then:

$$G_{line}^{final} = \lambda L\sqrt{\rho}\left[\langle\sigma\rangle_I^2 + \langle\sigma\rangle_E^2 - 2\langle\sigma\rangle_I\langle\sigma\rangle_E\right] \tag{2.13}$$

Given the assumption of spherical symmetry, the boundary length is solved as the circumference of a spherical cap, yielding $L = \pi\sqrt{4R^2 - h^2}$. As with the surface energy, this expression is for the final line tension only and must be compared to the baseline line tension to find ΔG_{line}.

2.3.3 Baseline surface energy and line tension

In order to calculate the free energy change upon bilayer complexation, the baseline energy of the NP surface must be determined as the sum of a line tension and surface energy term with equations similar to those described above. It is assumed that the NP surface is divided into at most two phases (corresponding to a Janus particle), and that the surface energy and line tension can be calculated in terms of A_1, the area of one of these two phases, and $\langle\sigma\rangle_1$, the average hydrophilicity of this phase. Numerically minimizing the sum of the surface energy and line tension for a given λ yields A_1, $\langle\sigma\rangle_1$, and the baseline free energy. Below λ_c, the energy will be minimized when $A_1 = 0$, implying only a single, homogeneous surface, while above λ_c, $A_1 > 0$ implying phase separation. The critical λ_c marking the ODT thus corresponds to the lowest λ where A_1 is greater than 0. Using this method, λ_c was found to be invariant as a function of R and was equal to 0.59 for $\phi = 0.5$ and 0.71 for $\phi = 0.4$ and $\phi = 0.6$.

2.3.4 Bilayer deformation

The NP-bilayer interaction could lead to deformations of the bilayer away from its unperturbed thickness in order to maximize hydrophobic matching. As a simple estimate of this deformation energy, we used a continuum model developed by Nielsen and Anderson [142, 143] that predicts the change in bilayer deformation energy due to thickness deformations. The model has been previously parameterized to match experimental results from the interactions between bilayers and transmembrane gramicidin channels, which have approximately the same size as the NPs under consideration. Based on their work and the choice of suitable fitting parameters the deformation free energy change is written as

$$\Delta G_{bilayer} = \left[278.0\left(\frac{R}{3.0}\right)^{1.023} + 77.0\right]\left(\frac{h - h_0}{2}\right)^2 \tag{2.14}$$

2.3.5 Interfacial energy

The final free energy change to consider is the interfacial energy of the system, reflecting the free energy change associated with changing the solvent conditions around each ligand (i.e. the hydrophobic effect). This free energy change can be calculated in terms of the penalty incurred by the exposure of ligands to unfavorable solvent conditions. Hydrophobic ligands exposed to aqueous solvent are penalized by the parameter γ while hydrophilic ligands exposed to the hydrophobic bilayer core are penalized by the parameter μ. The driving force for bilayer interactions is the minimization of the interfacial energy, since in the baseline state the hydrophobic ligands are necessarily exposed to aqueous solvent in this model and incur an energy penalty.

We can write the initial interfacial energy of the initial NP in terms of the phase fraction of hydrophilic ligands alone, since in principle the interfacial energy does not depend on whether the surface is mixed or homogeneous. The baseline interfacial energy is

$$G_{int}^{baseline} = A\rho(1-\phi)\gamma \tag{2.15}$$

In analogous fashion, we can calculate the interfacial energy of the internal (hydrophobic) and external (hydrophilic) regions upon complexation, with the energy based on the average hydrophilicities of those regions.

$$G_{int}^{+} = \frac{A_{+}\rho(1-\langle\sigma\rangle_{+})\gamma}{2}$$
$$G_{int}^{-} = \frac{A_{-}\rho(1+\langle\sigma\rangle_{-})\mu}{2}$$

The total change in interfacial energy is then given as:

$$\Delta G_{int} = \frac{\rho}{2}[A_{+}(1-\langle\sigma\rangle_{+})\gamma + A_{-}(1+\langle\sigma\rangle_{-})\mu \\ -2A(1-\phi)\gamma] \tag{2.16}$$

2.3.6 Conservation relations

A key assumption made in this model is that the total number of hydrophobic and hydrophilic ligands is fixed, and hence is determined by the initial phase fraction ϕ of the system. Since the total area of the system is also fixed, $\langle\sigma\rangle_{+}$ and $\langle\sigma\rangle_{-}$ can be determined from a conservation condition related to the relative areas of the two regions and the initial phase fraction:

$$\frac{A_{-}}{A}\langle\sigma\rangle_{-} + \frac{A_{+}}{A}\langle\sigma\rangle_{+} = 2\phi - 1 \tag{2.17}$$

where A is the total surface area of the NP. Note that the different areas can be further simplified to functions of R and h by applying geometric identities for the area of a spherical zone (A_{-}) and cap (A_{+}):

$$A_{-} = 2\pi Rh \tag{2.18}$$
$$A_{+} = 2\pi R(2R-h) \tag{2.19}$$
$$A = 4\pi R^2 \tag{2.20}$$

2.3.7 Janus penetration

When $\lambda/\lambda_c > 1$, the NP surface will tend to phase-separate into a Janus state consistent with Fig. 2-1b. In this case, the NP may penetrate the bilayer by the "Janus penetration" mechanism identified in simulations rather than by the three-region symmetric penetration mechanism considered here. The Janus penetration mechanism is preferred at high λ because retaining a two- rather than

three-region morphology reduces the line tension of the system, though at the cost of exposing more hydrophobic area to solvent. In this section the free energy change for Janus penetration, ΔG_{Janus}, will be calculated and compared to the free energy change for symmetric penetration to determine the dominant penetration mechanism.

Fig. 2-5 illustrates the proposed final state of the system upon Janus penetration. As in Fig. 2-4, the NP surface is divided into three regions denoted as A_+, A_-^I, and A_-^E, corresponding to the area of predominantly hydrophilic ligands exposed to solvent, the area of predominantly hydrophobic ligands exposed to the bilayer core, and the area of predominantly hydrophobic ligands exposed to the solvent. It is no longer assumed that there is symmetry around the bilayer midplane so that $A_+ \neq A_-^E$; this allows both the bilayer thickness h and the thickness of the exposed hydrophilic region h^E to vary in order to minimize the free energy change. It is assumed that the average hydrophilicity $\langle\sigma\rangle_-$ is identical in both regions A_-^E and A_-^I.

Calculation of the free energy change for Janus penetration follows the same lines as the previous calculation for symmetric penetration. The change in surface energy is identical to eq. (2.12), with the area $A_- = A_-^E + A_-^I$. The line tension is equal to 1/2 the value of eq. (2.13) since there are only two adjacent regions of differing hydrophilicity. Furthermore, the value L is now given by $L = 2\pi\sqrt{h^E(2R - h^E)}$ due to the new geometry of the system. The bilayer deformation term is assumed to be identical to eq. (2.14). In principle, the Janus penetration mechanism could involve additional deformation modes (such as bending or lipid tilt [144]) other than the thickness deformation assumed, but for simplicity the same expression is used. Finally, the interfacial energy must take into account that the region A_-^E is exposed to solvent; this gives a revised expression for the interfacial energy of

$$\Delta G_{int}^{Janus} = \frac{\rho}{2}[A_+(1 - \langle\sigma\rangle_+)\gamma + A_-^I(1 + \langle\sigma\rangle_-) + A_-^E(1 - \langle\sigma\rangle_-)\gamma \\ -2A(1 - \phi)\gamma] \tag{2.21}$$

To complete the analysis of Janus penetration, the expression for the different areas must also be updated. Again calculating areas based on geometric formulas for spherical caps and zones yields

$$A_+ = 2\pi R h^E \tag{2.22}$$
$$A_-^I = 2\pi R h \tag{2.23}$$
$$A_-^E = 2\pi R(2R - h - h^E) \tag{2.24}$$
$$A = 4\pi R^2 \tag{2.25}$$

Finally, the conservation relation eq. (2.17) remains the same, with $A_- = A_-^E + A_-^I$.

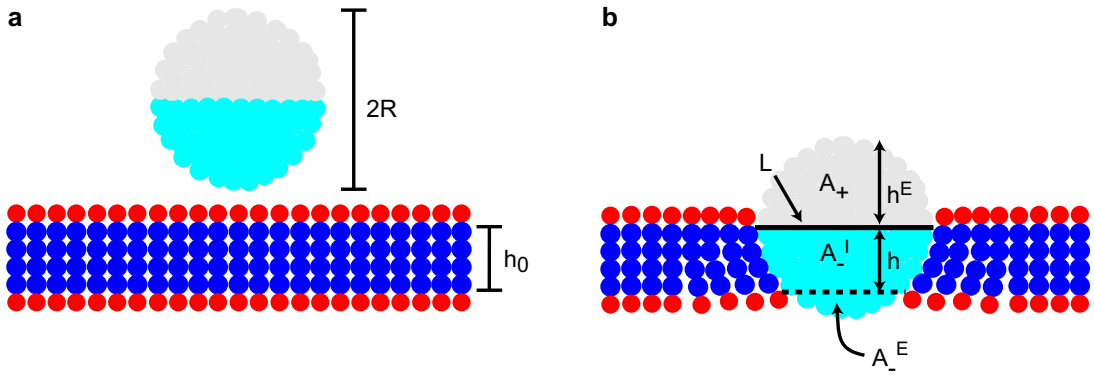

Figure 2-5: Schematic illustrating the different geometric variables considered for Janus penetration in the mean field theory. **a** The initial state. **b** The final state.

2.3.8 Theory results and discussion

To compare with simulation results, the full free energy change for both symmetric and Janus penetration was calculated for different values of γ, λ, and ϕ. In each case, the free energy change was minimized as a function of h to find the perturbed bilayer thickness for each set of parameters. For Janus penetration, the free energy change was further minimized as a function of h^E, with h^E constrained to the range of $0 \leq h^E \leq 2R\phi$ to be consistent with the Janus morphology. The grafting density ρ was set to 4.77 ligands/nm^2, in accordance with the typical density of surface monolayers [145].

In Fig. 2-6a, the change in free energy of each state is calculated for different values of ϕ with $R = 5$ nm, while in Fig. 2-6b the change is shown as a function of R with $\phi = 0.5$. In both figures, the thick contour lines represent where $\Delta F = 0$ for either symmetric or Janus penetration; that is, to the right of the contours (higher γ) penetration is thermodynamically preferred while to the left (lower γ) the free energy change for penetration is greater than zero and penetration is not expected. To distinguish whether symmetric or Janus penetration is preferred, the dashed contour lines in both figures indicate where the free energy change between the two states is zero. Values of λ and γ above the dashed lines indicate where Janus penetration is preferred over symmetric penetration while values of λ and γ below the dashed lines indicate where symmetric penetration is preferred. Together, these contour lines can be compared to the simulation results to show where different forms of penetration are preferred. These results are presented as a phase diagram for a single value of $R = 5$ nm and $\phi = 0.5$ in Fig. 2-7. The full contours for both Janus and symmetric penetration are drawn as red and yellow dashed lines respectively with the black dashed line again indicating where the free energy change between the two penetrated states is zero. The different regions of the phase diagram are colored according to the same scheme as Fig. 2-3 based on whichever penetrated state poses the largest free energy change from the baseline value.

Fig. 2-6a shows that for all measured values of ϕ symmetric penetration behavior is observed for the lowest value of γ when $\lambda/\lambda_c \approx 1$, agreeing with simulation results. As λ increases above its

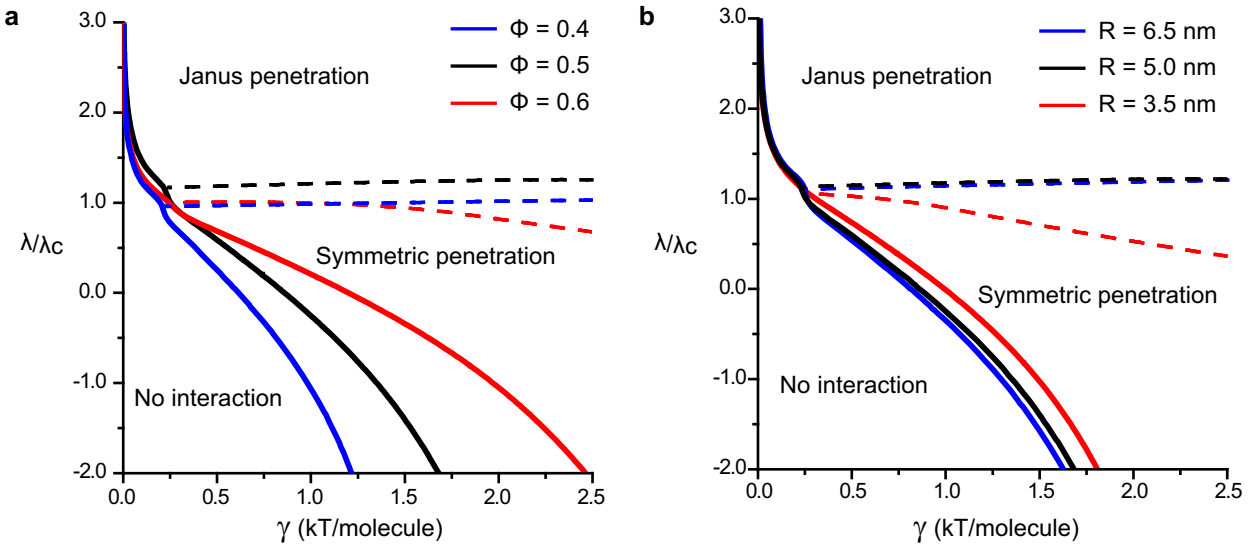

Figure 2-6: Results from theoretical free energy minimization, with contour lines marking where the change in free energy from the free to translocated state is equal to 0. Dashed contours indicate where the transition to Janus penetration is preferred over symmetric penetration. **a** Contours for changing the hydrophilic phase fraction ϕ for fixed $R = 5$ nm. **b** Contours for changing NP radius R for fixed $\phi = 0.5$.

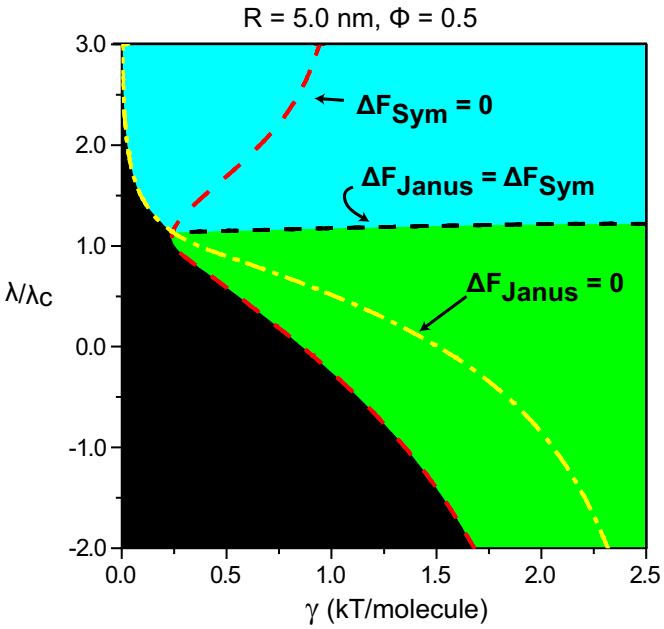

Figure 2-7: Phase diagram from theoretical results. The red dashed contour indicates where ΔF_{Janus}, the change in free energy from baseline to the Janus penetrated state, is equal to 0. The dashed black contour indicates where the $\Delta F_{Janus} = \Delta F_{sym}$, indicating the transition between one penetrated state being preferred over the other. Regions are colored according to the scheme in Fig. 2-3.

critical value, Janus penetration is instead preferred, again agreeing with simulation results. The preference of Janus penetration at high λ is due to the increase in line tension as λ increases; the Janus state minimizes the line tension by only having two distinct regions rather than the three associated with symmetric penetration. Because the line tension is lowest near the ODT, symmetric penetration is still preferred for values of λ slightly higher than λ_c. If the NP surface slightly prefers mixing (i.e. λ is slightly lower than λ_c) then the change in surface energy required to separate the surface into three regions is similarly low near the ODT. In either case, the perturbation due to the bilayer, captured in the change in interfacial energy, is sufficient to induce the three regions associated with symmetric penetration. It is particularly interesting to note that although the contours for symmetric and Janus penetration vary significantly for different values of ϕ, symmetric penetration is always preferred for roughly the same values of γ near the critical point.

Fig. 2-6b shows that the free energy change for penetration in either the symmetric or Janus state is roughly independent of NP diameter. As in Fig. 2-6a, symmetric penetration is still observed for the lowest value of γ when λ is near the critical point. This result is relevant given the known size-dependence of endocytosis [146], indicating that it may be possible to design NPs to penetrate non-specifically instead of achieving cellular uptake by endocytosis and then being trapped in endosomal compartments.

There are a few discrepancies between the theoretical results and simulation results that bear discussion. First, a comparison of Figs. 2-3 and 2-6a shows that in general the range of values of λ that prefer symmetric penetration is less broad in the theoretical results than in simulations. This difference can be attributed to the lack of fluctuations in the mean field model. However, both the theory and simulations do predict the important result that symmetric penetration is preferred for low values of γ or ϵ_{np} when $\lambda/\lambda_c \approx 1$. It should also be noted that at high ϵ_{np}, the simulations predict first Janus penetration then particle wrapping behavior as ϵ_{np} is increased, both results that are not obtained in the theory. The preference for Janus behavior at high ϵ_{np} can be attributed to kinetic trapping in the simulations. Because forming the three-region symmetric morphology necessarily relies on rearranging surface ligands across regions of the surface exposed to the bilayer core, at high values of ϵ_{np} the cost for moving hydrophilic ligands is prohibitively high, even if the final morphology is favored thermodynamically. It is probable that at long enough run times symmetric penetration would be observed in simulations even for large values of ϵ_{np}, but that is not observed in the simulations presented here. Wrapping is not considered in the theory because this would require incorporating single monolayer bending deformations into the continuum bilayer approximation which is beyond the scope of this study. Finally, the theory predicts that Janus penetration is observed even as $\gamma \approx 0$ if λ is sufficiently high, which is not indicated in Fig. 2-3. In simulations, it is observed that lipids tend to anchor to the curved NP surface, inducing a tilt deformation that comes at some small energetic cost that is not considered in the theory. This bilayer deformation would oppose penetration if the value of γ approaches zero, since then the driving force for penetration would also drop to zero. Again, these types of bilayer deformations are outside the scope of this study. Despite these differences between theory and simulations,

overall the results agree well and show the same qualitative trends, particularly with respect to the preference for symmetric penetration

Combined with the simulation results, the theoretical analysis suggests that penetration may be highly tunable if λ can be varied experimentally. Most important is the identification of symmetric penetration when the NP surface is near an ODT, since symmetric penetration mimics the morphology of transmembrane proteins and likely leads to stable NP complexation for long periods of time. Another interesting result is that the barrier for Janus penetration drops to nearly zero when $\lambda > \lambda_c$. This low barrier implies that Janus penetration may lead to stable pore formation when multiple NPs are present in order to further minimize exposed hydrophobic area [140, 134]. Finally, it is important to note the relatively low magnitude of the interfacial energy γ necessary to achieve symmetric penetration when the surface is near a phase transition, providing a design goal for physical systems.

2.4 Conclusions

In this Chapter, we demonstrated that a NP with an environmentally-responsive mixed hydrophobic/hydrophilic surface can non-specifically penetrate to the midplane of a lipid bilayer. Penetration depends on the NP rearranging its surface to maximize favorable hydrophobic interactions while minimizing the exposure of hydrophilic ligands to the bilayer interior. Using a simple Ising model to characterize the surface's preference for macroscopic phase separation, we found that the key parameter that governs penetration is λ, the interaction energy between neighboring ligands on the NP surface. When λ is near λ_c, the critical value for an ODT, both theory and simulation predict that the NP will translocate to the bilayer midplane even for small values of γ, the hydrophobic interfacial energy per ligand. During this type of symmetric penetration, the NP surface rearranges to form a single band of hydrophobic ligands exposed to the bilayer hydrophobic core and two caps of hydrophilic ligands exposed to solvent, forming a stable morphology similar to transmembrane proteins. If λ is above λ_c, a Janus morphology is instead preferred on the NP surface that also leads to penetration, though at the cost of leaving hydrophobic ligands exposed to solvent. From simulations, several other non-specific NP-bilayer interactions were also identified depending on the relative competition between the cost of ordering the surface and the gain in interfacial energy. The theory further predicts that if $\lambda/\lambda_c \approx 1$, then symmetric penetration would be observed for small values of γ independent of NP radius.

On the basis of these results, it is clear that the parameter λ and its critical value λ_c are crucial in determining penetration behavior. In principle, both λ and λ_c can be determined independently of bilayer interactions as they are a function of the NP surface composition and environment alone. This work suggests that several well-studied soft matter systems with known phase behavior may serve as suitable experimental analogues for the NPs discussed. Furthermore, the theory suggests that NP-bilayer interactions may be highly tunable based on modifying λ, which in general may be a function of environmental conditions like pH or temperature depending on the specific system

studied. Penetration behavior also depends on the interfacial energy γ; while this parameter may be more difficult to modify experimentally, near the ODT these results indicate that only a minimal value of γ is sufficient to drive symmetric penetration. These results suggest guidelines for the design of environmentally-responsive NPs that can complex with lipid bilayers by utilizing systems with known phase behavior.

Given the generality of this model, the conclusions extend beyond just alkanethiol-protected NPs to other similar NP compositions that demonstrate responsive behavior. For example, a similar system is NPs coated with mixed polymer brushes, rather than short chain alkane derivatives, yielding so-called "hairy" particles. In this system, λ is best represented by the Flory-Huggins interaction parameter χ and experimental studies have already demonstrated the formation of either a Janus [147] or mixed morphology [148, 149]. Polymer brushes can be designed to be stimuli-responsive, changing morphology as a result of exposure to different environmental conditions [150], including changing solvent conditions, temperature, or pH. This imparts an ability to change surface morphology in connection to the results identified in this work, and experiments have demonstrated the ability to translocate stimuli-responsive particles across a hydrophilic-hydrophobic interface [151, 152, 153, 154]. In addition, the NP core need not be gold, as triblock copolymers can form structures with similar morphologies [155, 156]. Similarly, polymerosomes have recently been assembled that undergo a phase transition in the corona [157], a process which affected cell uptake. It is possible that varying polymer composition to effect favorable interactions with the bilayer core could be used to drive non-specific translocation as described here. Another interesting system is a NP coated in an amphiphilic monolayer derived from V-shaped polymers [158, 159], which would maintain a fixed ratio of hydrophobic/hydrophilic ligands and could exhibit surface rearrangement. Finally, a recent class of NPs was designed to undergo a response to a change in solvent by exposing different ligands, mimicking this type of responsive behavior [160]. This large set of examples suggests that the basic understanding of environmentally-responsive NP interactions will be broadly applicable to a variety of experimental systems.

THIS PAGE INTENTIONALLY LEFT BLANK

Chapter 3

Environmentally-Responsive NPs: Local Rearrangement

Work in this chapter was published in:

R. C. Van Lehn, P. U. Atukorale, R. P. Carney, Y-S. Yang, F. Stellacci, D.J. Irvine, and A. Alexander-Katz, "Effect of particle diameter and surface composition on the spontaneous fusion of monolayer-protected gold nanoparticles with lipid bilayers" *Nano Letters*, **13**, pp. 4060-4067, 2013, DOI: 10.1021/nl401365n.

and

R. C. Van Lehn and A. Alexander-Katz, "Free energy change for insertion of charged, monolayer-protected nanoparticles into lipid bilayers" *Soft Matter*, **10**, pp. 648-658, 2013, DOI: 10.1039/C3SM52329B.

In the previous Chapter, we showed that a NP can spontaneously incorporate into the bilayer core if there is a sufficiently strong hydrophobic driving force by dynamically rearranging its surface properties. While there is experimental evidence suggesting that such a globally-responsive model is accurate over long timescales, it is not clear how long it takes the alkanethiol ligands in the amphiphilic NPs of interest to rearrange. Moreover, the highly coarse-grained model provided at best a qualitative description of the symmetric penetration process suitable for identifying general features of experimental systems, but it is unable to yield quantitative predictions suitable for direct comparison to experiments. In this Chapter, we will introduce a new model for probing the opposite extreme of environmentally-responsive behavior. In this *locally-responsive* model, the grafting positions of the ligands are assumed to be fixed over simulation timescales. We will also replace the highly coarse-grained model used previously with a new united atom model that provides near-atomistic resolution of the protecting ligands, allowing ligand fluctuations to be modeled in detail. Ligand fluctuations can be biased by the presence of the bilayer and thus environmentally-responsive behavior still occurs even in the absence of grafting point diffusion. Similar fluctuations have been shown previously in atomistic molecular dynamics simulations and are capable of giving rise to spontaneous monolayer asymmetry as would be expected in this system [145].

Using this new model, we will specifically focus on understanding the thermodynamics of the 'symmetric penetration' state identified from the globally-responsive model. This state appears likely to lead to the non-endocytic uptake of cells that was previously found experimentally [81]. Endocytosis is typically triggered from a surface-adsorbed state, where the membrane eventually

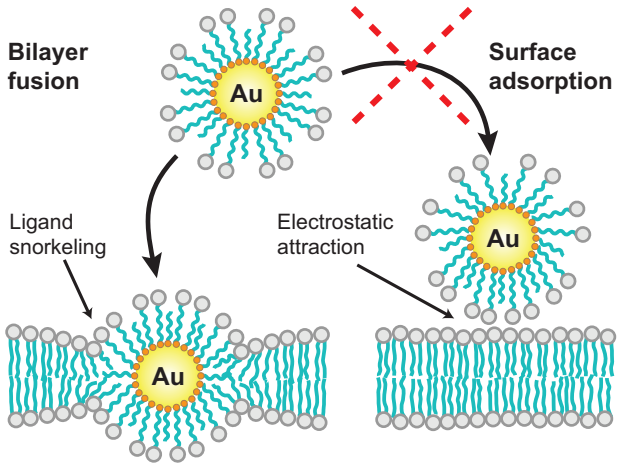

Figure 3-1: Schematic illustration of NP-bilayer fusion. Rather than adopt a surface adsorbed state due to electrostatic interactions, the particles insert into and fuse with the bilayer.

wraps around the NP to facilitate internalization [146, 40, 161]. In this system, surface adsorbtion may occur from strong electrostatic interactions between the NP and the membrane. In contrast, from the embedded state the NP could access either the extracellular or cytosolic side of the membrane in a true cell, potentially enabling direct penetration.

For monolayer-protected NPs to adopt this embedded configuration, charged ligands must distribute on either side of the bilayer. This state closely resembles the configuration adopted by transmembrane proteins and from symmetry considerations should be more thermodynamically stable than an asymmetric distribution of ligands on either side of the bilayer. We thus consider the free energy change for inserting a charged NP into the bilayer core from an initially solvated state. We propose that insertion is driven by the hydrophobic effect as fusing the NP with the bilayer shields hydrophobic ligands within the hydrophobic bilayer core [162]. In principle, stable fusion with the bilayer is challenged by the highly charged surfaces of the particles. The striped domains of these NPs have an average width of 0.6 nm [81, 85], significantly smaller than the typical thickness of the bilayer core, implying that insertion would expose anionic groups to the bilayer interior in an energetically unfavorable state [67, 72]. However, the ligand flexibility allows the ligands to deform and "snorkel" charges out of the hydrophobic bilayer core while simultaneously shielding the hydrophobic alkane backbone within the bilayer. Similar snorkeling behavior occurs in transmembrane proteins where arginine residues bend toward the lipid-water interface as described in the Introduction [72, 163]. Fig. 3-1 illustrates the proposed fusion mechanism, in contrast to a surface adsorption mechanism that would likely encourage endocytosis.

As the NP core diameter increases, the available free volume in the ligand monolayer is reduced and we expect there will be a maximum size above which snorkeling is strongly inhibited and insertion is no longer observed. Increasing the particle diameter also increases the amount of hydrophobic surface area initially exposed to water and hence the magnitude of the driving force for insertion. The competition between these effects implies that the propensity for NP insertion

will be maximized at an intermediate core size. Our simulation results show strong evidence to support this hypothesis, demonstrating for the first time that anionic NPs can insert into and fuse with lipid bilayers despite their highly charged surfaces and aqueous solubility. Moreover, by accurately modeling the ligand structures used experimentally by Verma and co-workers [81], we show that slight changes in the composition of the mixed surface monolayers can significantly influence the free energy change for insertion, providing results that can be mapped to experimental findings in the next Chapter.

3.1 Free energy decomposition

To describe the thermodynamics of the NP-bilayer fusion process, a novel implicit bilayer, implicit solvent model was developed. The model calculates the free energy change for moving an isolated particle in solution to the bilayer midplane with no consideration for the dynamics of translocation which will instead be considered in future Chapters. The total free energy change of the system, ΔG_{tot}, results from a competition between the hydrophobic driving force and the unfavorable penalties for charge insertion, bilayer deformation, electrostatic repulsion, and the reduction of ligand entropy which is written as:

$$\Delta G_{total} = \Delta G_{phobic} + \Delta G_{insert} + \Delta E_{elec} + \Delta E_{thick} - T\Delta S_{conf} \tag{3.1}$$

Here, ΔG_{phobic} is the change in the free energy of solvation of the system. ΔG_{insert} is the free energy cost for inserting charged ligand end groups into the hydrophobic core of the bilayer. ΔE_{elec} is the electrostatic energy change between charged end groups. ΔE_{thick} is the energy for changing the bilayer thickness. Finally, ΔS_{conf} is the conformational entropy change of the ligands upon insertion. This decomposition is similar in spirit to the mean field theory derived in the previous Chapter (eq. (2.7)) and is also similar to treatments of the free energy for the insertion of transmembrane proteins [164, 165], an analogous process. Each term in the decomposition will now be discussed in detail.

The change in solvation free energy, ΔG_{phobic}, represents the primary hydrophobic driving force in the system. Physically, this term is related to both the enthalpic and entropic cost of exposing hydrophobic surface area to water, which reduces the number of hydrogen bonds in the system and forces surrounding water molecules into ordered, low entropy states [162]. Previous studies have shown that a simple approximation for the magnitude of this hydrophobic force is to scale the solvent-accessible surface area, or SASA, by a phenomenological proportionality constant, γ [166, 167, 168, 169, 170]. We thus simply write:

$$G_{phobic} = \gamma SASA \tag{3.2}$$

The key parameter controlling the magnitude of the hydrophobic driving force is γ. The value of γ varies in the literature depending on the system under study and method of calculation [171].

We chose to test two different possible values of γ: 28 cal/mol/Å^2 [170] and 47 cal/mol/Å^2 [169]. Both values were derived from theoretical considerations, fit to experimental liquid alkane-to-water transfer free energies, and have been used to study analogous biophysical phenomena. The first value of 28 cal/mol/Å^2 was obtained by a linear fit of calculated SASA values to free energies for transferring a series of linear alkanes into water [170]. The SASA values were calculated using the same algorithm and probe size as in this work. The larger value of 47 cal/mol/Å^2 was obtained from a similar fitting procedure but takes into account a molar volume correction reflecting the larger size of the alkane solutes in comparison to the surrounding solvent [169]. Both values, or values approximately equivalent to them, have been used extensively in the literature. For example, the former value has been used to explain the solvation energy of transmembrane protein side chains [172, 173, 174], while the latter has been used to explain protein folding and aggregation in solution [175, 165]. Finally, these values match well with several recent reports on the free energy change for purely hydrophobic fullerenes partitioning into lipid bilayers [176, 177, 104, 178]. The range of insertion free energies from these reports is approximately -8.33 to -26.3 kcal/mol; assuming the diameter of a fullerene is approximately 1 nm and the free energy change is only from hydrophobic interactions, then this range would correspond to values of γ between approximately 16 cal/mol/Å^2 and 51 cal/mol/Å^2, similar to the values explored here. The SASA based model for hydrophobic interactions thus maps well to current literature and can approximate solvent effects without including explicit solvent interactions.

ΔG_{insert} is the change in the free energy associated with exposing charged ligand end groups to the hydrophobic core of the bilayer. Previous implicit bilayer simulations have treated this term using a generalized Born model where the bilayer core is treated as a region of low dielectric constant and electrostatic contributions are calculated accordingly [179], or the bilayer is treated as a region of decreasing solvent density based on comparison to simulations of protein side chain analogues [180]. We adopt a approach similar to the latter model and approximate the free energy penalty for insertion from free energy profiles for anion insertion into membranes [181, 182]. The penalty resulting from this approach takes into account free energy changes for observed behavior such as dragging water molecules into the bilayer environment, some lipid deformation, and any electrostatic effects. Furthermore, it directly accounts for any deviations in water density along the bilayer normal. The potential adopted is for a negatively charged side chain analogue in a dioleoylphosphatidylcholine (DOPC) bilayer [181], the closest approximation in the literature to the system studied here.

While ΔG_{insert} accounts for electrostatic interactions between charged end groups and the bilayer, ΔE_{elec} accounts for electrostatic interactions between charged end-groups with each other. Recent studies have shown that the electrostatic potential near the surface of charged monolayer-protected NPs can be well-described by Debye-Hückel theory [183, 184, 185]. The electrostatic energy between ligands is calculated via a screened Coulomb pair potential of the form:

$$\psi(r) = \frac{Q}{4\pi\epsilon r} e^{-r/\lambda_D} \tag{3.3}$$

Here, λ_D is the Debye length of the system. All simulations used a Debye length of 0.8 nm corresponding to a physiological salt concentration of 150 mM. The dielectric constant was set to 80 for all interactions due to the presence of aqueous solvent.

ΔE_{thick} penalizes changes in the thickness of the bilayer in the vicinity of the NP assuming in-plane radial symmetry around the embedded particle. Unlike the preceding three terms, this contribution to the free energy is calculated analytically for a given value of λ, a coupling parameter described below, using a continuum model of membrane deformation that has been previously parameterized to the mechanical properties of known lipids [143, 186]. For DOPC, the deformation energy in kcal/mol is:

$$\Delta E_{thick} = 202.5(\lambda - 1.0)^2 R^{0.815} \tag{3.4}$$

Here, R is the radius of a cylindrical inclusion that is calculated from the average radius of the particle and monolayer in the x-y plane.

The final free energy term, ΔS_{conf}, is the change in the conformational entropy of the ligand monolayer upon insertion into the bilayer. The entropy change is related to the decrease in the number of accessible system configurations as the effects of the bilayer are introduced. A detailed description of how this term is calculated will be presented in the next section.

3.2 United atom model for free energy calculations

Several of the free energy terms described in eq. (3.1) depend on the many degrees of freedom, including the preferred positions of the NP ligands and the thickness of the bilayer, that make the total free energy difficult to calculate analytically. Instead, a Monte Carlo method was developed to compute each of the different free energy terms by combining an united atom model for the ligand monolayer, an implicit bilayer to bias ligand fluctuations, and an implicit solvent model to estimate the hydrophobic driving force.

In the united atom model, ligands were divided into two categories: hydrophobic ligands, consisting of a sulfur head atom and alkyl backbone, and hydrophilic ligands, consisting of a sulfur head atom, alkyl backbone, and charged end group. For the simulations in this Chapter, the ligands were modeled after 11-mercapto-1-undecanesulfonate (MUS) and 1-octanethiol (OT) to mimic the experimental results that motivated this study [81, 187]. MUS has 11 carbon atoms along its backbone and an anionic sulfonate endgroup while OT has 8 carbons in its backbone. The structures of both ligands are shown in Fig. 3-2. The size of each united atom bead was based on established van der Waals radii [188]. Each CH_2 and CH_3 group in both the hydrophilic and hydrophobic ligands was represented by a single hydrophobic bead with a radius of 0.2 nm. Each sulfonate group in the hydrophilic ligands was represented by a single effective bead of radius 0.29 nm. Each sulfur atom bonded to the gold surface was represented by a bead of radius 0.185 nm. These three groups are represented in teal, white, and yellow respectively in Fig. 3-2 and Fig. 3-3. Bond lengths were fixed at 0.154 nm for hydrophobic-hydrophobic bonds and 0.183 nm for both hydrophobic-sulfur

and hydrophobic-hydrophilic bonds while bond angles were not constrained, effectively treating the ligands as freely-jointed chains. The NP surface was modeled as a hollow, spherical shell of individual gold beads. Ligands were grafted to the surface with a density of 4.77 ligands/nm^2 unless otherwise noted [145] and a sulfur-gold bond length of 0.23 nm.

Configurations of the system were sampled using Monte Carlo simulations as described in Appendix A. For each time step, a single hydrophobic or hydrophilic bead was randomly displaced with a step size of 0.07 nm. Gold and sulfur beads were fixed for the duration of the simulation. All attempted moves that led to hard sphere overlap between beads were rejected except for interactions between beads within 2 bonds of each other along the same ligand. Bonds were enforced by rejecting any attempted moves that led to a greater than 10% deviation from the equilibrium bond length. Any move that did not violate the bonding and hard sphere constraints was accepted with a probability P given by:

$$P = e^{-\Delta E/kT} \tag{3.5}$$

where ΔE is the change in system energy for moving the bead calculated as described below. The temperature was set to 300 K for all simulations.

To represent thickness deformations in the implicit bilayer, we introduced a coupling parameter, λ, that was incorporated into each of the free energy terms described in eq. (3.1). λ describes the fractional thickness of the bilayer at the interface with the NP. A value of $\lambda = 1.0$ corresponds to an unperturbed bilayer thickness, $\lambda = 0.0$ is the equivalent of no bilayer, and any intermediate value corresponds to a locally thinned bilayer. Fig. 3-2C illustrates the definition of λ. For DOPC, the unperturbed thickness is about 4.53 nm for $\lambda = 1.0$ [189].

Several of the free energy terms from eq. (3.1) were calculated from the Monte Carlo simulations. G_{phobic} was calculated by explicitly determining the SASA during simulations. The SASA was calculated for each simulation timestep using the Shrake-Rupley "rolling ball" algorithm [190] using 100 uniformly distributed mesh points per hydrophobic bead and a probe size of 1.4 Å to represent water solvation. The SASA was only calculated for hydrophobic beads as free energy changes related to the hydrophilic beads are captured in the G_{insert} term described below. The SASA reflects the unfavorable solvation of hydrophobic surface area by water, so the presence of the hydrophobic bilayer core and resulting decrease in solvent density in the core region decreases the SASA. To model the impact of the bilayer, a solvent density function, $\kappa(z)$, was defined as a function of the bilayer coupling parameter λ described in the main text. $\kappa(z)$ measures the effective solvent density at a distance z from the bilayer midplane ($z = 0$), where z is measured in nanometers. This function was approximated from molecular dynamics simulations of water in DOPC bilayers [181, 182] as:

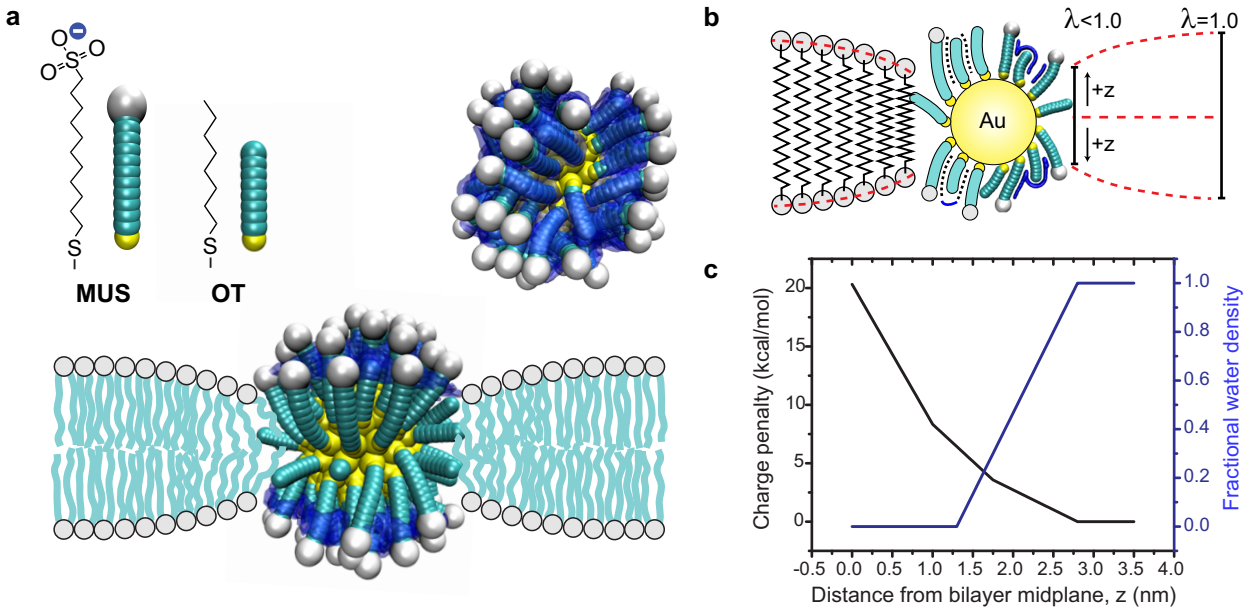

Figure 3-2: Schematic illustrating implicit bilayer, implicit solvent simulation methods. **a** Overview of united atom model for ligands; each CH_2 or CH_3 group was combined into a single hydrophobic bead (teal) and each sulfonate end group was a hydrophilic bead (white). Ligands were permanently grafted to the gold surface (yellow). Structures of the two ligands (MUS and OT) are shown next to their simulation representations. Two snapshots illustrate the NP in solution ($\lambda = 0.0$) and in a thinned bilayer ($\lambda < 1.0$). The SASA is represented as a blue surface and is reduced in the bilayer. **b** Illustration of spring-like bilayer deformation around an embedded NP. The coupling parameter λ defines the thickness of the bilayer at the interface. **c** Graphs of the charge insertion penalty in kcal/mol and fractional water density as a function of the distance, z, from the bilayer midplane, plotted for $\lambda = 1.0$.

$$\kappa(z) = \begin{cases} 0.0 & z \leq 1.3\lambda \\ \dfrac{z - 1.3\lambda}{1.5\lambda} & 1.3\lambda < z \leq 2.8\lambda \\ 1.0 & z > 2.8\lambda \end{cases} \tag{3.6}$$

All numerical prefactors have units of nm so that $\kappa(z)$ is unitless. Recall that $\lambda = h/h_0$ is the perturbed thickness of the bilayer at the interface and is also unitless. A plot of $\kappa(z)$ for $\lambda = 1$ is shown in Fig. 3-2. The simple linear approximation scales the effective water density at the position z and we assume scales the SASA as well, providing a driving force for hydrophobic ligands to prefer the bilayer interior compared to full exposure to aqueous solvent. The total solvation free energy of the system as a function of λ is then written as:

$$G_{phobic} = \gamma \sum_{i}^{beads} \sum_{j}^{mesh} \kappa(z_{ij}) A_{ij} \tag{3.7}$$

The first sum runs over all hydrophobic beads in the system, while the second sum runs over

all mesh points on that bead. For each mesh point, the SASA was incremented by an amount $\kappa(z_{ij})A_{ij}$ if the mesh point was not occluded by another bead in the simulation, where A_{ij} is the increment of the accessible surface area per point. The total change in solvation free energy for a given value of λ was calculated by subtracting the value of G_{phobic} in the baseline state, where $\lambda = 0.0$ and $\kappa(z) = 1.0$ for all z.

To calculate G_{insert}, an explicit potential taken from molecular dynamics simulations of anion partitioning into DOPC bilayers was applied to charged beads in the simulation [181, 182]. This potential is written as:

$$f(z) = \begin{cases} 20.32 - \dfrac{11.98z}{\lambda} & z \leq 1.0\lambda \\ 8.34 - \dfrac{6.36(z - 1.0\lambda)}{\lambda} & 1.0\lambda < z \leq 1.75\lambda \\ 3.57 - \dfrac{3.40(z - 1.75\lambda)}{\lambda} & 1.75\lambda < z \leq 2.80\lambda \\ 0.0 & z > 2.8\lambda \end{cases} \tag{3.8}$$

Here, $f(z)$ is the positive free energy change per ligand in kcal/mol as a function of z, the distance from the bilayer midplane ($z = 0$) in nanometers. The potential is scaled everywhere by λ to account for changes in the perturbed thickness of the bilayer. Only charged end groups on ligands marked as exposed to the bilayer, as described above, were subject to the penalty. Note that each charged end group was considered independently, although recent results suggest that the addition of multiple charged side chains leads to a non-additive energy barrier [191]. However, we assume that due to the symmetry of the spherical NP core the bilayer will tend to deform in a uniform manner to limit charge exposure as captured by the E_{thick} term, effectively taking into account any cooperative effects. Fig. 3-2 shows a plot of this potential for a value of $\lambda = 1.0$. The total energy associated with the insertion of charged groups into the implicit bilayer is simply:

$$G_{insert} = \sum_{i}^{charges} f(|z_i|) \tag{3.9}$$

where z_i is the z-position of bead i and the sum only runs over the charged hydrophilic beads in the simulation.

G_{elec} was also calculated by applying potentials between charged beads according to eq. (3.3). To account for the bilayer, the potential between charges on opposite sides of the bilayer was set to 0 to match the results of numerical solutions to the non-linear Poisson-Boltzmann equation near membrane surfaces [192, 193]. All ligand end groups were assumed to be charged with no possibility for charge regulation due to the low pKa of sulfonate. Based on these assumptions, the total electrostatic energy in the system is given by:

$$E_{elec} = -1.0e \sum_{i} \sum_{j>i} \psi\left(|r_i - r_j|\right) \tag{3.10}$$

Here, r_i is the position of the end group bead i and the sum runs over all charged beads in the simulation. Note that there is no dependence on λ as this term does not involve interactions with the bilayer.

G_{phobic}, G_{insert}, and E_{elec} together represent the main contributions calculated by the implicit solvent, implicit bilayer model. The analytical treatment for E_{thick} was calculated after simulations were finished based on the value of λ. This leaves the final term, S_{conf}, which cannot be calculated from pair potentials alone, but rather requires a method for computing the total free energy of the system as will be described in the following section. The change in each of these terms was calculated using the value computed for $\lambda = 0.0$ as a baseline, and thus each term in eq. (3.1) represents the change in that component relative to a particle isolated in solution, far from the bilayer.

3.2.1 Free energy calculations using BAR

A major contribution to the total free energy change for insertion is the conformational entropy change, ΔS_{conf}, of the monolayer ligands. In the baseline state, the ligands are relatively free to explore the spherical volume around the NP surface; however, in the embedded state, the significant penalty associated with the insertion of charged residues reduces the conformational freedom of end-functionalized ligands. We calculate this term from the total system free energy change using the Bennett acceptance ratio (BAR) method as described in Appendix A [194, 195]. BAR requires the definition of two thermodynamic states with distinct potential energy functions such that the energy of a given system configuration can be calculated for either state. In this system, a thermodynamic state is defined by choosing a value of λ corresponding to a particular bilayer thickness. The free energy change between state 0 with $\lambda = \lambda_0$ and state 1 with $\lambda = \lambda_1$ is equivalent to the free energy change associated with increasing the perturbed bilayer thickness around the embedded NP. For each simulation run, 15 values of the λ parameter were attempted, incrementing from an initial value of $\lambda = 0.0$ to a maximum value of $\lambda = 1.2$. For each value of λ tested, the simulation was first equilibration for 50,000 Monte Carlo timesteps per bead in the system, then configurations were recorded for 100,000 Monte Carlo timesteps per bead. Every 20 timesteps the energy of the system was calculated for both the current and next value of λ and these energies were saved for later input to eq. (A.64). These values were sufficient to obtain convergence via the BAR algorithm. The global free energy minimum for a particular simulation as a function λ was estimated by using a quadratic interpolation between the intermediate values of λ tested [196].

3.2.2 Summary of simulation workflow

To summarize the above sections, the following simulation workflow was performed:

- A value of λ was set for the simulation.
- 50,000 Monte Carlo timesteps per bead were performed as initial equilibration then 100,000

Monte Carlo timesteps per bead were performed as production with total system energies saved for both the current and next value of λ every 20 timesteps.

- For each timestep, a bead was randomly selected and displaced by up to 0.07 nm in a random direction. Moves were rejected immediately if bonding/hard sphere constraints were violated, otherwise they were accepted according to eq. (3.5) based on the change in system energy calculated for the current value of λ.

- The change in system energy was calculated from the change in the SASA (G_{phobic}) for hydrophobic beads. For hydrophilic beads, the change in the system energy was calculated from the change in the z-position (G_{philic}) and position relative to other hydrophilic beads (G_{elec}).

- The total energy for a particular system configuration was calculated from eq. (3.7), (3.9), and (3.10) for two values of λ simultaneously when output during the production stage of the workflow. In other words, while the configuration was *generated* from one value of λ, the energy was calculated for two (as required by the BAR algorithm).

- After all Monte Carlo steps were run, the value of λ was incremented to its next value and the Monte Carlo procedure was repeated.

- After simulations for all 15 values of λ were performed, all saved energy values were input into eq. (A.64) to calculate free energy changes between consecutive values of λ. The total free energy change for a particular value of λ was calculated by summing consecutive free energy changes relative to the value of $\lambda = 0.0$. The thickness deformation energy E_{thick} was also added to the free energy change according to eq. (3.4).

- The overall global minimum in the free energy change was found by numerical interpolation between the actual values of λ sampled. Individual free energy components could be found from the output of simulations, eq. (3.4), and subtracting the total energy from the total free energy to identify the entropic contribution. The value of λ that minimized the overall free energy change was also saved and identifies the thermodynamically preferred bilayer thickness.

This workflow and all simulations were performed using a C program developed in-house.

3.3 Ligand snorkeling stabilizes transmembrane state

The implicit solvent, implicit bilayer united atom simulation model developed here was used to predict the free energy change for translocating monolayer-protected NPs from an initial state in solvent to a final state embedded in the bilayer core. Fig. 3-3 shows several example snapshots of the simulation results for three different particle diameters and three different particle compositions. All diameters reported are the diameter of the gold core, excluding the length of the ligand layer,

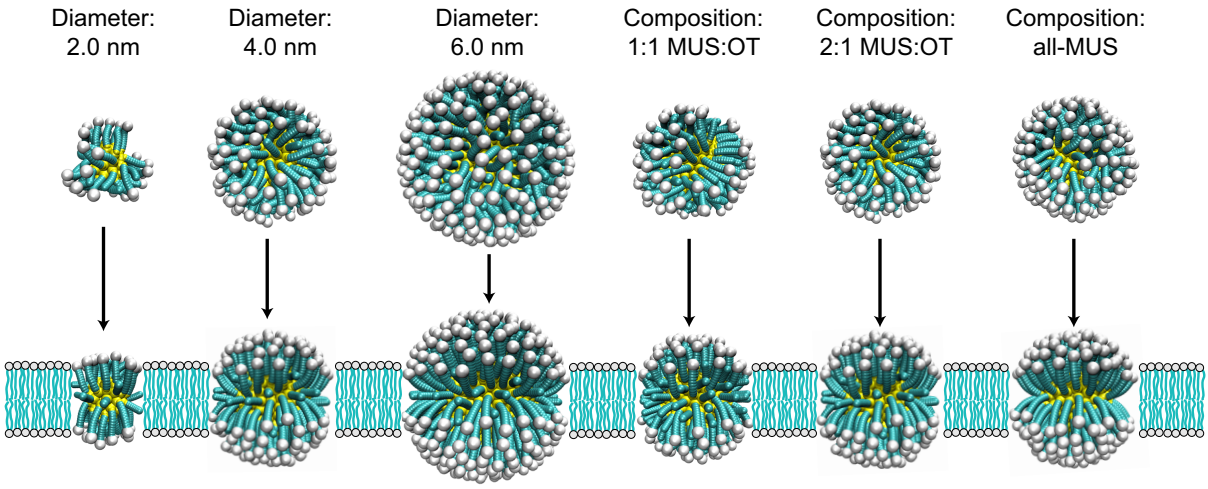

Figure 3-3: Example simulation snapshots for six representative particles. Particles are shown in both the baseline (solvated) state and the final (embedded) state, with the implicit bilayer drawn in as a guide to the eye. Note that the apparent free volume between the NP and implicit bilayer would not be expected in the physical system and is merely an illustration. The snapshots for the final state are taken for $\lambda = 1.0$, equivalent to an unperturbed bilayer thickness. The three NPs on the left have a 2:1 MUS:OT composition and vary in core diameter, while the three NPs on the right have a 4.0 nm core diameter and vary in monolayer composition.

to facilitate an easier comparison with experimental reports [81, 197]. The different compositions represent experimentally-achievable ratios of the two different ligand species. The implicit bilayer is drawn as a guide to the eye. These snapshots illustrate several important features of the NP-bilayer system. First, the ligands in the monolayer clustered in the initial state to decrease the SASA with clustering inhibited as the NP gold core diameter increased. Second, the hydrophilic ligands were observed to snorkel toward the interface in the final state, with charged hydrophilic beads moved away from the hydrophobic core. Finally, the hydrophobic ligands preferred to lie within the hydrophobic core of the bilayer to avoid exposure to water. The simulation results show that the NP monolayers deform to match the lipid bilayer, exhibiting an amphiphilic surface similar to those observed in transmembrane proteins and matching the symmetric penetration state predicted in Chapter 2.

To gain a more accurate picture of the conformational state of the NPs before and after insertion, Fig. 3-4 shows the average occupancy of all beads of the NP (top row) and average occupancy multiplied by the fraction of time the location was occupied by hydrophilic beads (bottom row) of a 2.5 nm core diameter 1:1 MUS:OT mixed NP in the solvated (left) and inserted (right) states. The average occupancy was calculated by dividing the simulation box into cubic grid with a grid separation of 0.1 nm. For each simulation configuration, each bead in the system was checked to see if it occluded grid points in which case a counter for that grid point and bead type was incremented. The graphs show the average of these counters over all simulation timesteps and further averaged by rotating around the normal to the membrane to yield a two-dimensional representation of spatial

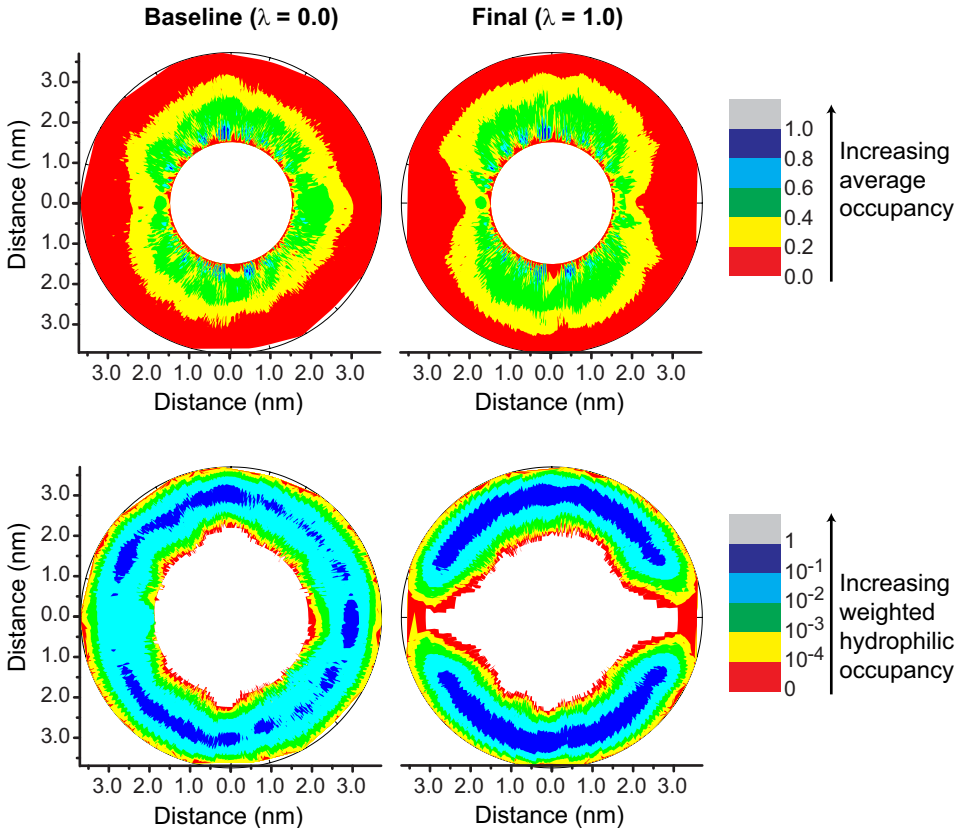

Figure 3-4: Representation of average spatial occupancy by all ligand beads (top row) and the occupancy multiplied by the fraction of time the location was occupied by a hydrophilic bead (bottom row) for the baseline and embedded states. in tThe average occupancy was calculated using a cubic grid as described he text. Results are shown for a 2.5 nm diameter 1:1 MUS:OT NP.

occupancy. The results confirm that in the baseline state all beads, including hydrophilic beads, are effectively able to explore the full conformational landscape around the NP, as would be expected in the absence of a bilayer perturbing the ligand conformations. In contrast, upon insertion the ligand conformations and average occupancies are biased toward the bilayer interface. The top right plot in Fig. 3-4 shows that the actual interface of the monolayer with the bilayer core region appears almost planar given the preference of hydrophobic ligands for the core region. This observation again implies that the embedded NP could strongly resemble a transmembrane protein. The bottom right plot shows that hydrophilic beads strongly prefer the bilayer-solvent interface on average as expected due to the prevalence of ligand snorkeling. The embedded NP thus assumes a state very similar to the symmetric penetration behavior predicted by the globally-responsive model with fluctuations of the ligand end groups giving rise to the effective rearrangement of surface properties.

3.4 Trends in insertion free energy change

The simulation snapshots from the previous section illustrate the process of ligand snorkeling, which would be expected to help stabilize the embedded state. Such snorkeling requires sufficient free volume for ligand fluctuations to occur. Because both the number of ligands and the relative free volume per ligand change as the NP's core diameter increases, it is expected that the free energy change for insertion will have a strong dependence on particle diameter. Similarly, the overall free energy change will be a function of the perturbed bilayer thickness, as thinning the bilayer eases snorkeling but is penalized by a spring potential. Fig. 3-5 shows the change in each of the free energy components described in eq. (3.1) as a function of the coupling parameter λ (top) and gold core diameter (bottom). On both graphs the total free energy change is drawn a solid thick black line, γ is fixed at 28 cal/mol/Å^2, and the particles have a 2:1 MUS:OT surface composition. A 2.5 nm particle core diameter is considered for the plot of free energy versus λ. From this plot, it is observed that the free energy penalty for charge insertion, ΔG_{insert}, steeply increases with λ reflecting the larger distance between hydrophilic ligands and nearby aqueous interfaces. This penalty is largely offset by the stronger driving force for insertion, ΔG_{phobic}, reflecting the ability to sequester more exposed hydrophobic surface area in thickened bilayers. The conformational entropy of the ligand monolayer also decreases as the bilayer thickness is increased due to the restricted configurations of hydrophilic ligands, although this is somewhat offset by the increased conformational flexibility of hydrophobic ligands within the core region. The balance of these three primary contributions along with the penalty for thickness deformations leads to an overall global free energy minimum around $\lambda = 0.80$. The perturbed thickness of the bilayer, h, is related to λ by $h = \lambda h_0$ where $h_0 = 4.53$ nm is the unperturbed thickness of the bilayer [189]. Thus, the global minimum at $\lambda < 1$ indicates that the bilayer prefers to locally thin at the interface with the embedded NP.

For each diameter in Fig. 3-5b, the overall free energy change was first minimized with respect to the perturbed bilayer thickness. As in Fig. 3-5a, the total free energy change is non-monotonic with respect to particle diameter due to both an increase in the magnitude of the hydrophobic driving force and increase in the magnitude of free energy barriers as the particle size increases. The increase in the hydrophilic penalty for insertion can be related to both the increase in the number of charged groups in the monolayer and the decrease in free volume per ligand as the diameter increases, inhibiting deformation and leading to the large entropic penalty at large particle diameters. The major result of this breakdown is the recognition of both a preferred particle diameter where the magnitude of the equilibrium free energy change is largest and a cutoff diameter where the sign of the free energy change becomes positive. This latter finding implies that NPs below the cutoff diameter would be expected to assume stable embedded positions in the bilayer, while larger particles would prefer to remain free in solution.

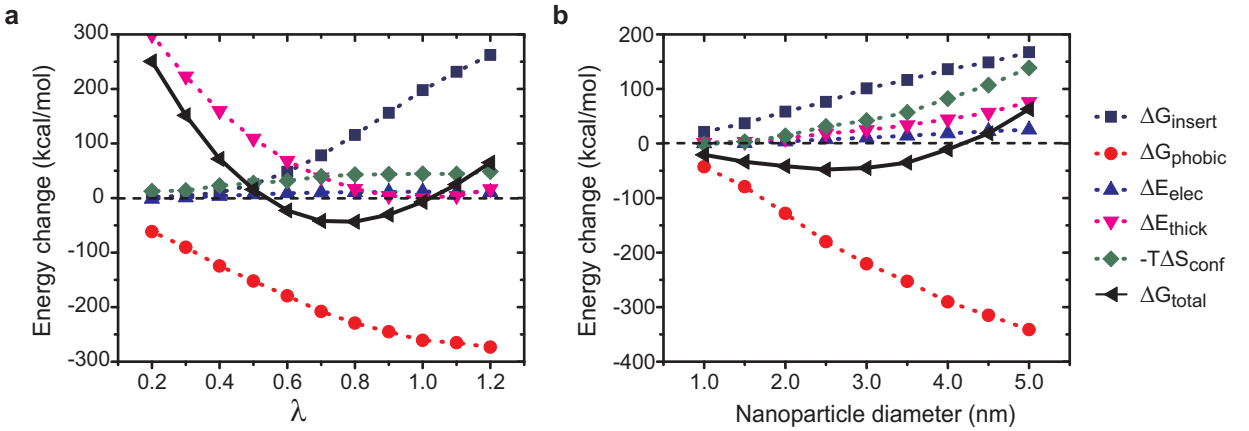

Figure 3-5: Breakdown of free energy components as a function of NP diameter and thickness for a 2:1 MUS:OT particle. γ is set to 28 cal/mol/Å^2. **a** Free energy components as a function of the coupling parameter λ, representing the fractional perturbed bilayer thickness, for a NP with a 2.5 nm diameter. The total free energy change is minimized for $\lambda < 1$, indicating local bilayer thinning. **b** Free energy components as a function of the NP diameter. The total free energy is minimized with respect to λ for each point.

3.5 Free energy of insertion for different NP diameters, compositions

Having established that the implicit bilayer, implicit model predicts a negative free energy change for insertion as a function of particle diameter, we can now explicitly model the different NPs studied experimentally to see whether there is a thermodynamic driving force for insertion. To match previous cell experiments [81, 187], the free energy changes for the insertion of particles with monolayer compositions of all-MUS, 2:1 MUS:OT, and 1:1 MUS:OT in random, striped, and perfectly mixed morphologies were calculated. γ was set to 47 cal/mol/Å^2. Fig. 3-6 shows images of the morphologies simulated as generated using the method detailed in Appendix B. The surface morphology was determined only by the relative positioning of the hydrophobic and hydrophilic ligand end points which are fixed for the duration of the simulation run. For each combination of surface composition and morphology, the particle gold core diameter was varied between 1.0 nm and 10.0 nm with resulting free energy changes shown in Fig. 3-6. As predicted, the free energy change for each particle type is a non-monotonic function of diameter with preferred core diameters at intermediate sizes where insertion was strongly favored followed by a sharp increase in the free energy until the overall change was positive, indicating a maximum cutoff diameter for stable insertion. The width and depth of the free energy curves shift dramatically when the surface composition is altered; all-MUS particles only have negative free energy changes for diameters less than ≈ 3.5 nm while adding more hydrophobic ligands to the surface increased both the embedding cutoff and the magnitude of the free energy change. However, there is no apparent difference in the free energy change for embedding between the three different morphologies as would be expected from cellular penetration experiments. All three morphologies – stripes, random, and mixed – show

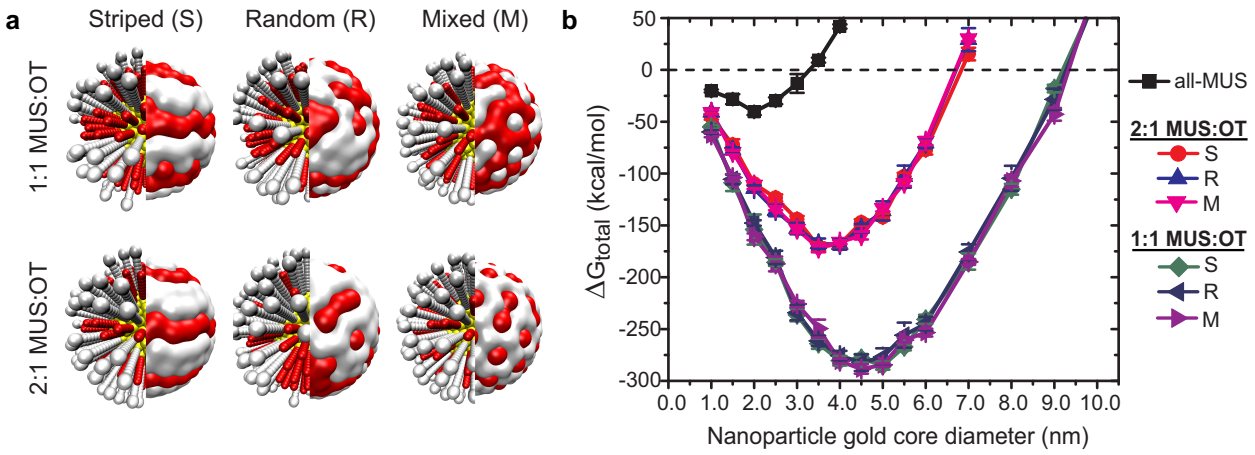

Figure 3-6: Simulation results and comparison to experiments. **a** Illustrations of three different surface morphologies simulated for both mixed monolayer compositions. The white surface indicates the position of MUS while red indicates OT. The surface morphologies differ only in the relative positions of the grafted ligand positions. **b** The change in free energy for embedding as calculated from simulations plotted as a function of NP core diameter for three different monolayer compositions and three different surface morphologies. The dashed line indicates where the total free energy change is 0.

nearly identical results, reflecting a minimal change in the free energy when ligand positions are switched on the NP surface.

These simulation results can be understood by considering the relative magnitude of the hydrophobic driving force and the ability of the protecting monolayer to snorkel charges out of the bilayer core. Because the ligand domains were small, the relative positioning of hydrophilic and hydrophobic ligands on the surface did not significantly affect the ability of the ligands to snorkel and hence there was no observed morphology distinction. Much more important than the surface morphology were the diameter of the NP and the composition of ligands in the monolayer. As discussed earlier, increasing the size of the NP increased the barrier to snorkeling by reducing ligand free volume. Similarly, increasing the relative proportion of hydrophilic ligands also inhibited snorkeling due to the bulkiness of the sulfonate end groups and increased electrostatic repulsion. In contrast, NP monolayers with additional hydrophobic ligands had larger amounts of exposed hydrophobic surface area in the baseline state that was shielded in the bilayer, leading to a greater hydrophobic driving force (c.f. Fig. 3-3). The combination of these factors led 1:1 MUS:OT particles to prefer embedding more strongly than 2:1 MUS:OT and all-MUS particles, independent of surface morphology. These simulations suggest that monolayer composition and particle size, not actual morphology, control the thermodynamics of fusion with lipid bilayers. In the next Chapters, we will consider other factors that may influence the insertion free energy and compare the predicted size cutoffs to those found experimentally.

3.6 Conclusions

In this Chapter, we developed a novel implicit bilayer, implicit solvent model which is used with an united atom Monte Carlo simulation methodology to find the free energy change for inserting an amphiphilic NP into a bilayer. Unlike the globally-responsive model described in Chapter 2, this new model does not permit the motion of ligand grafting points, instead only allowing local deformations of the ligand backbones. By modeling the ligands in near-atomistic detail and permitting realistic fluctuations, the simulations are able to capture local ligand deformations that give rise to changes in the effective surface properties exposed to the implicit bilayer. The fluctuations of the flexible oligomeric ligand backbones thus provide a mechanism for the NP surface to be environmentally-responsive, enabling favorable bilayer insertion as shown in Chapter 2.

Using this model, the free energy change for the insertion of NPs of a range of different core diameters was computed. The free energy change was found to have a strong dependence on NP size. As the NP core diameter increased ligand fluctuations were inhibited by the reduced free volume per ligand, leading to a strong energy barrier associated with the inability of ligands to deform to remove charges from the bilayer core. The dependence of favorable fusion on size led to the identification of size threshold for favorable insertion – in other words, above a certain NP core diameter the free energy change for fusion was found to be positive. This size threshold was found to shift to larger particle diameters if the monolayer composition included more hydrophobic OT ligands at the expense of the end-functionalized MUS ligands. However, the actual nanoscale morphology of the monolayer, or the relative locations of the ligand grafting points, was found to have no effect on the thermodynamics of embedding.

The results of the simulations performed here can be compared to the experiments on cell penetration from Verma et al [81]. In this paper, three different compositions were considered – 2:1 MUS:OT, 2:1 MUS:br-OT, and all-MUS. The 2:1 MUS:OT batch was found to exhibit the greatest non-endocytic uptake, followed by the 2:1 MUS:br-OT and all-MUS batches, which showed effectively zero uptake. The conclusion of this paper was that direct cytosolic access could only be obtained by the striped 2:1 MUS:OT NPs, and not NPs with a similar surface composition but different surface morphology (2:1 MUS:br-OT) or less hydrophobic surface (all-MUS). In contrast, the simulation results presented in this Chapter suggest that all-MUS NPs should penetrate into cells if they are synthesized with a small core size. In the paper by Verma and collaborators, the size of all of the NP batches was approximately 4.5 nm [81], which would be well above the size-threshold identified here for the all-MUS NPs but below the threshold identified for 2:1 MUS:OT. Our results thus suggest an alternative explanation, namely that direct penetration would be observed if the size of the batches was smaller. Similarly, these results indicate no difference between striped and mixed morphologies, seemingly in disagreement with 2:1 MUS:OT 2:1 MUS:br-OT results. However, the simulations show the importance of ligand fluctuations, which in principle could be inhibited by the bulky side groups attached to the br-OT ligands. Since the br-OT NPs did show some uptake, although less than MUS:OT [81], it is possible that the effect of the ligands was to shift the free energy curves to a lower size threshold that only allowed part of the synthesized batch to stably

embed. In the next two Chapters, we will further explore the conclusions of these simulations by providing additional experimental evidence to confirm simulation predictions. We will then apply the simulation methodology to additional NP compositions to provide design guidelines for the construction of NPs that optimally embed within lipid bilayers.

THIS PAGE INTENTIONALLY LEFT BLANK

Chapter 4

Experimental Evidence for NP-Bilayer Fusion

Work in this chapter was published in:

R. C. Van Lehn, P. U. Atukorale, R. P. Carney, Y-S. Yang, F. Stellacci, D. J. Irvine, and A. Alexander-Katz, "Effect of particle diameter and surface composition on the spontaneous fusion of monolayer-protected gold nanoparticles with lipid bilayers" *Nano Letters*, **13**, pp. 4060-4067, 2013, DOI: 10.1021/nl401365n.

 All experiments were performed by Prabhani U. Atukorale, Randy P. Carney, or Yu-Sang Yang, with proper contributions highlighted in the text.

In the previous Chapter, we introduced a novel free energy decomposition and accompanying simulation model for calculating the free energy change associated with insertion a NP from solution into the center of the bilayer. We found that the free energy change was negative for a wide variety of NP core diameters and particle sizes, implying that such NP-bilayer fusion should be thermodynamically favorable. In this Chapter, we present several pieces of experimental evidence for the fusion hypothesis and interpret the results in the context of the predictions of the simulation model. In addition, several additional experimental results in the literature are interpreted in terms of the NP-bilayer fusion hypothesis. The chief findings of the experiments indicate the preferential NP-bilayer fusion does occur in model cell membranes with a similar size dependence as found in the simulations. The size dependence of all-MUS NPs predicted from the simulations further correlates with the penetration of NPs into cells under conditions when endocytosis is inhibited. Finally, TEM imaging shows direct evidence of NP-bilayer fusion. Combined, these experimental results are in strong agreement with the simulation predictions and provide evidence for NP-bilayer fusion.

4.1 NP interactions with vesicles

As a first experimental method to test NP-bilayer interactions, lipid vesicles were synthesized to serve as a model system for non-specific NP-lipid interactions. Single-component giant multilamellar vesicles (GMVs) were formed from the zwitterionic lipid DOPC. DOPC stock solutions were prepared in chloroform and gently dropped onto lightly scratched glass. The chloroform was allowed to evaporate overnight and the resulting lipid films were hydrated in water vapor at 70°C for 6 hours. Following this step, the lipid films were bathed in 50 mM sucrose and the vesicles were allowed to form overnight also at 70°C. Vesicles were harvested gently and allowed to cool to

room temperature. All vesicle experiments were performed by Prabhani U. Atukorale under the supervision of Prof. Darrell J. Irvine.

NPs with either a 1:1 MUS:OT or all-MUS surface composition were prepared with the one-phase Brust synthesis according to previous methods and labeled with a red fluorescent BODIPY dye [198]. The synthesis was performed by Randy P. Carney. The mean core diameter of the 1:1 MUS:OT particles was 2.2 nm while the mean core diameter of the all-MUS particles was 4.15 nm. An external medium of 5 μg/mL calcein, a green fluorescent dye which does not passively diffuse through lipid bilayers, and 0.3 mg/mL BODIPY-labeled NPs in 50 mM glucose were added to the previously-prepared vesicle solution. The solution was allowed to equilibrate for 1-3 hours before confocal imaging.

Differential interference contrast (DIC) and confocal images of the DOPC GMVs in solution with either the all-MUS or 1:1 MUS:OT NPs are shown in Fig. 4-1. From these images, it is apparent that green calcein fluorescence was confined to the external solution and was not observed within vesicles. In contrast, red BODIPY fluorescence from the particles was observed to colocalize with the outer bilayer of the vesicles. Inner membranes within the multilamellar vesicles were also clearly outlined by red fluorescence as indicated by the boxed vesicles in Fig. 4-1 and confirmed by the DIC images. The DIC images further establish that those vesicles showing NP fluorescence throughout the vesicle core were GMVs composed of solid stacked layers of lipid, while unilamellar vesicles showed little/no free NP fluorescence in their interior, suggesting that particles preferentially embedded within available membranes. Similar results were obtained with particles of both surface compositions.

These observations imply several important findings that support the hypothesis of NP-bilayer embedding. First, the exclusion of calcein from the vesicle interior indicates that NPs do not disrupt the bilayer, agreeing with the non-disruptive mechanism observed in cells [81] and consistent with a lack of poration suggested by the NP-bilayer fusion model. Second, the localized BODIPY fluorescence from vesicle membranes, in comparison to the relatively weak background fluorescence, shows that the particles have a strong affinity for the lipid bilayer itself. In Appendix C, we provide evidence that the preference of the hydrophobic BODIPY dye for the membrane interior only allows for fluorescence when NPs are embedded, further supporting the embedding hypothesis. Finally, the BODIPY fluorescence from inner membranes in the multilamellar vesicles confirms that the particles can access inner membranes without the aid of an endocytic mechanism.

To further probe the interactions between vesicles and NPs, multilamellar vesicles were prepared from a mixture of DOPC (80 mol %) and DOPS (20 mol %) lipids in 50 mM sucrose and imaged in 50 mM glucose. The inclusion of DOPS, an anionic lipid, led to a negative charge at vesicle surfaces. Fig. 4-2 shows confocal microscopy images of BODIPY-labeled 1:1 MUS:OT particles and calcein added to DOPC-DOPS vesicles in the absence of salt (top) and in 150 mM NaCl (bottom). This salt concentration was chosen to mimic a typical biological environment. Calcein was still excluded from the vesicle interior in both salt concentrations. In the absence of salt, BODIPY fluorescence was only weakly observed from vesicle membranes compared to the background. This control provides

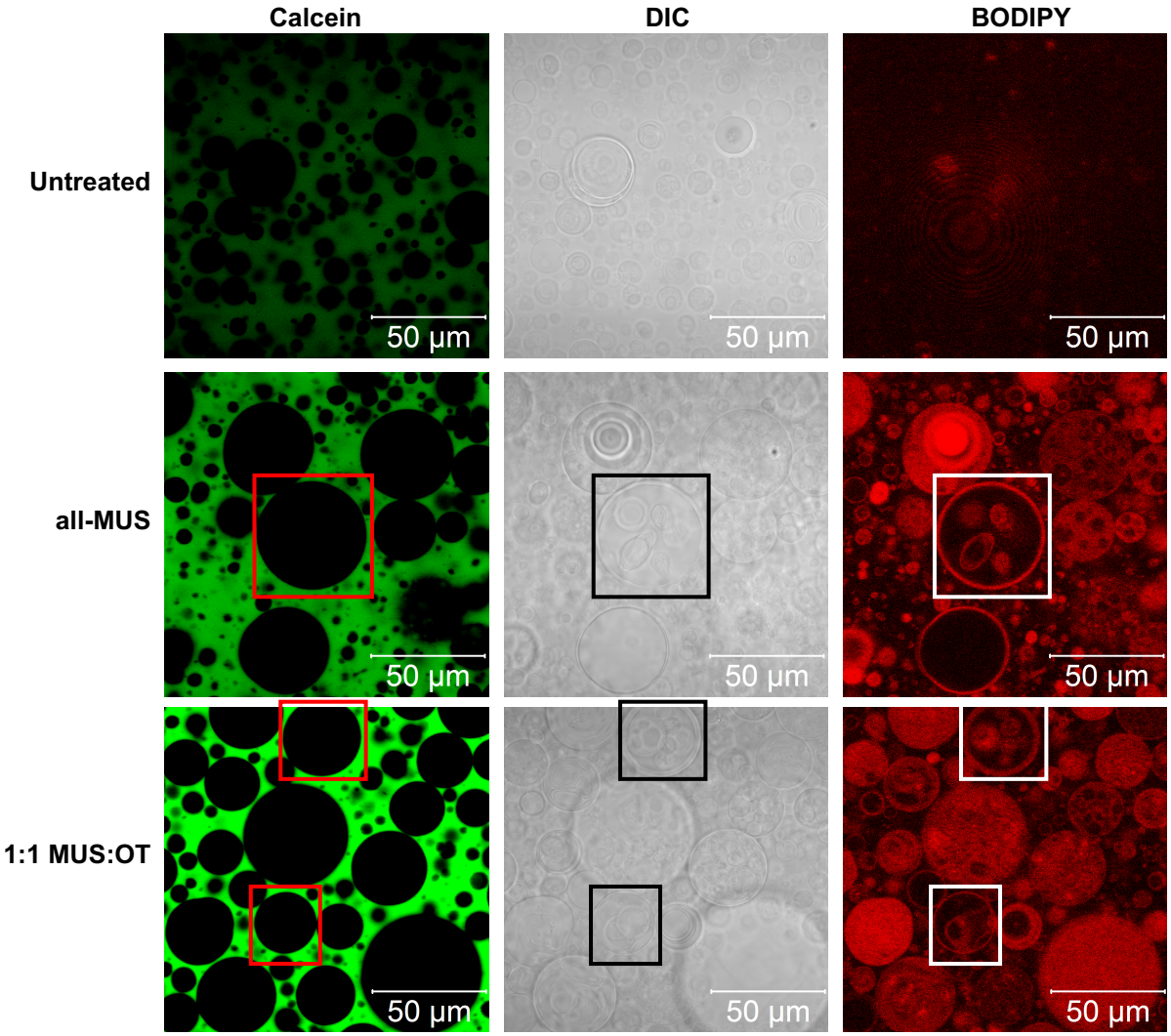

Figure 4-1: Confocal microscopy images of BODIPY-labeled NPs in solution with multilamellar single-component DOPC vesicles and the membrane impermeable dye calcein. Boxes indicate internal membranes with BODIPY fluorescence.

further evidence that the BODIPY signal observed within GMVs was not due to free dye in the particle suspension. In the presence of physiological levels of salt, BODIPY fluorescence was again observed from both internal and external vesicle membranes, similar to what was observed for pure DOPC. The addition of salt screened electrostatic interactions, reducing the repulsion between the anionic particles and like-charged vesicles. The occurrence of localized fluorescence, and thus some form of NP-bilayer interaction, is striking because previous simulation and experimental studies have shown that electrostatic interactions attract anionic NPs to the bilayer surface, even in zwitterionic membranes [106, 199]. In contrast, in this system NPs were observed to colocalize with bilayers even when electrostatic interactions were highly screened. This finding again supports the hypothesis that NPs are driven to embed within membranes via the hydrophobic effect rather than just adsorbing to the bilayer surface due to electrostatic interactions. Indeed, the confocal

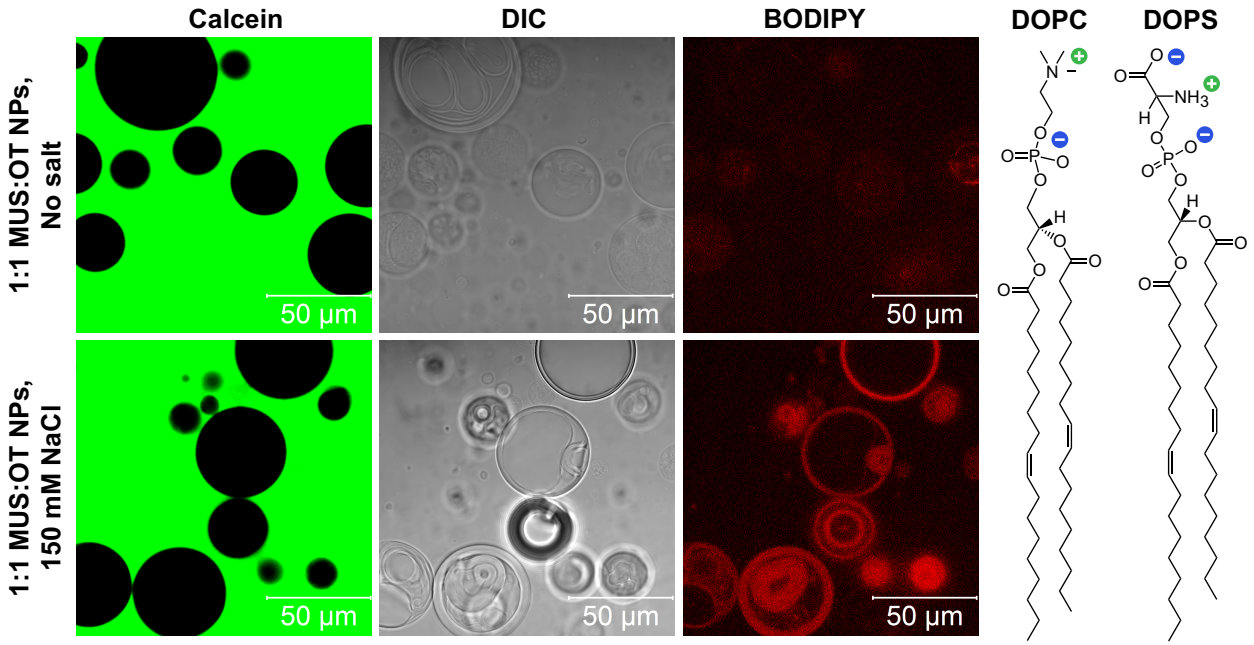

Figure 4-2: Confocal images of BODIPY-labeled 1:1 MUS:OT NPs in solution with multilameller, anionic 80% DOPC/ 20% DOPS vesicles without salt (top) and 150 mM NaCl (bottom).

images shown in Figs. 4-1 and 4-2 are similar to images of purely hydrophobic NPs reported in the literature that are known to embed within the hydrophobic bilayer core [200]. Similar results have also been reported recently for the incorporation of block copolymer-decorated NPs into block copolymer vesicles [201] as well as the incorporation of charged ligand-protected NPs into surfactant vesicles [202], providing evidence of the generality of this mechanism.

4.2 Electron microscopy

To further confirm that the BODIPY fluorescence reflects NP-bilayer fusion, single-component multilamellar DOPC vesicles were imaged using transmission electron microscopy (TEM). DOPC dried lipid films were rehydrated in the presence of 1:1 MUS:OT particles and ova AF546 proteins at room temperature. After vesicle assembly, the NP-vesicle solution was washed two times by centrifugation to remove excess freely dispersed proteins. TEM samples were prepared by placing 10 μL of the particle-vesicle solution on a Formvar/Carbon coated copper grid. After depositing samples for 20 minutes, the solution was blotted off using filter paper. 10 μL of aqueous phosphotungstic acid solution (1%, pH=7) was then applied to the grid for 15 seconds and the stain was blotted off again using filter paper. Samples were air dried before imaging. The sample preparation and TEM imaging were performed by Yu-Sang Yang under the supervision of Prof. Darrell J. Irvine.

Fig. 4-3 shows TEM images of NPs embedded within multilamellar vesicles at both 50 nm and 20 nm resolution, with red arrows drawn to point out particular examples. The NP cores were observed along the light regions corresponding to the hydrophobic core of the bilayer between the

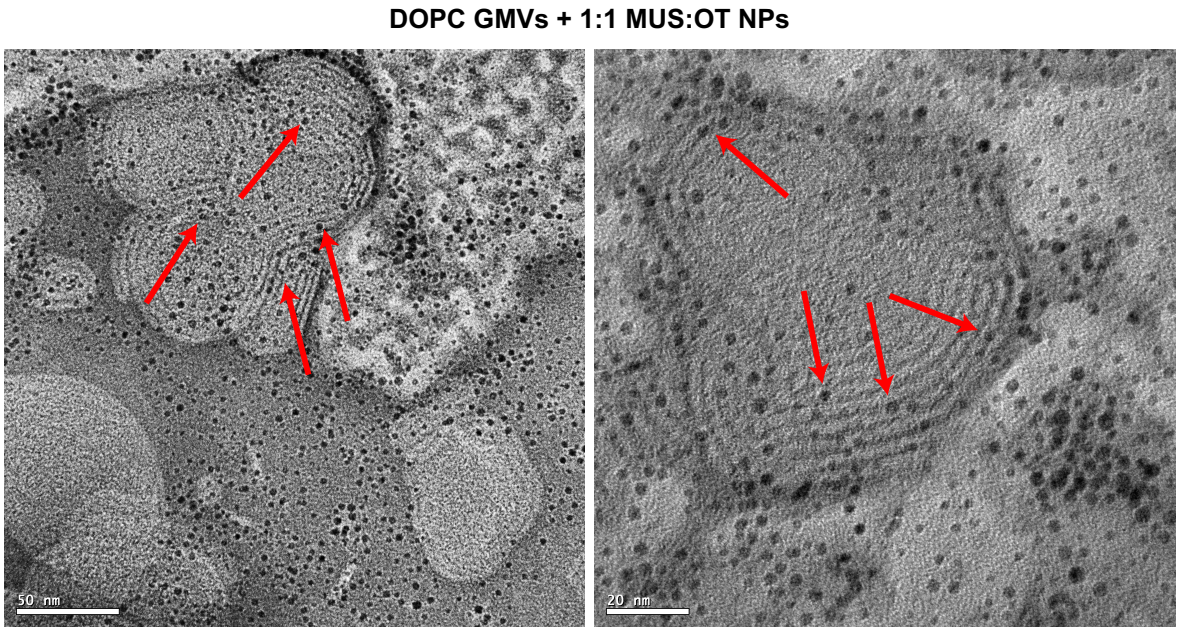

Figure 4-3: TEM images of DOPC multilamellar vesicles with 1:1 MUS:OT NPs in both 50 nm (left) and 20 nm (right) resolution. Red arrows are drawn to highlight NPs that are aligned with the lighter hydrophobic bilayer core regions.

dark lines marking the hydrophilic bilayer head groups regions. This observation is direct support of the embedding hypothesis as the charged NPs are able to colocalize with hydrophobic regions of the bilayer. The images also further confirm the multilamellar nature of the vesicles consistent with the images in Fig. 4-2.

4.3 Black lipid membranes

The fluorescence microscopy results provide strong evidence of preferential NP-bilayer interactions even under conditions when electrostatic interactions are screened, and moreover the preferential BODIPY fluorescence from internal membranes in GMVs suggest that NPs can bypass the membrane without disruption. These findings agree well with the general principles of the NP-bilayer fusion mechanism. One of the strong quantitative predictions of the simulation model, however, is that bilayer insertion is only favorable for NPs with core diameters below a composition-dependent threshold. To compare to simulation results, size-fractionated samples of NPs [198] with different monolayer compositions were added to a DOPC "black" lipid membrane (BLM). The BLM was assembled over a pore dividing two water reservoirs with 50 mM KCl in an electrochemical cell. Due to the inability for ions to passively diffuse across the bilayer core, the application of a potential difference across the bilayer leads to a build up of charge on opposing monolayers leading to an intrinsic bilayer capacitance. The quantity of embedded NPs was measured by calculating the change in the capacitance of the black lipid membrane upon the addition of particles to one of the

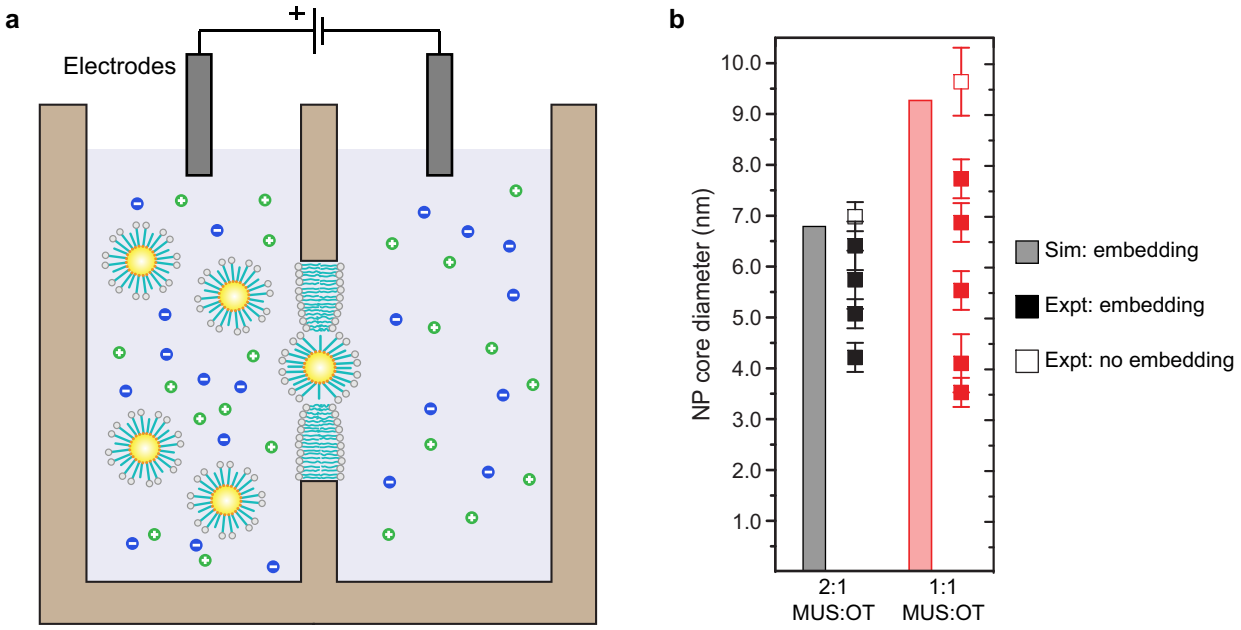

Figure 4-4: Nanoparticle interactions with single-component DOPC black lipid membranes. **a** Schematic of BLM apparatus, with NP embedded in a partition dividing two chambers. **b** Comparison of the BLM results and simulation predictions for 2:1 MUS:OT and 1:1 MUS:OT NPs.

two solvent reservoirs as described recently [197]. Fig. 4-4a shows a schematic of the experimental apparatus. All NP synthesis and BLM experiments were performed by Randy P. Carney under the supervision of Prof. Francesco Stellacci.

For NP samples that interacted with the bilayer, increasing the concentration of particles in the solution increased the capacitance of the bilayer until it eventually reached a plateau [197]. Adding additional particles to the other solvent reservoir failed to increase the capacitance change once the plateau was reached. This observation supports the insertion mechanism as the capacitance should continue to increase as particles were added to both sides of the bilayer if surface adsorption led to a capacitance change. This technique also allowed NP fusion to be measured for non-fluorescently labeled particles; however, the results were unchanged when BODIPY was conjugated to the NP surfaces.

Using this method, all-MUS, 1:1 MUS:OT and 1:1 MUS:OT particles of different size fractions were prepared and added independently to the BLM apparatus. For each particle composition, a threshold particle size fraction was determined where no capacitance change was observed at all. As predicted by the simulations in Chapter 3, the 2:1 MUS:OT particles had a smaller cutoff threshold than 1:1 MUS:OT. No fraction of all-MUS was observed to induce a capacitance change, but fractions with sizes smaller than the predicted cutoff could not be reliably synthesized in sufficient quantity for the BLM experiments [197]. A comparison between the size thresholds obtained from experiments and those predicted by the simulations is shown in Fig. 4-4b, with experimental core sizes estimated from the hydrodynamic radii measured for each particle fraction with 3.1 nm subtracted to approximate the size of the monolayer [81]. The simulation and experimental results

NP batch	Mean diameter (nm)
A	2.4 ± 0.3
B	2.9 ± 0.5
C	3.4 ± 0.8
D	4.9 ± 1.1
E	5.8 ± 1.4

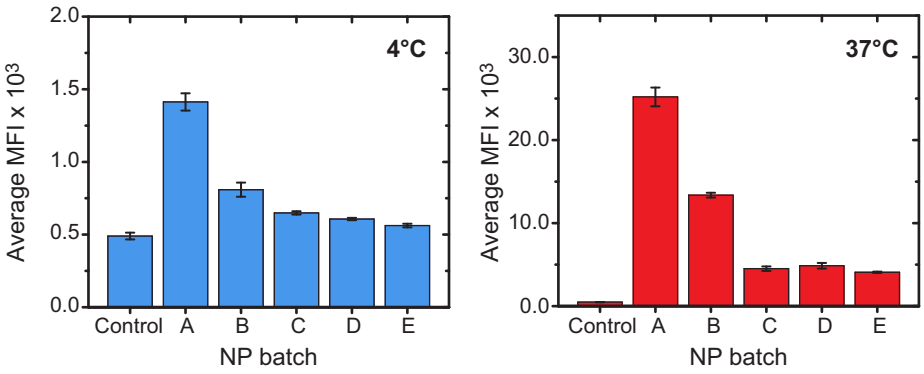

Figure 4-5: Size-dependence of cell penetration measured by flow cytometry at both 4°C and 37°C. Cellular uptake was measured by the median fluorescence intensity of BODIPY-labeled NPs confined to the cytosol. Five all-MUS NP batches of increasing diameter were fractionated as summarized. Error bars are the standard deviation of the MFI of three biological replicates.

show remarkable agreement, reinforcing support for the insertion hypothesis.

4.4 Cell experiments

The vesicle and BLM results showed strong evidence of NP-bilayer fusion in synthetic membranes, but there is still the question of whether this interaction occurs in cells. To test whether the penetration of NPs into cells is also size-dependent, consecutively-sized all-MUS NP batches were size-fractionated. all-MUS was chosen as a surface composition previously shown to not penetrate into cells via the energy-independent mechanism [81, 187]. 5 fractions with average gold core diameters ranging from 2.4 nm to 5.8 nm (labeled as batch A-E in Fig. 4-5) and a concentration of 0.3 mg/mL were fluorescently labeled with a BODIPY dye as in previous experiments. To test for the existence of free dye, the NP fractions were first incubated with red blood cells (RBCs), employing a recent protocol developed to test the presence of free dye [203]. Any fractions found to have free dye were not used. Each of the 5 fractions was then incubated with HeLa cells cultured following previously used methods [187, 203] at both 37°C and 4°C for 3 hours. The median fluorescence intensity (MFI) of BODIPY fluorescence for each fraction was analyzed using flow cytometry. Complimentary measurement using confocal imaging of particle uptake was performed with live cells using a Zeiss LSM 700 Inverted Microscope to visually confirm that dye was localized to the cell cytosol, indicating that increased BODIPY fluorescence was due to NP internalization. All cell experiments were performed Randy P. Carney under the supervision of Prof. Francesco Stellacci.

Fig. 4-5 shows the BODIPY MFI averaged over three biological replicates as a function of NP core diameter. For both temperatures, the average MFI was observed to decrease with larger particle sizes indicating a decrease in NP internalization. The average MFI reached a plateau value for batch C consisting of particles of mean diameter 3.4 nm, near the size threshold identified in

Fig. 3-6 and shown again in Fig. 4-4. The observation of intracellular fluorescence in excess of the control even at 4°C, where endocytosis is inhibited, indicates that penetration occurred by an energy-independent mechanism consistent with previous observations for 2:1 MUS:OT and 1:1 MUS:OT particles[81, 187]. The decrease in fluorescence intensity with larger particle batches correlates with the size-dependence shown for pure bilayer systems (c.f. Fig. 4-4) and indicates that the previous observation of no penetration by all-MUS particles may be due to the larger sizes studied in previous work ($\approx$ 4.5 nm core diameter [81]). These findings provide support for the hypothesis that NP-bilayer fusion is a critical step in the cell penetration pathway.

4.5 Conclusions

In this Chapter, we provided support for the NP-bilayer fusion hypothesis proposed in Chapter 3 using four different experimental techniques. Experiments with fluorescently-labeled NPs showed that the NPs colocalize to all available membranes when exposed to multilamellar vesicles, even interacting with internal membranes without allowing the escape of a hydrophilic dye. Moreover, the interactions also occurred with anionic vesicles in the presence of salt which should in principle minimize any electrostatic interactions that would facilitate surface adsorption. These results indicate that the NPs can non-disruptively interact with membranes consistent with the fusion hypothesis. TEM images further provide direct visual indication that NPs embed within the hydrophobic core of bilayers despite their highly charged surfaces, again agreeing with the results of Chapter 3. The size-dependence predicted by the simulation model introduced in Chapter 3 was further shown to predict both NP-bilayer interactions measured with a black lipid membrane and actual penetration of cells by a NP composition previously thought to be unable to access the cell interior. The matching between simulation and experiment provides strong quantitative evidence for the fusion hypothesis and furthermore demonstrates that NP-bilayer fusion may be the critical first step that enables cell penetration.

Finally, beyond the experiments on this system shown in this Chapter, multiple recent experimental studies on related systems support the NP-bilayer hypothesis using different techniques. In a study by Lee et al., 6 nm core diameter gold NPs were protected by a mixed monolayer consisting of mercaptoundecanoic acid (MUA) and octadecanethiol (ODT) [202]. These ligands are nearly identical to the ligands considered in this chapter, except ODT has ten additional alkyl groups in its backbone compared to OT. The authors then incubated a low concentration of these NPs with amphiphilic surfactant vesicles, which are chemically similar to lipid vesicles, and imaged the resulting solution using cryo-electron microscopy (cryo-EM). The cyro-EM images confirmed preferential NP-vesicle interactions that were interpreted in terms of the global rearrangement model outlined in Chapter 2. However, as shown in Chapter 3, such NP-vesicle interactions could occur even without global ligand arrangement, and the cryo-EM imaging technique cannot distinguish between the embedded state predicted in Chapter 3 and the states predicted in Chapter 2. The images thus provide strong support for NP-bilayer interactions in an analogous system that involves

the embedding of NPs in the hydrophobic core of the vesicle bilayer, although the exact structure of the surface cannot be determined.

In a second study by Tatur et al, 2 nm core diameter gold nanoparticles were protected by a 1:1 MUA:OT monolayer, again similar in size and chemistry to the NPs studied here [204]. A similar series of cationic, trimethylamine functionalized NPs were synthesized as well. DSPC floating lipid bilayers were then deposited on a solid substrate. A floating bilayer consists of a series of bilayers stacked vertically on a solid substrate; by stacking multiple bilayers, the topmost bilayer is able to fluctuate more freely than the bottommost bilayer thereby minimizing the influence of the substrate. NPs were then added to the floating bilayer a temperature above the melting point of the lipids. While the anionic NPs were found to exert a dehydrating effect that destabilized the bilayers, the cationic NPs were found to penetrate into the membrane and embed within the hydrophobic core as measured by neutron reflectivity experiments that clearly indicated the presence of gold in the hydrophobic bilayer region [204]. While the results with the anionic NPs do not seem to match the predictions of Chapter 3 or 4, the unusually high temperature needed to maintain a fluid bilayer due to the choice of lipid species may have impacted the measurements, especially given that similar disruption of a lower melting point lipid (DOPC) was not observed in any of the experiments shown here. However, the results with the cationic NPs perfectly match expectations, agreeing with both the simulation and experimental results and perhaps suggesting that the model generalizes to both cationic and anionic NP surfaces.

Finally, in a recent study by Gordillo et al [205], gold NPs of different diameters were synthesized and protected by a homogeneous monolayer of 1-mercaptoundecane-11-tetra(ethylene glycol), a ligand with a hydrophobic backbone of identical length as MUS but end-functionalized with a short four segment polyethylene glycol moiety which is water-soluble. The authors performed electrochemical measurements using a hanging mercury drop electrode coated with a DOPC monolayer to record bilayer interactions, a similar set up to the black lipid membranes discussed above. They found that 10 nm core diameter NPs did not record signals consistent with bilayer internalization, while smaller 2-3 nm core diameter NPs did. Furthermore, testing the same NPs on HeLa cells showed non-endocytic internalization of only the smaller 2-3 nm NPs. These results are highly consistent with BLM and cell studies reported above for a ligand system similar to the all-MUS NPs, albeit with a slightly less charged functional group. Given both the experiments here and other results in the literature, there is evidence from at least seven different experimental techniques from multiple research groups that support the basic predictions of NP-bilayer fusion.

THIS PAGE INTENTIONALLY LEFT BLANK

Chapter 5

Design Rules to Control NP-Bilayer Fusion

Work in this chapter was published in:

R. C. Van Lehn and A. Alexander-Katz, "Free energy change for insertion of charged, monolayer-protected nanoparticles into lipid bilayers" *Soft Matter*, **10**, pp. 648-658, 2014, DOI: 10.1039/C3SM52329B.

Reproduced in part by permission of The Royal Society of Chemistry.

and

R. C. Van Lehn and A. Alexander-Katz, "Fusion of ligand-coated nanoparticles with lipid bilayers: Effect of ligand flexibility" *Journal of Physical Chemistry A*, **Accepted**, 2014, DOI: 10.1021/jp411662c.

In the previous two Chapters, we developed a new implicit bilayer, implicit solvent model used to calculate the free energy change associated with translocating a NP from solution into a position embedded in the bilayer core. This model uses a local-rearrangement approximation in which the grafting points of ligands are fixed, but by explicitly modeling ligand chemistry in near-atomistic detail the fluctuations of the monolayer are able to still lead to the effective reorganization of surface properties in response to the presence of the bilayer. In Chapter 4, we presented a series of experimental evidence that substantially confirmed several aspects of the NP-bilayer fusion behavior predicted from this model, including the critical size-dependence for embedding which was observed in both model membranes and cells. Up until this point, we have focused solely on the NP compositions first used in the original paper from Verma et al. in 2008 [81] as explaining this cell penetration behavior was a prime motivation of this thesis. Having identified the NP-bilayer fusion mechanism as a potential explanation for the cell penetration observations, in this Chapter we will now consider the effects on the free energy of insertion associated with changes to system characteristics. We exploit the computational efficiency of the model to explore a large parameter space that includes NP size, monolayer composition, monolayer morphology, ligand chemistry, and grafting density. Our results show that changing the ligand length, grafting density, or magnitude of the hydrophobic effect can all shift the size thresholds predicted previously. We further show that morphology can shift this size cutoff only when the two ligand species are separated into large domains (i.e. Janus particles). The results provide guidelines for the design of *transmembrane nanoparticles* which may be useful for the engineering a new generation of drug delivery carriers or biosensors.

5.1 Magnitude of hydrophobic effect

Perhaps the most important tuning parameter in the implicit bilayer model is the magnitude of γ, the surface tension parameter that penalizes the SASA of the system (see eq. (3.2)). A larger value of γ increases the penalty for exposing SASA and thus increases the hydrophobic driving force for insertion. Fig. 5-1 shows the total free energy change for the insertion of an NP for $\gamma = 28$ and $\gamma = 47$ cal/mol/Å^2, corresponding to the two experimentally supported parameters previously identified from the literature [169, 170]. Testing both allows us to compare to previous experimental results to determine an appropriate parameter. Free energy curves are plotted for three different particle compositions: all-MUS, 2:1 MUS:OT, and 1:1 MUS:OT. Fig. 5-1 shows that the same qualitative features of the free energy curves are observed for both values. Changing the particle composition by increasing the ratio of hydrophobic ligands shifts the cutoff diameter to larger sizes and increases the depth of the free energy well. This result is consistent with an increased hydrophobic driving force as would be expected from monolayers with more hydrophobic ligands. The larger value of γ has larger cutoff diameters and greater free energy wells, again consistent with a stronger driving force for insertion. The major qualitative difference between the two SASA parameters is for all-MUS monolayers: lower γ predicts a negative free energy change only for the smallest particle size tested, which does not match experimental results from the previous Chapter. This discrepancy indicates that the value of $\gamma = 47$ cal/mol/Å^2 is likely more quantitatively accurate as the size thresholds predicted agree well with the approximate size range for particles used experimentally (c.f. Fig. 4-4 and Fig. 4-5). However, either value of γ is suitable to show qualitative changes in the free energy change upon changing system properties due to the similar results predicted by both. Given these similarities, we used both values to probe several changes in simulation conditions as described below, often using the smaller value of γ in order to reduce the computational burden of performing many simulations of larger particles while still retaining the same qualitative conclusions.

5.2 Effect of surface morphology on favorable fusion

In Chapter 3, it was shown that the arrangement of ligands into mixed, striped, or random morphologies had no effect on the free energy change (Fig. 3-6). Fig. 5-2 extends these results by considering two additional morphologies that may be obtained experimentally. The Janus morphology divides the surface into exactly two domains, one hydrophobic and one hydrophilic, corresponding to the case of macroscopic phase separation that may be realized for small NP diameters [86] or for mixed-ligands of similar length [91]. The patchy morphology contains larger islands of the minority component spaced in an approximate icosahedral arrangement to mimic patchy particles [93]. Both morphologies are shown in Fig. 5-2a next to the same three morphologies studied previously. All morphologies were generated for both 2:1 and 1:1 MUS:OT compositions using the method detailed in Appendix B.

Fig. 5-2b shows the free energy change for insertion of NPs with each of the five different mor-

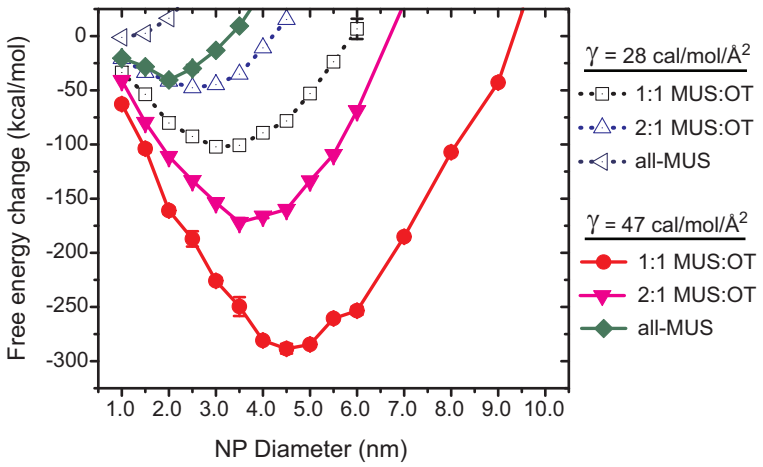

Figure 5-1: Free energy change for insertion as a function of NP gold core diameter for $\gamma = 28$ and $\gamma = 47$ cal/mol/Å^2 for all-MUS, 2:1 MUS:OT, and 1:1 MUS:OT surface compositions.

phologies for both 2:1 MUS:OT and 1:1 MUS:OT compositions. The all-MUS composition is also included for comparison and γ was set to 47 cal/mol/Å^2. For the striped and Janus morphologies, the value for each diameter was averaged over several possible rotations of the particle relative to the bilayer normal due to the anisotropy of the monolayer. From these curves, it is apparent that the striped, mixed, random, and patchy morphologies are all virtually indistinguishable from each other for both 2:1 and 1:1 MUS:OT compositions. The macroscopically-separated Janus morphology, however, shows significant deviation from the other four, exhibiting a smaller cutoff diameter. These results confirm that monolayer composition, but not morphology, plays a dominant role in determining the likelihood of insertion as long as some level of nanoscale mixing is present in the monolayer. These results are consistent with the understanding that ligand fluctuations are necessary for stable insertion and as a result small changes in grafting position have a negligible influence on fluctuations, while completely phase-separating the two components may lead to end groups that are unable to easily snorkel.

In Fig. 5-2, both the striped and Janus morphologies were averaged over several rotations of the particles with respect to the bilayer normal. To test the effect of this rotation, Fig. 5-3 details the free energy change for insertion of Janus and striped particles oriented at an angle θ with respect to the bilayer normal. Rotations of 0°, 30°, 60°, and 90° were tested for increasing particle sizes. For all simulations the rotation was fixed at the beginning of the simulation and was not allowed to vary throughout the simulation run. γ was set to 28 cal/mol/Å^2 to look only at qualitative behavior and reduce computational expense by simulating smaller NP diameters. For the Janus particle, rotating the particle from 0 to 90° led to an increase in the cutoff diameter and increase in the magnitude of the free energy well, indicating that the optimal angle for insertion was 90°. At this rotation, the bilayer split both the hydrophobic and hydrophilic regions in half, allowing the maximum number of hydrophobic ligands to insert into the bilayer while easily allowing hydrophilic ligands to snorkel to the surface. For the striped particle, the free energy change was relatively invariant to rotation,

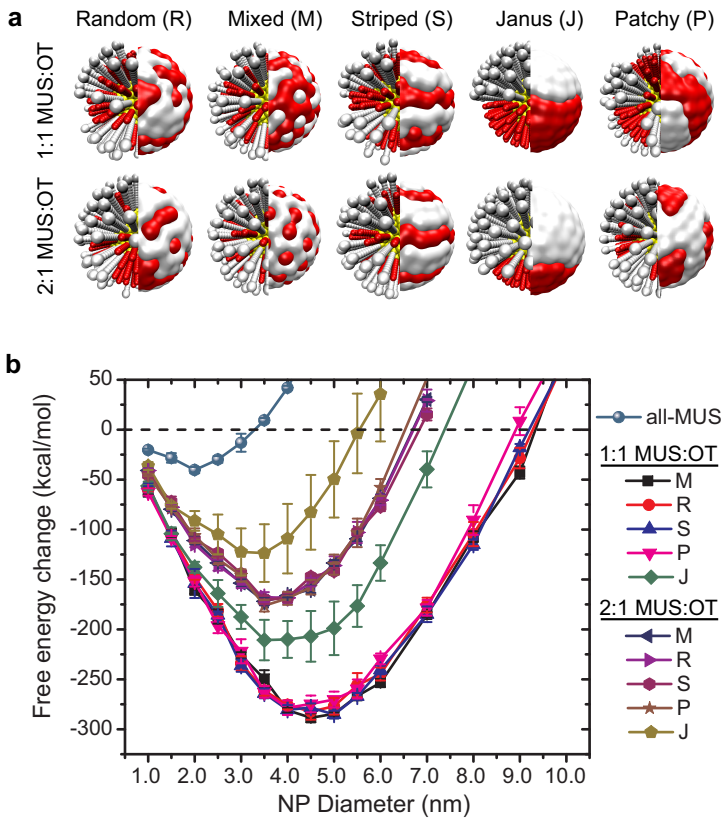

Figure 5-2: Free energy change for insertion as a function of NP diameter for five different morphologies for both 2:1 MUS:OT and 1:1 MUS:OT particles. **a** Illustration of five morphologies studied. The white/red surfaces indicate the position of MUS/OT grafting points respectively. **b** The free energy change for insertion for all five morphologies for both 2:1 MUS:OT, 1:1 MUS:OT, and a reference all-MUS NP composition. The free energy changes for the striped and Janus particles were averaged over several rotations of the particle with respect to the bilayer normal. γ was set to 47 cal/mol/Å^2.

with the only significant deviations occurring for intermediate particle sizes but not affecting the cutoff diameters. The variation with respect to rotation in the Janus case explains the larger error bars shown in Fig. 5-2. In the true physical system, presumably the NP would be able to freely rotate to adopt the most favorable rotation. In the case of the striped particles, these results indicate that free rotation would not significantly change the results given the rotational invariance of the free energy change. On the other hand, Janus particles may have significant differences in the free energy for rotation, or may prefer membrane associations that lead to wrapping by the bilayer rather than insertion [135, 108]. The results further confirm that nanoscale morphologies are effectively indistinguishable, even for the anisotropic striped morphology.

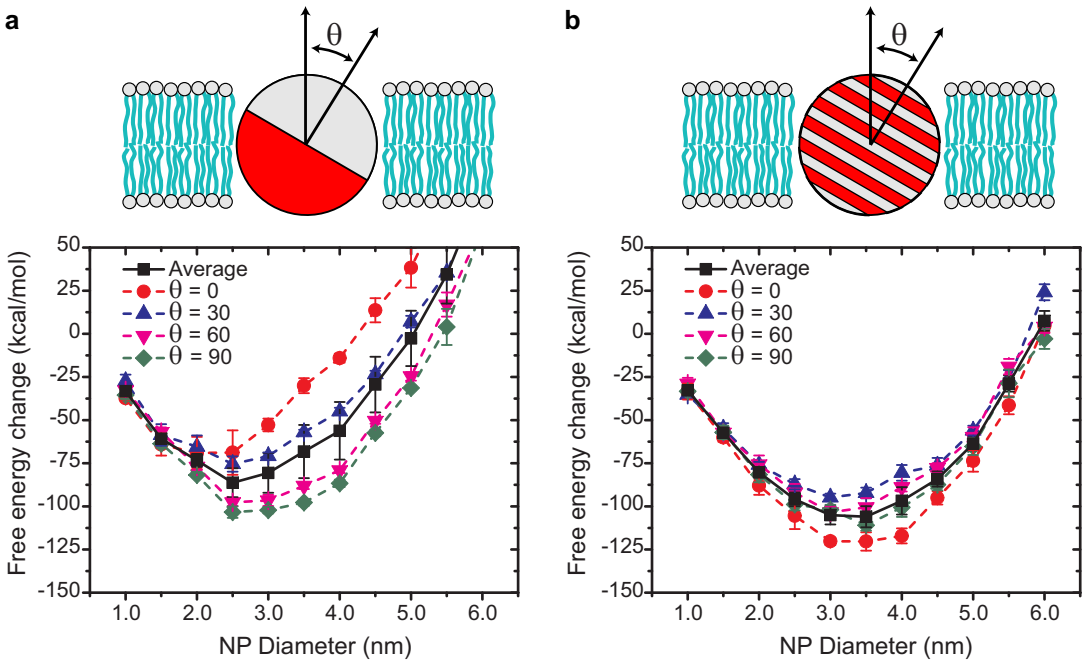

Figure 5-3: Free energy change for insertion of NPs with anisotropic monolayer morphologies as the particles are rotated with respect to the bilayer normal. γ was set to 28 cal/mol/Å^2. The schematic illustrates the definition of the rotation angle θ. **a** Rotation of Janus particles. **b** Rotation of striped particles.

5.3 Influence of ligand structure on insertion free energy change

The previous results indicate that changes in the nanoscale morphology of the monolayer make no difference in the free energy change for insertion. This finding is seemingly at odds with cell experiments that suggest monolayers with a mixed morphology exhibit a much lower propensity for cell penetration than monolayers with a striped morphology [81, 187]. In the cell experiments, the mixed morphology was induced by synthesizing ligands with branched octanethiol (br-OT) ligands in place of the linear octanethiol ligands [81, 187]. Branches consisted of single CH_3 groups attached to the 3rd and 8th carbons in the chain as shown in Fig. 5-4a. As the simulation results have shown the importance of ligand free volume in allowing ligand fluctuations, it is possible that the presence of branched groups reduces this free volume and inhibits embedding. The reduction in cell penetration would then be caused by the use of br-OT rather than the change in monolayer morphology.

To test this hypothesis, we explicitly simulated branching points by increasing the effective diameter of the 3rd and 8th beads in the br-OT ligands to 0.266 nm, equal to the geometric mean diameter of a CH-CH_3 group. Fig. 5-4 shows the free energy change for the insertion of NPs with 2:1 MUS:br-OT, 2:1 MUS:OT, 1:1 MUS:br-OT, and 1:1 MUS:br-OT, all with the mixed morphology. Replacing OT with br-OT in the ligand monolayers led to a decrease in the cutoff size for insertion and decrease in the magnitude of the free energy change, results consistent with inhibited ligand

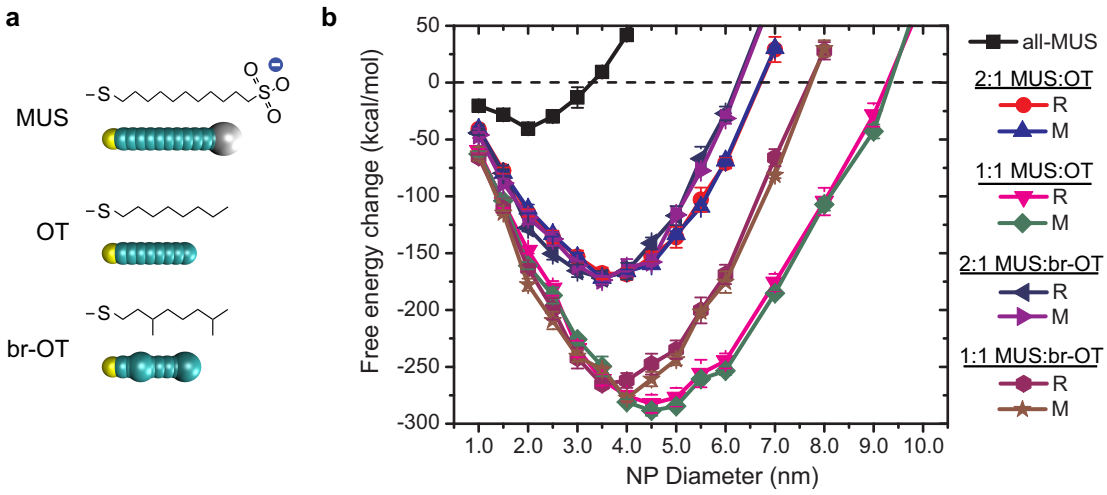

Figure 5-4: Effect of branched ligands. **a** Chemical structure and united atom representation of ligands, including br-OT. **b** Comparison of free energy change for insertion between NPs with linear and branched ligands. Particle compositions are all-MUS, 2:1 MUS:OT, 1:1 MUS:OT, 2:1 MUS:br-OT, and 1:1 MUS:br-OT with $\gamma = 47$ cal/mol/Å^2.

snorkeling. The effect is much stronger for 1:1 compositions as these contain a larger proportion of branched ligands, but there is still a small shift for the 2:1 composition. These results, combined with the result of Fig. 5-2 suggest that the decrease in particle uptake observed upon replacing OT with br-OT may be related to the reduction of monolayer free volume and consequential inhibition of ligand deformation, not a change in monolayer morphology. We also note that we treat the ligands as flexible chains and do not quantitatively account for torsional angle rotations that may also be inhibited by the presence of branched side chains. Such inhibited rotations may increase the compactness of the branched ligands and further inhibit penetration [206].

The effect of replacing OT with br-OT ligands points to the importance of ligand structure in determining the free energy change for insertion. To further test the influence of ligand properties, several different combinations of ligand lengths were simulated as these lengths can be easily tuned experimentally. The lengths of both hydrophobic and hydrophilic ligands were varied independently, allowing differences in the ligand lengths between the two different components to be tested as well. All simulations were run with a 2:1 hydrophilic:hydrophobic ligand composition and a mixed monolayer morphology with $\gamma = 28$ cal/mol/Å^2 to reduce computational expense but preserve qualitative trends. Fig. 5-5 shows the free energy changes for insertion of NPs with varying ligand lengths. The naming scheme used to identify ligands is schematically shown in Fig. 5-5a. Dotted lines indicate that the hydrophilic ligand has 5 more carbons in its backbone than the hydrophobic ligand, solid lines indicate a length difference of 3 carbons, and dashed lines indicate a length difference of 1 carbon.

The results illustrate that the most important factor in determining the free energy change for insertion is the length of the longer hydrophilic ligand. Increasing the length both increases the amount of hydrophobic surface area that can be shielded in the bilayer and increases the ability of

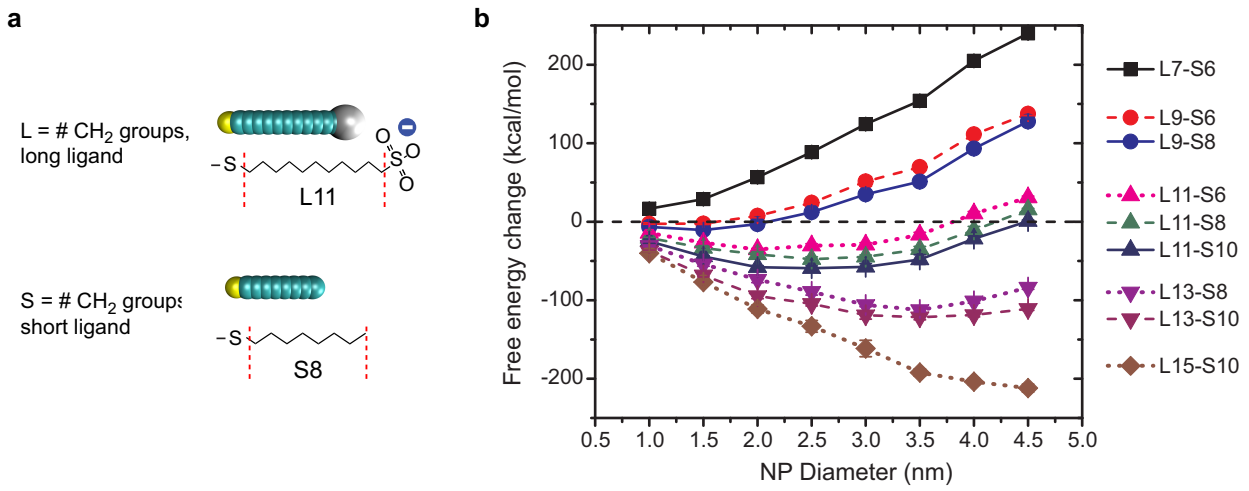

Figure 5-5: Effect of ligand length. **a** Naming scheme for mixed monolayers with ligands of varying lengths. MUS:OT is L11:S8 in this scheme as illustrated. **b** Free energy change for insertion of NPs with ligands of varying lengths. The ratio of hydrophilic:hydrophobic ligands was set to 2:1 with a mixed morphology for all simulations with $\gamma = 28$ cal/mol/Å^2.

ligands to snorkel to aqueous interfaces. These factors increase the cutoff diameter for insertion and magnitude of the free energy well. Increasing the length of the hydrophobic ligands led to slightly lowered free energy wells, but the difference was small compared to an increase in the length of the hydrophilic ligand. These results imply that the length difference between the two ligands is not a determining factor in driving insertion so much as the absolute lengths of the ligands themselves. However, it is important to note that we disregard any potential changes in morphology that could be driven by ligand length changes; for example, previous work has suggested that monolayers with no ligand length difference would lead to Janus particles [91] which would inhibit insertion as shown in Fig. 5-2. Furthermore, it is also possible that ligand crystallization could be enhanced for longer lengths which may inhibit the ligand flexibility necessary for insertion [207, 208].

5.4 Ligand grafting density strongly modifies size thresholds

As a last test of the importance of structural details for determining the free energy of insertion, the grafting density of ligands on NP surface was varied. In principle, the grafting density of ligands may depend on the particle radius [209, 210] which may then change the surface properties sufficiently to influence the free energy for insertion. Fig. 5-6 shows the free energy change for insertion of particles with 80% 90%, 100%, 110%, and 120% of the typical ligand density of 4.77 lig/nm^2. The composition of all particles was 2:1 MUS:OT in a mixed morphology with $\gamma = 28$ cal/mol/Å^2. The results indicate that increasing ligand density decreases the cutoff diameter and vice versa as would be expected again from the necessity for ligand deformation. As it is likely that increasing the size of particles will decrease the density of ligands on the surface due to the decreased volume per ligand for larger particles, these results indicate that the cutoff diameters

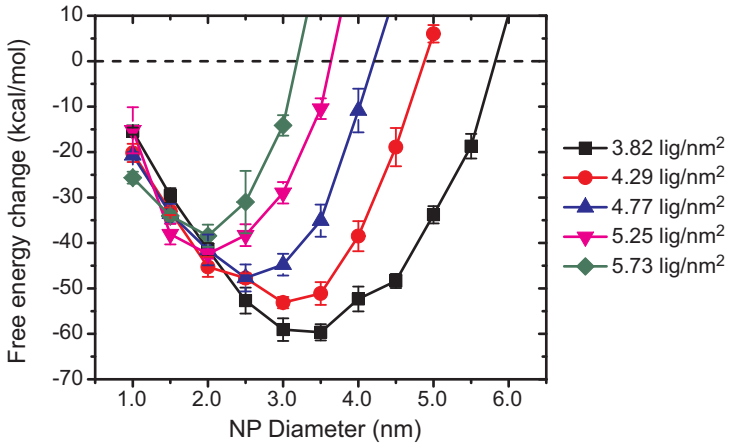

Figure 5-6: Free energy change for insertion as a function of the ligand grafting density for a 2:1 MUS:OT surface composition with $\gamma = 28$ cal/mol/Å^2.

predicted in Fig. 5-2 could be even larger in systems with variable grafting density.

5.5 Role of ligand flexibility in mediating stable insertion

In the united atom model used so far, ligands were modeled as having flexible alkane backbones that excluded volume but were unconstrained by bond angle restrictions, effectively maximizing chain flexibility. This simplifying assumption is adequate in the limit of high temperature or highly flexible ligands. For more rigid ligands, such as DNA, unsaturated alkanethiols, ligands containing alkane rings, fluorescent dyes, or alkanethiols at low temperature [211], the flexible backbone assumption is likely a poor representation of the physical system and may overestimate the ease of the snorkeling process. A variety of such ligands have already been reported for use in biological applications [212, 213, 214, 16]. In addition, cell penetration was experimentally observed at 4°C [81], a temperature chosen to block endocytosis that may also bias ligands toward more rigid backbone structures. It is thus important to understand how backbone flexibility may influence NP-bilayer fusion.

Taking the opposite extreme from the previous flexible backbone assumption, here the ligands are modeled as rigid rods with ligand flexibility only possible at the grafting site. We will refer to the original, freely-jointed approximation as the *flexible backbone* model for ligand fluctuations while the new rigid model will be referred to as the *rigid rod* model. In the rigid rod model, the previous united atom simulation method was modified so that the entire alkane backbone of the chain was treated as a cylinder of uniform diameter. Rather than move individual beads, the backbone cylinder was rotated around the fixed grafting point for each trial move. No other changes to the computation of the system energy were made.

Fig. 5-7 shows simulation snapshots of NPs inserted into the bilayer using both the flexible backbone (top) and rigid rod (bottom) models. Both snapshots are taken for the same 2.5 nm NPs

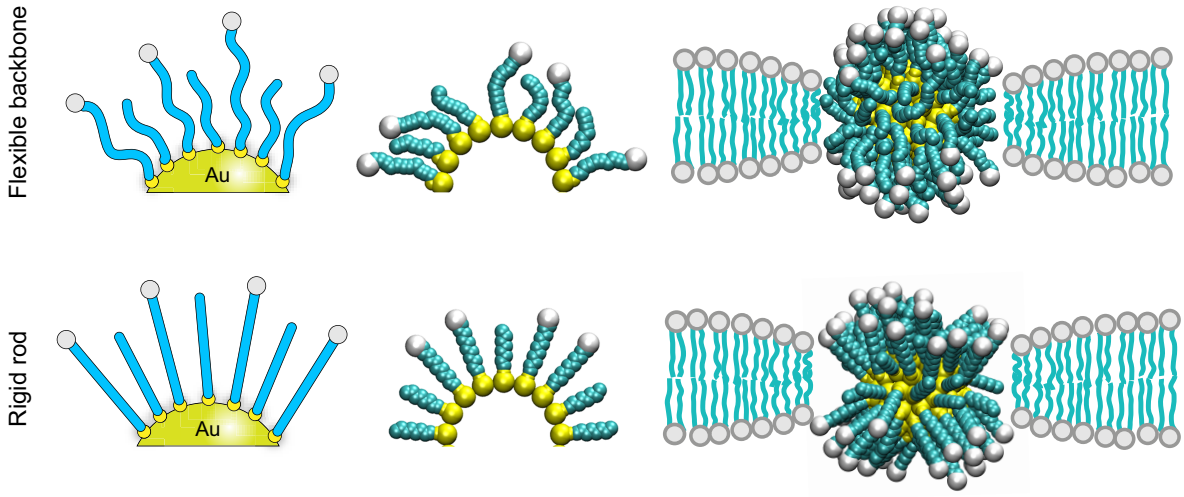

Figure 5-7: Difference between flexible backbone (top) and rigid rod (bottom) models. Simulation snapshots illustrate the ordered, cylindrical rods characteristic of the rigid rod model.

with 1:1 MUS:OT surface compositions. The snapshots illustrate the qualitative effect of the rigid rod approximation - in comparison to the flexible backbone model, the rigid rod model leads to increased unfavorable insertion of the charged end groups into the bilayer due to the lack of end group flexibility. This inhibited flexibility effectively acts as a barrier to snorkeling and would thus be expected to increase ΔG_{insert}, the primary free energy term opposing insertion.

Fig. 5-8 shows a breakdown of the total free energy change for insertion into each of the components identified in eq. (3.1) as a function of gold core diameter for both models. The surface composition for both particles was 2:1 MUS:OT and $\gamma = 47$ cal/mol/Å^2. Each point is plotted for the value of λ that minimizes the overall free energy change for that gold core diameter. The primary quantitative distinction between the two models lies in the value of ΔG_{insert}. As the gold core diameter increases, the free volume per ligand decreases and ligand fluctuations are reduced. The flexible backbone model permits end group and backbone deformations that aid snorkeling and enable the removal of end group charges from the bilayer even for small ligand free volumes. For the rigid rod model, charges are forced to be exposed to the bilayer by the inability of ligands to flexibly snorkel, increasing ΔG_{insert}, decreasing the overall free energy change G_{total}, and decreasing the size cutoff relative to the flexible backbone model. The same lack of flexibility slightly decreases the magnitude of the hydrophobic effect, ΔG_{phobic}, although the change is less pronounced than the effect on charge insertion.

Having established that the rigid rod approximation inhibits ligand fluctuations in the baseline state, Fig. 5-9 shows the effect of the rigid rod approximation on the total free energy change for bilayer fusion in comparison to the flexible backbone approximation. Fig. 5-9a and Fig. 5-9b show plots of the flexible backbone and rigid rod models respectively for all-MUS, 2:1 MUS:OT, and 1:1 MUS:OT monolayer compositions for the striped, mixed, and random morphologies in analogy to Fig. 3-6. The SASA parameter was set to $\gamma = 47$ cal/mol/Å^2 to provide quantitative estimates

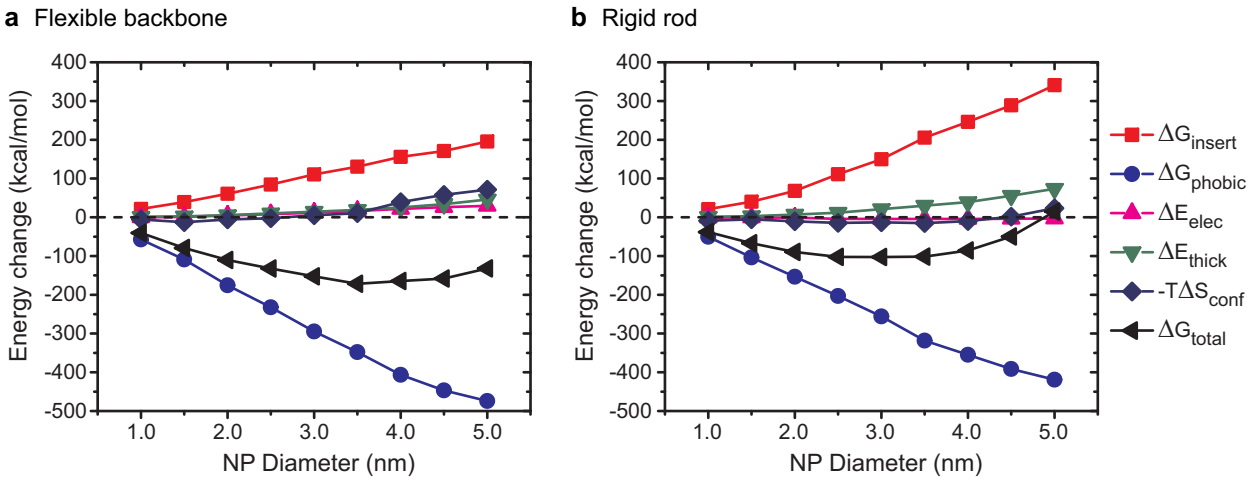

Figure 5-8: Breakdown of free energy terms from eq. (3.1) into individual components plotted as a function of the gold core diameter for a NP with a 2:1 MUS:OT surface composition and $\gamma = 47$ cal/mol/Å^2. **a** Flexible backbone model. **b** Rigid rod model.

of the free energy change for insertion. The same general trends are observed for both models. However, comparing the two models clearly shows that the reduced molecular flexibility imposed by the RR model greatly inhibits bilayer insertion as the magnitude of the free energy change decreases for all three surface compositions leading to smaller size thresholds, consistent with the breakdown in Fig. 5-8. Fig. 5-9c shows the area bounded by the two different approximations. The flexible backbone and rigid rod models can be thought of as opposite extremes of molecular flexibility, so the insertion free energy change for a real system with some restrictions on bond rotation should lie within the areas bounded by these two approximations.

5.6 Conclusions

In this Chapter, we finish the study of the thermodynamics of NP-bilayer fusion by using the previously described implicit bilayer, implicit solvent model to explore changes in the free energy change for insertion as a function of a wide variety of system characteristics. The results show that changing ligand chemistry, ligand length, and ligand grafting density all shift the size thresholds for stable embedding that were first predicted in Chapter 3 and confirmed experimentally in Chapter 4. We also show that ligand flexibility is not a pre-requisite for fusion to occur as long as the thiol bond allows free rotation of the ligand. Using a rigid rod model for ligand fluctuations appropriate to describe rigid ligands or low system temperatures, we find that the size threshold for embedding shifts to a lower value but has qualitatively similar behavior despite hindered backbone deformation. As a true physical system will have bond constraints subject to various restrictions on bond angles or dihedral angles that result in backbone flexibilities somewhere in between the rigid and fully flexible regimes, the flexible backbone and rigid rod models provide upper and lower bounds on the true free energy change for a physical system.

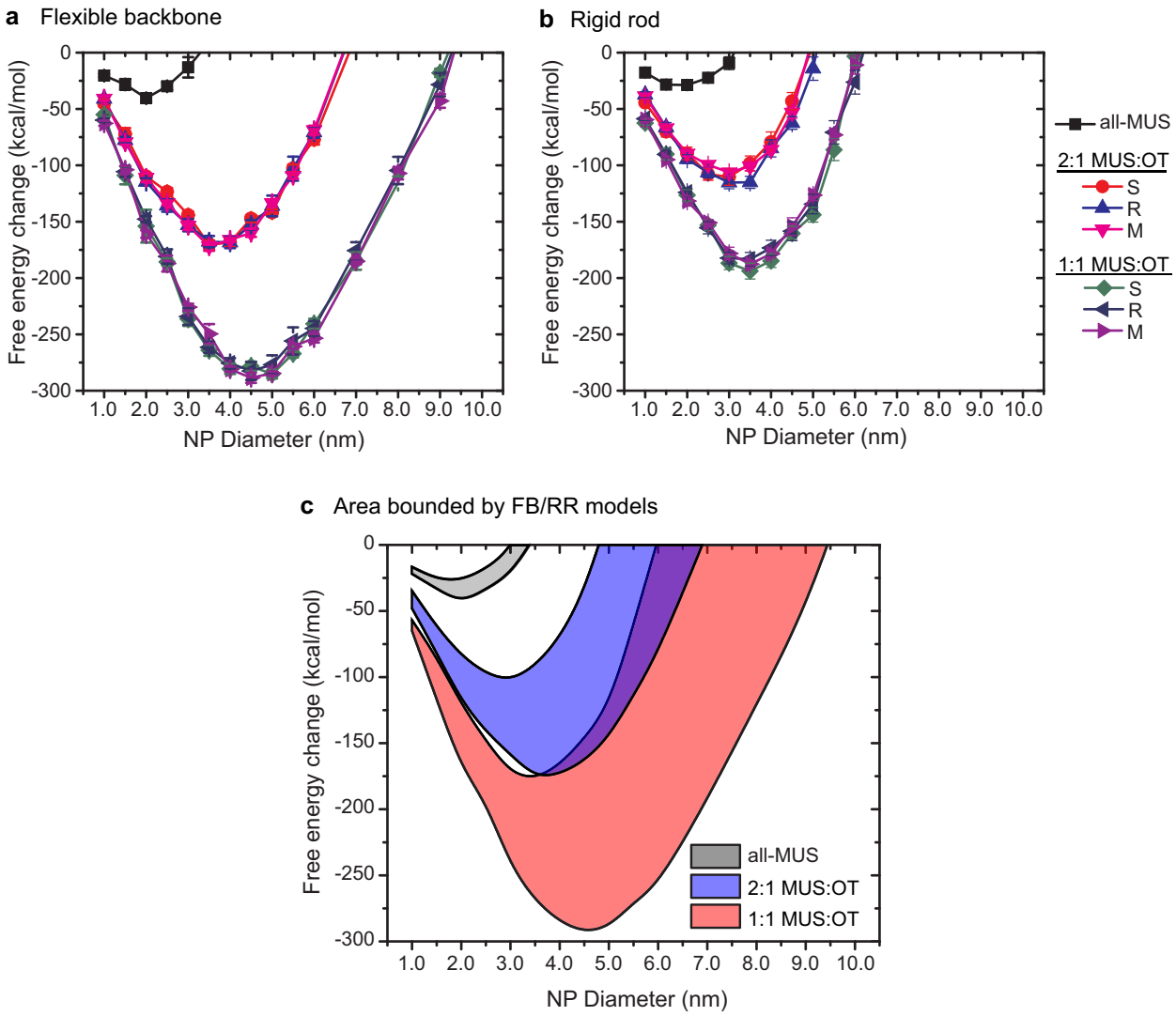

Figure 5-9: Comparison of free energy of insertion for both flexible backbone (**a**) and rigid rod (**b**) models. **c** Areas bounded by the two approximations.

The model and results discussed here may further explain the experimental results reported previously for cellular systems [81, 187]. In cells, the uptake efficiency of 2:1 MUS:OT striped particles was significantly larger than the uptake of all-MUS particles or 2:1 MUS:br-OT particles. The difference in uptake efficiency found experimentally correlates with the size cutoffs identified here - namely, the all-MUS particles have the smallest cutoff, followed by the br-OT particles and then the MUS:OT particles. While the cell system is certainly significantly more complex than the simplified model considered here, it is possible that the uptake results can be explained in part by the number of particles within a sample that were lower than the size cutoffs found in this work.

These results suggest that the two most important properties of the protecting monolayer are the flexibility of the ligands and the amount of exposed hydrophobic surface area in the initial state. Ligand flexibility relates to the length of ligands themselves, the relative ratio of

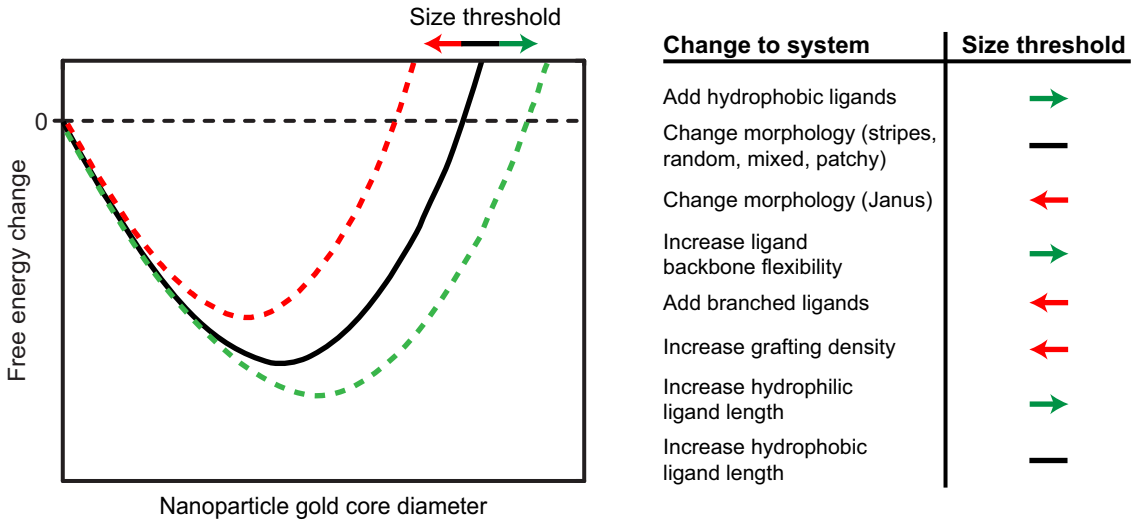

Figure 5-10: Summary of design rules for optimizing fusion propensity.

hydrophilic:hydrophobic ligands on the surface, and the size of the NP diameter. Similar considerations also govern the amount of hydrophobic surface area. From these considerations, we can suggest a series of possible design rules for NP monolayers that influence the thermodynamics of particle insertion as summarized in Fig. 5-10:

- Increasing particle size inhibits insertion.
- Increasing ligand lengths encourage insertion, independent of the length difference of the two ligand types.
- Increasing the relative number of hydrophobic ligands in the monolayer enhances insertion.
- Modifying morphology does not make a significant difference unless macroscopic phase separation occurs (i.e. Janus particles).
- Ligand structural changes that decrease free volume/fluctuations, such as the addition of branches, reduce fusion.
- Increasing the grafting density inhibits insertion due to the decrease in free volume.
- Rigid ligands with minimal backbone flexibilities penalizes insertion.

We expect that these design rules will be useful for constructing optimal monolayer-protected NPs for interactions with biological systems for applications in biosensing and drug delivery.

Part II

Kinetics of NP-bilayer interactions

THIS PAGE INTENTIONALLY LEFT BLANK

Chapter 6

Development of New Atomistic NP Model

Work in this chapter was published in:

R. C. Van Lehn and A. Alexander-Katz, "Structure of mixed-monolayer-protected nanoparticles in aqueous salt solution from atomistic molecular dynamics simulations" *Journal of Physical Chemistry C*, **117**, pp. 20104-20115, 2013, DOI: 10.1021/jp406035e.

In Part I of this thesis, we focused on developing an understanding of NP-bilayer thermodynamics using chiefly equilibrium Monte Carlo sampling. By developing an implicit bilayer, implicit solvent model capable of quickly simulating the free energy of insertion, we were able to identify conditions under which NP-bilayer fusion is thermodynamically favorable and develop design rules to tailor NP properties to maximize fusion propensity. However, a fundamental limitation of this model is the inability to accurately model system dynamics in the absence of explicit lipids or solvent. As such, we cannot use it to elucidate the energy barriers associated with fusion or the full pathway by which fusion occurs. Although several existing simulations have been conducted in an attempt to calculate similar pathways [215, 216, 217, 120, 118, 106, 218, 110, 107], no simulation model that used both explicit models of ligands and explicit models of lipids has shown fusion behavior, in part due to neglect of the important ligand fluctuations necessary to stabilize such behavior. To gain a full understanding of the fusion pathway, it is necessary to gain atomistic insight into ligand, lipid, and solvent degrees of freedom. Molecular dynamics simulations provide a mechanism to achieve this physical insight while preserving quantitatively accurate time scales. In this Chapter, we propose a new atomistically-detailed model of mixed-monolayer-protected NPs and perform an extensive structural characterization of the NP surface in preparation for simulations of NP-bilayer interactions.

Previous atomistic studies of monolayer-protected NPs have explored the role of ligand fluctuations in spontaneous domain formation [211, 145], the effect of morphology on the surrounding water density in mixed-monolayer-protected particles [219, 220], electrostatically-mediated ridge formation on faceted NPs [183], or the importance of considering the electrostatic properties and water interactions of small NPs [184, 221]. We expand on these studies by determining the effect that particle size, surface morphology, and the relative lengths of the two ligand species have on the structure of the monolayer in aqueous salt solution. We show that modifying the nanoscale morphology has little effect on the overall structure of the monolayer due to the flexibility of the alkane backbones of the protecting ligands. The free volume associated with the small particle diameters permits the ligand end groups to fluctuate to minimize electrostatic repulsion indepen-

dent of the exact grafting locations of the different ligand components. In contrast, increasing the particle diameter or increasing the length of the hydrophobic component both act to decrease the available free volume, inhibiting ligand fluctuations and effectively confining the ligands from steric interactions with adjacent neighbors. Our results reinforce the conclusion from Part I that surface composition, ligand structure, and particle size are the most important tuning parameters to consider in designing mixed-monolayer-protected particles.

6.1 Parameterization and choice of force field

The recent GROMOS 54a7 united atom forcefield [222], an update of the popular GROMOS 53a6 parameter set [223], was used to model the NP and surrounding solution. The GROMOS forcefield was chosen due to the similarity between the alkanethiol ligands modeled here and the general structure of lipids. A summary of the GROMOS force field is given in Appendix D. The topology of the MUS sulfonate end groups was adapted from a previous sulfonate parameterization by Hinner et al [224], with partial charges taken from *ab initio* simulations of sulfonate ionic liquids [225]. Following a typical GROMOS "building-block" approach, standard Lennard-Jones parameters were used for sulfonate atoms with only the charges re-parameterized [226].

The GROMOS 54a7 forcefield lacks parameters for gold so some modifications were necessary to accurately model the system. Gold-hydrocarbon Lennard-Jones parameters were adapted from a re-parameterization of the Hautman-Klein model for self-assembled aklanethiol monolayers [227] which has been successfully used to reproduce the tilt angle of ligands in planar self-assembled monolayers and is thus appropriate for studies of monolayer structure [227, 228]. The Hautman-Klein model originally represented the gold surface as a perfect plane, but later modifications by Tupper et al. [229] and Mahaffy et al. [230] replaced the planar representation with discrete atoms that interact with the alkanethiol hydrocarbons via a Lennard-Jones 12-6 potential compatible with the GROMOS forcefield. All other Lennard-Jones interactions were obtained using the values for gold presented in the UFF forcefield [231], although in practice only gold-hydrocarbon interactions were relevant due to the steric barrier posed by the protecting monolayer. The gold-sulfur-carbon bond angle and gold-sulfur-carbon-carbon dihedral angle at the NP interface were left unrestricted as in the Hautman-Klein model. This combination of forcefield parameters is commonly found in the self-assembled monolayer literature [211, 232, 210].

The gold surface itself was approximated as a rigid, hollow, perfectly spherical shell with constraints placed on neighboring gold atoms to maintain the rigidity of the spherical shell during simulations. The mass of the missing gold atoms in the hollow interior were redistributed to the surface gold atoms. The sulfur head groups of the bound ligands were distributed uniformly across the gold surface with a grafting density of 4.62 ligands/nm^2, yielding 58 ligands for a 2.0 nm core diameter NP in agreement density functional theory computations of monolayer structure [233, 184]. The gold and grafted sulfur atoms were not assigned partial charges since previous simulations have shown that the cumulative charge density approaches zero at the gold surface [184]. Although

the grafting density may be a function of surface area [209, 210], we assumed that it is identical for all particle sizes studied here. The simple spherical approximation may not be accurate for faceted small NPs [234] and the structure of the interface does not take into account other possible gold-sulfur binding motifs [233, 235, 82], but as the focus of this work is on the role of the ligand monolayer itself this treatment of the gold interface simplified the system significantly. The sulfur atoms were rigidly bound to the surface, inhibiting any possible diffusion of the grafting points along the gold surface to mimic the local-responsiveness assumption made in Chapters 3-5.

6.2 Verification of ligand structure in vacuum

The GROMOS 54a7 force field was parameterized primarily for interactions in solution, as is the case for most biomolecular force fields. However, most structural characterizations of ligand-protected NPs are performed in air or in vacuum. To facilitate a comparison with these experiments, we performed simulations of 2-6 nm dodecanethiol-protected NPs in both vacuum and water and calculated the dihedral properties as a measure of ligand flexibility. Dodecanethiol was chosen as a typical ligand characterized experimentally. The simulations in vacuum were performed at constant energy with no thermostat or barostat to model isolated NPs [236, 237]. Energy conservation was maintained using Gromacs version 4.6.1 in double precision with a shorter 1 fs timestep and without LINCS for bonding constraints. All cut-offs were extended to 5.0 nm and cut-off electrostatics were used since the system was completely uncharged. Finally, no periodic boundary conditions were used to represent an isolated system. The vacuum systems were first equilibrated with a velocity-rescale thermostat for 100 ps at 300 K to assign kinetic energies equivalent to room temperature before 5 ns of production were performed with no thermostat. The first 1 ns of the production simulation was discarded for analysis. Simulations of NPs in water were performed using the standard parameter set from Appendix D. A rhombic dodecahedral box was used with the box walls positions 0.75 nm from the extended all-*trans* ligands and filled with SPC water.

Fig. 6-1a shows the fraction of *gauche* conformations as a function of the position of the dihedral in the dodecanethiol chain for all NP diameters in vacuum. Dihedrals are numbered such that dihedral 0 is closest to the gold-sulfur interface. The results show a fairly high percentage of *gauche* defects that increases for smaller NPs and a higher fraction of defects for dihedrals farther from the gold-sulfur interface. For small NPs, there was still a high fraction of *gauche* conformers for the very first dihedral, indicating a preference for ligands bending near the surface. Fig. 6-1b shows the overall fraction of *gauche* conformations as a function of particle size for NPs in both vacuum and water. Similar results were obtained for both conditions, suggesting that experimental studies of NPs in air can inform studies of monolayer properties in solution, as well. The *gauche* fraction decreased approximately linearly with increasing NP core diameter as ligands have less free volume accessible to them. The typical fraction of defects was approximately 30%, a value agreeing well with simulations of pure alkane chains in the CHARMM, GROMOS, and OPLS force fields [238]. Notably, the OPLS all-atom force field was recently re-parameterized to properly

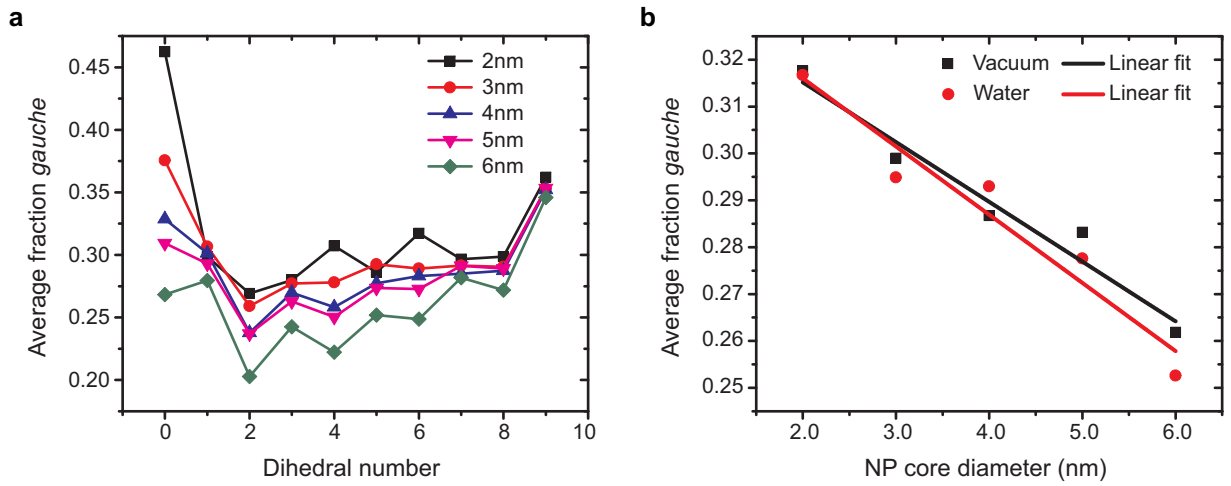

Figure 6-1: Ligand structure in vacuum and in water. **a** Fraction of *gauche* defects as a function of dihedral number for NPs of increasing core diameter in vacuum. Dihedral 0 is closest to the gold-sulfur interface. **b** Overall fraction of *gauche* defects as a function of core diameter for NPs in both water and vacuum.

calculate conformational properties of long alkanes, and only after re-parameterization produced similar results to those shown here [238]. The high percentage of *gauche* defects gives rise to significant monolayer flexibility. Similar behavior has been observed in recent all-atom simulations of ligand-protected nanocrystals in vacuum, even with explicit NP facets [239]. While several other examples of alkanethiol-protected NPs have shown significant "bundling" of ligands on the surface due to alignment between adjacent ligands [145, 211, 240], these effects are only associated with low-temperature systems [240] and may further be an artifact of the previous version of the OPLS force field [239]. The odd-even effects observed as a function of dihedral number also agree with previous simulation results of surface monolayers on both planar and curved surfaces [240, 208]. The present parameterization thus agrees well with related simulation studies.

Experimentally, there has been a significant amount of research characterizing the structure of alkanethiol monolayers on NPs as a function of size, ligand length, and temperature. While absolute *gauche*/*trans* fractions cannot be determined, several techniques have been employed to estimate the appearance of *gauche* defects. In work by Badia et al, differential scanning calorimetry was used to show that alkanethiol monolayers undergo reversible order-disorder transitions similar in nature to the gel-fluid transition exhibited by unsaturated bilayers, with order-disorder transition temperatures remarkably close to their lipid counterparts [241, 242]. As the GROMOS 54a7 parameter is based in part on correctly reproducing bilayer properties, this similarity indicates that the parameterization based on lipids is transferable to alkanethiol systems. Above the order-disorder transition, FTIR and NMR spectra show that the chains disorder and significant *gauche* defects appear, originating at the terminal methyl groups and propagating to methyl groups near the NP surface [242]. The simulation results show the same trend, especially in larger NPs, with *gauche* defects more prominent for bonds farther from the interface. Notably, the dodecanethiol ligands

studied have a melting point near 3°C and are in the liquid state in the simulations, while shorter ligands do not undergo a thermal transition at all and are always in the fluid state [241, 243]. The experimental percentage of *gauche* defects at either end of the grafted chains is estimated as near 5-25%, similar to the results we found [243]. FTIR and DSC studies of dodecanethiol-protected NPs with varying core sizes also showed a preference of higher numbers of *gauche* defects for smaller NPsd with a crossover to mostly *trans* conformers for larger NP sizes [243]. Finally, recent results with vibrational sum frequency generation spectroscopy have shown that FTIR may underestimate the fraction of *gauche* defects, and confirmed a strong size dependence with a larger number of *gauche* defects present in smaller NPs [244, 245]. The authors attribute this affect to the increasing free volume accessible to each ligand on smaller NPs, consistent with the findings in Fig. 6-1.

These results and accumulated simulation and experimental evidence suggest that the NP parameterization correctly captures the structure of the ligand monolayer. The ligands have large numbers of *gauche* conformations consistent with a fluid-like monolayer. The fluidity of the monolayer gives rise to significant ligand flexibility in both vacuum and water simulations which decreases with increasing core size. These results are all consistent with the assumptions made in Part I and match simulations of all-atom, faceted NPs [239]. As these simulations were performed with longer dodecanethiol ligands, shorter ligands such as octanethiol would be expected to have similar properties given the lack of an order-disorder transition [241].

6.3 Structural characteristics of NPs in solution

The previous section confirms that the atomistic NP model accurately captures the structure of purely hydrophobic monolayers and trends in the ligand conformations with varying NP core size, allowing for the characterization of mixed-monolayer-protected NPs in aqueous salt solution to match the desired experimental conditions. Several simulation systems of varying NP size, ligand length, ligand composition, and monolayer morphology were prepared. Each system included a physiological NaCl concentration of 150 mM plus sufficient counterions to neutralize the NP. As in the previous Chapters, ligand composition was varied by changing the ratio or lengths of the protecting ligands and the same striped, random, and mixed morphologies described in Chapter 3 were tested. A summary of the simulation parameters for different aqueous systems considered in this Chapter is shown in Table 6.1 and Fig. 6-2 shows several simulation snapshots of example systems. Ligand lengths are specified as the number of methylene groups, e.g. 11:8 is used to represent MUS:OT.

For all simulations, periodic boundary conditions were used with a rhombic dodecahedral box geometry to minimize the overall system volume given the approximately spherical symmetry of the system. The box was sized such that there was a distance of 1.2 nm from the box wall to the closest ligand on the NP in the initial state, all-*trans* state to eliminate interactions between periodic images. All simulations used the parameters described in Appendix D with the temperature fixed at 310 K. Simulations were first equilibrated in the NVT ensemble for 2 ns, then in the NPT

Table 6.1: Summary of aqueous simulation systems

NP core diameter and type	Ligands	Water	Ions (Na/Cl)	Atoms
2.0 nm, 11:8, all-MUS	58	11,772	94/36	36,548
2.0 nm, 11:8, 1:1, Mixed	58	11,987	65/36	36,961
4.0 nm, 11:8, 1:1, Mixed	232	19,900	185/69	63,551
6.0 nm, 11:8, 1:1, Mixed	522	38,718	404/143	124,795
8.0 nm, 11:8, 1:1, Mixed	928	53,557	683/219	175,963
4.0 nm, 11:8, 1:1, Random (1)	232	19,859	185/69	63,428
4.0 nm, 11:8, 1:1, Random (2)	232	19,863	185/69	63,440
4.0 nm, 11:8, 1:1, Random (3)	232	19,846	185/69	63,389
4.0 nm, 11:8, 1:1, Striped	232	19,916	185/69	63,599
4.0 nm, 11:11, 1:1, Mixed	232	19,447	185/69	62,540
4.0 nm, 11:14, 1:1, Mixed	232	20,785	190/74	66,912
4.0 nm, 11:17, 1:1, Mixed	232	26,200	207/91	83,539
4.0 nm, 11:17, 1:1, Striped	232	26,179	207/91	83,476
4.0 nm, 11:17, 1:1, Random	232	26,204	207/91	83,551

ensemble with the Berendsen barostat for 2 ns, then a final 16 ns of equilibration were run in the *NPT* ensemble with the Parrinello-Rahman barostat. Data for analysis was then generated over 100 ns of production runs using the same parameters as the last 16 ns of equilibration. All simulations were performed using Gromacs version 4.6.1 [246].

Data analysis was performed using a combination of default Gromacs tools and code developed in-house. The radial electrostatic potential of the system was calculated following Heikkilä et al. [184] by applying Gauss' Law with a spherical Gaussian surface of radius r to obtain the electric field as:

$$\mathbf{E}(r) = \frac{Q_{enc}}{4\pi\epsilon_0 r^2} \tag{6.1}$$

where Q_{enc} is the cumulative charge enclosed within the spherical shell and ϵ_0 is the dielectric permittivity. The electrostatic potential, $\Psi(r)$, is then simply expressed as:

$$\Psi(r) = \int_0^r \mathbf{E}(r')dr' = -\frac{Q_{enc}}{4\pi\epsilon_0 r^2} \tag{6.2}$$

Calculating $\Psi(r)$ thus requires an estimate of the cumulative enclosed charge for each r. To reduce error associated with treating the ions as point charges, the charge was spread over a spherical grid centered on each ion with a Gaussian spread function that decayed to 0 at the distance σ associated with the Lennard-Jones parameters for that atom. Grid points were separated by a distance of 0.01 nm; decreasing the grid separation further did not change the results.

Ligand tilt angles were calculated from the dot product of a vector drawn from the center of mass of the gold shell to the grafted sulfur atom and a vector drawn from the grafted sulfur atom to the end of the ligand chain. The chain end was defined as the terminal sulfur atom in

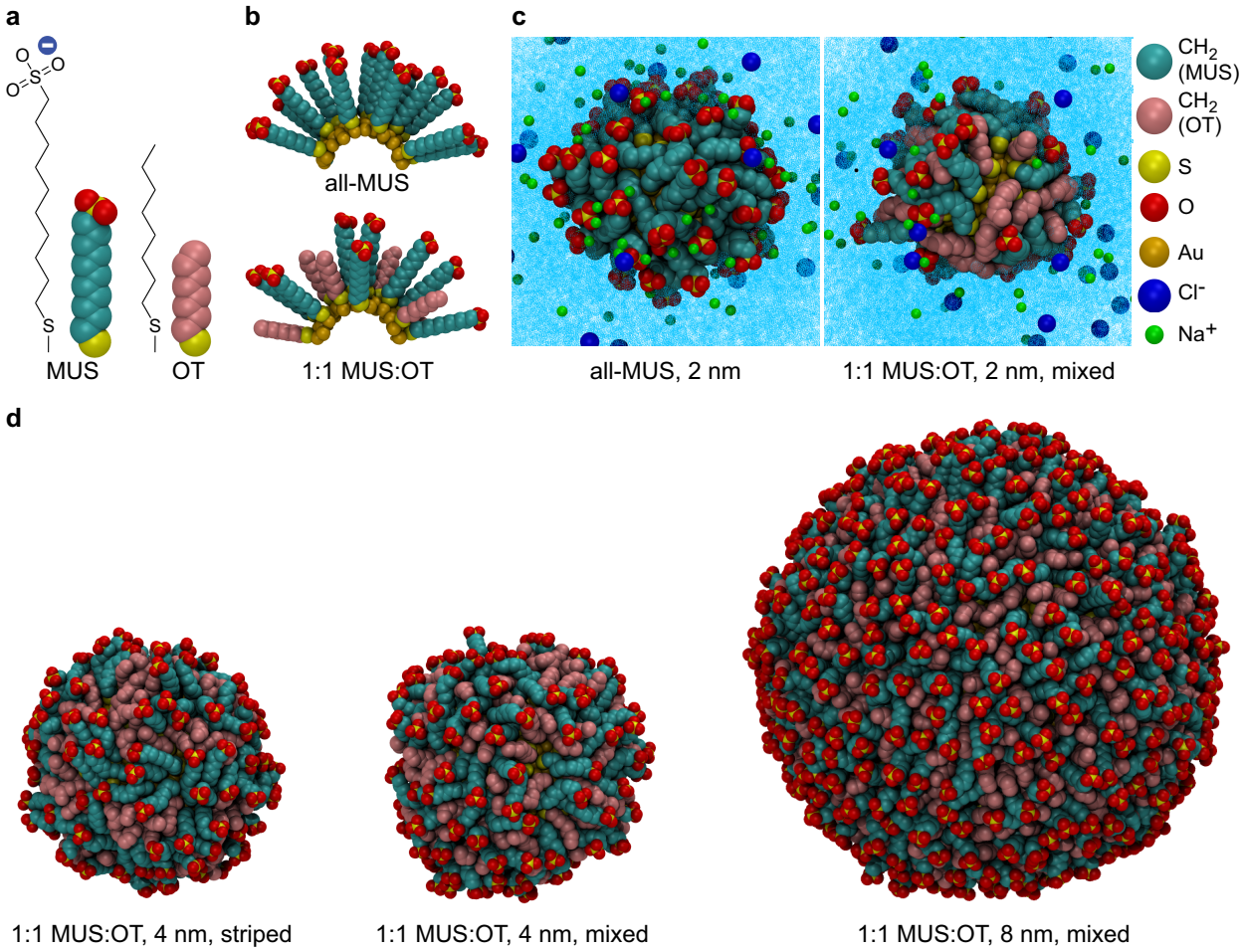

Figure 6-2: Simulation representation of united atom molecular dynamics model. **a** Structures of MUS and OT with corresponding simulation representations. **b** Example snapshots of 2 nm core diameter NPs with initial all-*trans* ligand positions. **c** Example snapshots of 2 nm core diameter NPs in salt solution after 120 ns. Atoms are colored according to legend on right with water as a blue background. **d** Additional simulation snapshots of of various NPs after 130 ns. Water and ions are not drawn for clarity.

the charged sulfonate end groups or the terminal CH_3 bead in the hydrophobic ligands. Via this definition, an all-*trans* ligand oriented radially outward from the gold surface would have a tilt angle of approximately 0°. Tilt angles were computed for each ligand species independently and averaged over all ligands in the monolayer.

Root mean square fluctuations (RMSF) of the ligands were calculated by averaging the RMSF of each atom in each ligand to compute the average RMSF per ligand. The RMSF per atom was defined as:

$$RMSF = \left(\frac{1}{T} \sum_{i=1}^{T} (\mathbf{r}_i - \mathbf{r}_{avg})^2 \right)^{1/2} \tag{6.3}$$

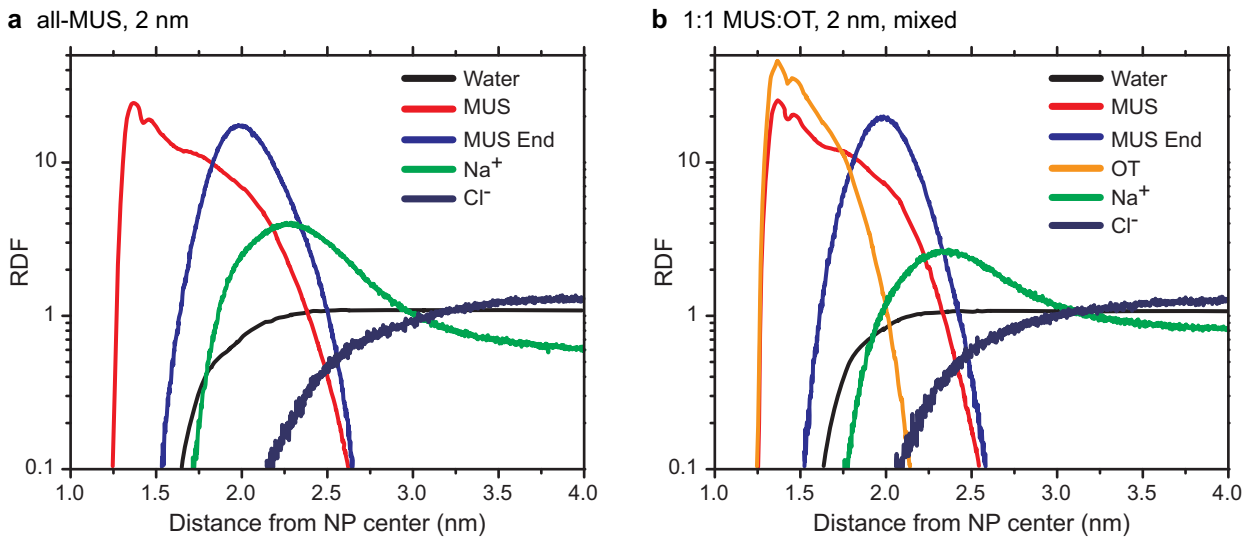

Figure 6-3: Radial distribution functions of 2 nm core diameter NPs. **a** RDF for all-MUS NP. **b** RDF for 1:1 MUS:OT NP.

where the average runs over T samples, $\mathbf{r}_i$ is the i^{th} position of the atom, and $\mathbf{r}_{avg}$ is the average position of the atom. The T samples were chosen from a trajectory where the rotation and translation of the gold shell were removed to eliminate these contributions to the RMSF. The T samples were taken every 500 ps to ensure that ligand positions were uncorrelated.

The radius of gyration, solvent-accessible surface area, distribution of torsional angles, radial distribution functions, and average number of hydrogen bonds per charged end group were all calculated using default Gromacs analysis tools [246].

6.3.1 Comparison of mixed and homogeneous monolayers

As a first test of system properties, 2 nm 1:1 MUS:OT and all-MUS NPs were simulated with example post-equilibration snapshots shown in Fig. 6-2. The snapshots again illustrate the fluid nature of the monolayer at 310 K with no visual indication of domain formation or crystallization in either case, agreeing with the vacuum/water simulations. A diffuse layer of counterions collects on the surface (green beads in Fig. 6-2c). The images also show the tendency of the ligands to fold toward the gold surface due to the unfavorable interaction with water, effectively minimizing the solvent-accessible surface area as discussed in previous Chapters.

Radial distribution functions (RDFs) of the same two 2.0 nm particles are shown in Fig. 6-3 to gain more detailed insight into the structure of the NP interface. The RDF measures the local number density of a particular bead type at a distance r from the gold center normalized by its average number density. On both plots, RDFs for the gold shell and grafted sulfur head groups for the thiol ligands are not included as the positions of these beads were fixed relative to the gold shell center of mass during the simulations. The radius of the gold core was 1.0 nm and on both plots the alkanethiol peaks decay to zero at a distance of about 1.25 nm, corresponding to the radius of the

gold core plus the size of the gold-sulfur bond (≈ 0.23 nm [82]). The center of mass of the sulfonate end group is assigned a separate curve from the overall MUS ligand density to more clearly identify where the charged end groups reside relative to the interface (labeled as MUS End). As expected from the relative lengths of the 11-carbon backbone MUS and the shorter 8-carbon backbone OT, the MUS end group curve peaks at a distance farther from the gold surface than the bulk of the hydrophobic ligand density for the 1:1 MUS:OT case. Furthermore, the average hydrophobic ligand density is closer to the gold surface than the hydrophilic density due to this length difference. Aside from the addition of this OT curve, the qualitative features of both systems are largely identical. The broad peaks for the ligands indicate the flexibility of these species, agreeing with the simulation snapshots, and similarly the enhanced peak for sodium ions near the MUS end groups is consistent with the observed counterion cloud. Both ion species and water plateau to bulk values far from the interface as expected from Debye-Hückel theory. This plateau behavior confirms that the simulation box is sufficiently large to prevent artifacts from finite size effects. It is also interesting to note that there is effectively zero water penetration toward the gold surface due to the protecting effect of the hydrophobic ligand layer. Finally, the all-MUS RDF compares favorably to similar structural characterizations of NPs coated with cationic or carboxylated end groups [184], confirming that the parameterization of sulfonate does not induce any significant distortions of the system.

6.3.2 Ligand fluctuations determined by NP size and ligand lengths

Having verified that the simulation model reproduces sensible structural properties, we next explore how ligand structure depends on properties of the NP. Given the importance of ligand fluctuations in determining favorable bilayer interactions (Chapter 3/5), it is particularly important to understand how these ligand fluctuations may be modified by changes to the NP size or ligand composition.

For a fixed ligand grafting density, increasing the diameter of the particle reduces the amount of free volume accessible to each ligand on the surface, inhibiting ligand fluctuations. Fig. 6-4a shows the ligand tilt angle distribution of MUS and OT ligands for NPs with 2 nm, 4 nm, 6 nm, and 8 nm core diameters and 1:1 MUS:OT surface compositions. Solid lines show the tilt angle of the hydrophilic MUS ligand while dashed lines indicate the tilt angle of the hydrophobic OT ligand. The tilt angle distributions for both ligand species shift toward smaller values as the particle diameter increases, consistent with a reduction in the free volume per ligand as the surface curvature is increased. The snapshots in Fig. 6-2d illustrate this effect as the ligands for the smaller 2 and 4 nm NPs tend to lie down and distort to avoid water exposure while the ligands on the 8 nm NP extend radially away from the surface. For the 8 nm particles, the average tilt angle for both the hydrophilic and hydrophobic ligands is near 30°, similar to the tilt angle calculated for homogeneous monolayers on flat surfaces [227]. This analysis may indicate that the surface of NPs with diameters of ≈ 10 nm may already have a sufficiently large curvature that the structural properties are similar to those of flat surfaces. The shift in distribution also agrees with previous results showing a similar decrease in the average tilt angle with size for homogeneous monolayers on spherical substrates [211]; for the MUS:OT ligands, however, the presence of charged end groups

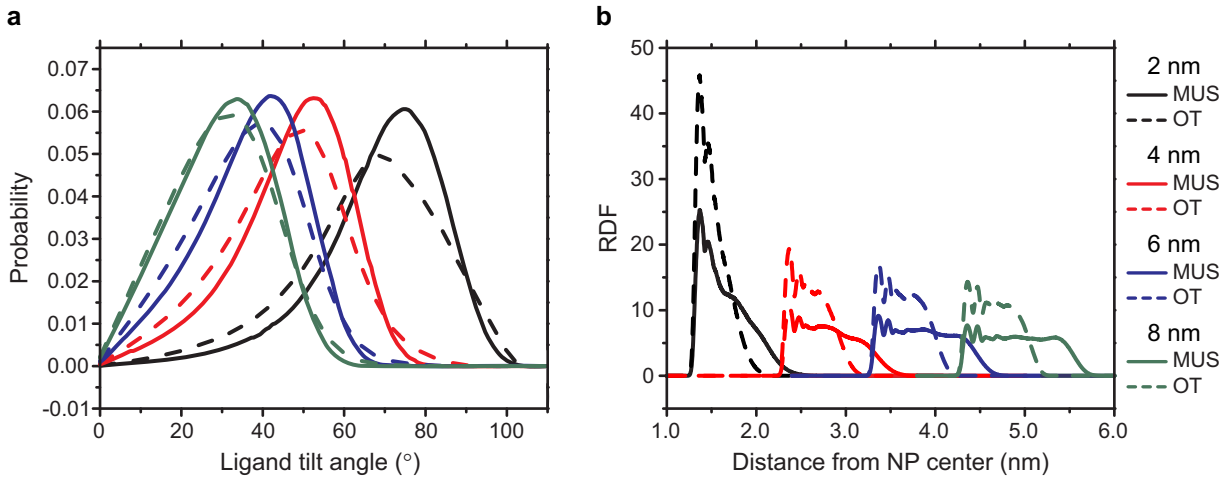

Figure 6-4: Ligand structure as a function of NP core diameter. **a** Tilt angle distributions for 1:1 MUS:OT surface compositions for 2 nm, 4 nm, 6 nm, and 8 nm NPs. **b** RDFs of both ligands for same set of NPs.

and multiple ligand species inhibits the ordering observed for homogeneous alkyl monolayers. Fig. 6-4b shows RDFs of both ligands for all four particle sizes. As the NP size increases, the RDFs for both ligands become broader and less peaked indicating a greater tendency for the ligands to extend farther from the gold surface in agreement with the tilt angle results.

The effect of this shift on average tilt angle is further explored in Fig. 6-5 which shows the correlation between the average root mean square fluctuations per atom in each ligand species and the average tilt angle as a function of particle size. As the average tilt angle decreases, the spatial fluctuations of the ligand chain similarly decrease. This observation is consistent with a physical picture in which each ligand fluctuates through a cone of free volume confined by steric interactions with adjacent ligand chains [91]. Increasing the particle diameter thus inhibits ligand fluctuations as the free volume accessible to each ligand is reduced, confirming findings from the previous united atom model.

While increasing the size of the particle core decreases the fluctuations of both ligand species, consistent with a decrease in free volume, it is unclear what effect changing the relative ligand lengths would have. This system feature is particularly important given the variety of ligand compositions reported in the literature, including both cases where the hydrophilic ligand species is longer than the hydrophobic one [83, 81] and the opposite case where the hydrophobic ligand is longer than the hydrophilic one [84, 85, 219, 202]. In Chapter 5, we also showed that longer ligands increase the driving force for bilayer insertion (c.f. Fig. 5-6). To explore the effect of varying ligand lengths, we fixed the length of the hydrophilic ligand while increasing the length of the hydrophobic ligand. Ligand length will be referred to by the number of CH_2 or CH_3 groups in the ligand backbone, so that the MUS:OT composition discussed so far would be described as a 11:8 composition. All particle diameters were fixed at 4.0 nm with mixed morphologies and a 1:1 ratio of the hydrophilic:hydrophobic ligands.

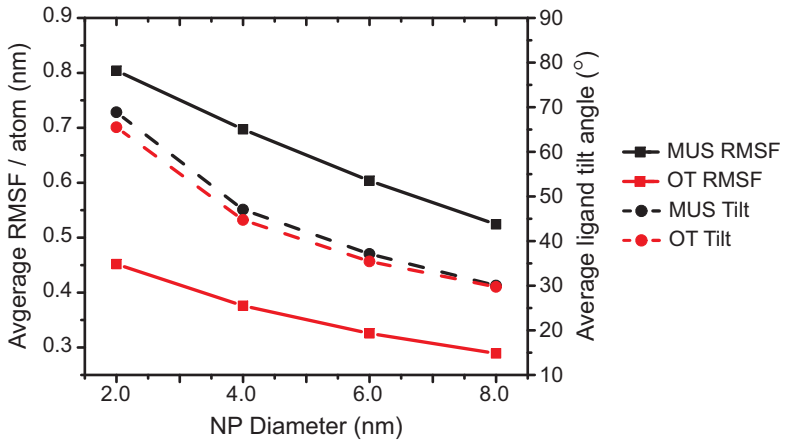

Figure 6-5: Ligand fluctuations compared to tilt angles as a function of NP core diameter. The RMSF per atom and average ligand tilt angle are shown for both MUS and OT ligands for the same four NP diameters considered in Fig. 6-4.

Fig. 6-6a shows tilt angle distributions of the hydrophilic and hydrophobic ligands as a function of increasing hydrophobic ligand length in analogy to Fig. 6-4a. For increasing hydrophobic ligand length, the hydrophilic ligand tilt angle is shifted to smaller values while the hydrophobic ligand tilt angle shifts to larger values. In analogy with the previous results from varying the NP diameter, these results show that increasing the hydrophobic ligand length effectively confines the hydrophilic ligands. This confinement effect is further confirmed by comparing the root mean square fluctuations with the average tilt angle. Fig. 5-6b shows that these two quantities are again highly correlated, implying that an increase in hydrophobic ligand length inhibits hydrophilic ligand fluctuations while enhancing the fluctuations of the longer hydrophobic ligands.

The reason for the confinement of hydrophilic ligands can be observed in Fig. 6-7a, which shows side-by-side simulation snapshots of 11:8 particles and 11:17 particles, the two extremes of ligand length tested here. The first row shows the ligands in their initial all-*trans* configuration to illustrate that the long hydrophobic ligands initially extend farther from the interface than the MUS end groups. After equilibrating in solution, these ligands "bend" to avoid exposing hydrophobic surface area to solution (second row). The strong driving force for the solvation of the charged MUS end groups thus sets the location of the water-monolayer interface and the hydrophobic ligands, regardless of length, reside below this position independent length. The last row of images further confirms this bending behavior by showing the entire surface of the two NPs. This strong bending behavior explains the large average hydrophobic tilt angle evident in Fig. 6-6 as bending would be calculated as a large tilt angle. The confinement of the hydrophilic ligands is similarly explained by the increased local density in the monolayer necessitated by ligand bending, leading to inhibited fluctuations and hence a decreased tilt angle. Further evidence of the bending effect is shown in the two RDFs in Fig. 6-7b which show that the hydrophobic ligands are confined closer to the NP surface than the MUS ligands for both compositions. The 11:17 RDF has a pronounced peak in the

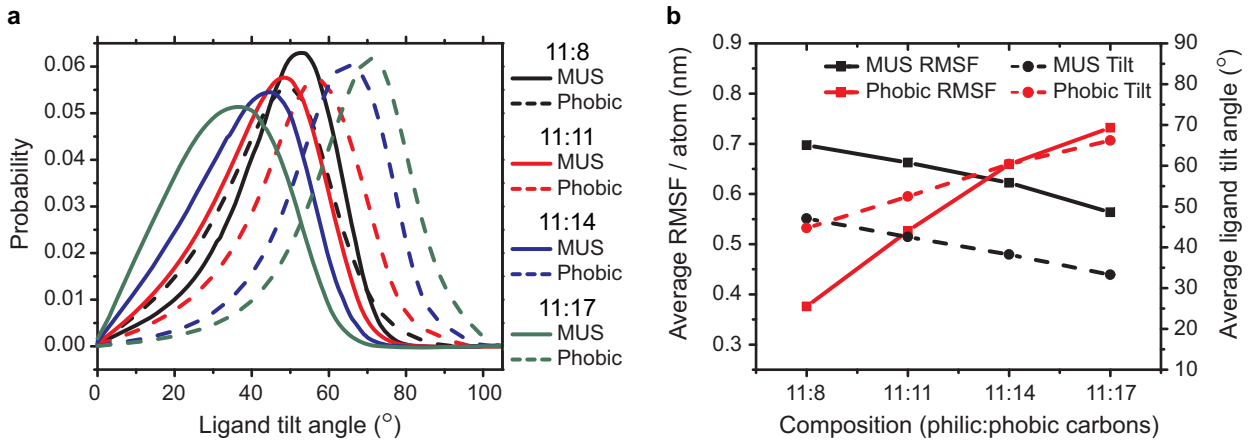

Figure 6-6: Ligand structure and fluctuations for increasing hydrophobic ligand length. **a** Average tilt angle of both MUS and hydrophobic ligands for a 1:1 composition with four different ligand lengths. The NP core diameter is 4.0 nm. **b** The RMSF per atom and average ligand tilt angle for both ligands for the same four ligand lengths.

hydrophobic ligand density left of the position of the MUS end groups indicative of the increased density packed into the ligand monolayer. The plots also show that the MUS end group peak shifts to slightly farther distances in the 11:17 case, consistent with the decrease in hydrophilic tilt angle observed in Fig. 6-6.

6.3.3 Morphology has no effect on NP properties

The previous results show the critical effects that NP diameter and ligand lengths have on the properties of the interface due to the inhibited fluctuations of the grafting ligand layer. Another factor that may influence the properties of the interface is the nanoscale arrangement of the ligands into different morphologies as studied in Chapters 3 and 5. To test whether any differences in ligand properties emerge from changing the ligand morphology we used the same random, mixed, and striped morphologies studied in Chapter 3 (see Fig. 3-6) and generated following the method in Appendix B.

Table 6.2 summarizes the results of a series of structural characterizations of 4.0 nm NPs with the three different morphologies, including three different realizations of a random surface to yield a total of five distinct ligand arrangements. 4.0 nm NPs were chosen because this diameter is close to the typical value used experimentally [81] and is sufficiently large that morphology distinctions are observed experimentally [86]. Parameters calculated include the average hydrophobic SASA; the average number of hydrogen bonds formed; the average tilt angle of the MUS and OT ligands; root mean fluctuations of each ligand species; and the fraction of *gauche* dihedral conformations for MUS and OT ligands averaged over the entire chain. Standard deviations are reported for each measurement. For each of these measurements, the five different ligand arrangements showed nearly identical values, indicating no ability to distinguish the nanoscale morphology on average.

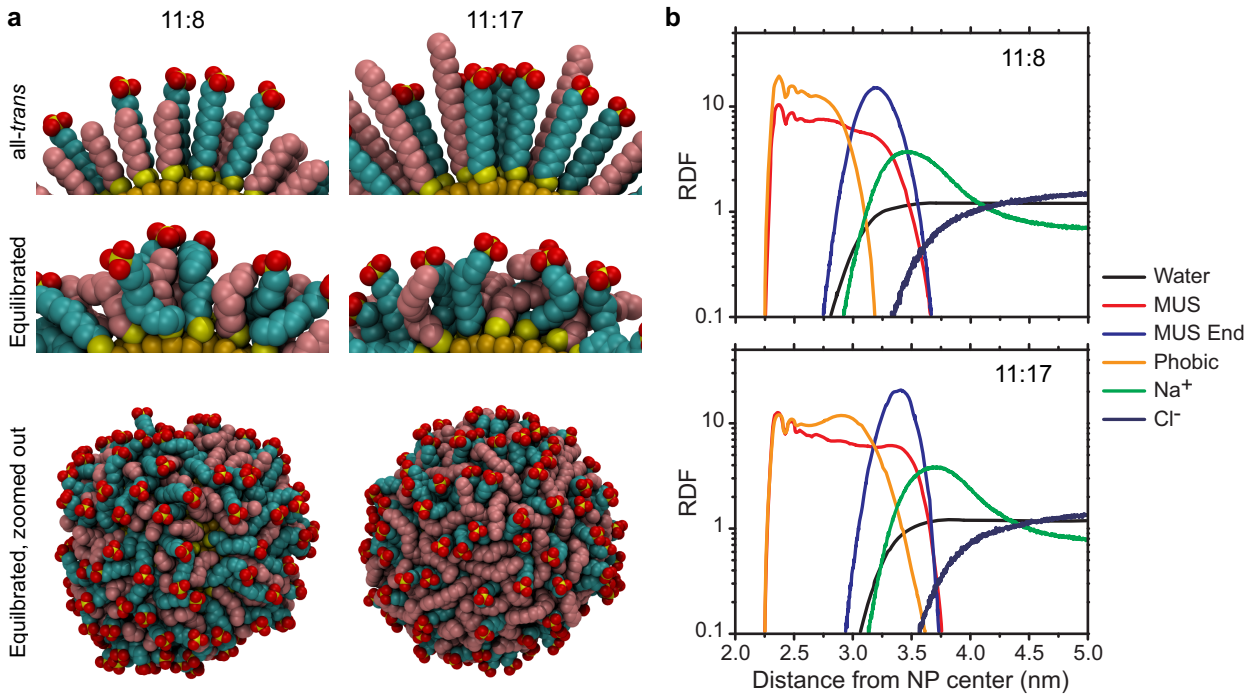

Figure 6-7: Bending of long hydrophobic ligands to avoid water exposure. **a** Simulation snapshots of NPs with 4.0 nm core diameter and 1:1 11:18 or 11:17 ligand compositions. The all-*trans* snapshots illustrate relative length differences prior to simulation. The equilibrated snapshots show the system after 100 ns of simulation with water and ions omitted for clarity. **b** RDFs of all system components for 11:8 (top) and 11:17 (bottom) ligand compositions.

These results again make sense given the small diameter of the NP core, allowing extensive ligand fluctuations that ultimately define the structural properties of the interface rather than the positions of the actual grafting points. The similarity in measurable structural characteristics is indicative of the tendency for charged head groups to maximize their separation due to electrostatic interactions while the hydrophobic backbones avoid water exposure. These driving forces lead to similar structural characteristics independent of grafting positions. Finally, we note that a recent study showed similar similarities between different morphologies using a different atomistic force field [117].

To further show the similarity between the three types of morphologies in solution, the relative positions of the charged ligand end groups were compared using end group-to-end group RDFs with three curves corresponding to mixed, striped and random morphologies shown in Fig. 6-8. For 1:1 MUS:OT NPs, all three curves show very similar behavior, each exhibiting two local maxima corresponding to preferred end group separations. These peaks are consistent with the charged sulfonate groups uniformly distributing to minimize electrostatic repulsion, leading to preferred end group separations rather than a continuous distribution of possible separations. The inability to differentiate between the different morphologies again indicates that ligand fluctuations drive all particle types into similar instantaneous morphologies independent of the location of grafting

Table 6.2: Comparison of morphologies for 4.0 nm NPs with 1:1 MUS:OT compositions

	Mixed	**Stripes**	**Random (1)**	**Random (2)**	**Random (3)**
SASA (nm^2)	183.35 ± 3.89	183.22 ± 3.93	183.83 ± 4.02	183.53 ± 3.88	183.62 ± 3.95
# H-bonds	744.1 ± 12.3	743.7 ± 12.3	744.0 ± 12.3	744.0 ± 12.3	743.9 ± 12.3
MUS tilt (°)	47.05 ± 13.91	47.12 ± 13.83	46.91 ± 14.07	47.19 ± 13.99	47.31 ± 13.97
OT tilt (°)	44.72 ± 15.31	44.63 ± 15.54	44.54 ± 15.60	44.02 ± 15.73	44.27 ± 15.60
MUS RMSF (nm)	0.697 ± 0.019	0.683 ± 0.032	0.687 ± 0.026	0.683 ± 0.031	0.688 ± 0.030
OT RMSF (nm)	0.376 ± 0.010	0.375 ± 0.011	0.375 ± 0.012	0.371 ± 0.011	0.372 ± 0.011
MUS frac. *gauche*	0.322 ± 0.050	0.322 ± 0.049	0.321 ± 0.048	0.321 ± 0.049	0.322 ± 0.050
OT frac. *gauche*	0.313 ± 0.037	0.317 ± 0.037	0.316 ± 0.037	0.315 ± 0.037	0.315 ± 0.037

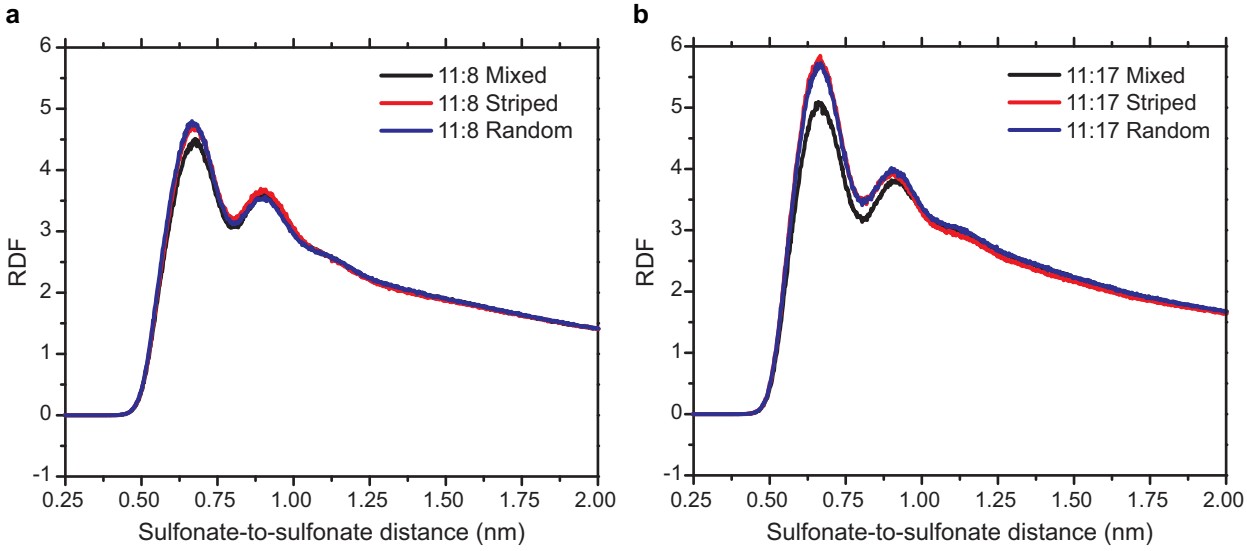

Figure 6-8: Hydrophilic sulfonate end group-to-end group RDFs for mixed, striped, and random morphologies. **a** End group RDFs for 2.0 nm 1:1 NPs with 11:8 ligand lengths. **b** End group RDFs for 2.0 nm 1:1 NPs with 11:17 ligand lengths.

points, qualitatively agreeing with the snapshots in Fig. 6-2. As the findings in the previous section showed that increasing the hydrophobic ligand length confines hydrophilic end group fluctuations and thus minimizes the ability of the end groups to uniformly distribute, Fig. 6-8b shows the same RDFs for 11:17 NP compositions. When the MUS ligands are more confined, the RDF for the mixed morphology is distinguishable from the other two morphologies, but the position of the peaks are the same indicating the same preferred sulfonate separations. The random and striped morphologies are still indistinguishable. These results, combined with the similarity of the average structural quantities in Table 1, indicate that nanoscale morphological changes have minimal discernible effect on the properties of the NPs in solution over even the short nanosecond timescales studied here.

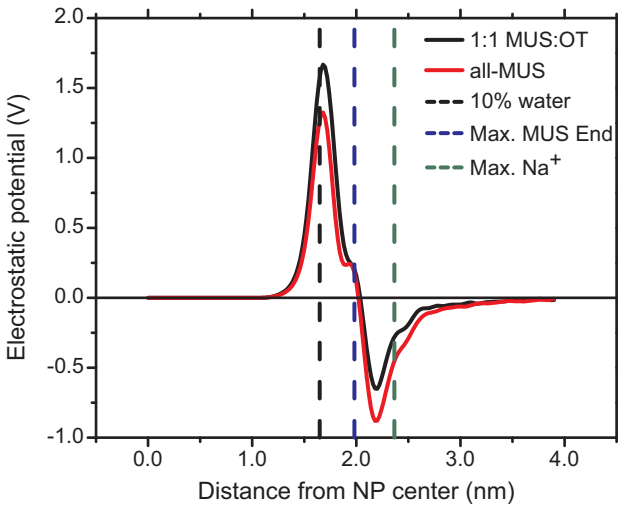

Figure 6-9: Electrostatic potential radially away from center of 2 nm core diameter NPs. Dashed vertical lines indicate positions of system constituents based on RDFs in Fig. 6-3.

6.3.4 Electrostatics

Another important property of the NP surface is the electrostatic potential as this modulates interactions with biomaterials in solution or with the bilayer surface. Fig. 6-9 shows the average radial electrostatic potential for the same two NPs as in Fig. 6-3. Three regimes of behavior are evident which are denoted by vertical dashed lines corresponding to relevant distances from Fig. 6-3. The black vertical line indicates the distance where the water density is 10% of its bulk value which approximates the maximum distance that water penetrates toward the gold core. The positive peak in the electrostatic potential at this position indicates that these water molecules are oriented such that a positive hydrogen atom is closer to the gold surface than the negative oxygen atom. The blue dashed line indicates the peak density of the anionic MUS end groups which is approximately invariant between the two surface compositions. The anionic groups flip the sign of the electrostatic potential which then reaches a maximum shortly before the green dashed line that indicates the maximum density of sodium counterions. For distances in excess of the counterion maximum the potential decays to zero as expected from Debye-Hückel theory. The overall shape of the potential is nearly identical between the 1:1 MUS:OT and all-MUS surface compositions with the major quantitative difference lying in the magnitude of the potential at both the positive and negative peaks. However, the potential decays to zero over approximately the same length scale (i.e. the Debye length) and thus measurable zeta potentials are unlikely to differ significantly as is indeed observed for similar particle compositions [81]. Combined with the RDFs in Fig. 6-3, Fig. 6-9 thus suggests that replacing MUS ligands with OT ligands does not significantly alter the structural or electrostatic properties of the interface.

The electrostatic potential as a function of radial distance is plotted on the same axes for increasing NP diameter and for increasing hydrophobic ligand length in Fig. 6-10. The same general trends previously reported in Fig. 6-9 are observed; first, a strong positive peak in the

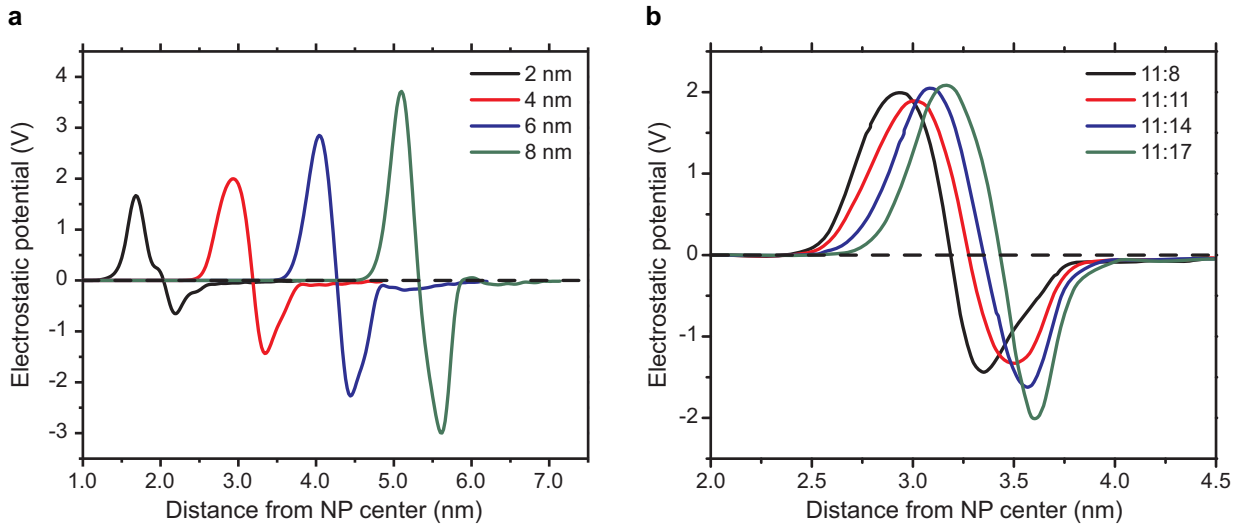

Figure 6-10: Electrostatic potential as a function of NP core diameter and ligand length. **a** Potential near 1:1 MUS:OT NPs with increasing core diameters. **b** Potential near 2 nm core diameter NPs with a 1:1 ratio of philic:phobic ligands. The ligand lengths are specified by the number of carbons in the philic/phobic ligands respectively.

potential corresponding to oriented water molecules appears, followed by a large negative peak at the position of the anionic end groups, followed by a gradually decay of the potential to zero at large distances. The major distinction between different sizes is only in the relative magnitude of the peaks, their widths, and their positioning, as would be expected from the change NP diameter and the incorporation of additional MUS ligands. For increasing ligand length, the shape of the potential is unchanged with only small shifts in the location of the peaks due to the confinement of the MUS end groups leading as discussed previously. This analysis suggests that the electrostatic properties of all NP types are similar at distances in excess of the screening length.

6.4 Potential model weaknesses

One potential weakness of the NP model is the assumption that the polarizability of the gold core is negligible by replacing the gold core with a hollow shell. In principle, treating the gold core as a true conductor could lead to image charge effects that might influence the behavior of the system. While there has been a recent force field parameterized for polarizable gold surfaces [247], to our knowledge no model for polarizable gold NPs exists despite several other simulations of gold NPs in solution [106, 145, 184, 221]. We believe that it is safe to neglect image charge effects for this system for several reasons. First, if the distribution of external charges is spherically symmetric on average, then the induced image charge distribution will also be spherically symmetric. Since the gold core must be charge neutral, the net external field will also be zero following Gauss law using a spherical dividing surface. Second, even if fluctuations in the charge distribution break this spherical symmetry, previous simulations have shown that many-body interactions between

metal surfaces and adsorbates can lead to a cancellation of image charge interactions. For example, simulations of water or other small molecules adsorbed on flat gold surfaces have shown a net cancellation of image charge effects even for a single monolayer of water [248, 249, 250, 251]. As the system we study is primarily water it might be expected that similar cancellations may occur in regions of enhanced charge density.

Another potential weakness of the model is the parameterization of the sulfonate end groups. A recent re-parameterization of the carboxylates in the CHARMM force field has demonstrated that determining partial charges from only *ab initio* calculations may lead to artificial ion or solvent interactions in solution [252]. Despite these potential issues, the results from this model are reasonable. In particular, previously reported radial distribution functions of system components from this model are very similar to those calculated with other NP compositions, including NPs with amines or carboxyl functionalized ligands that are included within the standard GROMOS force field [184]. This structural similarity suggests that the exact nature of the end group parameterization may not induce significant changes to the system if the end group charge is preserved. Furthermore, the GROMOS force field was parameterized with the SPC water model which does not reproduce certain important water properties, such as the dielectric constant [253], that may be a source of error in excess of any possible errors from the sulfonate parameterization.

6.5 Conclusions

In this Chapter, we introduced a new all-atom model for monolayer-protected NPs and used molecular dynamics simulations to explore the structure of the NPs in 150 mM aqueous salt solution. Simulations were performed on a series of simulation systems to understand the effect of the gold particle diameter, nanoscale morphology, and relative ligand lengths on the structure of the monolayer at 310 K and 1 bar, typical biological conditions. Our results confirm the ligand flexibility that was necessary for the fusion behavior predicted in Chapters 3-5 and we show that ligand fluctuations decrease with increasing NP diameters as expected. We further show that increasing the length of the hydrophobic ligands exerts a confining effect on the hydrophilic ligands as the excess hydrophobic material must be sequestered within the monolayer, removing free volume. This extreme bending behavior could impose a severe entropic penalty on the hydrophobic ligands that may affect particle solubility or short-range interactions with other molecules. Our results also show no ability to distinguish between nanoscale morphology, even if hydrophobic ligands are long, consistent with our findings in Chapter 5. Finally, we show that the electrostatic potential is dipolar in nature near the water-ligand interface due to oriented water molecules with the general shape of the potential independent of NP properties.

The trends obtained from our simulations indicate that when considering the properties of mixed-monolayer-protected NPs in solution, the particle size and choice of relative ligand lengths can have a significant effect on system properties and thus NPs with differing ligand lengths cannot be considered as chemically identical. Conversely, morphology seems minimally important to the

determination of properties in contrast to existing reports in the literature [81, 214, 187, 254, 255]. However, we must emphasize that by construction the size of the ligand domains considered for the three different morphologies are on the order of only a few Å to match experimental observations [81]; it is likely that NPs with macrophase-separated domains, such as Janus particles, would demonstrate more significant differences as has been shown previously shown [219]. Similarly, in Chapter 5 we showed that explicitly including branched ligands can modify free volume and affect properties; as these ligands are used to modify morphology, it is possible that their inclusion could determine monolayer properties. Finally, we have not looked in detail at the interfacial behavior of water molecules, and it is possible that some change in the surrounding water could be coupled to nanoscale morphology. These questions will be answered in future work. Nonetheless, these results are important in establishing that particular care for considering the exact morphology of the particle surface may not be necessary for many applications given the structural similarities between the resulting monolayers.

Chapter 7

Spontaneous NP Insertion into Bilayer Defect Edges

Work in this chapter was published in:

R. C. Van Lehn*, M. Ricci*, P. H. J. Silva, P. Andreozzi, J. Reguera, K. Voïtchovsky, F. Stellacci, and A. Alexander-Katz, "Lipid tail protrusions mediate the insertion of nanoparticles into model cell membranes" *Nature Communications*, **5**, 4482, 2014, DOI: 10.1038/ncomms5482.
* Both authors contributed equally.

Reproduced with permission from the Nature Publishing Group. All experimental studies were performed by Maria Ricci, Paulo H. J. Silva, Patrizia Andreozzi, and Javier Reguera as attributed in the text.

In Part I, we showed that there is a thermodynamic driving force for the stable fusion of NPs with lipid bilayers as a function of the size of the NP core diameter and the composition of the protecting monolayer. However, the pathway by which the NP translocated from an initial state in solution to the membrane-embedded equilibrium state was unclear. In this Chapter, we use a combination of atomistic molecular dynamics simulations and experiments to gain insight into the kinetic barriers that may affect the insertion of the NPs. The pathway must involve the contact between hydrophobic material in the monolayer and the hydrophobic core of the bilayer as in similar situations reported in the literature: for example, recent studies on peripheral protein binding have suggested that hydrophobic residues may contact the hydrophobic core of the bilayer through "hydrophobic defects" [256], while the pathway of vesicle-vesicle fusion involves the contact of lipid tails via stochastic protrusions into solvent [257, 258, 259, 260, 261]. Both of these processes are enhanced by bilayer curvature [257, 262, 263]. Preliminary experimental results on supported lipid bilayers from the Stellacci group have also suggested that NP-bilayer interactions are only observed in the presence of either bilayer defects or excess curved lipid aggregates, such as micelles (personal communication). We thus hypothesize that NP insertion will be enhanced when NPs encounter bilayers possessing significant curvature.

Unbiased simulations support this hypothesis by showing spontaneous insertion within nanoseconds at the highly curved edge of a bilayer ribbon but not through its planar face. We confirm this result experimentally by showing that NPs will enter supported lipid bilayers only in the presence of large defects and that insertion is localized near defect edges. Having established this agreement between simulations and experiments, we use committor analysis to identify the transition state for NP insertion from multiple unbiased trajectories [264, 265] and we show that it involves the protrusion of a lipid tail into solvent, a configuration resembling the point-like pre-stalk transition for vesicle-vesicle fusion [62]. The use of two opposite extremes of bilayer curvature indicates that

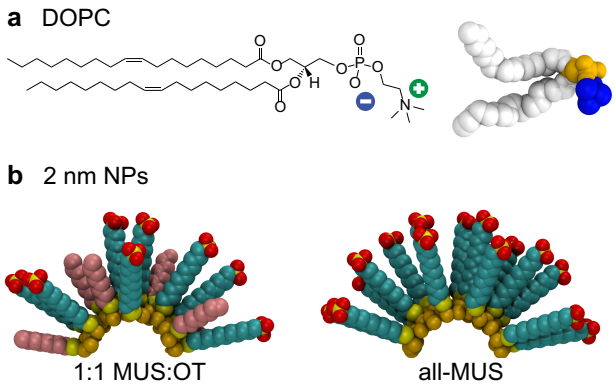

Figure 7-1: Snapshots of system components. **a** DOPC, a zwitterionic lipid previously used in vesicle experiments (Chapter 4). **b** 1:1 MUS:OT and all-MUS NPs with core diameters of 2.0 nm, as studied in Chapter 6.

significant kinetic barriers may inhibit insertion even when fusion is thermodynamically favorable in low curvature systems, and suggest that these kinetic barriers may be minimized in fusogenic systems. The unbiased simulation methodology thus suggests one possible defect-mediated pathway for NP-bilayer fusion mediated by contact with lipid tail protrusions. While large bilayer defects may not occur in physical systems, the finding that tail protrusions trigger insertion is widely applicable to planar systems as well.

7.1 Simulation and experimental methods

7.1.1 Simulation system preparation

The NPs used the same parameterization detailed in Chapter 6 and Appendix D. Two NP compositions were simulated: 1:1 MUS:OT and all-MUS, as shown in Fig. 7-1. Given the invariance between striped, random, and mixed morphologies found in Chapter 6, only the uniform, mixed morphology was used for the 1:1 MUS:OT NPs in this work.

The DOPC bilayer was assembled as a ribbon following the protocol described recently by West et al [266]. First, 200 DOPC lipid molecules were assembled into a bilayer in 150 mM aqueous NaCl solution and equilibrated for 100 ns at 310 K and 1 bar pressure. Lipids were hydrated to a level of 45 water molecules per lipid [267]. After equilibration, the 200 lipid bilayer was duplicated along the x-axis and the box size was increased to add an additional 10 nm of water between the edges of the bilayer in the x-direction. The ribbon system was then further equilibrated for another 100 ns. To minimize ribbon tilting in the z-dimension and prevent periodic images from interacting with each other, the phosphorus atoms in two lipids of the bilayer were constrained to move only in the x/y dimensions. These constrained lipids were selected to be in the same monolayer, with one lipid in the center of the ribbon and the other closer to the edge far from where the NP was eventually placed. This methodology successfully limited ribbon tilting while still permitting full

lipid fluctuations and not interfering with NP insertion. Simulation parameters were identical to those in Appendix D. All simulations were run with the Gromacs package version 4.6.1 [246].

7.1.2 Experimental methods

All chemicals for the NP synthesis were purchased from Sigma Aldrich except for the ligand MUS, which was synthesized following the procedure of Verma et al [81]. All NPs were synthesized following a modification of the procedure reported by Zheng et al [268]. The solvent used was a 10% DI-water in dimethylformamide (DMF) mixture. The targeted amounts of chloro (triphenylphosphine) gold(I) (Sigma), MUS plus OT ligands, and the reducing agent borane tert-butylamine (Sigma) complex were measured and dissolved separately by sonication in 20 mL glass vials to form a 2:1 MUS:OT monolayer composition. The gold salt solution was added to ≈100 mL of the solvent mixture at room temperature in a 250 mL round bottom flask under magnetic stirring (≈800 rpm), followed by the addition of the thiol mixture. After 10 min, the solution became turbid and the reducing agent solution was added. The flask was capped with a condenser and brought to reflux between 120 and 125°C. The reaction was stirred for 1.5 hours, then the heat was turned off and the solution was cooled at room temperature, under stirring, for another 1.5 hours. The flask was placed in a 4°C fridge overnight after which the product precipitated and the supernatant was discarded. The product was washed 3 to 5 times by suspending and centrifuging (5500 rpm) in acetone then ethanol. Finally, the product was washed 5 times with DI-water using Amicon Ultra-15 centrifugal filter devices (10k NMWL). All NP synthesis and characterization was performed by Paulo Silva, Patrizia Andreozzi, and Javier Reguera under the supervision of Prof. Francesco Stellacci.

DOPC lipids in chloroform were purchased from Avanti Polar Lipid (Avanti Polar Lipids, Alabama, USA). The needed amount was put in a glass vial and the chloroform was let to evaporate overnight under vacuum. The phosphate buffer (PBS), previously filtered with 200 nm singers filter, was added in the same vial to obtain a final concentration of 1 mg mL^{-1} DOPC in PBS which was sonicated for 10 min and vortexed. Successively, 1 mL of 1 mg mL^{-1} DOPC in PBS was extruded 21 times at room temperature through a membrane with 100 nm pores (PC Membranes 0.1 μm, Avanti Polar Lipids, Alabama, USA). The solution obtained was successively diluted 10 times, obtaining a final concentration of 0.1 mg mL^{-1} of DOPC vesicles in PBS. This solution was used in both atomic force microscopy (AFM) and quartz crystal microbalance with dissipation (QCM-D) experiments as described below.

The silicon oxide substrates were obtained from p-doped silicon wafers. Substrates with the desired dimensions were cut with a diamond tip and successively cleaned. The supported lipid bilayers for the AFM experiments on silicon wafer were obtained via vesicle deposition. A drop of 0.1 mg mL^{-1} solution of DOPC vesicles in PBS was put on top of the substrates and the system was heated to 40°C for 20-30 minutes. The PBS was successively exchanged at least 3 times before transferring the substrates to the Teflon Petri dish for the AFM measurement.

All the AFM measurements were carried out in liquid with a commercial MFP-3D AFM (Asylum

Research, Santa Barbara, CA, USA). We used a triangular silicon nitride cantilever (TR400-PSA, Olympus, Japan) with a nominal stiffness of $k = 0.23$ N m^{-1} or a rectangular silicon nitride cantilever (RC800-PSA, Olympus, Japan) with a nominal stiffness of $k = 0.05$ N m^{-1}. The cantilevers were fully immersed in the liquid for the experiment. If required, we intentionally dewetted the lipid bilayer to create defects. The system was then allowed to thermalize at room temperature for 30 to 60 minutes in order to minimize drift before acquiring data. The AFM was operated in amplitude-modulation mode ('tapping' in the AFM commercial software) with the setpoint/free amplitude ratio ($A/A0$) as high as possible (typically $A/A0$ ¿ 0.8). The samples were imaged in standard PBS. A series of force curves were first performed to confirm the presence of the bilayers, then the tip was withdrawn from the surface and 100 μL of 10 mg mL^{-1} NP solution was added. Immediately afterwards, contact with the surface was again established and we followed the change in time of the surface topography. Image analysis was performed using SPIP (Image Metrology, Denmark), Gwyddion (http://gwyddion.net) and Igor Pro (Wavemetrics, Lake Oswego, OR, USA). The images were flattened and eventually low-pass filtered to remove high frequency noise.

All the QCM-D measurements were carried out with the commercial QCM-D machine Q-Sense E4 (Biolin Scientific/Q-Sense, Västra Frölunda, Sweden) connecting the four sensors to a standard Ismatec IPC-N 4 peristaltic pump (IDEX Health & Science GmbH, Wertheim, Germany). Before the beginning of the experiments the sensors were placed in the chambers, sealed and heated to 40°C. The QCM-D experiments were performed at this temperature to help the formation of the DOPC bilayer during the initial stage of the experiment. We prepared glass vials, previously cleaned and filled with Milli-Q water, PBS, NP solution and 0.1 mg mL^{-1} of DOPC vesicles (100 nm in diameter) in PBS. The solutions were put in a water bath at 45°C during the experiments and before insertion into the tubing system to avoid the formation of air bubbles in the Teflon tubes and in the QCM chambers. The flux velocity used in all experiments was of 100 μL min^{-1} unless the presence of an air bubble was detected. The first step in the actual experiment was to flush using only PBS for at least 30 minutes, allowing the system to equilibrate. The standard value of frequency drift obtained was of less than 1 Hz per minute. Subsequently the suspension of lipid vesicles in PBS was injected and the signal of bilayer formation was recorded. After 10 minutes, new PBS solution was injected to remove any extra unfused vesicles in solution. At this stage the system was left to equilibrate for 30 minutes. All AFM and QCM-D experiments were performed by Maria Ricci under the supervision of Prof. Kislon Voïtchovsky and Prof. Francesco Stellacci.

7.2 Unbiased simulations show spontaneous NP insertion at bilayer edges

The lipid bilayer was modeled as a DOPC "ribbon" immersed in a 150 mM NaCl solution with two edges of the bilayer exposed to solvent. At equilibrium, lipids along the two water-exposed edges deform to minimize exposure of the hydrophobic core to water, creating a highly strained edge with extreme curvature. Two possible starting configurations for NPs were tested: the NP was

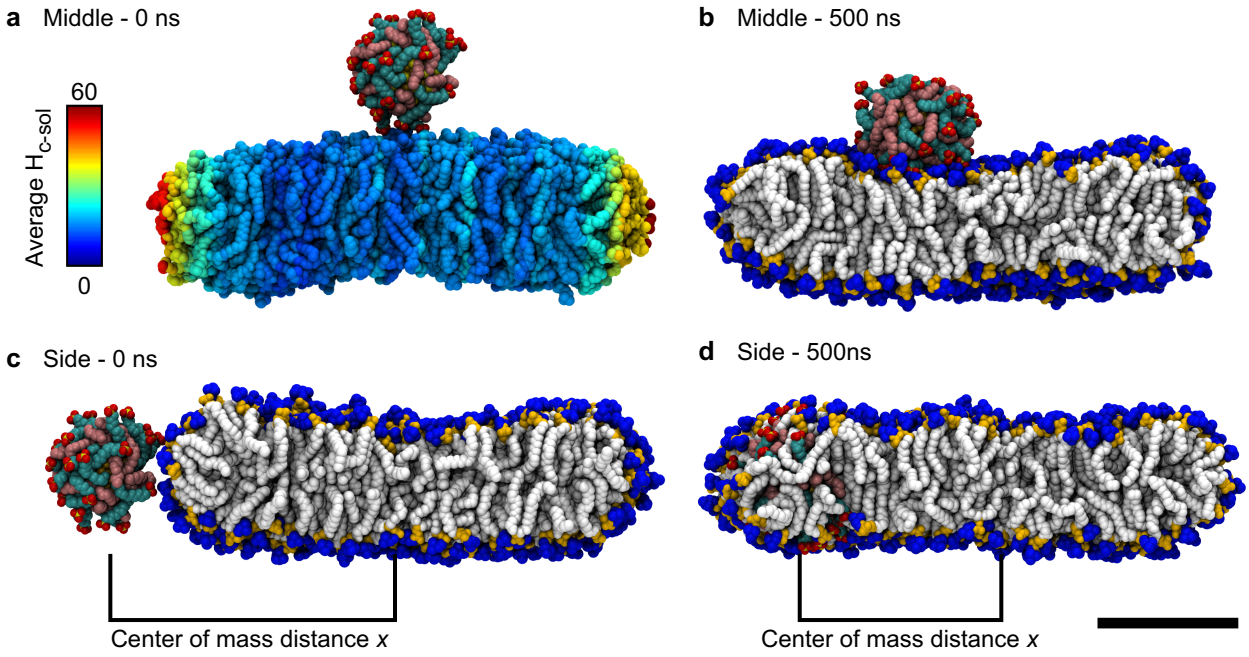

Figure 7-2: Simulation snapshots of interactions between NPs and bilayer ribbons. The scale bar is 5 nm for all images. **a** A 1:1 MUS:OT NP placed in the middle configuration representative of interactions between NPs and planar bilayers. Lipids are colored by H_{c-sol}, the number of atoms in water molecules that are in contact with hydrophobic lipid tail atoms. **b** A NP in the middle configuration after 500 ns, still adsorbed to the surface. **c** A NP in the side configuration representative of interactions between NPs and highly curved bilayers. **d** A NP in the side configuration after 500 ns after spontaneously inserting into the ribbon

placed either above the middle of the ribbon (Fig. 7-2a/b) or near the bilayer edge (Fig. 7-2c/d). These configurations are representative of experiments with an NP approaching a planar bilayer or highly curved bilayer, respectively. Fig. 7-2a further illustrates the distinction between these two starting points by coloring all lipid head groups according to the average number of atoms in water molecules within 0.5 nm of any hydrophobic lipid tail bead, H_{c-sol}. From this image it is clear that NPs placed near the bilayer edge will encounter lipids that are much more prone to water contact than lipids near the planar face of the ribbon.

A series of 6 unbiased 40 ns simulations with a 1:1 MUS:OT NP placed in the "middle" configuration showed no insertion, although electrostatic interactions between the anionic MUS end groups and the bilayer attracted the NP to the surface. Prolonging 1 of these simulations to 500 ns showed that the MUS:OT NP diffused along the bilayer surface without inserting (Fig. 7-2b). 6 similar 40 ns simulations were carried out for both all-MUS and MUS:OT NPs placed in the "side" configuration. 3 of the 6 simulations with a MUS:OT particle and 1 of the 6 simulations with an all-MUS particle showed spontaneous NP insertion into the bilayer. One of the simulations showing insertion for each particle type was prolonged to 500 ns to obtain a full unbiased pathway for spontaneous fusion as shown in Fig. 7-2d and Fig. 7-3. To gain insight into the insertion pathway, we tracked the evolution of the distance Δx between the center of the NP and the center

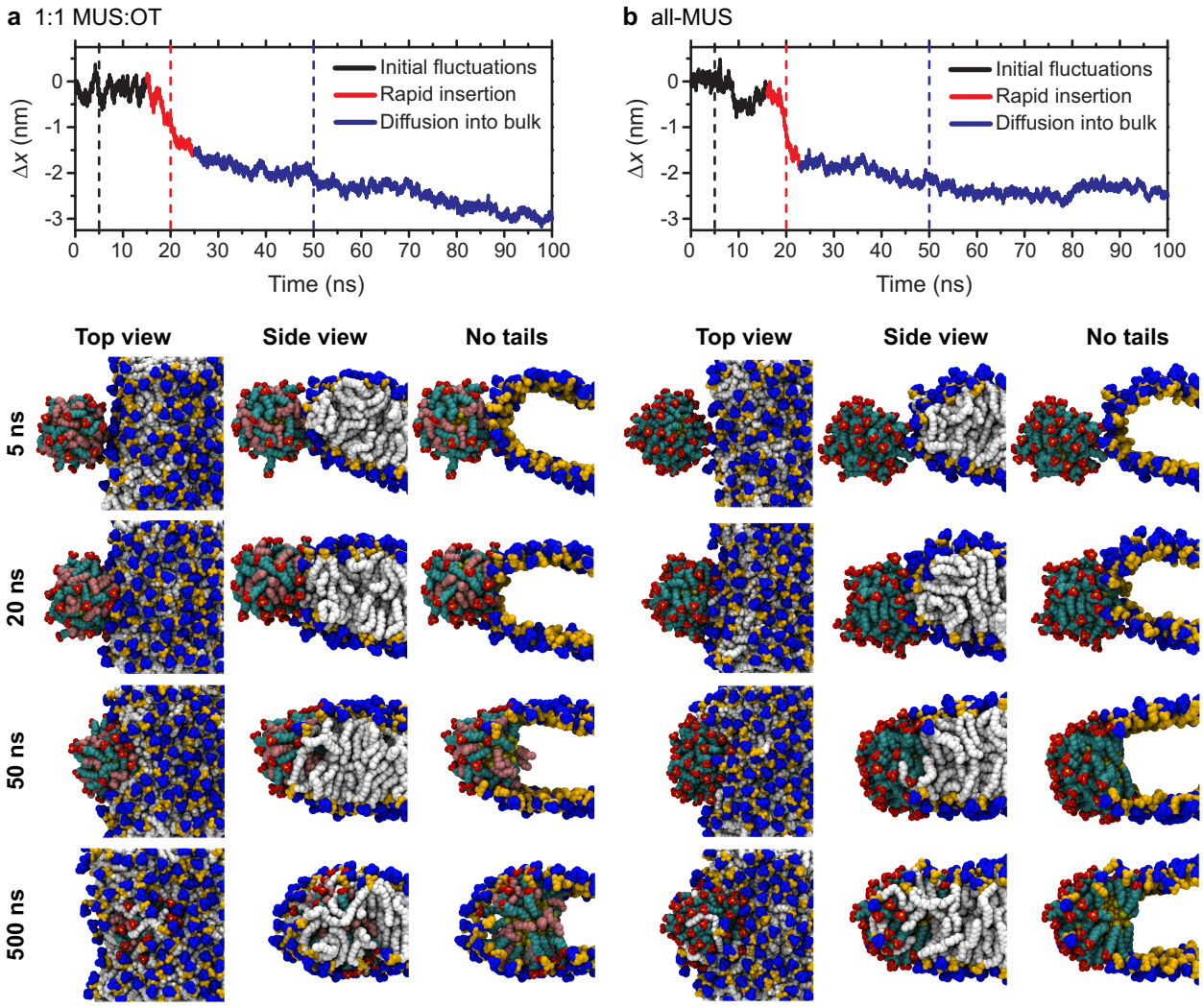

Figure 7-3: Summary of unbiased insertion of both NPs. Plots of the change in distance Δx between the center of the NP and center of mass of the bilayer are shown for the first 100 ns of insertion for both 1:1 MUS:OT (**a**) and all-MUS NPs (**a**). Three regimes of behavior are indicated by different colored lines. Representative snapshots are shown at 5 ns, 20 ns, 50 ns, and a full 500 ns for both NPs. Snapshots are shown for a side view, a side view with lipid tails removed to emphasize ligand positions, and a top-down view.

of mass of the ribbon relative to the initial NP starting position. Results from the first 100 ns of the 500 ns trajectories are presented in Fig. 7-3 for both types of NP together with snapshots of representative system configurations. Δx is negative in all cases, consistent with a decrease in the distance between the NP center and ribbon center from the initial starting position where $\Delta x = 0$.

The insertion of the NPs into the bilayer occurred in three stages (Fig. 7-3). At the beginning of the simulation (black line), the particle first fluctuated through the water surrounding the bilayer, with electrostatic interactions attracting it to the bilayer edge as shown in the first snapshot. A few nanoseconds later, the NP rapidly inserted into the bilayer through the highly strained edge

as shown by the sharp decrease in Δx (red line). During this rapid penetration, the hydrophilic end groups were consistently solvated by snorkeling toward the nearest aqueous interface while the hydrophobic ligands of the MUS:OT particle extended into the middle of the bilayer where the density of lipid tail groups was lower. These ligand conformations are evident in the snapshots with the lipid tails removed in Fig. 7-3. After this period, the NP continued to slowly insert into the bilayer until Δx began to plateau (blue line). In this plateau region, the hydrophilic end groups lined the bilayer edge in a conformation nearly identical to the edge lipids. The final snapshots at 500 ns illustrate that the 1:1 MUS:OT has penetrated sufficiently far into the bilayer that the edge has reformed and the NP obtains the transmembrane state predicted in Part I. The snorkeling behavior predicted from the implicit bilayer model is clearly observed in the simulation snapshots from this atomistic representation as well. The unbiased simulations show that both all-MUS and 1:1 MUS:OT NPs can spontaneously insert through the highly-curved bilayer edge on short simulation time scales while no insertion is observed through the planar bilayer surface. It must be emphasized that these simulations were completely unbiased; no external potential was applied to force NP insertion, a technique frequently used in similar simulations [107, 110] that may induce unphysical system configurations.

7.3 Experimental results on NP-lipid bilayer interactions confirm edge preference

To confirm the simulation results, the interactions of amphiphilic NPs with both defect-free and defect-rich SLBs were studied using AFM and QCM-D. We used polydisperse NPs with a mean gold core size of 5-6 nm coated with a 2:1 MUS:OT monolayer [197, 81, 187] as an intermediate composition between the all-MUS and 1:1 MUS:OT compositions studied in simulations. The NPs were large enough to not form Janus morphologies [86] but sufficiently small that insertion would be expected for a significant portion of the NPs based on the size thresholds identified in Part I.

An example of a SLB that appears defect-free in the area imaged by the AFM is shown in Fig. 7-4a. The image in Fig. 7-4b was recorded after the addition of a concentrated 2:1 MUS:OT NP solution to obtain a final concentration of roughly 1 mg mL^{-1}. No substantial changes in the surface topography were observed, suggesting no local interaction between NPs and the SLB. Since AFM can only study a small portion of the bilayer surface, QCM-D was used to study the uptake of NPs by the whole sample [269, 270]. QCM-D measurements on the perfectly formed bilayer (insets of Fig. 7-4a and Fig. 7-4b) confirmed that no change to the bilayer had occurred upon NP addition as evident in the quasi-constant frequency and dissipation signals.

Using the same preparation method but on a different sample we were able to obtain the bilayer shown in Fig. 7-4c. This defect-rich SLB contained many lipid islands rich in boundaries and separated by distances much larger than the size of the NPs. Upon addition of the same MUS:OT NPs used for the experiment in Fig. 7-4b, clear deposition of the particles near and at the SLB boundaries was observed from changes to the bilayer topography. We interpret the

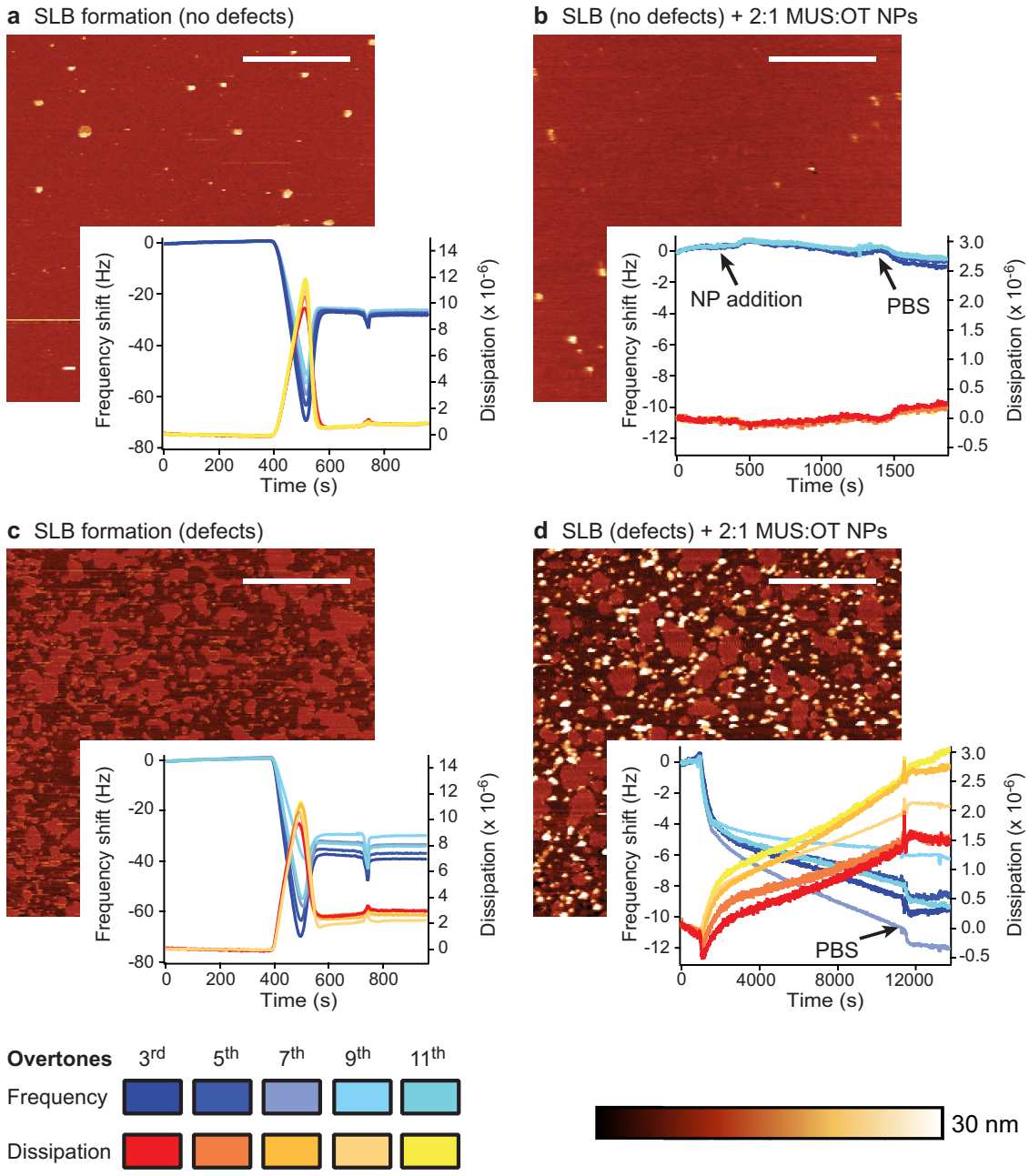

Figure 7-4: 2:1 MUS:OT NP interactions with planar supported lipid bilayers. Interactions were measured with both AFM (images) and QCM-D (insets). Scale bars are 3 μm in all AFM images. All experiments were performed by Maria Ricci. **a** Defect-free SLB after formation by vesicle fusion. **b** Defect-free SLB after subsequent addition of a solution of 1 mg mL^{-1} 2:1 MUS:OT NPs in PBS. Black arrows indicate the times when NPs were added and when PBS was added to remove excess particles. **c** Defect-rich SLB after formation by vesicle fusion. **d** Defect-rich SLB after addition of 2:1 MUS:OT NPs in PBS.

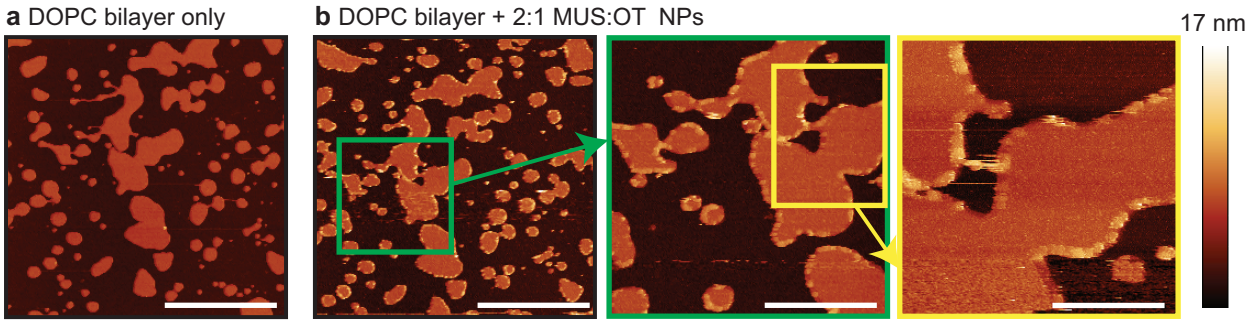

Figure 7-5: Interactions of NPs with SLBs in the presence of large defects imaged by AFM. **a** Initial observation of lipid patches in the absence of added NPs. The scale bar is 2 μm. **b** The addition of 2:1 MUS:OT NPs to the solution leads to the formation of a lighter area surrounding the defect edge as is clearly observed in the enlarged images. The scale bars are 2 μm, 800 nm, and 400 nm from left to right.

localized increase in height as clusters of NPs inserting into the lipid bilayer. The QCM-D results substantially confirm this observation. The signals recorded during the SLB formation are presented in the inset of Fig. 7-4c: the lower value of the QCM-D frequency shift, the split of the overtones, and a higher dissipation value are indications of an incompletely formed lipid bilayer. Upon the addition of NPs to the defect-rich bilayer (Fig. 7-4d), a decrease in the frequency shift and increase in the dissipation were recorded. This is a clear signature of extra-mass attachment on the sensor. The shifts in frequency and dissipation were maintained even after the removal of extra particles by flowing PBS into the QCM-D chamber (black arrow in Fig. 7-4d).

The combined AFM and QCM-D data show that MUS:OT NP insertion occurs mainly in the presence of membrane defects. To gain an improved understanding of the dynamics and spatial localization of the NPs, we used bilayers with larger lipid patches and followed the fate of the lipid region immediately surrounding defects (Fig. 7-5). After the addition of 2:1 MUS:OT NPs, light regions appear in the vicinity of the membrane edges in the AFM images. This change in topography is consistent with preferential particle insertion at the bilayer edge (c.f. Fig. 7-4). The protruding regions persist tens of nanometers away from the edges, suggesting that particles can extend their interaction into the bilayer bulk.

These experiments indicate that NPs do not insert into perfectly planar, defect-free SLBs, but are able to strongly attack the edges of large membrane defects. The findings are in strong agreement with the unbiased simulations which showed no membrane insertion through planar bilayers (akin to the defect-free SLBs) but immediate insertion through the highly-curved ribbon edges (akin to the defect-rich SLBs). Moreover, the experiments indicate that this behavior persists over time scales much longer than obtainable in simulations and suggest that NPs can diffuse from the edge of defects into the bilayer bulk.

7.4 Identifying transition state for insertion

To understand why curvature mediates insertion, committor analysis was used with the atomistic simulations to identify the transition state for NP insertion [265, 264]. For a system with two stable basins A and B in its free energy landscape, the committor, p, is the probability that a trajectory initiated at a particular configuration will reach basin B before reaching basin A. The committor has a value of 0 for configurations in basin A and 1 for configurations in basin B, with intermediate configurations lying in between these two extremes. If the committor is calculated for configurations lying on a transition path that connects these two basins, then the transition state can be identified as the configuration that has a value of $p \approx 0.5$ where the system is equally likely to transition to either basin. The committor thus can yield information about transitions in the system without defining a particular reaction coordinate for the dynamic trajectory. Committor analysis has been successfully used to identify the transition state in protein folding and vesicle fusion simulations similar to the system studied here [259, 264].

Fig. 7-6 schematically illustrates the principle of committor analysis and defines the basins A and B for this study. The contour plot represents a generalized free energy landscape projected onto two collective variables. The free energy basins are represented by the lowest-energy blue contours and are a function of both collective variables. The thick black line represents a trajectory through phase space obtained from an unbiased simulation that connects both basins. That is, the path is found from the natural dynamics of the simulation rather than chosen *a priori* and by connecting both basins it is a transition path. At several points along the trajectory, system configurations are extracted and used to launch several short unbiased trajectories after randomizing initial particle velocities. These short trajectories are represented as arrows pointed toward one of the two basins. The value of the committor is the fraction of the trajectories that commits to basin B over a short time scale. The transition state for the original transition path is identified by the red point and corresponding red arrows where an equal number of trajectories commits to either basin. In general, there may be many possible trajectories between basin A and B, each of which will have (at least one) transition state associated with it; the collection of transition states identified from a series of different trajectories is thus referred to as the transition state ensemble [265].

The committor was calculated by first extracting a series of starting configurations in 1 ns intervals between the 12 ns and 22 ns time points for both trajectories shown in Fig. 6-3. Additional, more fine-grained starting points were then extracted after initial analysis to more accurately locate the transition state. For each starting configuration, 20 simulations were run for 2 ns each after first randomizing the starting velocities of all particles. This short time was possible because of the rapid decrease in Δx that marks initial commitment to insertion. The length of the short trajectories should be on the order of the commitment time [265], so 2 ns was sufficient to gauge commitment and also permitted large numbers of simulations to be run. An additional 20 simulations were run if $0.05 < p < 0.95$ after the initial 20 simulations to improve sampling.

We associate basin A with a particle in solution and basin B with a particle inserted into the bilayer; because both basins were visited during the unbiased simulations, the trajectories are

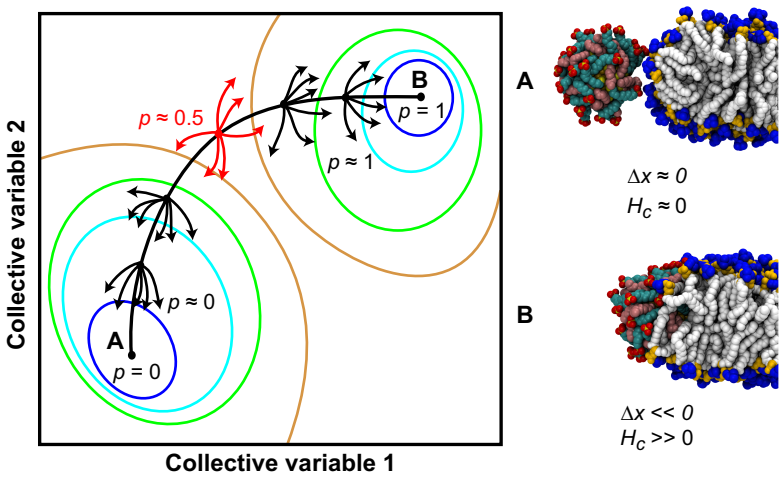

Figure 7-6: Overview of committor analysis. Two basins, A and B, are associated with a NP in solution or inserted into the bilayer ribbon, respectively, as shown in the snapshots. An idealized free energy landscape is represented by the colored contours as a function of two collective variables with the thick black line denoting a transition path across this landscape connecting the two basins. The value of the committor is determined as the percentage of short trajectories launched from various points along the path that commit to basin B as illustrated by the short arrows.

transition paths. Simulations were characterized as committed to basin A or B as judged by two order parameters: the previously defined distance Δx and the number of hydrophobic contacts, H_c, between lipid tail atoms and hydrophobic atoms in the ligand monolayer. A hydrophobic contact was counted if two atoms were within 0.5 nm of each other. These parameters were selected on the basis of observations during the unbiased trajectories. A trajectory was marked as committed to B if $\Delta x < -1.0$ nm and if $H_c > 50$ at the end of the run trajectory. A trajectory was marked as committed to A if $\Delta x > -0.5$ nm or if $H_c < 5$. Finally, simulations that did not meet either criteria at the end of the run were marked as uncommitted and did not contribute to the calculation of p. This typically occurred when the distance had decreased below the threshold but the number of hydrophobic contacts, while possibly greater than zero, was still less than the threshold and fluctuated during the trajectory. Images of the configurations associated with both basins are illustrated in Fig. 7-6.

Fig. 7-7 shows the value of p as a function of the starting configuration time for both MUS:OT and all-MUS NPs. The committor correctly goes from values near 0 for starting times corresponding to the initial surface fluctuation regime discussed previously to a value of 1 for times consistent with the insertion regime. The value of $p \approx 0.5$ is found for a time $t = 17.66$ ns for the 1:1 MUS:OT particle and $t = 18.10$ ns for the all-MUS particle. The similarity in this transition time for both particles is likely coincidental. It must be emphasized that the value of the committor does not need to increase monotonically as a function of time for this unbiased trajectory. Fig. 7-7a indeed shows that the committor increases at $t = 13$ ns before decreasing and eventually increasing again. This behavior corresponds to the system reaching a particular configuration

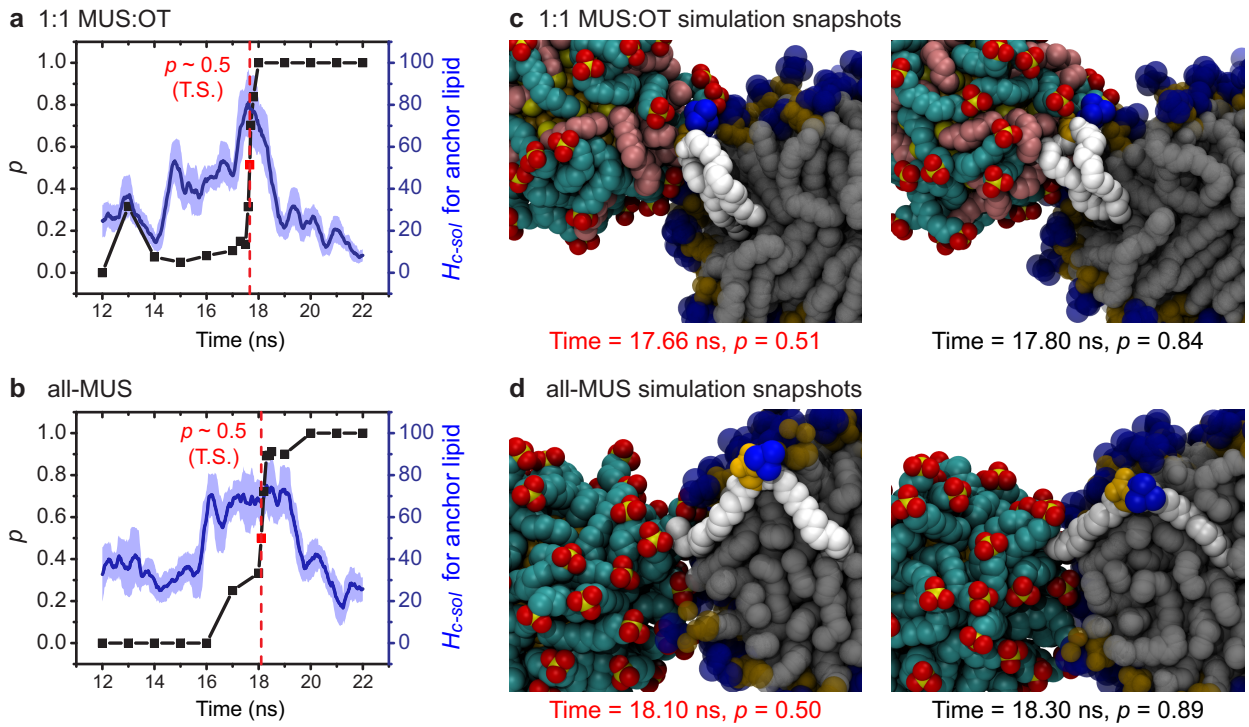

Figure 7-7: Identification of the transition state for insertion. Plots of the committor, p, are shown as a function of time for insertion of the 1:1 MUS:OT **(a)** and all-MUS **(b)** NPs. The committor obtains a value of $p \approx 0.5$ at the transition state (T.S.), labeled in red. The number of hydrophobic contacts between solvent atoms and the single anchor lipid, H_{c-sol}, is shown in blue. Snapshots during and immediately after the transition state **(c, d)** are shown for both particles with the anchor lipid emphasized. Some lipids are removed for clarity.

where it is more likely to commit to insertion, but does not actually proceed to insertion from that configuration, instead committing at a later time after reaching another configuration that favors insertion. Fig. 7-8 clarifies this behavior by showing a schematic illustration of the free energy of the system projected onto a one-dimensional generalized reaction coordinate which represents the path described previously. The schematic illustrates the time evolution of the system drawn along this path. The transient increase in the committor at $t = 13$ ns indicates that the system enters a state with a higher probability of inserting into the bilayer during the unbiased trajectory, but it does not actually commit to insertion until a few nanoseconds later. If a reaction coordinate for this path were known, the simulations could be biased to force the system to evolve along the reaction coordinate in which case the committor would be a monotonic function of time, but that was not done here due to the uncertainty in the reaction coordinate.

The key feature of the transition state ($p \approx 0.5$) is the protrusion of an aliphatic lipid tail into solvent and into contact with aliphatic groups in the NP monolayer. Analysis of the transition state for both trajectories revealed that only a single lipid tail was in contact with the NP surface in both cases (highlighted in Fig. 7-7). This "anchor" lipid remained in contact for the duration of the simulation as the NP inserted into the bilayer. For contact to occur between the anchor lipid

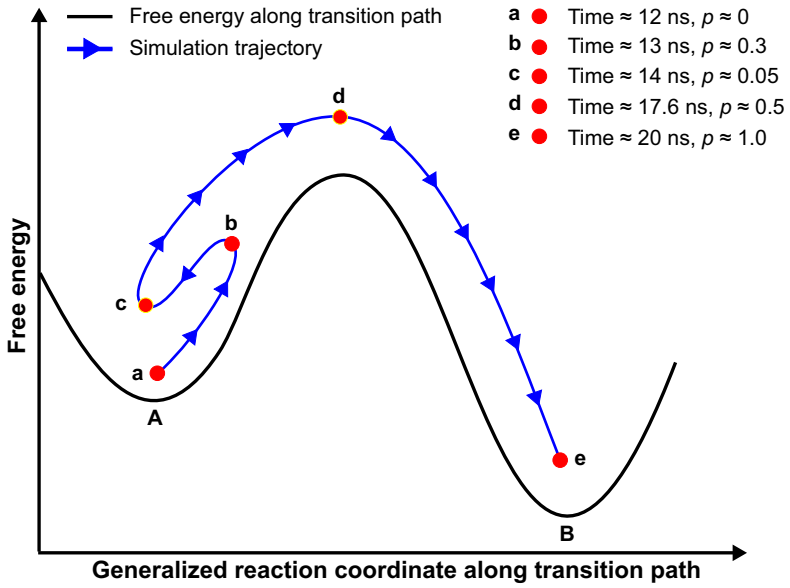

Figure 7-8: Depiction of non-monotonic behavior of committor as a function time. The plot projects the transition path onto a 1D generalized reaction coordinate that connects the two basins. Points in red correspond to times from Fig. 7-7a.

and the NP, hydrophobic atoms in the lipid tail must first spontaneously fluctuate into the solvent region. Fig. 7-7a and Fig. 7-7b show the number of atoms in water molecules within 0.5 nm of any hydrophobic tail atoms in the anchor lipid, H_{c-sol}, as a function of time, representing the amount of water unfavorably contacting the lipid of interest. Each point in Fig. 7-7 is averaged over ± 100 ps to smooth fluctuations with the standard deviation of this smoothing indicated by the transparent area. For both particles, the transition state coincides with a peak in H_{c-sol} which then decreases as p approaches 1. The broader transition for the committor for the all-MUS particle is similarly accompanied by a broader increase in H_{c-sol}. These curves thus indicate that the transition state occurs when the anchor lipid is maximally exposed to water, a highly unfavorable state, and is close enough to contact the NP. To alleviate this solvent exposure, the lipid either relaxes back to the bulk of the bilayer or instead shields hydrophobic material within the NP monolayer, triggering bilayer insertion. The snapshots in Fig. 7-7c and Fig. 7-7d illustrate this process by highlighting the anchor lipid during and immediately following the transition state as it first protrudes into the solvated bilayer head region, increasing H_{c-sol}, then preferentially increases contact with the particle.

The recognition that insertion is initiated by the fluctuation of a lipid tail into solvent prior to contact with the NP explains why insertion is only observed at the highly curved bilayer edge in both simulations and experiments. At the bilayer edge, lipid tail protrusions into solvent are significantly enhanced in comparison to tail fluctuations in the middle of the bilayer ribbon, consistent with the higher average water contact shown in Fig. 7-2a. NPs are thus more likely to contact a tail fluctuation that initiates insertion. This finding may imply that systems in which tail fluctuations

are enhanced will generally reduce the kinetic barriers to insertion as discussed below.

7.5 Similarities to vesicle-vesicle fusion

The prominent feature of the transition state identified in Fig. 7-6 is the protrusion of lipid tail into solvent prior to contact with the NP surface, a phenomenon extremely similar to the pre-stalk transition state proposed for vesicle-vesicle fusion [62]. Several recent simulation studies have shown that the pre-stalk transition for vesicle-vesicle fusion may involve the fluctuation of either a single lipid tail into solvent in a splayed configuration similar to the snapshots in Fig. 7-6d, or the fluctuation of two lipids from adjacent bilayers that make contact in the water layer between two vesicles in a configuration similar to the snapshots in Fig. 7-6c [258, 260, 257, 259, 261, 271, 272]. Several more examples of NP-lipid contacts are shown in Fig. 7-9 and resemble these two states. As these configurations are likely members of the transition state ensemble, it appears that both states that lead to the formation of a stalk in the case of vesicle fusion can also initiate NP-bilayer fusion. Furthermore, previous simulations that did show vesicle-vesicle fusion did not observe fusion between vesicles and planar lipid bilayers [257, 271], similar to our observations of NP fusion with ribbon edges but not planar faces. Similarly, it has been shown previously both theoretically and experimentally that lipid tail protrusions and thus vesicle-vesicle fusion are enhanced for highly curved systems [257, 273], again agreeing with the results for the bilayer edge state presented here.

Based on the findings from these vesicle studies and the current results, we conjecture that the same factors that enhance vesicle-vesicle fusion by stabilizing lipid fluctuations and the pre-fusion intermediate may also reduce the energy barrier for NP-bilayer fusion. Some examples of these factors are the presence of bilayer packing defects [274], the lipid composition [275], and the generation of membrane stresses via transmembrane proteins [259]. While future work will be needed to establish that such factors affect NP insertion, there is some evidence in existing experimental results that supports the idea that enhanced lipid fluctuations reduce the barrier for NP insertion. In this Chapter, hard substrates were used to support the planar lipid bilayers which may reduce lipid mobility by stabilizing the contacting lipid head groups [276, 277]. This effect likely reduced the probability of tail protrusions, further limiting the insertion of NPs into the defect-free bilayers. In contrast, suspended lipid bilayers require less compressive force for fusion [278] and consequently measurements on suspended DOPC bilayers have indicated particle insertion [197, 204]. While these suspended bilayers were also planar, the absence of a substrate allows for bilayer fluctuations, increasing the probability of lipid tail protrusions. Similarly, the experiments in Chapter 4 showed that NPs fused with lipid vesicles without allowing the passage of an impermeable membrane dye. This can be explained by the increased probability of tail fluctuations with increasing vesicle curvature due to larger amounts of exposed hydrophobic surface area [273]. The comparison between NP-bilayer fusion and vesicle-vesicle fusion is thus consistent with this study and previous experimental results, but future work will be necessary to fully establish that the kinetic barrier for NP insertion decreases in more fusogenic systems. In particular, a systematic study of curvature to

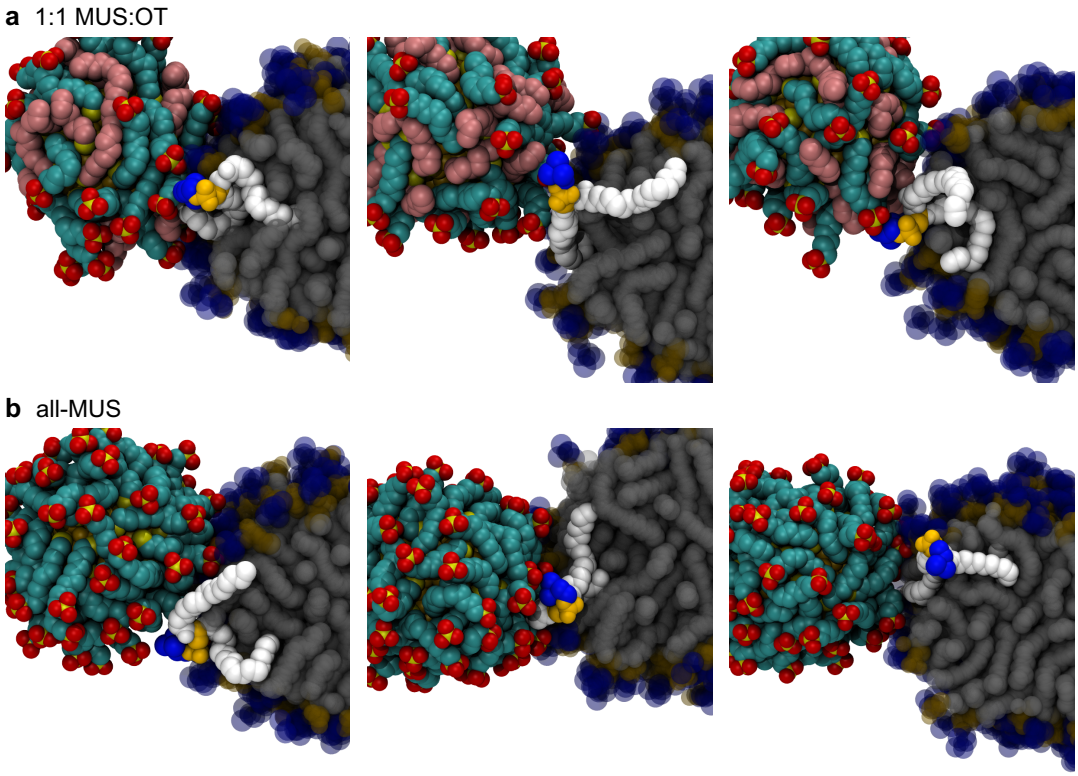

Figure 7-9: Additional snapshots of initial lipid contacts with NP monolayers. Snapshots are identified as possible members of the ensemble of transition states. Each snapshot was taken from a simulation trajectory generated during committor analysis that proceeded to commit to insertion.

identify protrusion likelihood between the two extremes represented by the ribbon model would be invaluable in determining the effect of curvature on NP insertion. Recent computational methods have been developed to facilitate such a study and will be employed in future work [262, 263].

7.6 Insertion driven by hydrophobic effect

The identification of the transition state for insertion as coinciding with the first hydrophobic contact between the NP monolayer and lipid tails implies that insertion is mediated by the hydrophobic effect, as would be expected based on the free energy calculations in Part I. To demonstrate that the driving force for insertion can be related to hydrophobicity, the hydrophobic solvent-accessible surface area (SASA) was calculated with the Gromacs tool *g_sas* using the method of Eisenhaber et al [279]. The SASA was measured using a probe radius of 0.14 nm as was also done in Part I.

Fig. 7-10a shows that the SASA of the NP significantly decreases upon insertion which leads to a decrease in the free energy penalty for hydrophobic solvation [162]. The SASA of the bilayer itself remains relatively unchanged during insertion, implying that it is NP properties that primarily drive insertion (Fig. 7-10b). The magnitude of the hydrophobic driving force is estimated from the SASA by multiplying by a phenomenological parameter $\gamma = 4.7$ kcal mol^{-1} nm^{-2} as in Chapter

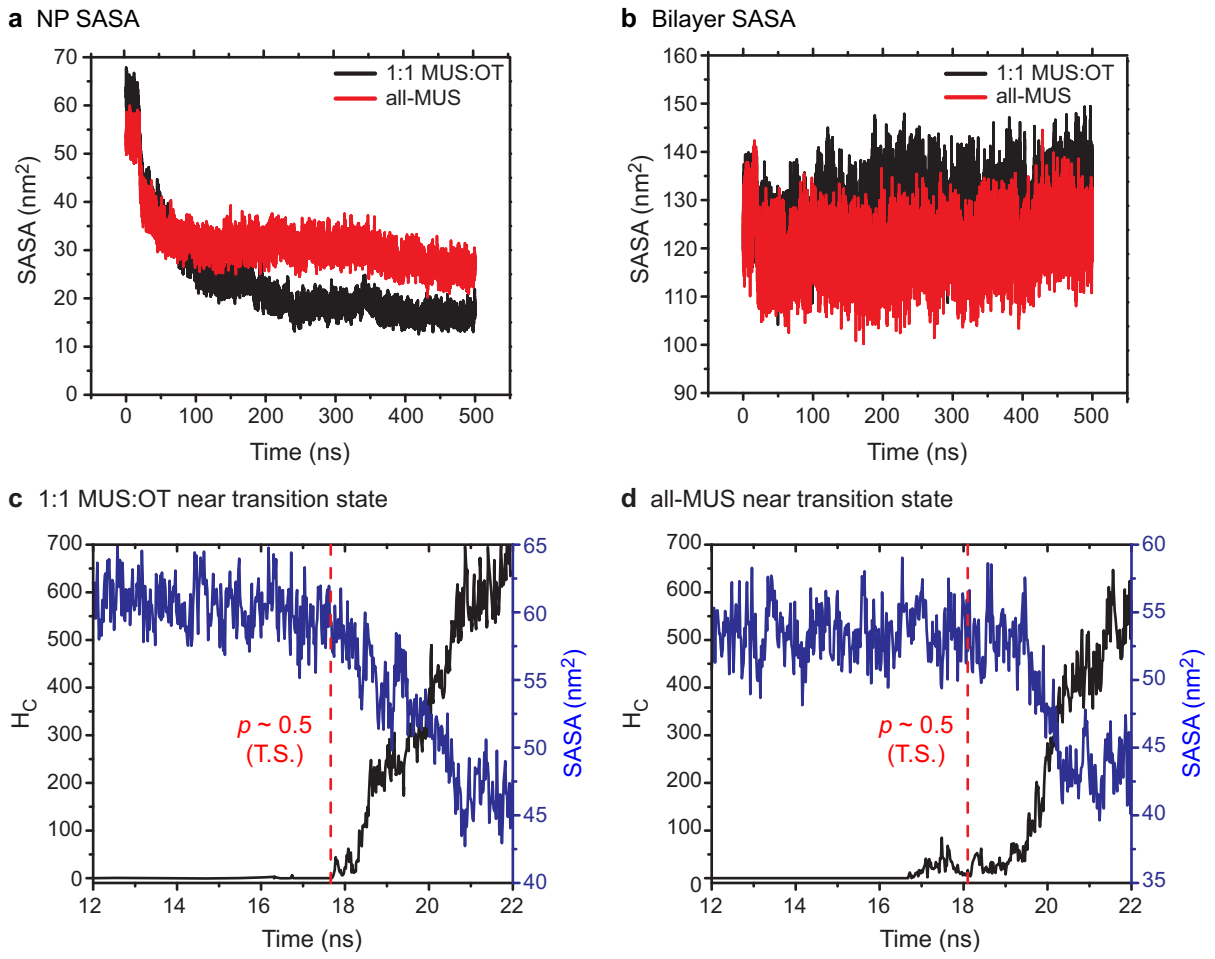

Figure 7-10: Hydrophobic solvent-accessible surface area of system during insertion. The SASA is decomposed into contributions from NP ligands **(a)** and bilayer **(b)**. The SASA for both the 1:1 MUS:OT **(c)** and all-MUS **(d)** NPs decreases significantly after passing the transition state (red dashed line) as the number of hydrophobic contacts simultaneously rises.

3, yielding upper bounds on the free energy change for hydrophobic solvation of -133.8 and -207.9 kcal mol^{-1} for the all-MUS and 1:1 MUS:OT particle respectively. These results indicate a strong hydrophobic driving force emerging primarily from NP properties alone. Fig. 7-10c and Fig. 7-10d further emphasize that the initial decrease in the SASA coincides with the transition state and with the increase in hydrophobic contacts between the bilayer and the NP. The SASA and H_C are shown for both the all-MUS and 1:1 MUS:OT particles over the 12-22 ns time period shown in Fig. 7-7. For both particles, the transition state occurs at the same time that H_C begins to rise and the SASA begins to decrease, indicating that the driving force for insertion is the hydrophobic effect.

The SLB experiments also suggest that NPs can diffuse into the middle of the bilayer, far from the defect points, due to the size of the perturbed domains in Fig. 3-5. Such diffusion is not observed over the time scale of the simulations with Δx reaching a plateau before 500 ns for both NP compositions. This plateau indicates that another energy barrier confines NPs near the defect

edge and is likely related to the cost for lipid rearrangement when re-creating the bilayer edge. To determine if there is a driving force for further insertion into the bilayer, we performed brief simulations with NPs fully embedded in the bilayer bulk. NPs were embedded in the bilayer by first creating a hole and then iteratively growing the NP into this void. Similar computational techniques are used to insert transmembrane proteins into bilayers [280]. A 2.0 nm all-MUS NP, 2.0 nm 1:1 MUS:OT NP, and 3.0 nm 1:1 MUS:OT NP were all embedded using this method and the average SASA was measured to estimate the driving force for diffusion from the edge-inserted state to the center of the bilayer. From these simulations, the driving force for further diffusion into the bilayer bulk was estimated as -22.1 kcal mol^{-1} for the 2.0 nm all-MUS NP and -107.7 kcal mol^{-1} for the 3.0 nm 1:1 MUS:OT NP. However, the SASA was unchanged upon further insertion of the 2.0 nm 1:1 MUS:OT NP. Inspection of the simulation snapshots at 500 ns (Fig. 7-3) indicates that unlike the all-MUS and larger MUS:OT NPs, the 2.0 nm MUS:OT NP has penetrated far enough into the bilayer that its edge has already been recreated. This particle has effectively penetrated into the bulk and further diffusion will likely occur but on a time scale longer than simulation times.

7.7 Proposed pathway for defect-mediated insertion

Based on these considerations, we propose a pathway for edge-defect mediated insertion of NPs into planar bilayers (Fig. 7-11). Simulation snapshots of 2.0 nm all-MUS particles illustrate the variety of states through which the system transitions. First, the NP begins in solution (a) before electrostatic attraction drives the particle to the bilayer edge in a metastable state (b). The system then transitions through a first transition state associated with the fluctuations of lipid tails (T.S. 1), with the magnitude of the energy barrier related to the fusogenic properties of the bilayer. Driven by the hydrophobic effect, the particle then transitions to a metastable state inserted into the bilayer edge (c) where the hydrophobic SASA has decreased. A second barrier associated with the re-creation of the bilayer edge (T.S. 2) must then be crossed before the NP can attain a minimum free energy state in the bulk of the bilayer (d). The magnitude of this barrier may also depend on NP properties; for example, the 2.0 nm 1:1 MUS:OT NP was observed to penetrate far enough into the bilayer that the edge reformed, implying a lower energy barrier for diffusion into the bulk as indicated by the dashed line in Fig. 7-11. Finally, while the experiments suggest that NPs insert at the defect edge then diffuse into the bulk as described in this pathway, it is also possible that previously embedded NPs may increase the probability of planar insertion in their vicinity by disrupting bilayer structure and enabling NPs to transition from state (a) to (d) directly. The effect of embedded NPs on bilayer structure will be the subject of Chapter 11.

The requirement of hydrophobic contact between both the lipid tails and hydrophobic material in the NP monolayer further suggests that monolayer properties should have a significant impact on the likelihood of insertion. The smaller number of successful insertions by all-MUS particles than MUS:OT particles observed in the simulations may be related to the lower probability that a lipid tail fluctuation contacts hydrophobic material in the all-MUS NP monolayer. It is likely that NP

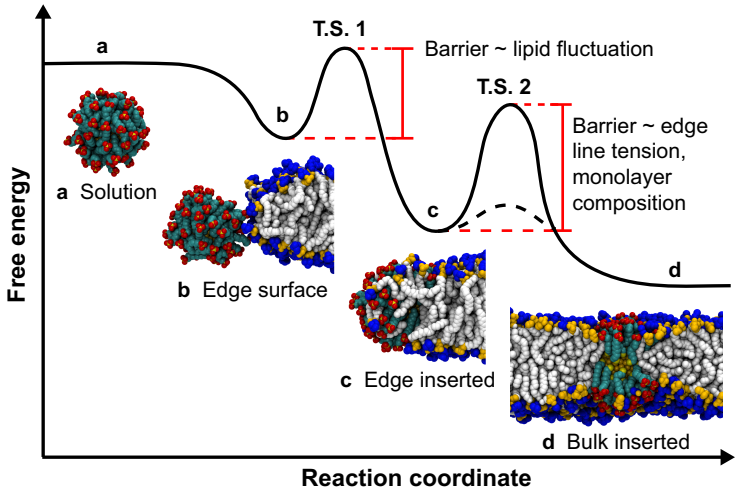

Figure 7-11: Schematic of proposed pathway for defect-mediated bilayer insertion of NPs. From solution, the NP proceeds through multiple metastable points illustrated by the simulation snapshots.

properties such as particle size, ligand composition, and ligand length also affect the probability of this hydrophobic contact. However, the key observation that lipid tail protrusions initiate insertion by contacting hydrophobic alkanethiol backbones for both all-MUS and MUS:OT NPs indicates that this behavior may be general to a wide variety of monolayer compositions as this general chemical motif is prominent in a number of NP systems [83, 30, 202, 281, 282, 16]. Moreover, the strong agreement with experimental results that used polydisperse particle batches with a larger mean core size than used in simulations implies that the pathway is similar for a range of particle core diameters. We thus hypothesize that this pathway may occur for a wide variety of NP systems other than the ones studied here.

7.8 Conclusions

In this Chapter, we show using unbiased atomistic molecular dynamics simulations that NPs can spontaneously fuse with lipid bilayers on short, nanosecond timescales in the presence of large bilayer defects. Fusion was observed for both all-MUS and 1:1 MUS:OT NPs, with the extent of the eventual penetration of the NP into the bilayer bulk dependent on the NP composition. Experiments on supported lipid bilayers further confirmed this result by showing preferential interactions between NPs and the edge of large bilayer defects, but no interactions for perfectly planar bilayers. Using committor analysis, we further showed that the distinct behavior between NPs encountering the bilayer edge or planar face can be explained by the much higher likelihood that NPs will contact lipid tail protrusions at the highly curved defect edge. Such protrusions appear rarely on planar interfaces and were found to be necessary to trigger NP insertion.

The pathway for NP-bilayer fusion identified in this Chapter thus complements the previous findings from Part I by showing one potential mechanism by which NPs can achieve a transmem-

brane state. The strong similarity of the NP-bilayer fusion process to the pre-stalk transition state for vesicle-vesicle fusion may allow these NPs to be used to probe the properties of fusogenic systems, and furthermore may suggest that these NPs present new opportunities for devising novel strategies for endosomal escape, drug delivery, and controlled biodistribution, all important research avenues for enhancing treatments based on nanomedicine. In particular, the protrusion-mediated insertion process may imply that the NPs would be particularly active at regions of the body where vesicle fusion occurs frequently, such as neural synapses. Identifying the enhancement of NP-bilayer fusion in such systems will be a focus of future work. It is important to emphasize that defect-mediated insertion may not explain the incorporation of NPs into vesicles and cells as these processes occur without dye leakage as discussed in the Introduction and Chapter 4. However, the identification of protrusions as necessary to trigger insertion may indicate that over long timescales protrusion-mediated insertion occurs even in the absence of defects, as will be explored in the following Chapters. The key finding of this work is thus the identification of lipid protrusion contact as the onset of NP-bilayer fusion.

THIS PAGE INTENTIONALLY LEFT BLANK

Chapter 8

Analysis of Lipid Protrusions in Planar Bilayers

In the previous Chapter, we showed that NPs can spontaneously and rapidly insert into bilayers containing large defects by contacting protruding lipid tails that appear at the defect edge. Both experiments and simulations suggest that similar insertion does not occur into planar bilayers, likely because the rate of protrusions occurring is low. However, the experiments in Chapter 4 clearly indicate that in bilayer systems that have some fluctuations or curvature, such as vesicles or non-supported planar bilayers, NPs can insert over sufficiently long timescales. In support of the protrusion-mediated insertion mechanism, then, the question is whether protrusions do occur in planar bilayers and with what frequency. Moreover, it is also an open question as to how bilayer properties might influence the rate of protrusion occurrence in order to design NPs to target specific bilayer components.

In this Chapter, we present analysis of protrusion likelihood in planar bilayers of differing composition. We first show that protrusions do appear with a low frequency that depends on the bilayer composition and temperature. Protrusions can be categorized into two different modes based on the identify of the protruding atom. We next analyze the thermodynamics of inducing a protrusion by computing the potential of mean force (PMF) for the process. We show that the thermodynamic barrier for protrusions is nearly identical independent of protrusion type or lipid composition, suggesting that differences in protrusion frequency rely solely on kinetic effects. Finally, we compare the PMFs for protrusions to those of related lipid deformations, such as lipid flip-flop and lipid desorption, in order to establish the likelihood of this process. These findings shine significant physical insight into the likelihood of observing spontaneous protrusions in planar homogeneous bilayers which has applications in understanding the rate-limiting step in both vesicle-vesicle fusion and NP-bilayer fusion.

8.1 Simulation systems

All systems simulated were modeled using the GROMOS 54a7 force field using the parameters in Appendix D. The only difference in parameters was the use of a semiisotropic rather than anisotropic barostat as the bilayers were prepared to span the entire x-y plane of the box. Five different lipid bilayers - DLPC, DMPC, DPPC, POPC, and DOPC - were constructed by extracting 64 lipids from the 128 lipid pre-equilibrated bilayers provided by Poger et al [283]. All five lipid species have zwitterionic phosphatidylcholine head groups and differ only in the number and saturation of carbon atoms in the tail groups. The 64 lipids were resolvated to a solvation level of 50-60 water molecules per lipid then equilibrated for 100 ns. Fig. 8-1 shows the structures of the different lipid species simulated and Table 8.1 summarizes each of the relevant simulation systems. One system, DOPC, was prepared twice, once at 300 K and once at 323 K. All simulations were performed using

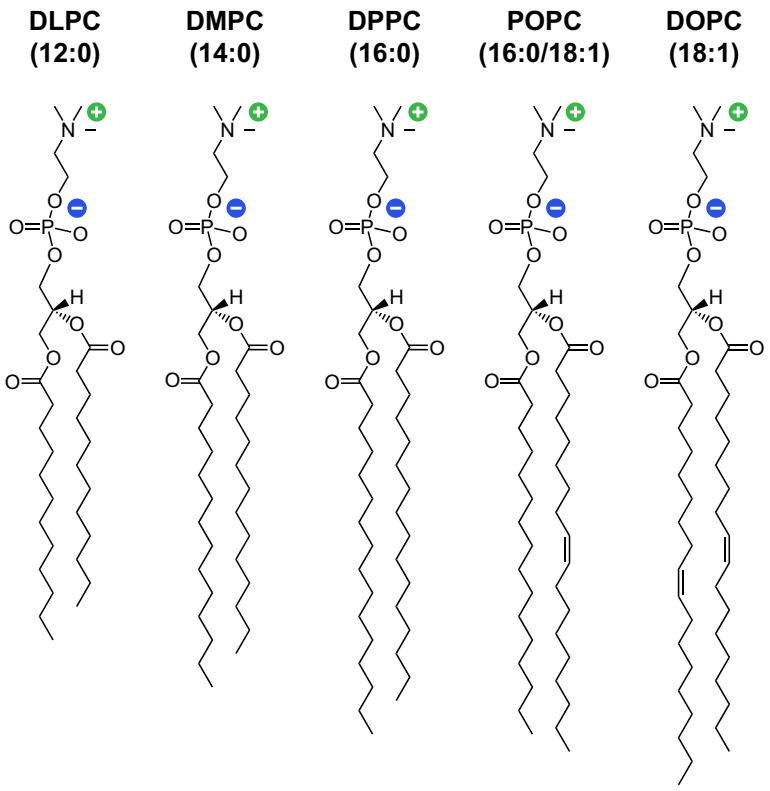

Figure 8-1: Chemical structures of five different lipid species simulated. Names are written both as common abbreviations and as ratio of number alkyl groups per chain:number of double bonds.

Gromacs version 4.6.1 [246].

Table 8.1: Summary of simulation systems

Lipid type	**Lipids**	**Water**	**Atoms**	**Temp. [K]**	**Expt. melting temp. [K]**	**Area per lipid [nm^2]**	**Bilayer thickness [nm]**	**U.S. windows**
DLPC	64	3,983	14,637	323	271	0.659	2.84	20
DMPC	64	3,650	13,894	323	297	0.655	3.19	23
DPPC	64	3,849	14,747	323	314	0.633	3.45	26
POPC	64	3,443	13,657	323	271	0.654	3.69	26
DOPC	64	3,959	15,333	323	256	0.676	3.64	26
DOPC	64	3,959	15,333	300	256	0.674	3.66	26

8.2 Unbiased protrusion frequency

As a first test in determining the likelihood of observing protrusions, all bilayers were simulated for 200 ns and protrusion events were recorded. Two simulations were run from different initial conditions for each bilayer type. A protrusion was defined by any hydrophobic atom in a lipid

tail extending more than a threshold distance, d_p, beyond the lipid's phosphorus atom. d_p is schematically illustrated in Fig. 8-4. A similar definition was previously used by Kasson et al. in their analysis of protrusions relevant to vesicle-vesicle fusion [259, 284]. To obtain only the protrusion frequency, an event was only counted if the same atom was not protruding in the previous simulation snapshot. Snapshots were recorded every 20 ps.

Fig. 8-2 shows the fraction of total protrusions for each of the different atoms in the two lipid tails for a DOPC lipid at 300 K. Fig. 8-1a illustrates the numbering scheme used to categorize the bead IDs in Fig. 8-2b. There is a general trend of two peaks in the protrusion frequency. The first peak, corresponding to the atoms most likely protrude, occurs for atoms near the glycerol group in either lipid tail. These atoms are closest to the lipid-water interface. The probability of protruding then decreases with increasing distance from this interface until increasing again for a second peak for atoms near the ends of the lipid tails, with the last atom in the tail having the highest protrusion frequency. The two peaks can thus be used to designate two types of protrusions - "elbow" protrusions, where atoms near the head group protrude into water, and "splay" protrusions, where atoms near the end of the tails protrude by distorting the entire tail conformation. The dashed vertical line in Fig. 8-2b separates the two modes and is defined by the position of the minimum in protrusion likelihood as function of bead ID. Fig. 8-2c shows snapshots identifying both protrusion types. It should be noted that there may be a functional difference between the two different protrusion modes. For example, in previous unbiased simulations by Kasson et al, vesicle fusion was triggered by contact between two "elbow" snapshots (see Fig. 4 in Ref. [259]). However, in multiple related studies, fusion was induced by only a single "splay" protrusion that spanned the solvent region between two apposed vesicles [258, 257, 261]. Both protrusion modes are thus implicated in fusion processes, although it is possible that splay protrusions are more likely to induce fusion. Finally, note that protrusions of both types are observed to initiate insertion of NPs in Chapter 7 (Fig. 7-9).

To compare protrusion frequencies between different lipids, Fig. 8-3a shows the overall protrusion frequency per lipid in terms of the number of unique protrusions per lipid per nanosecond. The protrusion frequency is shown for three increasing values of d_p, representing protrusions extending farther into the solvent-rich head group region. The unbiased results show first that protrusions in general are rare events, occurring over $\approx$100 ns time scales independent of lipid type for even the smallest threshold value for identification. In comparing the lipid types, it is apparent that the higher temperature DOPC bilayer has a larger frequency than the lower temperature system, reflecting additional thermal energy to drive protrusions. POPC also consistently exhibits the fewest protrusions of the high-temperature systems. Lipids with asymmetric tails are known to inhibit fusion, so this observation may be consistent with previous experimental findings [285, 257]. However, notably there are no large differences between any of the same-temperature lipid species for any value of d_p, nor is there any noticeable trend that maps to lipid properties in Table 8.1 or to structural properties such as tail saturation. The results thus appear to indicate that protrusions occur with nearly the same frequency independent of lipid choice.

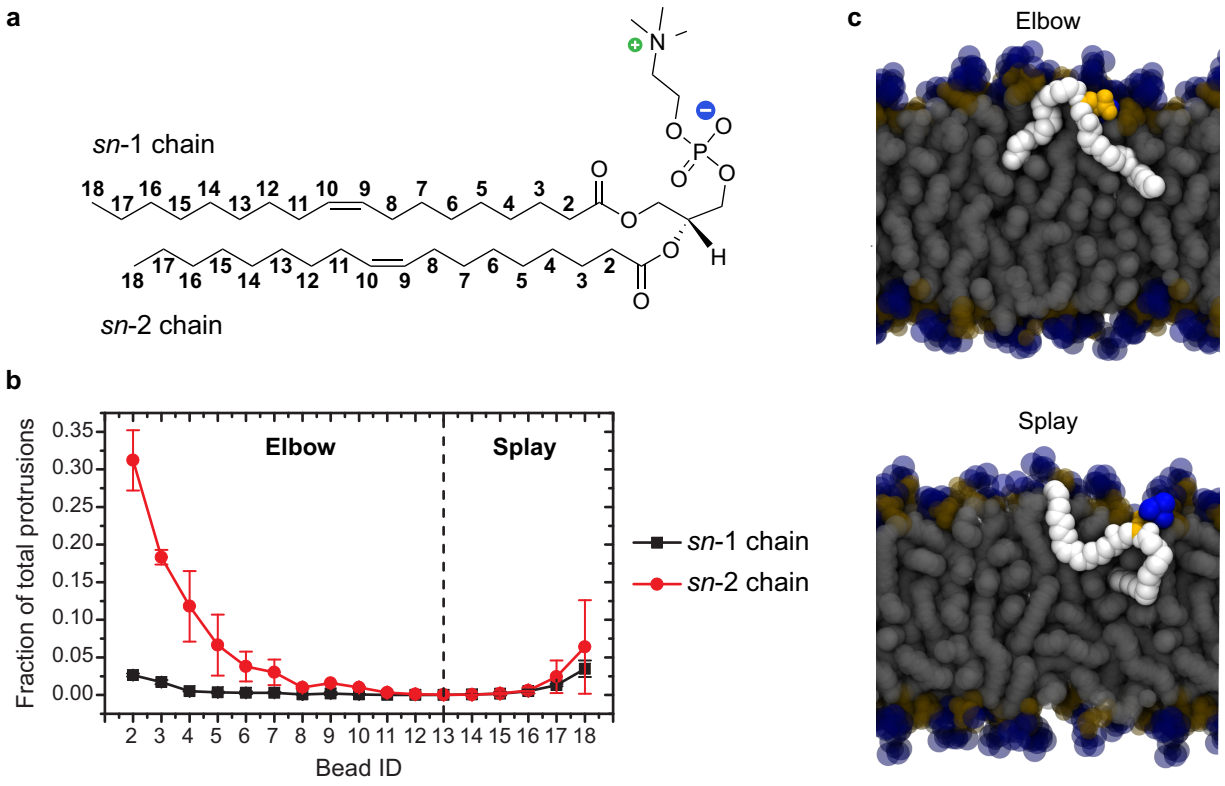

Figure 8-2: Relative protrusion occurrence for different tail beads. **a** Numbering scheme for the two lipid tails used to identify different tail beads. **b** Relative protrusion frequency for each bead ID, expressed as a fraction of the total number of protrusions. **c** Representative snapshots of "elbow" and "splay" protrusions identified from the ID of the protruding bead.

Fig. 8-3b shows the fraction of total protrusions that can be classified as elbow protrusions for different values of d_p. The results show that as the protrusion threshold increases the relative propensity for splay protrusions increases for all lipids studied. This finding indicates that splay protrusions are more likely to reach farther into solvent which may explain the reason that this protrusion mode is more commonly implicated in vesicle fusion by crossing the thin solvent region between two nearby vesicles.

8.3 Potential of mean force for protrusions

To explain the trends observed in the unbiased protrusion measurements, the potential of mean force (PMF) was measured for a variety of different protruding beads and lipid species using the weighted-histogram analysis method as described in Appendix A. The reaction coordinate for umbrella sampling was defined as the distance of the pulled bead from the center-of-mass (COM) of the bilayer projected onto the membrane normal (i.e. the z-axis). Umbrella sampling windows for all bilayers were spaced by 0.1 nm with the number of windows chosen based on the thickness of the bilayer (see Table 8.1). For each umbrella sampling window, a single united atom bead in

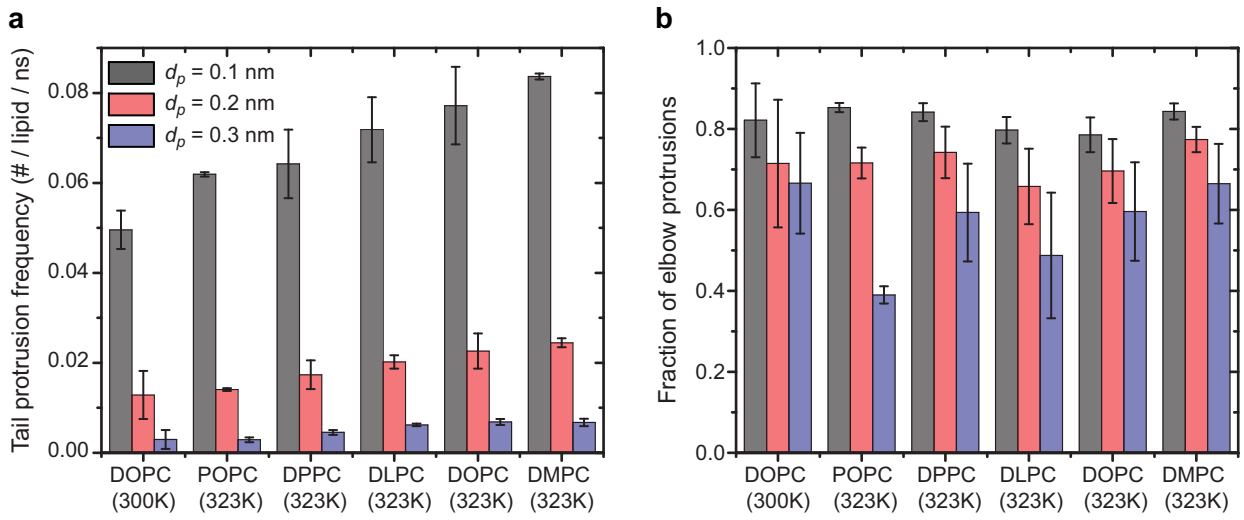

Figure 8-3: Unbiased protrusion frequencies for several lipid compositions. **a** Protrusion frequency for three different identification thresholds, d_p. **b** Relative fraction of elbow protrusions as a function of protrusion threshold.

a chosen lipid tail was first pulled away from the bilayer COM for 2 ns by applying a harmonic potential between the bead's initial position and the desired position with a spring constant of 500 kJ/mol/nm^2. The spring constant was then increased to 3000 kJ/mol/nm^2 for another 2 ns of equilibration (with a Berendsen barostat) before another 70 ns of umbrella sampling was performed with the same spring constant and a Parrinello-Rahman barostat. All atoms of the lipid being pulled were excluded from the bilayer COM calculation.

To increase sampling without additional computational expense, two lipid protrusions were induced simultaneously by pulling on atoms in both monolayers simultaneously. A similar method has been used previously in the study of lipid flip-flop and lipid desorption [286, 287]. The two lipids were chosen to be spaced apart by at least 3 nm in-plane to minimize any possible lipid-lipid interactions. Finally, to minimize the overall bilayer disruption, the two different atoms were pulled to different positions such that the sum of the distances to which both beads were pulled was a constant. Fig. 8-4 illustrates the pulling workflow by illustrating the two beads that are pulled simultaneously and how the separation between the two atoms is always maintained. After the completion of umbrella sampling, the PMF was calculated using the program *g_wham* with 201 bins [288]. The use of the two-lipid umbrella sampling methodology allowed two uncorrelated PMFs to be generated simultaneously; all plots in the results are the average of both PMFs with corresponding error bars.

Fig. 8-5 first shows the PMF for pulling atoms in DOPC at 300 K. Fig. 8-5a is the PMF for pulling on the last bead in the *sn*1 tail, which tends to reside at equilibrium in the center of the bilayer. The PMF is graphed on the same axes as the electron densities of the unperturbed system, which illustrate the distribution of lipid tails, water, and the phosphate atoms in the system. The dashed vertical lines indicates the maximum of the phosphate density ($d_p = 0$) to

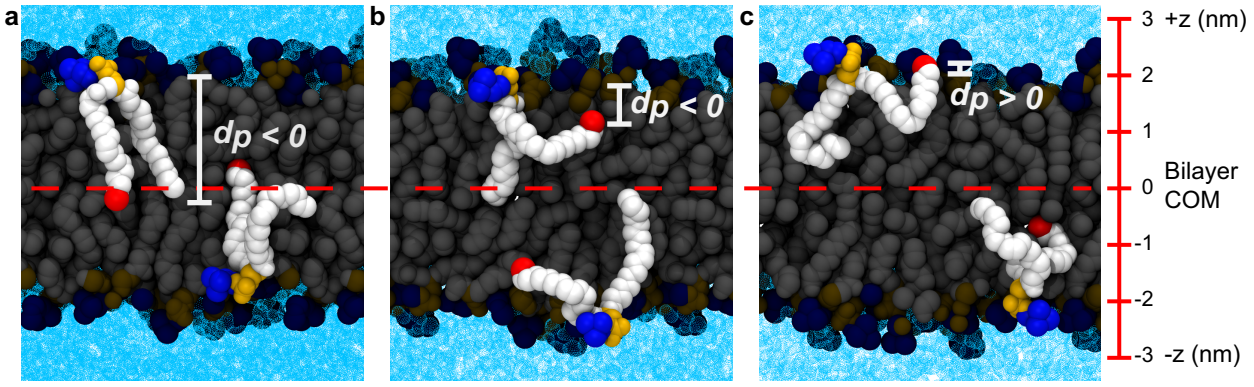

Figure 8-4: Simulation snapshots illustrating protrusion workflow for a DOPC bilayer. Single atoms in two lipids in opposite monolayers are pulled simultaneously. Pulled atoms are shown in red; the remainder of each pulled lipid is shown using a space-filling view. Lipid tails are in white, phosphate groups in yellow, choline groups in blue, and water in cyan. The dashed line indicates the COM of the bilayer and distances along the z-axis are indicated. **a** Equilibrated bilayer with no constraints on target atoms. **b** Top lipid atom pulled to 1.3 nm, bottom to 1.2 nm. **c** Top lipid pulled to 2.0 nm, bottom to 0.5 nm.

guide comparisons to the thresholds set in the previous section. The plot shows two regimes – the PMF first increases linearly until the lipid tail density peaks, at which point the slope of the PMF sharply increases. This distance coincides with the head group region of the bilayer where the water density begins to increase, suggesting that water contact in this interfacial region is the primary barrier to protrusions. Fig. 8-5b shows PMFs for pulling on four different beads in the *sn*1 tail. Matching expectations from Fig. 8-2, the beads near the glycerol group and tail end had the lowest free energy barrier for reaching the water-lipid interface (dashed vertical line), corresponding to the elbow and splay modes respectively. The barrier for both the elbow and splay protrusions is nearly identical suggesting that water contact is the main contributor to the PMF as this does not depend on the location of the bead in the lipid tail.

Fig. 8-6 shows PMFs for inducing splay protrusions in each of the different lipid species. The distance is rescaled to be the distance between the pulled bead and the maximum of the phosphate peak in each bilayer to account for variations in bilayer thickness. The dashed vertical lines again indicate $d_p = 0$ to match the lines in Fig. 8-5. Fig. 8-6a first shows a comparison between the three different saturated lipids. The PMFs have nearly identical slopes and magnitudes at the phosphate interface, indicating that the length of the lipid tail does not thermodynamically affect protrusion likelihood. Fig. 8-6b compares PMFs between unsaturated lipids tails (DOPC and POPC) with saturated lipid tails (DPPC and POPC) of the same length. Again, regardless of lipid species the PMFs appear identical, although the unsaturated lipids have a slightly lower protrusion barrier. These results are consistent with the observed unbiased protrusion frequencies, with the similarity in the PMFs reflecting the similarity in observed protrusion frequencies independent of lipid type.

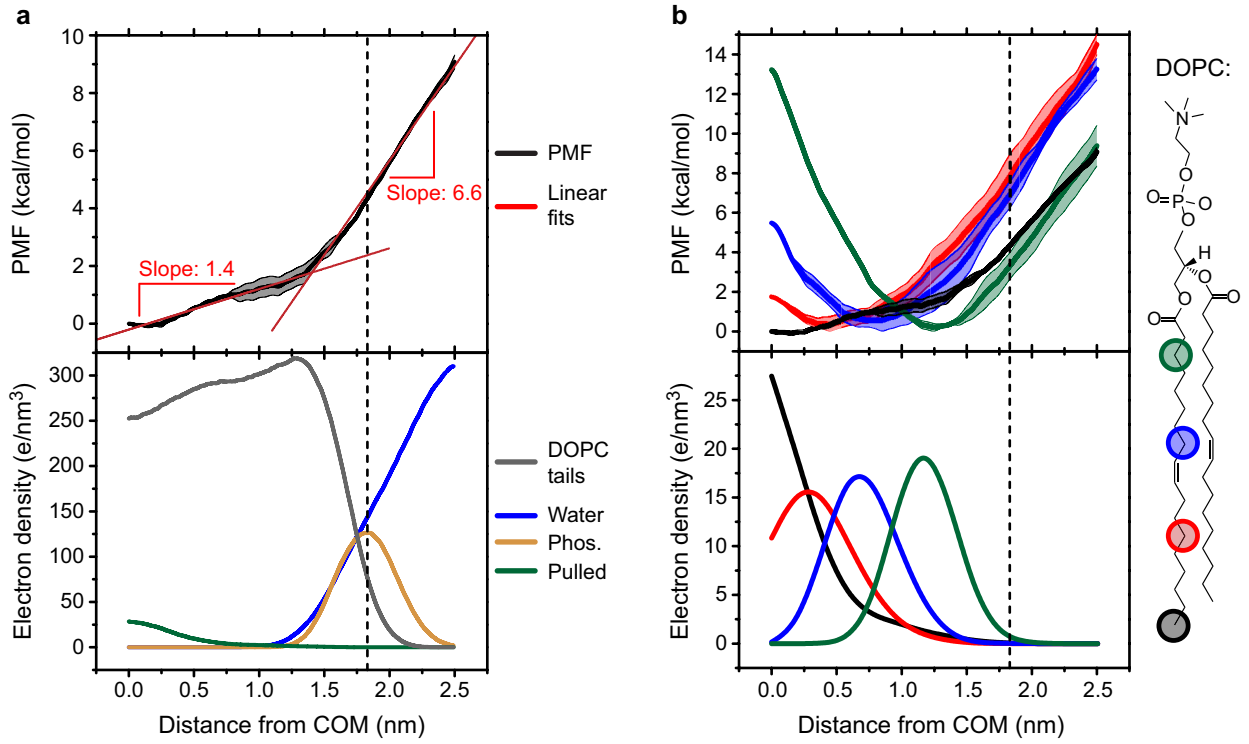

Figure 8-5: PMFs for DOPC protrusions. **a** Comparison of PMF for inducing splay-protrusion to electron densities of key system components. **b** Comparison of PMFs for inducing protrusions from different tail beads

8.4 Conclusions

The results from the unbiased simulations and PMF workflows combined indicate that the protrusions do happen at a measurable, although low, frequency in planar bilayers. The results also show that the exact choice of lipid composition seems to be less important than the protrusion mode, with splay protrusions becoming more likely to be observed farther from the bilayer-water interface.

From the PMF, the free energy cost for inducing protrusions to the NP-bilayer interface is approximately 5 kcal/mol, or 8.4 kT at 300K, and the barrier grows with a slope of 6.6 kcal/mol/nm or 11.1 kT/nm. The total cost for a protrusion is on the order of 10 kT for a protrusion to be accessible in the surrounding aqueous solvent. While this represents a reasonable free energy barrier, it is comparable to other related membrane processes that occur over similar timescales as experiments on NP-bilayer fusion. From atomistic molecular dynamics simulations on similar lipid systems the barrier for water crossing a membrane has been estimated as 7.8 - 11.7 kT depending on the lipid species [289], the cost for opening a membrane pore is approximately 17.6 to 31.2 kT [290], lipid flip-flop has a barrier of approximately 31.2 to 37 kT [286, 287], and cholesterol flip-flop has a barrier of approximately 7.0 to 16.0 kT [291, 292]. Compared to these similar processes, it is apparent that the barrier for observing a protrusion is sufficiently low that they would be expected

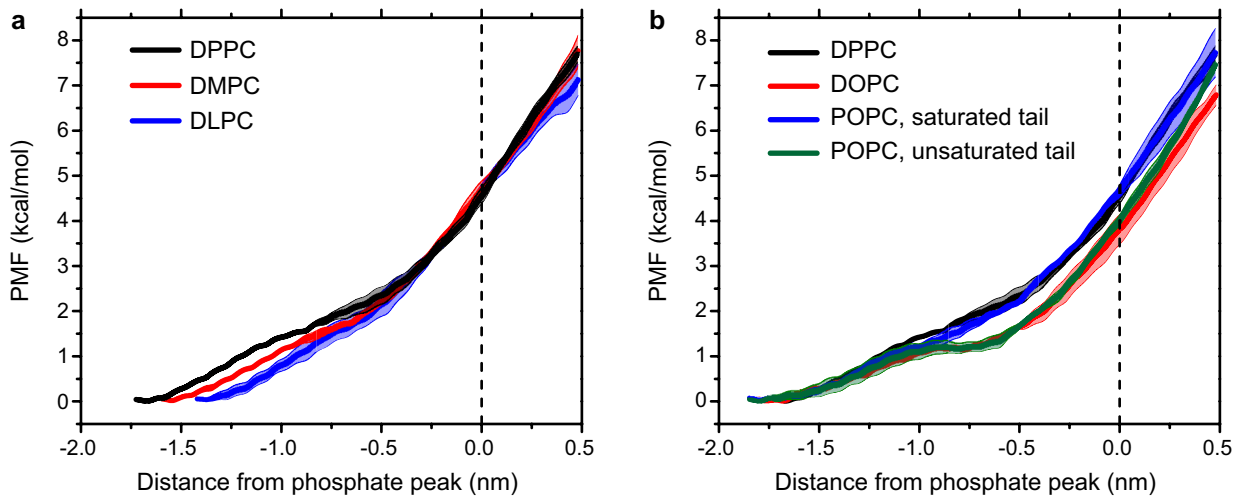

Figure 8-6: PMFs for splay protrusions from different lipids. **a** PMFs for saturated lipids. **b** PMF comparison between unsaturated and saturated lipids, including the asymmetric lipid POPC.

to appear with reasonable frequency over experimental timescales even in the absence of defects studied in Chapter 7, barring any other constraints (e.g. the presence of a supporting substrate).

Chapter 9

Lipid Protrusions Mediate Insertion into Planar Bilayers

In the previous two Chapters, we found that contact with lipid tail protrusions initiates the insertion of NPs into bilayers with large defects (Chapter 7), and we also found that similar protrusions can occur in planar bilayers over sufficiently long timescales (Chapter 8). In this Chapter, we combine these findings to show that if a NP contacts a lipid protrusion along the planar face of a bilayer the NP can rapidly fuse without additional bias. Insertion is facilitated by hydrophobic ligands that extend into the bilayer while hydrophilic end groups snorkel to the aqueous interface following a similar pathway to that shown in Chapter 7. This observation confirms that contact with lipid protrusions is at least one possible pathway for NP insertion into defect-free lipid structures. We further show that NPs with longer hydrophobic ligands can engage in a second pathway by first anchoring to the membrane without insertion before protrusions spontaneously occur over a shorter time scale than expected in an unperturbed bilayer. Finally, we propose that after inserting into one monolayer, charged ligands can "flip" to the distal monolayer following a similar pathway as spontaneous ion permeation. This Chapter suggests a full kinetic pathway for NP-bilayer fusion that does not involve bilayer disruption, consistent with previous experimental results.

9.1 Workflow for induced NP-protrusion contact

Given the unlikelihood of observing spontaneous protrusions as shown in Chapter 8, a multiple step workflow was performed to achieve NP-protrusion contact with minimal bias. All simulations were conducted with 2.0 core diameter NPs (using the parameterization of Chapter 6) and the same DOPC bilayer ribbons used in Chapter 7. It was found that the free boundary of the ribbon was necessary to observe insertion as discussed below. Two NP compositions were investigated - 1:1 MUS:OT, as in Chapter 7, and 1:1 MUS:HDT, where HDT (heptadecanethiol) is a 17-carbon hydrophobic ligand previously studied in Chapter 6.

Protrusions were induced in the top monolayer of the ribbon by pulling 3 different lipid tail atoms along the z-axis to a distance of 0.3 nm beyond the plane formed by the phosphorus atoms in the upper monolayer. Pulling was achieved by applying an umbrella potential to the desired atoms with a force constant of 500 kJ/mol/nm^2. The last atom in the *sn*1 tail of each lipid was selected in order to induce a protrusion in a "splay" configuration (as defined in Chapter 8) similar to what has been previously implicated in driving vesicle fusion [258, 257, 261]. The lipids were chosen to be spatially separated in the top monolayer to prevent interactions between protrusions. Fig. 9-1a shows snapshots of the three protruding lipid tails from the top and side. To prevent curvature from being induced in the ribbon due to the applied pulling force, the phosphorus atoms of all of the DOPC lipids in the bottom monolayer were constrained to prevent motion in the z-direction. With the pulling potential still enforced to prevent protrusions from relaxing, a pre-equilibrated NP and

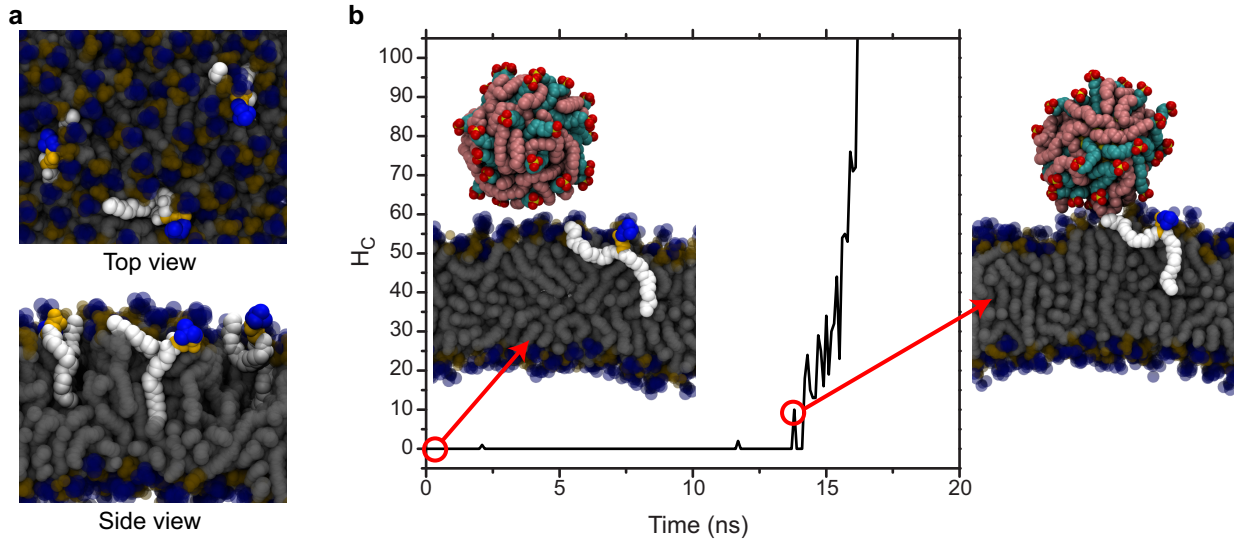

Figure 9-1: Workflow for inducing NP-protrusion contact. Snapshots are shown for 1:1 MUS:HDT NP. **a** Three protrusions were pulled to a distance of 0.3 nm above the plane of phosphorus atoms by applying an umbrella potential. Snapshots illustrate their in-plane separation and the extent of pulling. **b** Searching simulations were launched from a NP initially positioned above the bilayer and were monitored for NP-protrusion contact by measuring H_C as a function of time. The configuration corresponding to initial NP-protrusion contact (circled with snapshot) was extracted as a starting point for probing simulations.

counterions were introduced near the bilayer surface and allowed to diffuse freely for 40 ns. The total size of the system after adding the NP was 400 lipids, 47,974 water molecules, 167 Na^+ ions, and 138 Cl^- ions. During these "searching" trajectories, the number of hydrophobic contacts, H_C, between any protruding lipid tail and the NP monolayer was monitored. A hydrophobic contact was defined as two hydrophobic atoms within 0.5 nm of each other. Six searching simulations were run for each of the two NP compositions.

During the searching simulations, the NP diffused along the bilayer surface and occasionally encountered the protruding lipid tails, leading to increases in the calculated value of H_C. Fig. 9-1b shows the time evolution of H_C during an example searching simulation starting from the configuration shown in the snapshot. H_C stays near zero as the NP traverses the surface until eventually encountering a protrusion where H_C rapidly increases. The circled value indicates an example configuration with contact between the NP and the protrusion. Notably, all searching simulations that led to initial NP-protrusion contact eventually led to insertion (as shown by the large increase in H_C for Fig. 9-1b), indicating that if a protrusion is continuously forced NP insertion occurs readily. From these simulations, four configurations where the NP was in contact with a protrusion were extracted for each NP composition with varying values of H_C. The outcome of the searching simulations was thus a set of system configurations where a single lipid protrusion was in contact with the NP.

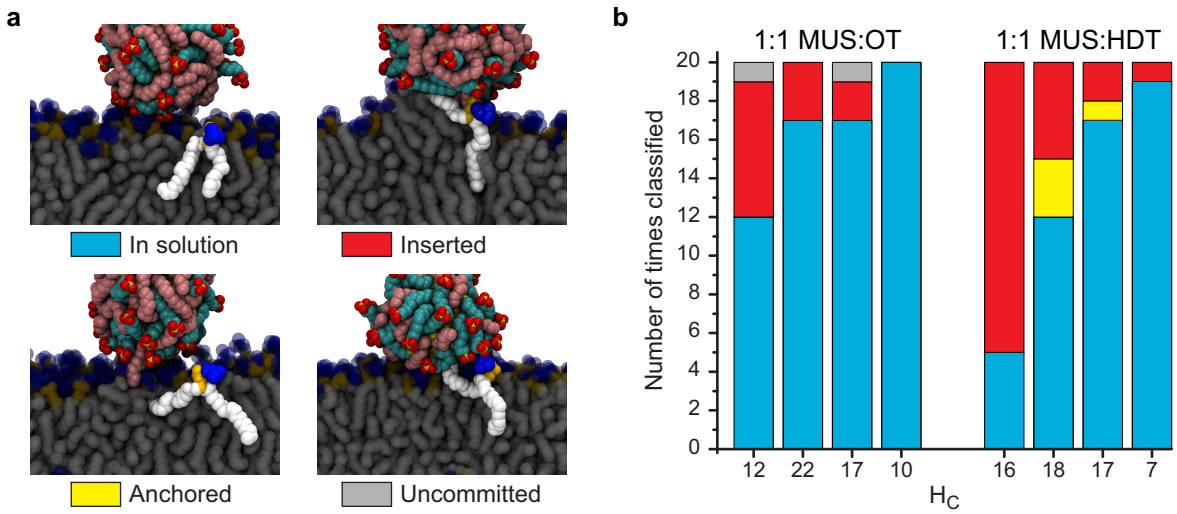

Figure 9-2: Summary of probing trajectories. **a** Snapshots of four different behaviors identified in the text. **b** Number of probing trajectories sorted into each of the four behaviors. Starting configurations are labeled with the initial value of H_C between the NP and protrusion and ordered by the number of observed insertion events.

9.2 Insertion probability for different NPs

For each of the configurations extracted from the searching trajectories, 20 short "probing" simulations were launched. Prior to each probing trajectory, the velocities of all particles were re-sampled from a Boltzmann distribution at 310 K then the simulations were run with all constraints on the system removed with the exception of restraints on two lipid head groups in the bottom monolayer to prevent the ribbon from rotating. After 5 ns, a probing trajectory was classified into one of four categories based on the value of H_C and visual inspection of the final configuration. Fig. 9-2a shows snapshots indicating the four different behaviors with the initially-protruding lipid highlighted in each one. If H_C dropped to zero, the NP was classified as "in solution" due to the relaxation of the protrusion without insertion occurring. If $H_C > 100$, the NP was classified as "inserted" as the rapid rise in H_C indicated the onset of further insertion. The snapshot illustrates that this rise in H_C occurs as lipid tails begin to form a stalk-like intermediate. For $0 < H_C < 100$, two possibilities were found. First, the NP could be "anchored", in which case the protrusion relaxed back into the bilayer bulk but a hydrophobic ligand from the NP remained in contact with the bilayer core, albeit not necessarily in contact with the originally protruding lipid. This behavior was only identified for the MUS:HDT NPs. Second, the NP could still be "uncommitted", in which case the protrusion did not relax over the 5 ns time scale and the protrusion remained in contact with the NP. All uncommitted trajectories were extended an additional 5 ns to see if the protrusion relaxed, and if not were then classified as uncommitted.

Fig. 9-2b shows a comparison of the relative frequency for each of these states for each of the four starting points of both NPs. The plot is color-coded according to the labels in Fig. 9-2a. It is clear that the MUS:HDT NP on average records much more frequent insertion events,

potentially reflecting the stronger hydrophobic driving force due to the greater SASA of the long ligands. The anchoring behavior is also only observed for the MUS:HDT NPs. However,there is no apparent correlation between the initial value of H_C and eventual insertion frequency as both MUS:OT and MUS:HDT NPs were selected to have similar amounts of hydrophobic contact yet show very different insertion frequencies. Moreover, changing H_C for a particle NP type did not correlate with the number of insertion events. It is possible that this merely reflects poor averaging as only 20 trajectories were run given the computational expense of these simulations. There may be some dependence on H_C as the configuration with the smallest H_C for both NPs led to the lowest insertion probability, which would reflect a weak initial "bond" to the hydrophobic core.

9.3 Unbiased insertion occurs following protrusion contact

From the set of probing trajectories that led to insertion, three trajectories were selected for each NP composition and continued to 400 ns to ascertain the insertion pathway. Each of the extended trajectories were selected from probing trajectories that originated from different extracted frames. Similarly, one trajectory for each NP was launched for 400 ns as a control with the NP introduced above a bilayer with no induced protrusion. As in the probing simulations, all of these extended simulations were run without any additional bias.

Fig. 9-3a shows the solvent-accessible surface area (SASA) of the NP as a function of time for the first 150 ns of two trajectories for each NP composition. In Chapter 3 and 5 the reduction of the SASA was shown to drive NP insertion, a result confirmed in Chapter 7. Fig. 9-3 generalizes this result to the planar geometry. Starting from the time of first contact with the protrusion (at 0 ns), the SASA rapidly and monotonically decreases for both NP types before beginning to plateau after 150 ns. For comparison, the dashed horizontal lines indicate the average values of the SASA for both NPs over the last 100 ns of the 400 ns trajectories. The decrease in the SASA confirms the strong hydrophobic driving force for insertion with the greater decrease for the MUS:HDT NPs perhaps explaining the higher probability of insertion shown in Fig. 9-2.

Fig. 9-3 also shows representative snapshots of both NPs during the initial insertion. At 5 ns, both NPs have minimal hydrophobic contact with lipid tails, reflected in the small decrease in the SASA. The MUS:HDT NP however has already extended some hydrophobic ligands into the core region. By 25 ns, both NPs have begun to insert into the top monolayer of the bilayer, triggering the generation of significant bilayer curvature as volume in only one of the two monolayers is excluded. The need to generate curvature may also explain why insertion was not observed experimentally in planar supported bilayers in Chapter 7, as the presence of the substrate would inhibit curvature generation. As the NP continues to insert into the bilayer, the hydrophobic ligands begin to extend farther into the bilayer for both NPs. By 150 ns, the curvature has begun to relax as the NP fully inserts into the top monolayer and the extended ligands anchor the NP to the bottom monolayer as well. There is still no evidence of charged ligands crossing the bilayer as they instead continue to snorkel to the original aqueous interface. By 150 ns, the necessity to maintain this charge solvation

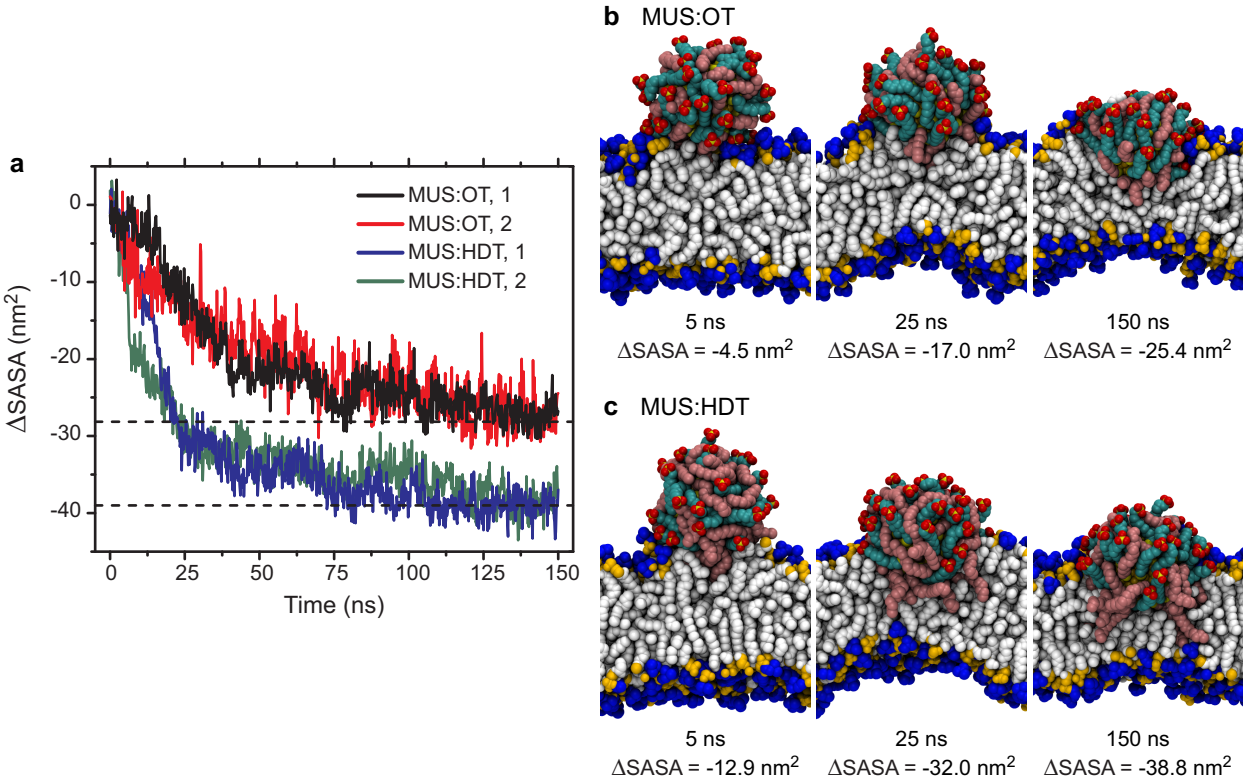

Figure 9-3: Features of initial insertion for both NP compositions. **a** SASA as a function of time for both NP compositions over first 150 ns after NP-protrusion contact. The dashed horizontal lines indicate the average value of the SASA between 300-400 ns for both NP compositions. **b** Representative snapshots of MUS:OT insertion with corresponding SASA changes. **c** Representative snapshots of MUS:HDT insertion with corresponding SASA changes.

leads to a significant strain on the ligands that are grafted to positions farthest from the interface. The sequence of snapshots thus illustrates that insertion occurs rapidly, generates transient bilayer curvature, and ends with the NPs partially inserted into the bilayer but with all charged end groups still trapped on one side of the bilayer in a highly strained configuration.

For comparison with the SASA results in Fig. 9-3, the distance between the NP center of mass and the center of mass of lipids within a cylinder passing through the NP center of mass along the z-axis was calculated. The cylinder had a radius of 2.0 nm but the center of mass of the lipids was only determined for lipids at least 1.0 nm away from the center of the cylinder. The need for an outer radius was to prevent the COM measurement being skewed by curvature effects while the inner radius was to prevent the measured COM of the bilayer from being biased by excluded volume effects during insertion. The distance between the NP and the selected lipids was then projected along the z-axis. Fig. 9-4 shows both the change in the SASA and change in the NP-bilayer distance, Δz, as a function of time for the full 400 ns trajectories of all six NPs. The baseline values are calculated as the average of the values for the control simulations. As expected, both the SASA and distance between NP and bilayer show similar trends, confirming that the SASA

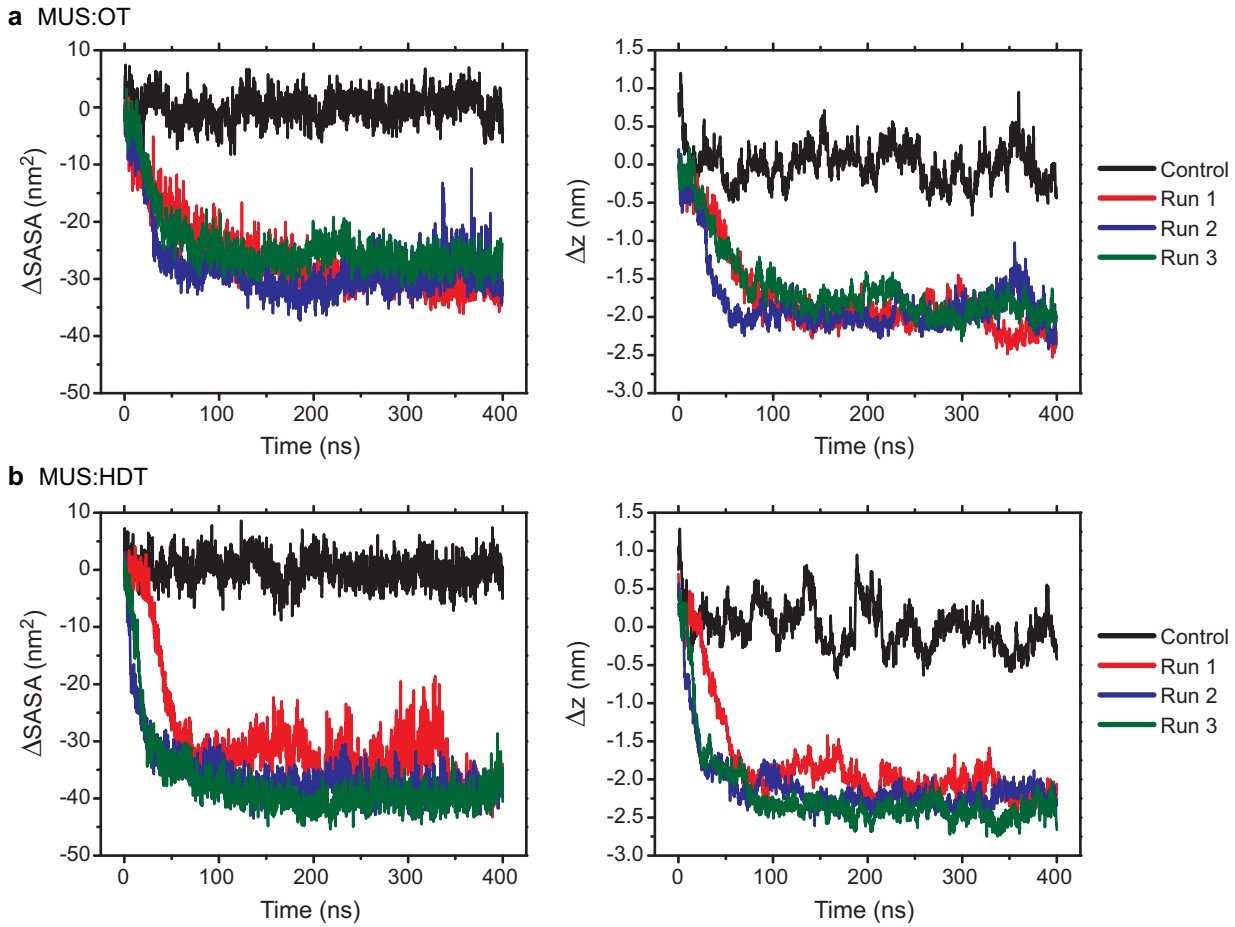

Figure 9-4: Order parameters for full insertion trajectories. **a** Change in SASA and distance between NP and bilayer as a function of time for MUS:OT NPs, including protrusion-free control. **b** Change in SASA and distance between NP and bilayer as a function of time for MUS:HDT NPs, including protrusion-free control.

decrease serves as a suitable order parameter for NP insertion. Furthermore, the values clearly plateau by approximately 150 ns with no significant change over the remainder of the trajectory, and moreover plateau at nearly the same values independent of the starting configuration. The values of both $\Delta SASA$ and Δz are also slightly larger in magnitude for the MUS:HDT NPs than the MUS:OT NPs as expected. In contrast, no change in either parameter is observed for the control simulations on average. However, there are large fluctuations in Δz as the control NPs diffuse along the bilayer surface. These fluctuations are partially due to bilayer undulations and partially due to the rough topography of the bilayer. The lack of significant fluctuations in the SASA over the time period further illustrates its superiority as an order parameter for insertion.

Fig. 9-5a and Fig. 9-5b show several more snapshots from the MUS:OT and MUS:HDT trajectories respectively, focusing on the initial 10 ns of insertion prior to the generation of significant bilayer curvature. Only ligands and lipids in hydrophobic contact are highlighted to emphasize the evolution of the NP-bilayer interface. The snapshots illustrate initial ligand-lipid mixing that is

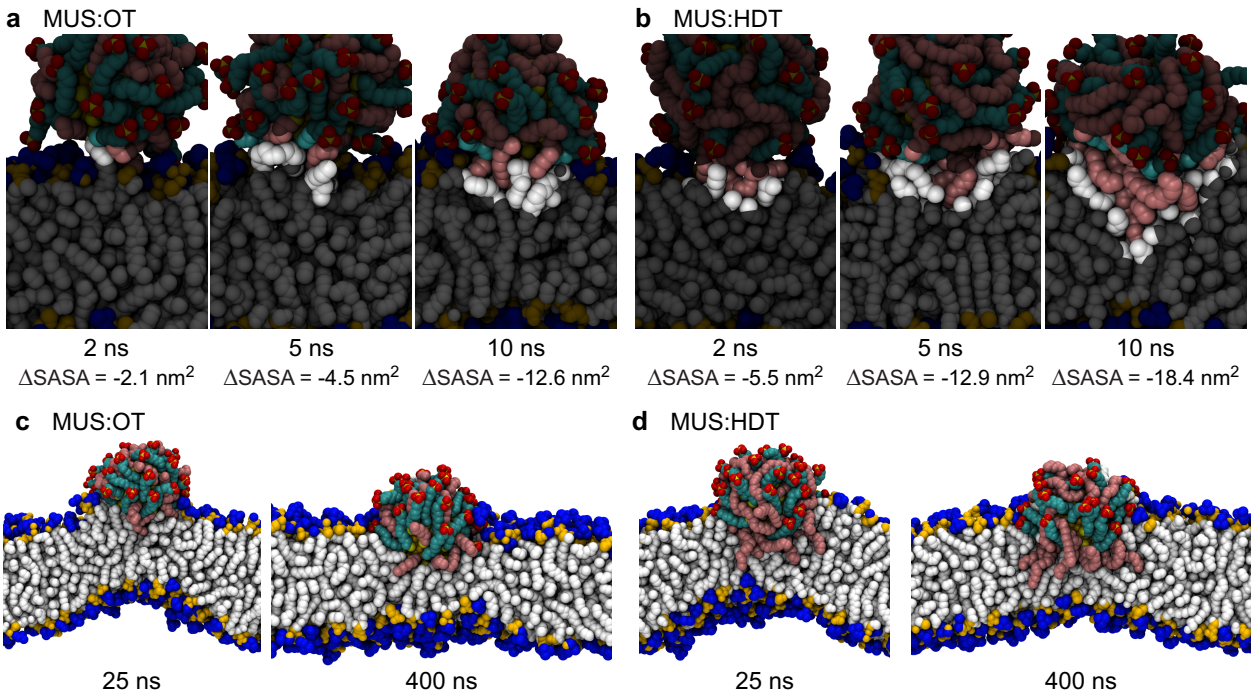

Figure 9-5: Additional snapshots during NP insertion. **a** Initial insertion and recruitment of lipids/ligands during initial 10 ns of insertion for MUS:OT NPs. Ligands and lipid tails in hydrophobic contact are highlighted. **b** Initial insertion for MUS:HDT NPs. **c** Curvature generation and eventual relaxation for MUS:OT NPs. **d** Curvature generation and relaxation for MUS:HDT NPs.

reminiscent of the recruitment of lipids to a nascent stalk during the early stages of vesicle-vesicle fusion. After the initial protrusion contact, all NPs that begin to insert are able to recruit additional lipid tails and hydrophobic ligands to the growing site of NP-bilayer fusion, again mimicking the stalk formation pathway. The snapshots show the disruption of lipids from the bilayer as both head group and tail groups rearrange to accommodate contact with the NP. Fig. 9-5c and Fig. 9-5d show that after this initial stalk formation, the both NPs induce the curved intermediates previously shown in Fig. 9-2. By 400 ns, the snapshots show that the curvature has largely relaxed for both NPs, implying that even with the NP still inserted into a single monolayer and without any boundary conditions on the bilayer ribbon lipid rearrangements can relax in the vicinity of the NP.

During the control simulations, the NPs were observed to diffuse along the bilayer surface as shown in Fig. 9-4. No insertion was observed for either NP after 400 ns. However, monitoring the value of H_C did show occasional transient spikes consistent with some hydrophobic contact between the NP and the bilayer, even without a protrusion being induced. Fig. 9-6 shows H_C as a function of time for both control NPs as well as snapshots of configurations with large H_C values. The snapshots show behavior that would be consistent with configurations induced from the workflow described above. In the first snapshot (labeled with a black dot), a lipid tail is in

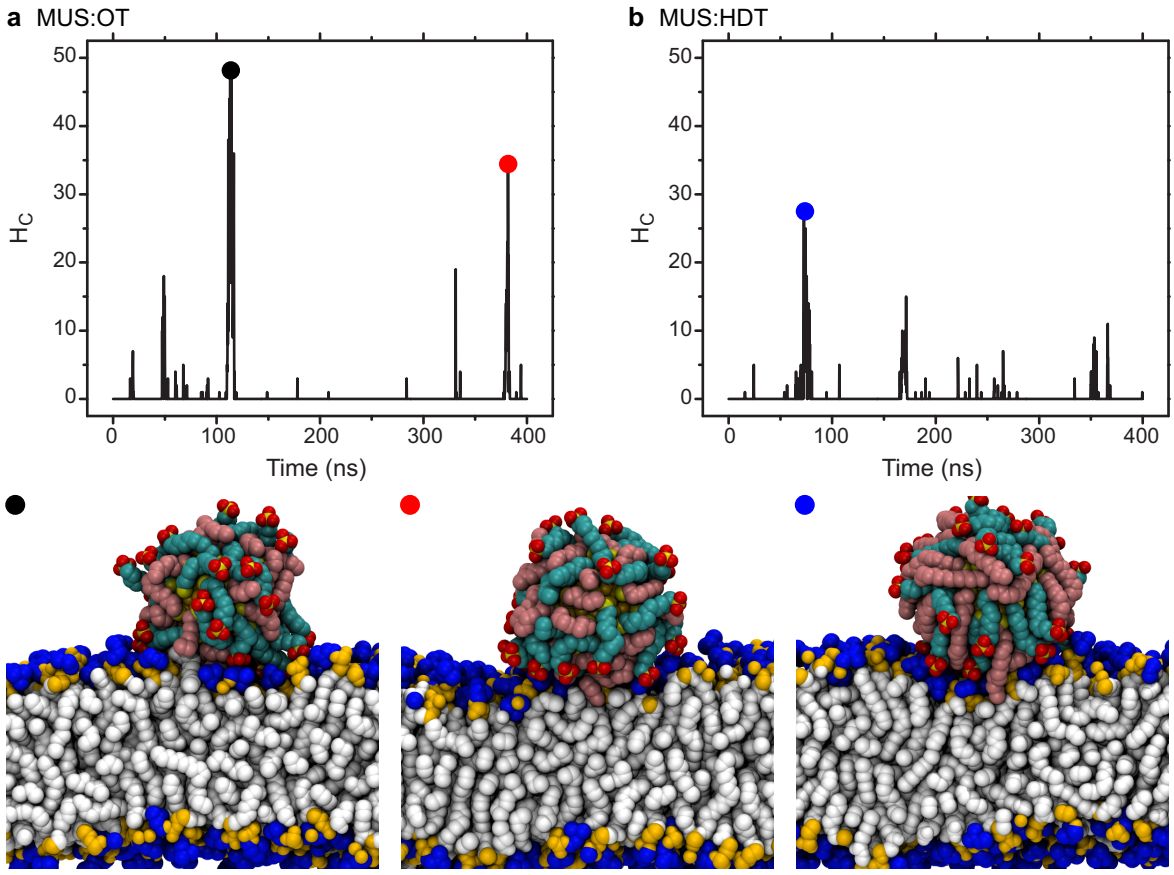

Figure 9-6: Control simulations show sparse hydrophobic contact with bilayer. **a** H_C as a function of time for MUS:OT NP. **b** H_C as a function of time for MUS:HDT NP. **c** Snapshots of high H_C configurations identified during control simulations.

contact with a MUS:OT NP, indicating that a protrusion occurred but did not induce insertion. Given that even with induced protrusions insertion occurs only a fraction of the time (c.f. Fig. 9-2), this observation is consistent with the results. The observation that lipid protrusions can occur, albeit rarely, indicates that the biases applied to induce protrusions are realistic and do mimic actual rare events consistent with Chapter 8. The snapshot labeled with the red dot resembles an attempt at MUS:OT anchoring. Finally, the last snapshot shows an attempt at MUS:HDT anchoring with a ligand inserting partially into the hydrophobic core before the system again relaxes, although it persists for longer period of time. The finding that occasional spikes in H_C do happen during completely unbiased simulations, with configurations resembling those induced by the biased workflow, supports the idea that spontaneous insertion would be observed over sufficiently long periods of time agreeing with experimental results in unsupported systems. However, we again emphasize that these are clearly rare events as none of the transient increases in H_C led to insertion, agreeing with the relatively low proportion of trajectories that lead to insertion during the probing simulations.

9.4 Long hydrophobic ligands facilitate membrane anchoring

The four trajectories shown in Fig. 9-3, as well as a fifth MUS:OT trajectory, all show similar pathways for insertion. All of these trajectories also originated from "inserted" initial configurations as defined in Fig. 9-2. However, a third MUS:HDT trajectory was continued from an initial configuration that was "anchored" as defined in Fig. 9-2. Fig. 9-7 shows the change in the SASA for the first 100 ns of insertion with accompanying snapshots for the anchored trajectory, labeled as MUS:HDT 3, and compared to a trajectory from Fig. 9-3. The major difference between the two trajectories is an initial plateau region in which the SASA for the anchored simulation remains approximately constant in contrast to the insertion pathway which involves an immediate and rapid decrease in the SASA. After 20 ns, the SASA begins to decrease until plateauing at a value similar to the value observed in the other insertion trajectories. The snapshots illustrate the role of the long hydrophobic ligands in facilitating this secondary pathway. The snapshot at 5 ns show a single ligand pushing through the head group region of the bilayer and intercalating within the lipid tail region. This conformation is reminiscent of lipid-anchored proteins, which also can bind to the membranes through a hydrophobic tail inserted into the bilayer [293]. The persistence of this anchoring allows the NP to remain in close contact with the membrane surface until a spontaneous lipid protrusion occurs at 11 ns. The protruding tail associates with the anchored ligand and makes contact with the monolayer, initiating the slow decrease of the SASA. This configuration again mimics stalk formation during vesicle fusion. The snapshot at 20 ns shows the addition of a second hydrophobic ligand to the nascent stalk and the continued local deformation of lipid tails. The SASA begins to decrease significantly once these additional molecules come into contact, then continues to decrease until plateauing. The snapshot at 100 ns illustrates a conformation effectively identical to those shown for the non-anchored trajectories in Fig. 9-3 and Fig. 9-5. The anchored insertion pathway thus occurs via a distinct initial state but still proceeds after the appearance of an lipid tail protrusion and ends in a similar final configuration.

The appearance of a spontaneous tail protrusion 11 ns after the start of the anchoring pathway is surprising given the extremely small frequency with which such protrusions are observed. As discussed in Chapter 8, splay protrusions at a distance of 0.3 nm beyond the phosphate groups, the distance chosen to initiate insertion in this Chapter, occur with a frequency smaller than 0.001 protrusions/lipid/ns, implying that they should be typically observed on microsecond timescales (see Fig. 8-3). The observation of a spontaneous protrusion in only 11 ns implies that the presence of the anchoring ligand affects the protrusion frequency. This possibility is further suggested by the close association of the tail with the ligand as shown in Fig. 9-7. As the results of Chapter 8 indicate that contact with water is the primary barrier to tail protrusions, the close contact between the lipid tail and the hydrophobic ligand could reduce this barrier by effectively dehydrating the NP-lipid interface. Fig. 9-8 proposes this possibility. First, the PMF for a splay lipid tail protrusion was calculated following the same procedure as in Chapter 8 but with a 150 mM NaCl concentration and at 310 K to match the conditions of the insertion simulations. The PMF is effectively identical to what was calculated previously. The dashed vertical line indicates the 0.3 nm threshold to which

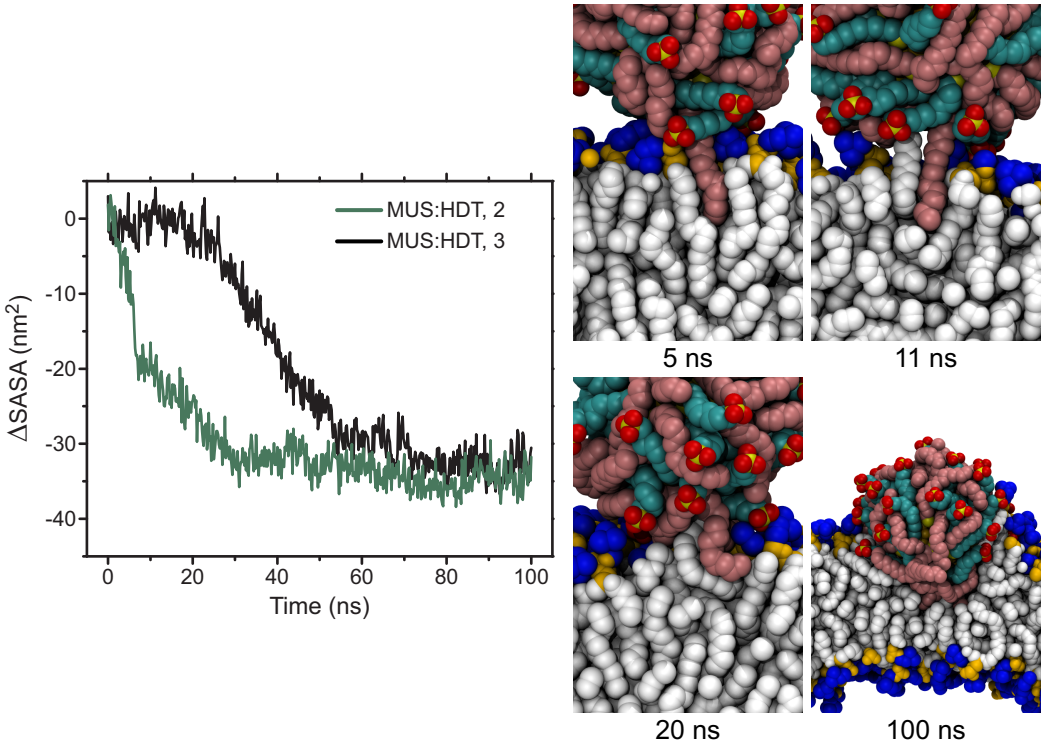

Figure 9-7: Insertion pathway following initial ligand anchoring. The change in SASA is plotted for the first 100 ns of an trajectory initiated from an anchored configuration (MUS:HDT 3) and compared to a trajectory from Fig. 9-3 (MUS:HDT 2).

protrusions were induced in the unbiased simulations. The barrier is approximately 11 kT, agreeing with previous results and indicating that the appearance of the protrusion is not due to a change in the PMF due to the presence of ions or a higher system temperature. The snapshots show a splay protrusion at the 0.3 nm threshold in both the pure bilayer and in the presence of the ligand anchor. It is clear that the protrusion in the anchor case protrudes to a similar distance. The red dashed line thus indicates the proposed PMF in the presence of the anchor - the hydrophobic contact reduces the barrier, allowing a protrusion to occur with a much lower barrier and thus much smaller timescale than expected in a pure bilayer.

The trajectory in Fig. 9-7 is a single example of an anchored NP that eventually inserted after the spontaneous protrusion of a nearby tail, but in principle the timescale for such a protrusion occurring could be longer than the typical time that the ligand stays anchored. Furthermore, the probing simulations only ended in anchoring behavior for MUS:HDT NPs, not MUS:OT NPs, indicating that anchoring may only be stable for the NPs with longer ligands. To test whether anchoring can persist long enough for protrusions to occur, we developed a workflow to estimate the timescales for both processes. First, ligand anchoring was induced by pulling the end of a HDT ligand into the bilayer from an initial starting configuration extracted from the control simulations. The ligand was pulled at a rate of 1 nm/ns to the same depth as measured for the anchoring ligand in the unbiased simulation, averaged over the first 10 ns of the trajectory in Fig. 9-7. Ten such

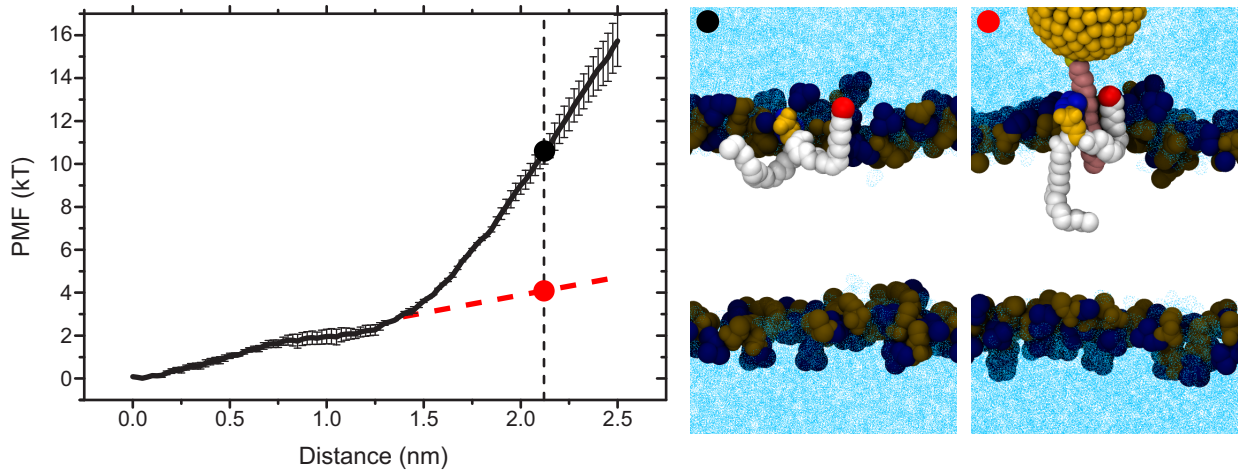

Figure 9-8: Proposed PMF for protrusions near anchored NPs. The PMF for a splay protrusion in a planar DOPC bilayer at 310K and 150 mM salt is shown and is the approximately the same as the PMFs in Chapter 8. The dashed red line indicates the proposed PMF of a protrusion in the presence of an anchor ligand. Snapshots show the close association of a splay protrusion with an anchor ligand relative to a protrusion in a pure bilayer.

configurations were generated from different starting points extracted from the control simulation. An additional ten simulations were launched from the configuration at 5 ns in the trajectory in Fig. 9-7 but with different randomized velocities. Finally, ten simulations were conducted for MUS:OT as well with an OT ligand pulled into the bilayer to the same depth as the HDT ligand. Each system was equilibrated for 4 ns with an umbrella potential applied to maintain the anchoring. The simulations were continued from the end of the equilibration with no bias applied and H_C between the NP and the bilayer was monitored. These simulations were used to determine the time until H_C dropped to zero, indicating the detachment of the NP from the bilayer. Following the equilibration of the MUS:OT NPs, it was found that 2 of the 10 simulations had no hydrophobic contact after equilibration and 2 of the simulations had already triggered insertion during the equilibration process. These 4 trajectories were discarded as unsuitable starting configurations. The remaining 6 anchored trajectories had similar initial values of H_C as the HDT simulations and could be used as a suitable comparison to calculate the detachment time. In a separate workflow, the ten post-equilibration configurations for the MUS:HDT NPs were continued with the bias maintained to retain anchoring and H_C was monitored. These simulations were used to determine the approximate time anchoring had to be maintained before a spontaneous protrusion occurred as judged by a rapid rise in H_C and visual inspection. For both sets of simulations, runs were ended after 50 ns if neither NP detachment nor protrusion behavior was observed.

Fig. 9-9 summarizes the behavior of the different anchoring simulations. Fig. 9-9a shows the number of hydrophobic contacts between the NP and bilayer as a function of time for three representative trajectories - one MUS:OT trajectory with no bias, one MUS:HDT trajectory with no bias, and one MUS:HDT trajectory with the anchoring bias maintained. The two unbiased

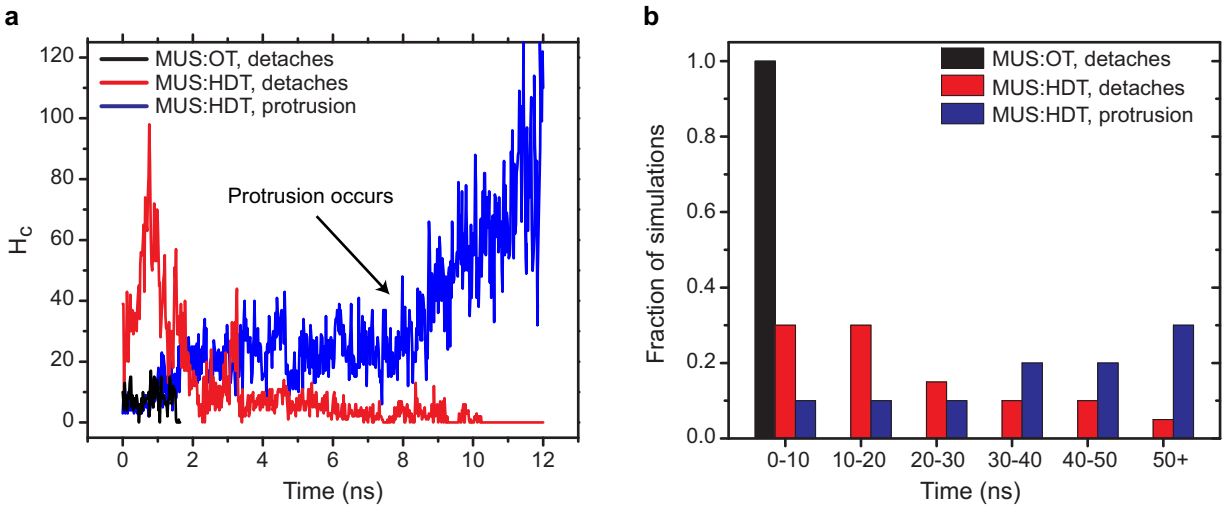

Figure 9-9: Time scales for anchor detachment vs. protrusion appearance. **a** Representative trajectories showing H_C during the detachment of a MUS:OT and MUS:HDT NP and the appearance of a protrusion near a MUS:HDT anchored NP. **b** Histogram showing fraction of simulations with detachment/protrusion times within the range specified.

trajectories both have H_C drop to 0, indicating that the NP detaches as labeled in the figure. The unbiased MUS:HDT ligand detaches several nanoseconds after the MUS:OT ligand. The biased MUS:HDT trajectory illustrates a strong increase in H_C after approximately 8 ns that occurs after a spontaneous lipid protrusion similar to what was observed in Fig. 9-7. Fig. 9-9 summarizes the detachment/protrusion times for all simulations as a histogram showing the fraction of simulations in which the NP detached or a protrusion occurred within the specified time range. The results show that all MUS:OT NPs detach in under 10 ns, while a significant fraction of MUS:HDT NPs stay anchored well in excess of 20 ns. No significant difference in detachment time scale was observed for MUS:HDT NP configurations originated from either the control simulations or extracted directly from the trajectory in Fig. 9-7. For the simulations with constrained ligand anchoring, protrusions occurred in under 50 ns for 70% of the simulations, overlapping with the duration of anchoring for the MUS:HDT NPs. Surprisingly, none of the unbiased simulations ended with spontaneous insertion; however, given the relatively long timescale until protrusions appear this likely just confirms that even with initial anchoring insertion is still an unlikely process.

These results show that MUS:HDT NPs, and not MUS:OT NPs, can successfully anchor to bilayers for a long enough time that protrusions may spontaneously occur to trigger insertion as was observed in the unbiased trajectories. This finding opens up the possibility that NPs with long hydrophobic ligands can insert into bilayers like peripheral proteins by first interacting with hydrophobic lipid packing defects as opposed to protruding lipid tails. Such defect-mediated binding has been recently shown for proteins interacting with mixed bilayers [256]. Embedding thus is likely more probable when NP monolayers include long hydrophobic ligands capable of anchoring as it enables a second pathway for spontaneous insertion.

9.5 Importance of free boundary condition

One of the important aspects of the protrusion-mediated insertion workflow described in the previous sections is the use of a bilayer ribbon with a free, water-exposed boundary rather than a more typical bilayer that spans the x-y plane of the simulation box. In Chapter 7, the ribbon setup was exploited to test interactions with the high curvature bilayer edge. Here, however, the use of ribbons was continued due to preliminary findings that the use of a box-spanning bilayer inhibited NP insertion, potentially due to the use of periodic boundary conditions. To test whether a fully periodic bilayer would show insertion behavior, a 392 lipid DOPC bilayer was equilibrated for 100 ns in a square box with semi-isotropic pressure coupling following typical techniques. First, the same workflow used with the ribbons was attempted - a single protrusion was induced to a distance of 0.3 nm above the phosphate groups, searching simulations were conducted with a MUS:OT NP to acquire configurations with limited contact between the NP and bilayer, then unbiased probing simulations were launched. However, this workflow did not lead to the observation of any insertion events. To test an even more extreme deformation, three lipid protrusions were induced adjacent to each other in the bilayer and the NP was pulled into contact with the protruding lipid tails using an applied force. The resulting configuration had a much larger value of H_C due to significant NP-protrusion contact, as shown in Fig. 9-10a. Despite this, after 10 ns the protrusions relaxed and no insertion was observed. Given the failure of this simulation to yield insertion despite significant bias, we suspected that the free boundary of the ribbon is necessary to observe insertion. It is also possible that significantly larger box-spanning bilayers may be suitable to allow curvature changes to decay by the box edge, but this possibility was not investigated due to the computational expense of such simulations and the success of the ribbon workflow.

To further explain the need for a free boundary, Fig. 9-10b shows the length of the ribbon along the x-axis as a function of time during the insertion of an MUS:OT NP over 400 ns. The length is determined as the difference between the maximum and minimum x-coordinates of the ribbon during insertion. The plot shows that the length fluctuates significantly, experiencing deviations on the order of 1-1.5 nm during approximately 10 ns of simulation time. The simulation snapshots in Fig. 9-10 further demonstrate that these fluctuations are not just because of lateral expansion of the ribbon from incorporating the NP, but because of the significant curvature of the ribbon. Such curvature would be damped by the boundary conditions that enforce a planar bilayer edge. The increase from 0-15 ns occurs as the NP first excludes volume and expands the bilayer, the decrease from 15-50 ns is due to curvature, and the final decrease between 50-150 ns is the relaxation of curvature during continued NP insertion. The large changes in dimension as well as the curved boundaries are unlikely to be well-captured in a planar bilayer with full periodic boundary conditions, even with pressure coupling. We thus believe the free boundary provided by the ribbon is necessary despite the need for additional water molecules, increasing the system size. We note that a recent study on similarly-sized NPs interacting with bilayer also suggested that bilayers with fixed boundaries may inhibit penetration behavior, similar to our suggestion here [112]. Finally, the necessity for a free boundary (i.e. zero surface tension conditions) may further explain the ex-

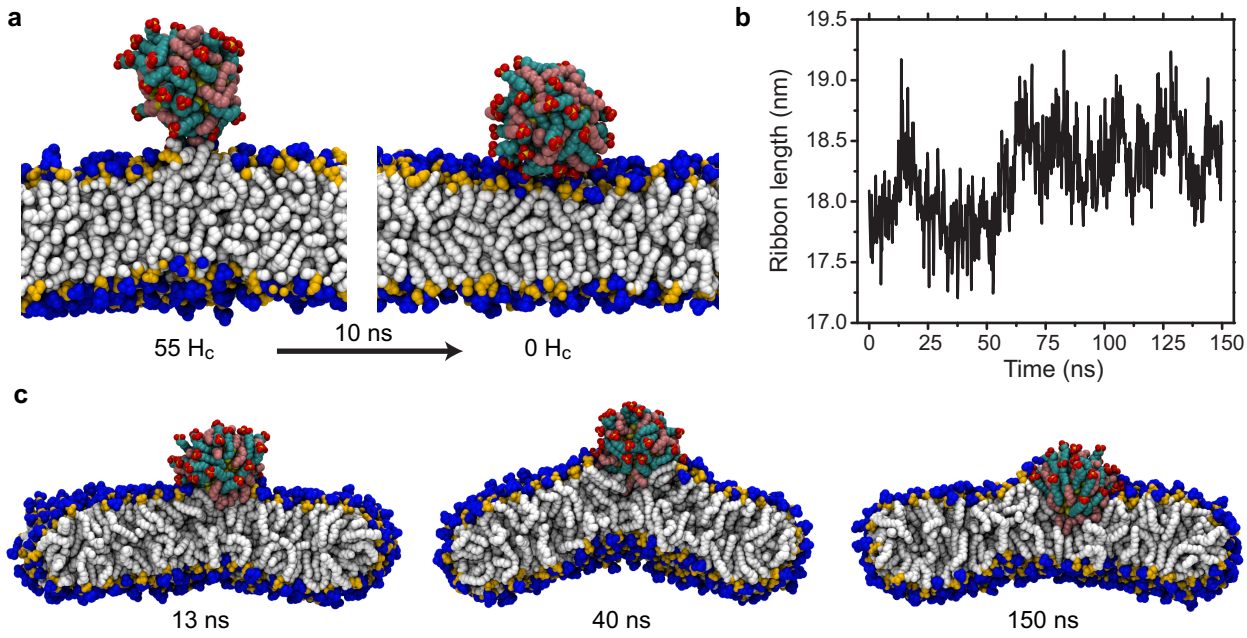

Figure 9-10: Necessity of free boundary condition for modeling NP-bilayer insertion. **a** Snapshots illustrating no observed insertion in box-spanning bilayers even with significant initial hydrophobic contact and multiple induced protrusions. **b** Ribbon length fluctuations during spontaneous insertion over 150 ns, leading to changes on the order of 1-1.5 nm. **c** Snapshots illustrating extreme curvature and length deformations of ribbon.

perimental observation of no NP insertion from Chapter 7. In the case of a supported lipid bilayer, interactions with the substrate would likely inhibit both the curvature and bilayer expansion that is necessary for insertion to occur. In comparison, a free, fluctuating bilayer as in a vesicle or cell would easily enable such bilayer deformations to occur, reconciling the results of Chapter 4 and Chapter 7.

9.6 Ligand flipping is potential pathway to fully-embedded state

The simulation results above show the partial insertion of NPs from solution into the bilayer. However, charged end groups were not observed to cross the bilayer core in any simulations. Instead, all charged ligands were restricted to one monolayer, leading to significant ligand strain. From symmetry considerations, it seems likely that embedding a NP in only one monolayer is less favorable than the full transmembrane configuration predicted in Part I. As qualitative support of this, the NPs in Chapter 7, which entered bilayers via the bilayer edge, always evenly split ligands between the two monolayers when there was no barrier for the transfer of ligands from one monolayer to the other prior to edge insertion. The lack of a similar ligand distribution in the partially inserted state suggests that the large barrier for ions to cross the hydrophobic bilayer core inhibits the NP from assuming a fully transmembrane configuration. Assuming the transmembrane configuration is stable over long time scales, the pathway for the transfer of ligands from one side of the bilayer

to the other must be resolved.

In this section we propose that the charged ligands can "flip" through the bilayer directly with minimal bilayer disruption. This pathway would be similar to the spontaneous transfer of charged moieties through the bilayer, a process that has been investigated extensively for ions, charged amino acids, and other charged solutes. The general transition path observed involves the formation of transient water defects around charged solutes coupled to local deformations of the bilayer in order to avoid direct exposure of the charges to the low-dielectric constant membrane core [72, 191, 294, 295, 296, 297, 298]. Surprisingly, the magnitude of the energy barrier for ion crossing has recently been found to depend largely on bilayer properties rather than the chemistry of the ion, in large part due to the necessity of membrane deformations to stabilize the water defect [295]. In this sense, ion translocation is similar in spirit to lipid flip-flop, where the charged head groups of the lipids are continuously solvated and flip-flop induces local membrane deformations to stabilize high energy states [287]. Finally, ion permeation is dependent on the bilayer thickness, with thinner bilayers presenting a lower barrier to translocation [299].

For partially-inserted NPs, the physicochemical similarities between the MUS ligands and charged amino acids suggest that translocation of the charged end groups could occur via a similar pathway. Moreover, the local bilayer thickness is significantly perturbed during partial insertion, leading to thinning that should lower the barrier for insertion (this deformation will be investigated in more detail in Chapter 11 as well). The NP system is also highly asymmetric unlike most systems studied previously - specifically, the large number of charged side chains on one side of the bilayer creates a large electrostatic potential that can be reduced by flipping ligands equally between the two monolayers. It is thus possible that the barrier for charged ligand insertion is lower than expected for ions in pure bilayers.

We use an umbrella sampling workflow typical of previous studies on ion permeability to calculate the potential of mean force for ligand flipping. Previous studies have shown that standard 1D umbrella sampling is sufficient to identify free energy barriers as long as the system size and order parameter are chosen carefully to avoid finite size effects and barriers due to orthogonal reaction coordinates. [296, 294, 297]. We first chose to reduce the system size by extracting the NP and all lipids within a 8.2 nm x 8.2 nm square area around the NP from the final configuration of the first MUS:OT run. This square area was then embedded within an existing 392 lipid bilayer, removing any overlapping lipids, then equilibrated for 50 ns. The final system consisted of 334 lipids solvated to 64 water molecules per lipid in a 150 mM salt concentration plus counterions to neutralize the NP. The new simulation box contained 83,338 atoms compared to the 166,987 in the ribbon system. The planar system was chosen due to minimal box vector perturbations reported in previous simulations of ion translocation, eliminating the need for a free boundary as discussed in the previous section. The 334 lipid system size was chosen over smaller systems to eliminate finite size effects [296] and because the membrane thickness plateaued before reaching the box wall (measured using techniques discussed in detail in Chapter 11), ensuring no artifacts from enhanced bilayer disruption between periodic images.

After system preparation, initial configurations for umbrella sampling were generated by slowly pulling a chosen ligand through the bilayer. The reaction coordinate for U.S. was defined as the distance, Δz, between the center of mass of sulfonate in the ligand of choice and the center of mass of phosphorus atoms in the distal lipid monolayer projected onto the z-axis (i.e. membrane normal). Only phosphorus atoms in the opposing leaflet were considered because the significant disruption of head groups due to the NP in the proximal monolayer would interfere with the calculation of the reaction coordinate. A similar choice was shown to be superior in simulations of both cell-penetrating peptide and ion translocation [53, 300]. The ligand to be pulled was chosen by monitoring the value of the reaction coordinate for all ligands during the 50 ns equilibration. The ligand with the smallest average value of the reaction coordinate was selected. The end group was pulled across the bilayer at a rate of 0.1 nm/ns using a harmonic potential with a spring constant 3000 kJ/mol/nm^2. Configurations spaced 0.1 nm apart were then extracted and umbrella sampling simulations were launched from each for 20 ns and with the same spring constant. The PMF was calculated using WHAM with the first 10 ns of each window discarded as equilibration.

Fig. 9-11 shows the PMF as a function of Δz for "flipping" a single ligand. Snapshots of four representative points are shown. In each snapshot, the restrained ligand is highlighted, water is explicitly drawn as cyan beads, and nearby sodium counterions are drawn in green. Lipid head groups are also highlighted to illustrate local bilayer deformations while the remainder of the system is darkened to emphasize the components of interest. The PMF is set to zero at its minimum and correctly corresponds to the starting point of the trajectory from which starting configurations were generated ($\Delta z \approx 3.05$ nm). The first snapshot shows the initial position of the ligand at the lipid-water interface. As Δz decreases, corresponding to the movement of the ligand end group into the hydrophobic core region, the PMF increases as expected. The snapshot illustrates the formation of a local water defect that solvates the charged end group even within the core region of the bilayer. Lipid head groups nearby also deform slightly to facilitate this state and a counterion is also always in the vicinity of the sulfonate end group to partially neutralize its charge. The maximum of the PMF corresponds to the formation of a "water bridge" linking the two bilayer leaflets. The snapshot illustrate a single-file line of water extending throughout the entire bilayer to fully solvate the end group. The lipid head groups of the bottom monolayer also deform significantly to facilitate this water contact. Upon another slight decrease in Δz, the ligand breaks through to the other interface, allowing the water bridge to dissolve and leading to a local minimum in the PMF. The bilayer deformation cannot relax, however, as the ligand is insufficiently long to fully cross the bilayer without inducing local deformation.

The ligand flipping pathway qualitatively resembles ion translocation as expected, with the formation of a water bridge as previously predicted in thin bilayers [299, 300]. The full barrier for this process is estimated as 26 kT, a value significantly lower than the barriers for lipid flip-flop in DOPC ($\approx 37kT$ [287]) or for ion penetration in DPPC ($\approx 41kT$ [295]), and similar in value to the permeation of ions through thinner DMPC bilayers [299]. The thickness of DMPC bilayers is approximately 2.3 nm based on the distance between phosphate peaks [299]; this distance is roughly

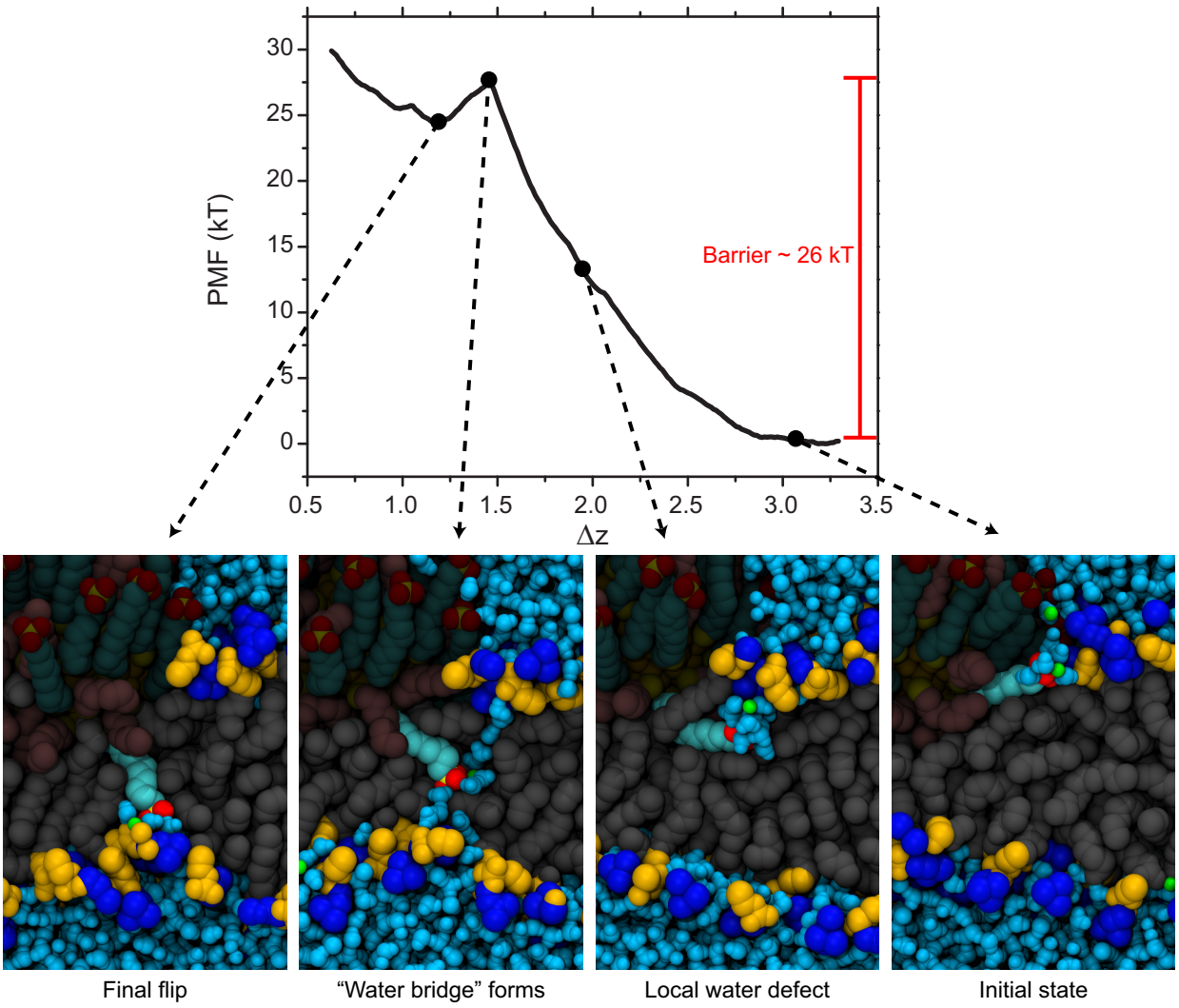

Figure 9-11: Pathway for ligand flipping and an estimate of the PMF for a single flip. From its starting point snorkeled toward one monolayer, the ligand crosses the bilayer while continuously solvated by water. Snapshots for the times indicates are shown with the pulled ligand highlighted and water shown explicitly in cyan.

equivalent to the spacing between the two metastable points in the PMF. This comparison suggests that local thinning induced by the NP is the major factor reducing the magnitude of the PMF. Finally, the timescale for flip-flop in DMPC bilayers has been estimated as on the order of seconds [301] - given the similarity between lipid flip-flop and ligand flipping in terms of both the pathway and energy barrier, ligand flipping may occur on a similar time scale, providing a mechanism for full embedding over experimentally accessible times.

9.7 Conclusions

In this Chapter, we show that contact between a NP and a lipid tail protrusion can trigger rapid insertion of the NP into a planar, defect-free bilayer. These results expand upon the findings of Chapter 7 and Chapter 8 which showed that contact with protrusions at bilayer edges can trigger insertion and that protrusions occur in planar bilayers over long timescales. NP-protrusion contact is necessary, but not sufficient, to drive insertion, as only a fraction of all simulations started from configurations with such contact proceeded to insertion. Monolayer properties appeared to play a significant role as the MUS:HDT NPs were much more likely to insert than the MUS:OT NPs. During insertion, the bilayer exhibited significant curvature induced by the NP which appear to be necessary to stabilize the insertion process. Such curvature would be inhibited on supported lipid bilayers, providing additional evidence for the lack of insertion observed experimentally on planar systems. At the end of 400 ns, however, the curvature appeared to be alleviated for both MUS:OT and MUS:HDT systems. We also found that MUS:HDT NPs could transiently "anchor" to the bilayer by extending a single ligand into the bilayer core prior to insertion. The barrier for lipid protrusions near an anchored ligand appeared to be low judged on the observation of spontaneous protrusions near anchored NPs, possibly due to local dehydration of the NP-lipid interface. This finding suggests that NPs should be engineered to include long ligands as potential "hooks" to help facilitate the kinetics of embedding. Finally, we propose one potential pathway for the "flipping" of charged ligands across the bilayer to obtain a fully transmembrane orientation. We show that such a pathway is similar to the translocation of ions in thin bilayers and likely occurs over similar timescales that would be accessible experimentally.

The results presented in this Chapter show a complete mechanism for the insertion of NPs into a transmembrane configuration. The proposed pathway consists of the NP first adsorbing to the bilayer surface, driven by electrostatic interactions, before eventually encountering a stochastic lipid protrusion and inserting into a single lipid monolayer. From this partially inserted states, ligands occasionally flip across the bilayer, with the barrier for flipping toward the distal leaflet lower due to the weaker electrostatic potential in the opposing leaflet. Over time, more ligands flip to drive the NP to a transmembrane configuration via a ratchet-like mechanism. Importantly, at no point during any of these transitions is there significant disruption consistent with bilayer poration - rather, ligand flipping requires only small water defect formation and transient bilayer perturbations. The pathway is thus non-disruptive in agreement with both vesicle (Chapter 4) and previous cell studies [81]. We must stress that the protrusion-mediated pathway is only one possibility, and we cannot rule out other possible insertion mechanisms. Similarly, by only umbrella sampling along a single reaction coordinate, we cannot eliminate other potential mechanisms for ligands to cross the bilayer. However, the mechanism we present for both NP insertion and ligand flipping matches expectations from experiments, reconciles the results of Chapter 7 and Chapter 8, and agrees well with existing literature on ion translocation, and thus we believe it is likely a dominant mechanism for NP insertion.

Part III

Cooperative interactions between NPs

THIS PAGE INTENTIONALLY LEFT BLANK

Chapter 10

NP-NP Aggregation Controlled by Ligand Shell

Work in this chapter was published in:

R. C. Van Lehn and A. Alexander-Katz, "Ligand-mediated short-range attraction drives aggregation of charged monolayer-protected gold nanoparticles" *Langmuir*, **29**, pp. 8788-8798, 2013, DOI: 10.1021/la400756z.

In the previous Chapters, we considered the interactions of a single NP with a lipid bilayer, effectively considering an infinitely dilute NP solution. However, this extreme is difficult to realize in a true physical system so interactions between NPs must also be considered. In this Chapter, we will first study the interactions between two NPs in solution to ascertain conditions under which particle aggregation may occur. While aggregation in principle is opposed by electrostatic interactions between ligand end groups, the same hydrophobic driving force that leads to bilayer insertion may also induce NP aggregation before NPs reach the bilayer interface. Aside from the possibility that the NPs precipitate out of solution, aggregation also likely inhibits the ability of NPs to insert into bilayers as their effective size will increase, reducing the driving force for insertion following the conclusions of Part I of this thesis. It is thus important to understand the conditions under which NP aggregation might be expected in order to optimally design NPs to interact with bilayers without agglomerating in solution.

The aggregation of charged colloidal particles is typically described using Derjaguin-Landau-Verwey-Overbeek (DLVO) theory, which combines an attractive van der Waals term with a mean field electrostatic term to predict the potential of mean force between two particles [281, 302]. While DLVO theory is appropriate for large colloidal particles which can be well-described by continuum assumptions, at smaller length scales the surfaces of NPs can no longer be described uniformly given the topography of the protecting monolayer. Moreover, DLVO attributes attractive interactions solely to van der Waals forces; for small NPs, however, the magnitude of van der Waal forces is minuscule for all but the smallest separation distances. Other continuum approaches have focused on the role of ligand deformation in purely hydrophobic monolayers which are stabilized by steric interactions [303, 304], but these models neglect the influence of charged groups that confer solubility in aqueous environments. Continuum methods may prove even less applicable to more complex NPs systems with monolayers containing multiple ligand species. Understanding the interactions that govern the aggregation of water-soluble monolayer-protected NPs with small core sizes thus requires a more explicit representation of molecular details.

Several previous theoretical and simulation studies have examined charged monolayer-protected

NP aggregation, focusing on the kinetics of aggregate formation [305, 114], role of charge regulation in electrostatic interactions [306], the effect of environmental salt conditions [307, 308, 309], and the influence of mobile charges on the particle surface [310]. Several of these studies have posited short-range attractive interactions between particles without elucidating their origin. Both experiments and a simple physical model for monolayer-protected NPs have also suggested that ligand-ligand attractive interactions can induce NP aggregation [311]. Despite the volume of literature on aggregation, however, a detailed microscopic understanding of how surface ligands may stabilize charged NP aggregates is still lacking. As properties of the ligand monolayer can be tuned synthetically, gaining a microscopic understanding will lead to rules for engineering monolayers to maximize either dispersion or aggregation as desired.

In this Chapter, we calculate the change in free energy for bringing two NPs together from infinite separation. In analogy to the finding that bilayer fusion is stabilized by the flexibility of ligands in the NP monolayer, we show that two NPs may similarly exhibit environmentally-responsive behavior upon coming in close contact by adopting monolayer conformations that reduce the exposure of hydrophobic material to water. The driving force for aggregation is then the hydrophobic effect [162] due to effective ligand-ligand attractive interactions, not purely van der Waals interactions as suggested in DVLO theory. This ligand-mediated short-range attraction requires that the monolayers deform to maximize favorable interactions and that the resulting decrease in unfavorable water interactions compensates for electrostatic repulsion between the charged end groups and any resulting entropic change in the system, again in analogy to the case of NP-bilayer fusion. Fig. 10-1a schematically illustrates this behavior.

To understand this ligand-mediated aggregation process, we adapt the united atom, implicit solvent model previously used to model bilayer insertion to instead model NP-NP aggregation. We calculate the free energy change of dimerization of two particles as a function of the separation between their surfaces. We show that ligand deformation both provides a driving force via the hydrophobic effect and rearranges charges to minimize electrostatic repulsion. As a result, the diameters of the NPs influence their tendency to aggregate as do the properties of the ligands themselves. We show that slight changes to the system, such as a change in ligand length or salt concentration, can lead to pronounced differences in the free energy changes for aggregation. This study thus provides both an explanation for the aggregation of alkanethiol-protected NPs as well as design guidelines to either prevent or encourage dimerization in similar systems.

10.1 Model for free energy change of aggregation

We consider a system of two NPs with gold core diameters between 1.0 and 3.0 nm, each protected by an alkanethiol ligand monolayer composed of the same ligands studied previously. The goal of this work is to find the equilibrium free energy change associated with moving the two particles from an initial surface-to-surface separation of $D = \infty$ to a desired separation D. Following from the free energy decomposition in eq. (3.1) from Chapter 3, the total free energy change is assumed

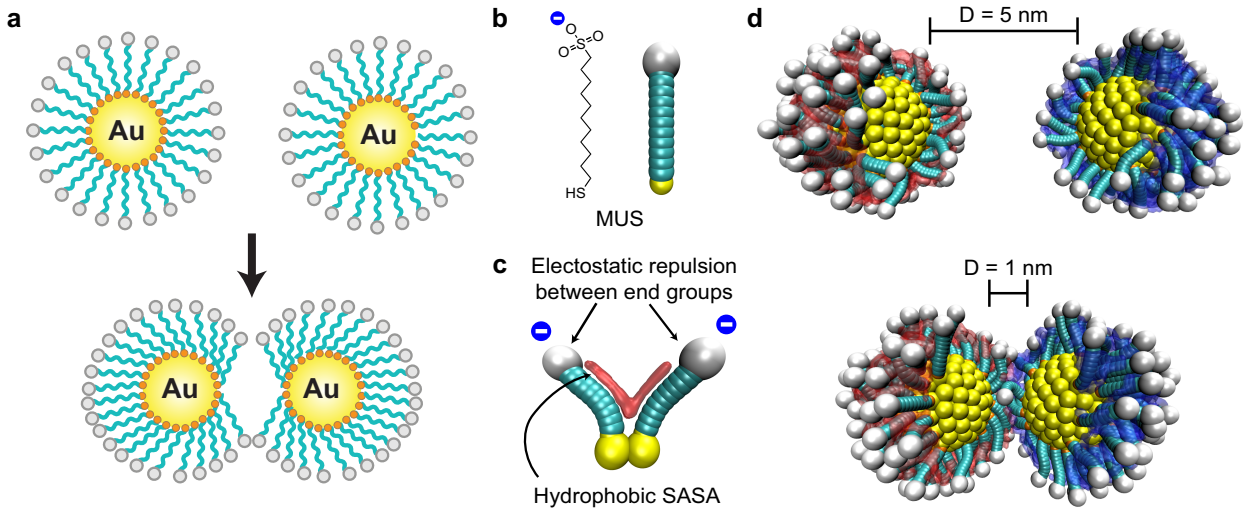

Figure 10-1: Illustration of united atom, implicit solvent simulation methodology. **a** Schematic of proposed aggregation behavior mediated by ligand deformation. **b** United atom model of MUS using same color scheme and model as in Part I of this thesis. **c** Illustration of electrostatic repulsion between hydrophilic beads and depiction of the solvent-accessible surface area (SASA) of two ligands drawn as a red surface. **d** Example simulation snapshots of two NPs with the total SASA for each drawn in distinct red/blue colors. Some ligands are removed so that the deformation of the remaining ligands is apparent.

to be the sum of four terms, each of which is a function of D:

$$\Delta G_{total}(D) = \Delta E_{elec}(D) + \Delta G_{phobic}(D) + \Delta E_{core}(D) - T\Delta S_{conf}(D) \tag{10.1}$$

Here, ΔE_{elec} is the change in electrostatic energy due to repulsion between like-charged end groups, ΔG_{phobic} is the change in the solvation free energy of the hydrophobic ligand backbones, ΔE_{core} is the core-core van der Waals attraction between the NPs, and ΔS_{conf} is the change in the conformational entropy of ligands in each monolayer. The driving force for aggregation is the sum of ΔG_{phobic} and ΔE_{core}; as the particles approach each other, the ligand monolayers interact to minimize the amount of hydrophobic surface area exposed to solvent (ΔG_{phobic}) while the gold cores attract via van der Waals forces (ΔE_{core}). Aggregation is opposed by repulsive electrostatic interactions (ΔE_{elec}) and the reduction in available ligand configurations at close separation (ΔS_{conf}). With the exception of ΔE_{core}, these terms are all also included in the free energy decomposition associated with bilayer insertion as discussed in Chapter 3.

To compute the change in the free energy, a similar united atom, implicit solvent model was used as in Part I of this thesis. Ligands were modeled using the same united atom representation as used previously and the solvent-accessible surface area (SASA) was calculated in an identical fashion. Fig. 10-1 shows an illustration of the united atom methodology, including simulation snapshots with the SASA drawn for two NPs. However, several modifications to the methods were made to take into account interactions between two NPs rather than between a NP and an implicit

bilayer. We used the multistate Bennett acceptance ratio (MBAR) methodology derived by Shirts and Chodera to calculate the total free energy change of the system from the simulation results [312]. As with the previously used BAR method, MBAR requires a system to be described in terms of several intermediate thermodynamic states with defined potential energy functions such that the energy of any given system configuration can be calculated in each intermediate state. A thermodynamic state was defined by the value of a coupling parameter, λ, which is incorporated into the calculation of each system energy component as described below. λ can be interpreted as defining the relative magnitude of interactions between the two NPs. λ varies from $\lambda = 0.0$, corresponding to two NPs at infinite separation with no interactions between them, to $\lambda = 1.0$, corresponding to the two particles at a finite separation D with full interactions. Intermediate values of λ were used to improve the convergence of the free energy methodology by scaling NP-NP interactions and have no physical meaning. The total free energy change for moving the two particles from infinite separation to distance D is the change in the free energy between the state for $\lambda = 0.0$ and the state for $\lambda = 1.0$. Each term in eq. (10.1) incorporates a dependence on λ to facilitate the MBAR calculation as will be detailed below.

ΔE_{elec} was calculated in simulations using a screened Coulombic interaction assuming that the surface potential of the particles is sufficiently low that Debye-Hückel theory can be applied [183, 185, 313]. Under this assumption, the potential between charged bead i and charged bead j is:

$$\Psi(i,j,r_{ij}) = f(i,j)\frac{Q}{4\pi\epsilon_0\epsilon_r r_{ij}}\exp\left(-\kappa r_{ij}\right) \tag{10.2}$$

where Q is the number of charges, $1/\kappa$ is the Debye length of the system, ϵ_0 is the permittivity of free space, ϵ_r is the dielectric constant, and r_{ij} is the distance between two hydrophilic beads (not to be confused with the surface-to-surface separation D between NPs). In all simulations the dielectric constant was set to 80 to represent aqueous solvent [302] while the Debye length was varied to account for different salt concentrations. The function $f(i,j)$ captures the dependence on the coupling parameter λ:

$$f(i,j) = \begin{cases} \lambda & \text{if bead } i \text{ and } j \text{ are on different NPs} \\ 1 & \text{if bead } i \text{ and } j \text{ are on the same NP} \end{cases} \tag{10.3}$$

The total electrostatic energy of the system is then:

$$E_{elec} = -1.0e\sum_{i}^{beads}\sum_{j>i}^{bead}\Psi(i,j,|r_i - r_j|) \tag{10.4}$$

where e is the elementary charge and every hydrophilic bead is assumed to have exactly one charge located at its center. Charge regulation effects are assumed to be negligible given the low pKa of sulfonate, although for other end groups charge regulation may be a critical factor [306]. The summations run over all charged beads in the system.

ΔG_{phobic} was determined from the change in the hydrophobic SASA of the system as the NPs approach each other. As in Chapter 3, we approximate the free energy for hydrophobic solvation as:

$$G_{phobic} \approx \gamma SASA \tag{10.5}$$

The same two values of γ used in Part I were also used here, expressed in different units as 4.72 kT/nm^2 (= 28 cal/mol/Å^2) [170] or 7.92 kT/nm^2 (= 47 cal/mol/Å^2) [169], where the temperature was set to 298 K. The SASA was calculated using the same algorithm detailed in Chapter 3 with the exception of a new dependence on λ. The total free energy due to the exposure of hydrophobic surface area is written as:

$$G_{phobic} = \sum_{i}^{beads} \sum_{j}^{mesh(i)} g(i,j) A_{mesh} \gamma \tag{10.6}$$

$$g(i,j) = \begin{cases} 0 & \text{if mesh point } j \text{ on bead } i \text{ is occluded by a bead on the same NP} \\ \lambda & \text{if mesh point } j \text{ on bead } i \text{ is occluded by a bead on a different NP} \\ 1 & \text{if mesh point } j \text{ on bead } i \text{ is not occluded} \end{cases} \tag{10.7}$$

ΔE_{core} was calculated from the Hamaker expression for the effective van der Waals attraction between two macroscopic spheres, an expression typically used for the calculation of attractive interactions between colloids or NPs [302, 305]. This approach gives the effective interaction energy as:

$$E_{core} = -\frac{A_H}{6}\left[\frac{2R_1R_2}{r^2-(R_1+R_2)^2} + \frac{2R_1R_2}{r^2-(R_1-R_2)^2} + \ln\left(\frac{r^2-(R_1+R_2)^2}{r^2-(R_1-R_2)^2}\right)\right] \tag{10.8}$$

where A_H is the Hamaker constant and $r = D + R_1 + R_2$ is the center-to-center distance between the two NPs. The Hamaker constant varies depending on the composition of the NPs and intervening solvent medium. In this system, we assume that both NPs are gold and that the intervening solvent is entirely hydrocarbon, based on the alkanethiol protecting monolayers on both NPs. The Hamaker constant for gold in hydrocarbon media is given as 35×10^{-20} J or 85.2 kT at 298 K [302]. Because this energy term is dependent only on the NP core diameters and their separation, and not on the positions of ligands in the monolayer, the contribution was calculated analytically and added to the other free energy terms determined during simulations with no need for a λ dependence. van der Waals interactions between the alkanethiol ligands themselves are implicitly included in the value of the SASA parameters from above as the parameters are derived from bulk, not molecular, measurements. This term is the only one in which the distance D explicitly appears; D is taken into account in the other free energy terms by fixing the positions of the gold cores during simulations.

ΔS_{conf} is defined as the difference between the change in the system free energy and the change in the system energy. In this system, the configurational entropy change of the ligands is related to the deformation of the ligand monolayers at close separation. It is expected that the configurational entropy should be much higher for $\lambda = 0.0$ (no NP-NP interactions) than $\lambda = 1.0$, where hard sphere interactions between ligands limit the available configurations of the system. However, MBAR requires a method to capture changes in the configurational entropy for intermediate values of λ in order to properly converge. To account for the reduced number of configurational states as λ increase from 0.0 to 1.0, an additional fictitious "soft sphere" potential was used to penalize interactions between ligands on separate NPs [314, 94]. This potential, $E_{overlap}$, biases the configurations generated during simulations using intermediate values of λ but does not affect the calculation of the total system energy change for $\lambda = 0.0$ and $\lambda = 1.0$, the values corresponding to infinite separation and separation D respectively. The soft sphere potential may be visualized as effectively growing each bead from zero diameter for $\lambda = 0.0$ to the full van der Waals diameter for $\lambda = 1.0$. The potential is defined by:

$$\beta E_{overlap} = \sum_{i}^{NP1} \sum_{j}^{NP2} f(i,j) \tag{10.9}$$

$$f(i,j) = \begin{cases} \lambda\kappa(1 - \frac{r_{ij}}{\sigma_{ij}}) & r_{ij} \leq \sigma_{ij} \\ 0 & r_{ij} > \sigma_{ij} \end{cases} \tag{10.10}$$

The potential was computed between all beads on one NP with all beads on the other NP; beads on the same NP always interacted via hard sphere interactions. Here, σ is the sum of the radii of the two overlapping beads and κ is a positive constant to penalize overlap. κ was set to a value of 20.0 kT so that significant overlap is possible for values of $\lambda \approx 0.05$, while hard sphere behavior is obtained as $\lambda \to 1$ due to the large penalty for any overlap. This particular value of κ was selected by comparing the rate of convergence obtained via several other values. By this definition of the soft sphere potential, setting $\lambda = 0.0$ allows the free motion of ligands on separate particles through each other, which is effectively equivalent to positioning the particles at infinite separation. For intermediate states, overlap between ligands from separate particles provides an energetic input into the MBAR calculation that allows for the calculation of a full free energy.

Fig. 10-2 illustrates the soft sphere scheme and dependence of ligand configurations on λ as well as the dependence of all system energy components on λ for two 2.0 nm core diameter NPs at a separation $D = 1.0$ nm. Fig. 10-2a shows the breakdown of free energy components as a function of λ. $\Delta E_{total} = \Delta E_{elec} + \Delta E_{overlap} + \Delta G_{phobic}$ is the change in the system energy for a given value of λ relative to the baseline value of $\lambda = 0.0$ and is used as the input into the MBAR equation as detailed below. ΔG_{total} is the change in the free energy for a particular value of λ relative to $\lambda = 0.0$ and is the output of the MBAR methodology. The value of ΔG_{total} for $\lambda = 1.0$ is the equilibrium free energy for moving the particles to a separation of D; the intermediate values are for illustration of the method only. ΔS_{conf} is calculated as the difference between the ΔG_{total} and ΔE_{total} and

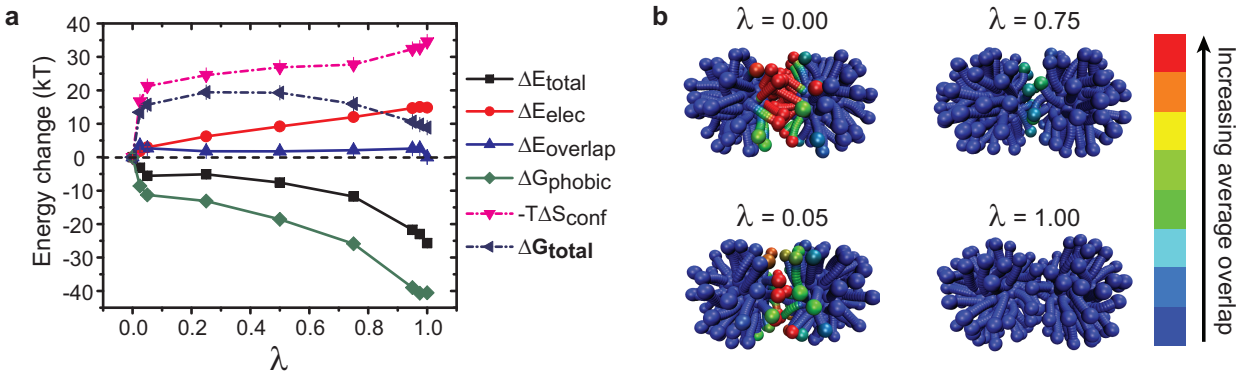

Figure 10-2: Overview of methodology for coupling to λ. **a** Plot of change in free energy terms as a function of λ, including the change in the total free energy and conformational entropy of the system, for two particles at a separation $D = 1.0$ nm. As λ increases, interactions between the NPs are gradually increased in magnitude until they are fully interacting at $\lambda = 1.0$. **b** Snapshots illustrating overlap in the soft sphere scheme.

correctly penalizes increasing values of λ associated with decreasing ligand configurations. Also notable is that both the conformational entropy term and the SASA term are larger than the other energy terms, but have approximately equivalent magnitude and opposite sign. This observation is due to the similar physical mechanism underlying both terms – ligand deformation costs entropy, but results in a decrease of the SASA consistent with the hydrophobic effect. The relative decrease in SASA compared to the decrease in entropy thus determines the magnitude of the overall driving force for aggregation. Finally, $\Delta E_{overlap}$ correctly goes to 0.0 at both $\lambda = 1.0$ and $\lambda = 0.0$ so that its value is only used to enhance convergence and improve the approximation of ΔS_{conf}, but does not directly contribute to ΔG_{total}. Fig. 10-2b shows simulation snapshots that illustrate the importance of the soft sphere potential, $E_{overlap}$. Beads are colored by the average amount of overlap during the simulation. As λ increases, the amount of overlap permitted between ligands on opposite NPs decreases up to the hard sphere limit at which point $E_{overlap} = 0$. Permitting overlap for intermediate states as shown enables an accurate approximation of ΔS_{conf} which is essential to properly calculate repulsive interactions at close NP separation.

10.1.1 Free energy calculations with MBAR

In MBAR, the free energies of a set of K thermodynamic states are determined by self-consistently solving the equation:

$$f_i = -\ln \sum_{j=1}^{K} \sum_{n=1}^{N_j} \frac{\exp[-u_i(\mathbf{x}_{jn})]}{\sum_{k=1}^{K} N_k \exp[f_k - u_k(\mathbf{x}_{jn})]} \tag{10.11}$$

Here, f_i is the free energy of state i, N_j is the number of equilibrium system configurations drawn from state j, u_i is the potential energy function of state i, and $\mathbf{x}_{jn}$ is the n^{th} configuration of the system drawn from state j. The potential energy function u_i is defined entirely by the value

of λ used to calculate the terms in eq. (10.1). The equation must be self-consistently solved for the set of f_i after drawing the N_j samples from each of the K states; the result is a set of free energies that can be used to calculate free energy changes between different states (the absolute values all involve an additive constant, so only differences are meaningful). MBAR is thus similar in spirit to BAR, but information from all K states is considered simultaneously, rather than only taking into account free energy differences between two consecutive states. MBAR typically leads to improved convergence as a result.

For a given value of the interparticle separation D, the free energy change for moving the particles from infinite separation to D is computed as the difference between the free energy of the state for which $\lambda = 1.0$ (fully interacting at position D) and the state for which $\lambda = 0.0$ (non-interacting corresponding to infinite separation). However, sampling from only these two values of λ would require generating a very large number of system configurations to obtain convergence. One advantage of MBAR is the ability to improve convergence by sampling with intermediate values of λ, corresponding to partially interacting NPs as just described. As only the convergence of the two end states is required to compute the free energy change for a given D, the selection of the number of intermediate states with intermediate values of λ and the number of samples N_j drawn from each state was based on trial-and-error to determine the optimal efficiency of convergence.

10.1.2 Simulation procedures

To generate system configurations, a Monte Carlo algorithm was employed. For each Monte Carlo move, a random bead was selected from the simulation system and displaced with a step size of 0.07 nm. Any moves violating bonding considerations or hard sphere overlap with beads on the same particle (or opposite particle for $\lambda = 1.0$) were immediately rejected. Any move that did not violate the bonding and hard sphere constraints was accepted with a probability P given by:

$$P = e^{-\Delta E/kT} \tag{10.12}$$

where $\Delta E_{total} = \Delta E_{elec} + \Delta E_{overlap} + \Delta G_{phobic}$ is the change in the entire system energy computed on the basis of the potentials defined in the previous section. All moves with $\Delta E_{total} < 0$ were always accepted.

Simulations were performed using a multiple step methodology that permitted the calculation of free energies using MBAR while still ensuring configurations generated at different NP separations were physically related. First, single particles of different diameters, monolayer properties, salt concentrations, etc. were equilibrated separately in initial simulations. For all NPs, the grafting monolayer density was fixed at 4.77 ligands/nm^2 unless otherwise noted [145]. Next, two pre-equilibrated particles were selected and moved slowly together, rejecting any configurations that led to hard sphere overlap. These simulations were performed with $\lambda = 1.0$ to ensure that all configurations were physically possible (i.e. obeyed hard sphere overlap). From these trajectories, a configuration was selected for each desired value of D and used as a starting configuration for a

set of simulations with decreasing values of λ. During the simulation, the gold cores were fixed at the desired distance D and were not permitted to move, so that only the ligands fluctuated in space. For each value of λ, the particles were equilibrated for 50,000 steps per bead, then configurations were sampled for another 400,000 steps and recoded every 20 steps. The values of λ used were 0.0, 0.025, 0.05, 0.25, 0.5, 0.75, 0.95, 0.975, and 1.0. The number of λ values, the values selected, and the number of Monte Carlo steps were all chosen by systematically comparing parameters to obtain fast convergence of the free energy change. Within the equilibrium Monte Carlo methodology, the number of Monte Carlo moves only affects the convergence of the free energy and does not have a connection to a physical timescale. After configurations were sampled for all values of λ at the desired value of D, the free energy change between the state of infinite separation ($\lambda = 0.0$) and the state corresponding to D ($\lambda = 1.0$) was computed with the MBAR methodology using the saved configurations. In other words, for each saved configuration generated with one particular value of λ, the system energy was computed for all values of λ and this information was used in eq. (10.11). This method was repeated ten times from different starting configurations for each value of D to obtain appropriate averaging. The exception was simulations where at least one particle had a diameter of 3.0 nm which were only repeated six times due to the computational expense of modeling these larger particles. This simulation methodology was performed using a C program written in-house.

10.2 Characteristic features of aggregation

Fig. 10-3 shows the breakdown of free energy components defined in eq. (10.1) as a function of the surface-to-surface distance D between two like-sized NPs with 2.0 nm core diameters. The salt concentration was set to 150 mM, representative of biological systems, and a SASA parameter of $\gamma = 0.0472$ kT/nm^2 was used. Because the terms corresponding to the hydrophobic effect (ΔG_{phobic}) and conformational entropy change ($-T\Delta S_{conf}$) are both large in magnitude, opposite in sign, and related to the deformation of ligands, these terms are combined and graphed as a sum instead of as individual components to show the net driving force (see Fig. 10-2).

At large D, the free energy change is dominated by electrostatic repulsion between the two NPs. However, once the distance between the two NPs decreases such that the ligands in the two respective monolayers interact, the additional terms corresponding to the change in exposed hydrophobic surface area and the change in ligand conformational entropy become dominant. Both of these terms increase in magnitude as D decreases reflecting the increasing deformation of the monolayers which shields more hydrophobic area while decreasing the possible configurations of the deformed ligands. Finally, the van der Waals contribution due to core-core attraction plays a role at small particle separations, but the contribution is relatively minor. For this set of parameters, a local free energy minimum with a depth of approximately 5 kT is observed for an interparticle separation of 0.8 nm, implying that a dimer could result from two particles being kinetically trapped in a metastable state if the electrostatic barrier is overcome. This barrier corresponds to about

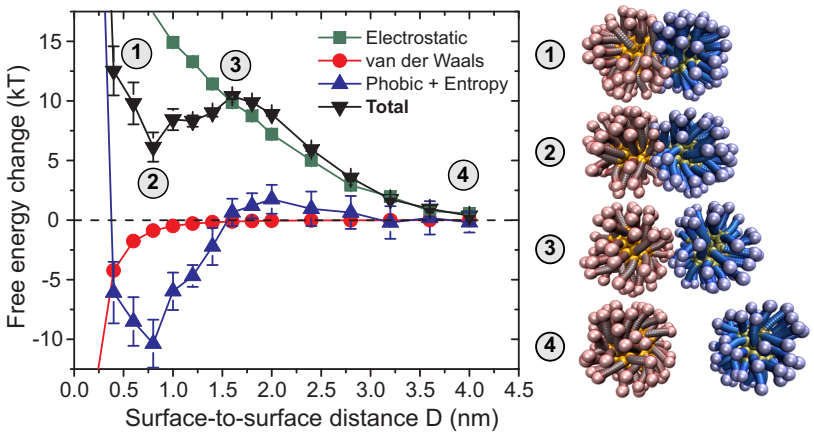

Figure 10-3: Plot of free energy components versus interparticle separation and system simulation snapshots for a typical set of NP parameters. The salt concentration is set to 150 mM, the particles both have diameters of 2.0 nm, and the value of the SASA parameter is set to 0.0472 kT/nm^2. The free energy components for the change in the SASA (i.e. the hydrophobic effect) and change in ligand conformational entropy are graphed as a sum. Example snapshots illustrate the degree of ligand deformation for four characteristic positions. The separate particles are tinted with red and blue respectively to illustrate deformation along their interface.

3 kcal/mol at room temperature, a barrier on the same order of magnitude as the strength of a hydrogen bond in water [302]. Fig. 10-3 also illustrates simulation snapshots of four representative points along the trajectory. The four points correspond to close repulsive separation (point 1), a metastable position (point 2), the point of maximum repulsion (point 3), and the baseline state of effectively infinite separation (point 4), with each NP colored distinctly to demonstrate the extent of deformation at each point.

To further elucidate the interactions between particles as a function of separation, Fig. 10-4 shows plots of the average hydrophilicity and average scaled hydrophilicity of the system for each of the four positions labeled in Fig. 10-3. These plots were computed by first meshing the entire simulation box with evenly-spaced grid points separated by a distance of 0.1 nm. Configurations of the system were then sampled for $\lambda = 1.0$ and each grid point recorded the number of times it was excluded by hydrophobic or hydrophilic beads. The average hydrophilicity is defined for each grid point as the number of times it was excluded by hydrophilic beads divided by the number of times it was excluded by hydrophobic beads so that larger values of the hydrophilicity correspond to spatial regions that are predominantly occupied by hydrophilic beads. The average scaled hydrophilicity is the hydrophilicity multiplied by the total number of times the grid point is excluded by at least one bead divided by the total number of configurations sampled. The hydrophilicity alone thus provides information about the average arrangement of hydrophilic and hydrophobic beads in the system, while the scaled hydrophilicity provides information about the preference of hydrophilic beads for certain areas of the system. Given that the system has cylindrical symmetry around the x-axis, the plots are graphed in two dimensions as a function of the distance along the x-axis and the radial distance from the x-axis; grid points with a z-coordinate greater than 0 are drawn along

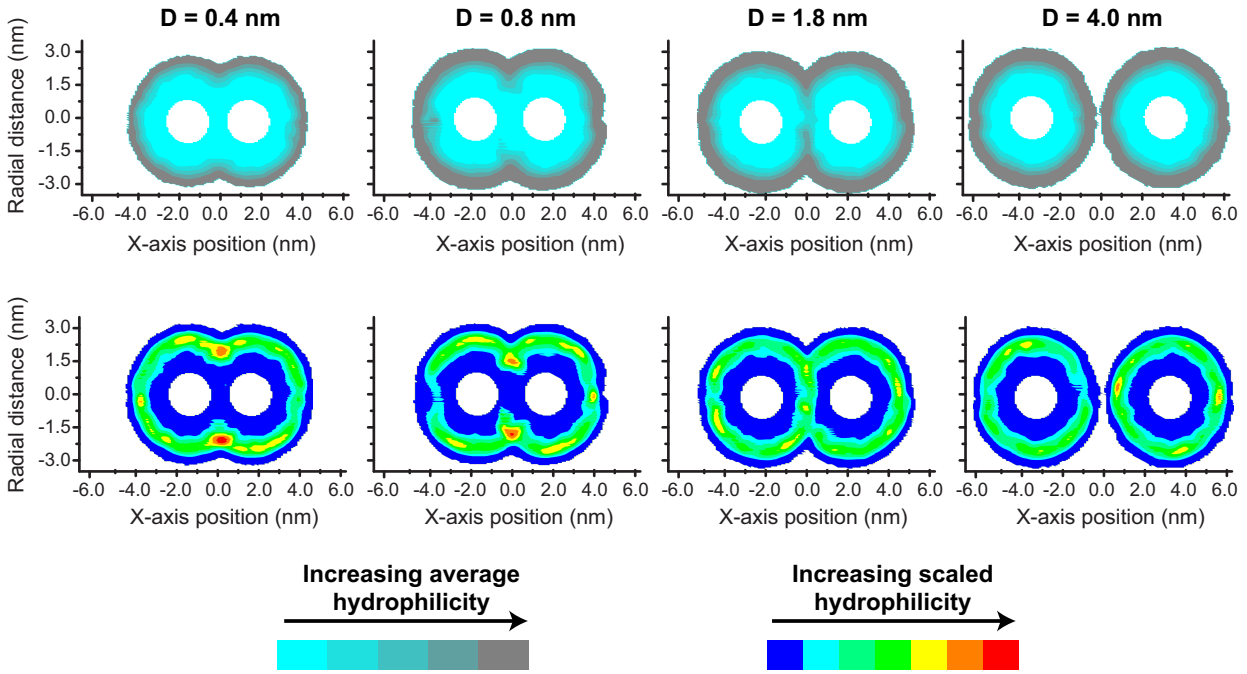

Figure 10-4: Plots of average hydrophilicity and scaled hydrophilicity (definitions in text) for four particle separations. The simulation parameters and particle separations are identical to those shown in Fig. 10-3.

the positive radial axis.

The four sets of plots demonstrate the physical origins of the trends shown in Fig. 10-3. At close separation ($D = 0.4$ nm), the average hydrophilicity shows that the interfacial region between the two particles is entirely hydrophobic because of the deformation of ligands to associate hydrophobic beads together while excluding hydrophilic ones. Moreover, the scaled hydrophilicity shows that the density of hydrophilic beads is particularly high near the interface of the two particles, demonstrating the constraints of ligand positioning that lead to entropic penalties. At the metastable state ($D = 0.8$ nm), the same basic trends are observed but the density of hydrophilic material at the interface is spread over a larger volume, diminishing the entropic penalty while still preserving the favorable association of hydrophobic material. This observation explains the dominance of the SASA term over the entropic term that leads to metastability at this position. At $D = 1.8$ nm, the plots show that the interface between the two particles contains a significant amount of hydrophilic material. This state corresponds to a maximum electrostatic penalty as the charge density at the interface is high. The lack of interfacial hydrophobic beads also indicates a minimal decrease in the SASA and hence minimal attractive interactions. Finally, at $D = 4.0$ nm, the plots show the typical uniformity of hydrophilic beads around each separate NP with slight regions of higher density due to the tendency of ligands to cluster in the baseline state. Overall, this analysis illustrates the correspondence between ligand deformation, as judged by the displacement of hydrophilic beads, and the relative attraction of the NPs.

10.3 Size-dependence of aggregation

The importance of ligand deformation raises the question of how NP core size affects aggregation. Given that ligand deformation is necessary to stabilize short-range aggregation, it would be expected that aggregation would be less favorable for larger particles where ligand fluctuations are inhibited as was shown to be the case for bilayer insertion (see Chapters 3-5).

Fig. 10-5 shows the free energy change associated with the aggregation of the six possible combinations of particles with sizes of 1.0, 2.0, and 3.0 nm for a SASA parameter of $\gamma = 0.0472$ kT/nm^2 and salt concentration of 150 mM. The general trend of the curves is as expected – aggregation between larger particles is increasingly unfavorable, with the size of the NPs both determining the height of the electrostatic barrier and the depth of the metastable point (if one exists). For NP combinations where at least one of the NPs has a diameter of 1.0 nm, the total free energy change has metastable state induced by ligand interactions. The simulation snapshots in Fig. 10-5b illustrate that the large amount of free volume accessible to ligands in small NPs allow for favorable deformation even when interacting with a larger NP, while two large NPs effectively retain uniform surfaces with minimal deformation due to the lack of ligand free volume. This result implies that in polydisperse samples of particles the smallest particles may be expected to aggregate with either other small particles or NPs with larger core diameters. A metastable point is also observed for two particles with identical diameters of 2.0 nm as previously noted. However, particle combinations of 2.0 - 3.0 nm and 3.0 - 3.0 nm both show large free energy barriers consistent with inhibited deformation and high electrostatic penalties and would be expected to disperse in solution. Note that because the x-axis is plotted as a function of the distance between the particle surfaces, the length scale of ligand interaction is approximately the same for all particle combinations, leading to similar trends for each combination shifted depending on the relative magnitudes of the attractive and repulsive interactions.

Fig. 10-6 shows the free energy change for aggregation of the same six particle combinations, but now with a SASA parameter of $\gamma = 0.0792$ kT/nm^2 and still at 150 mM salt concentration. In contrast to the previous results, for an increased SASA parameter changing the relative particle sizes only affects the height of the electrostatic barrier, with all particle combinations demonstrating thermodynamically-favored aggregated states. The plots indicate a significant qualitative difference in behavior compared to the previous results with a smaller SASA parameter; in this case, any aggregates that form would be stable long periods of time as the barrier for dissociation is significantly larger than the barrier for initial aggregation. Furthermore, the similar free energy changes between different particle sizes implies that the ligand-mediated attractive interactions compensate for the increased electrostatic repulsion as size increases.

The difference in behavior in these results, both quantitatively and qualitatively, underscores the importance of choosing an appropriate SASA parameter to describe the hydrophobic effect in this system. The two representative SASA parameters considered here have both been used to explain biological phenomena; for example, the value of $\gamma = 0.0472$ kT/nm^2 has successfully reproduced hydrophobic interactions between transmembrane proteins and lipid bilayers [172], while

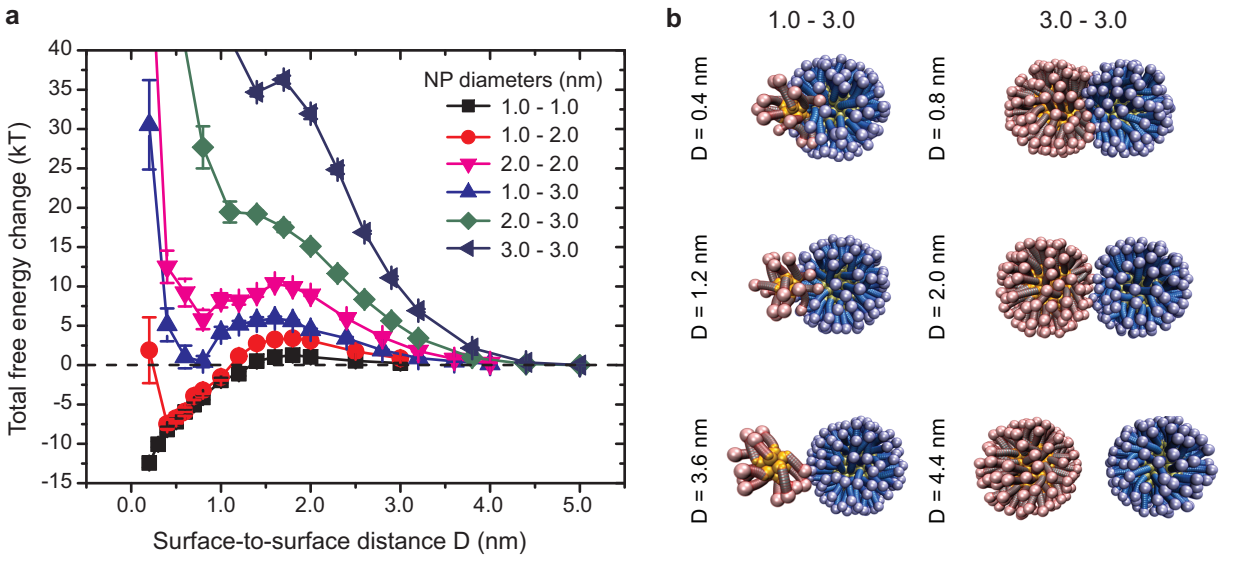

Figure 10-5: Aggregation of NPs with different core diameters. **a** Free energy change as a function of particle separation for different particle sizes. The salt concentration is set to 150 mM and $\gamma = 0.0472$ kT/nm^2. **b** Example simulation snapshots of a 1.0 - 3.0 NP combination and a 3.0 - 3.0 NP combination.

the value of $\gamma = 0.0792$ kT/nm^2 has been applied (with curvature corrections) to explain protein folding and ligand-receptor interactions [175]. In Chapters 3-5, it was determined that the larger SASA parameter ($\gamma = 0.0792$ kT/nm^2) was more appropriate for describing the insertion of a NP into the bilayer. However, this does not necessarily indicate that it is correct to use this parameter for describing NP aggregation. As the SASA parameter depends on geometric variables and the governing length scale of hydrophobic interactions, it is difficult to determine an appropriate parameter *a priori*. However, because the qualitative aggregation behavior is different, an appropriate SASA parameter, and thus solvent quality, may be determined experimentally in future work by observing if aggregation is strongly size-dependent. Given the relatively small range of NP sizes considered here due to computational limitations, it is likely that the same trends identified for the smaller value of γ will appear for larger NP sizes as well.

10.4 Modifying NP interaction free energies

The dependence on NP size shows the importance of both long-range electrostatic repulsion and short-range ligand-mediated attraction in controlling the free energy change for aggregation. In principle, it would be ideal to vary these long- and short-ranged terms independently by varying system characteristics. One key environmental property that may change depending on application is the local salt concentration, which modifies the Debye length of the system. In the simple Debye-Hückel screened Coulombic model used here, modifying the Debye length leads to significant changes in the electrostatic energy barrier. Fig. 10-7 shows the free energy change for aggregation

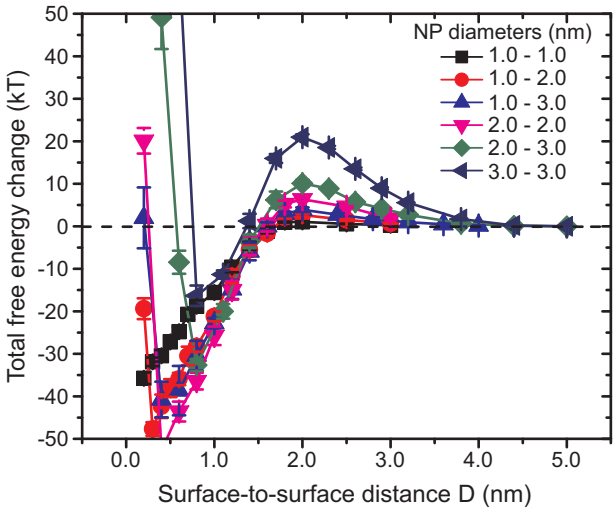

Figure 10-6: Free energy change as a function of particle separation for different particle sizes. The salt concentration is set to 150 mM and $\gamma = 0.792$ kT/nm^2.

between two NPs with core diameters of 2.0 nm with Debye lengths of 0.8 nm, 1.36 nm, and 2.5 nm, corresponding to salt concentrations of 150 mM, 50 mM, and 15 mM respectively [302]. Both values of the SASA parameter are used with open symbols representing the larger value (0.0792 kT/nm^2). As the Debye length increases, the effective electrostatic repulsion becomes strong due to lessened screening between charges, increasing the magnitude of the energy barrier for aggregation. However, at very short separations, there is still a slight attractive well corresponding to ligand-ligand attraction for both SASA values. For a stronger SASA parameter this attractive term can still dominate even in the case of strong electrostatic repulsion, emphasizing again the importance of ligand deformation to stabilize aggregation.

Just as modifying the salt concentration controls the magnitude of the long-range electrostatic energy barrier, changing ligand lengths should modify the short-range attractive interactions. Longer ligands have more hydrophobic surface area exposed to water on average as the ligands fluctuate on the surface which would increase the hydrophobic driving force. Similarly, within the united atom model the additional free volume due to the extended diameter of the ligand shell allows for more flexibility of the ligands to stabilize aggregated states. The inverse reasoning applies to shorter ligands, which have both less hydrophobic surface and less ability to freely deform due to more close packed head groups. Fig. 10-8 shows free energy changes for 2.0 - 2.0 nm complexes with ligands with 8, 11, and 14 CH_2 groups along the backbone with accompanying simulation snapshots. The salt concentration is set to 150 mM and the SASA parameter is set to $\gamma = 0.0472$ kT/nm^2. As suggested, there is a vast disparity in the interaction free energies between the three different ligand lengths. Particles with the shortest ligands show an effectively monotonic increase in the free energy for association due to the minimal decrease in SASA and strong penalty for deformation at short associations. Conversely, particles with long ligands have

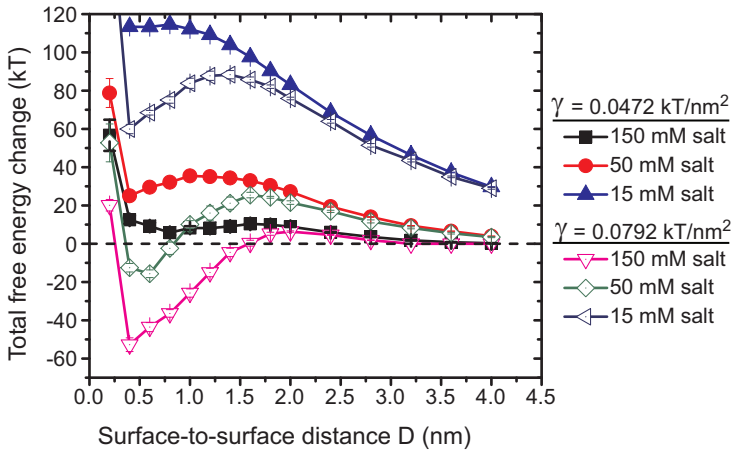

Figure 10-7: Free energy changes versus separation for three different salt concentrations and both values of γ. The particle core diameters are both set to 2.0 nm.

stable aggregation points at close separations, corresponding again to the greater flexibility and increase hydrophobic surface area of these long ligands. The simulation snapshots illustrate the disparity in flexibility, with the short ligands effectively retaining a uniform distribution of end groups while the longer ligands are able to deform to stabilize close NP-NP association. While in principle longer ligands may crystallize in real systems [315], this analysis still underscores the importance of tuning ligand sizes even for relatively small changes in the alkanethiol backbone.

Aside from the lengths of the ligands in the monolayer, another critical system property that may be modified synthetically is the grafting density of the ligands on the NP surface. In general, the grafting density may be a function of the particle size [209, 210] or may be tuned by synthetic methods [316, 317]. To test the role of grafting density, particles were prepared with 80%, 90%, 100%, 110%, and 120% of the 4.77 ligands/nm^2 grafting density used in other simulations, corresponding to grafting densities of 3.82, 4.29, 4.77, 5.25, and 5.72 ligands/nm^2 respectively. Fig. 10-9 shows free energy changes for 2.0 - 2.0 nm dimers with ligands with 11 CH_2 groups, a salt concentration of 150 mM, and with $\gamma = 0.0472$ kT/nm^2. Increasing the grafting density increases the energy barrier associated with long-range electrostatic repulsion and decreases the magnitude of the free energy well observed at close particle association. The increase in the electrostatic barrier is consistent with the increasing number of charged groups at higher grafting densities, as expected. The decrease in the magnitude of the free energy well is related to the reduction in the free volume per ligand at higher densities, minimizing the ability of ligands to deform to stabilize aggregation. This inhibited ligand deformation at high grafting density is similar to the steric stabilization of larger colloids, and increasing the grafting density in this system thus acts to enhance both electrostatic and steric repulsion. While these curves show that at higher grafting densities aggregation should not occur, the results from Fig. 10-7 suggest that a larger value of γ can lead to aggregation even when a substantial barrier exists for $\gamma = 0.0472$ kT/nm^2. As the more accurate value of γ is unclear as discussed previously, aggregation may still occur in the physical system

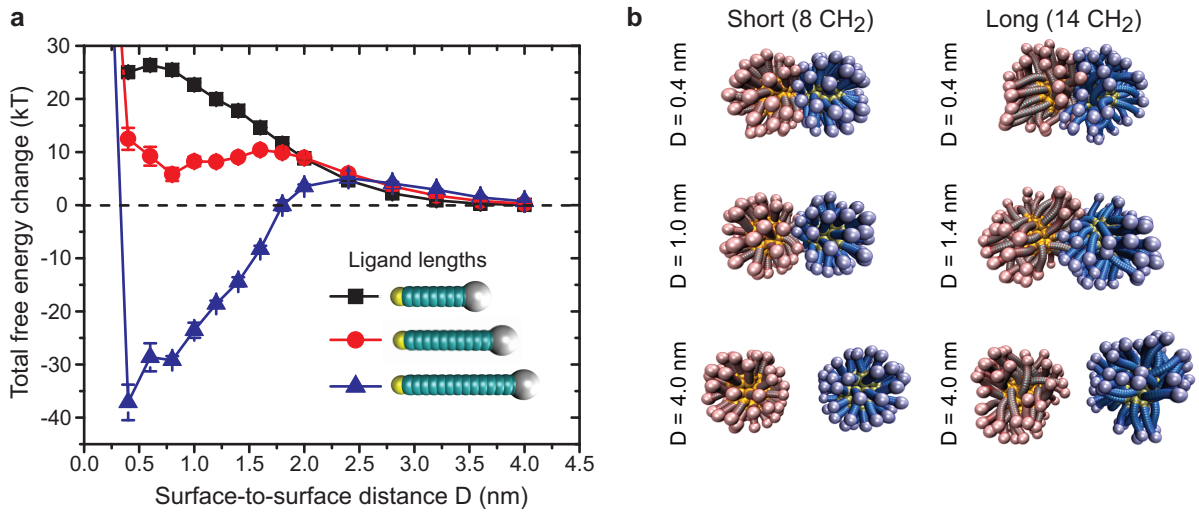

Figure 10-8: Aggregation of NPs with varying ligand lengths. **a** Plots of the free energy change as a function of particle separation for ligands with 8, 11, and 14 alkyl groups along the alkanethiol backbone. The relative ligand lengths in the united atom model are shown in the bottom right. All particle diameters are set to 2.0 nm, the salt concentration is 150 mM, and $\gamma = 0.0472$ kT/nm^2. **b** Example simulation snapshots of NPs with either short 8 alkyl group ligands (left) or long 14 alkyl group ligands.

despite the strong barriers shown here for high grafting densities. However, the general trend of increased barriers for increased grafting density should be independent of γ as in Fig. 10-7.

10.5 Mixed ligand monolayers

Up to this point, the free energy change for aggregation has only been computed between two NPs that are functionalized with entirely end-functionalized ligands to demonstrate general principles that control stable aggregation. However, these NPs were shown to be the least likely to fuse with bilayers (Chapters 3-5) and are of less interest than NPs with mixed ligand monolayers. As the previous results of demonstrated, however, NP aggregation is driven by the minimization of hydrophobic surface area and it would thus be expected that NPs with mixed, amphiphilic monolayers should exhibit a pronounced tendency to aggregate in comparison to their fully end-functionalized counterparts due to the addition of hydrophobic material to the monolayer.

To examine the aggregation behavior of mixed monolayer NPs, we simulated particles with 1:1 and 2:1 ratios of hydrophilic:hydrophobic ligands to match experimental systems [81]. As in the previous simulations, hydrophilic ligands were composed of 11 hydrophobic beads and a single bulkier hydrophilic bead (i.e. MUS). Hydrophobic ligands, by contrast, replaced the final hydrophilic bead with another hydrophobic bead, leading to chains of 12 hydrophobic beads. As a result, the hydrophobic ligands have more hydrophobic surface area, do not exhibit electrostatic effects, and have approximately the same ability to deform as the hydrophilic ligands. The particle

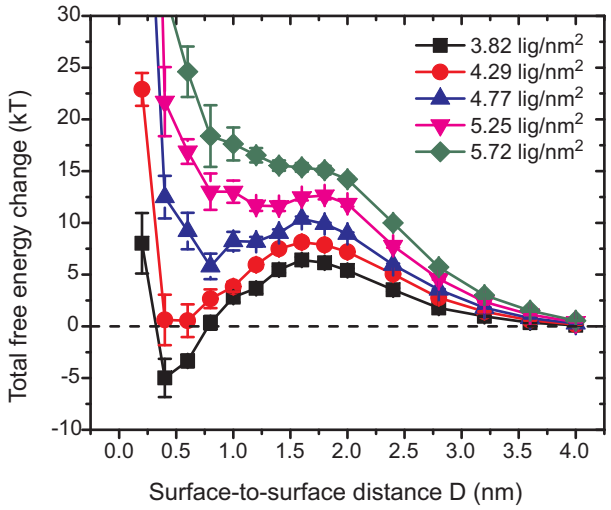

Figure 10-9: Plots of the free energy change as a function of particle separation for monolayers with grafting densities of 3.82, 4.29, 4.77, 5.25, and 5.72 ligands/nm^2, representing 80%, 90%, 100%, 110%, and 120% of the 4.77 ligands/nm^2 grafting density used in other simulations. All particle diameters are set to 2.0 nm, the salt concentration is 150 mM, and $\gamma = 0.0472$ kT/nm^2.

surfaces were created by selecting hydrophilic ligands and replacing with hydrophobic ligands in an approximately "checkerboard" manner to create as uniform a coverage of the surface as possible. The rest of the simulation methodology was conducted as previously described for particles coated with all-hydrophilic particles.

Fig. 10-10 shows results for the 1:1, 2:1, and all-MUS particle surfaces. The general profile is the same, exhibiting a long-range electrostatic barrier followed by short-range attractive well, with the value of the energy barrier decreasing with decreasing hydrophilic ligands. Similarly, increasing the number of hydrophobic ligands increases the strength of the short-range attractive interactions consistent with a stronger hydrophobic effect. Modifying the surface composition in a mixed system, then, can be thought of as simultaneously changing both the long-range and short-range interactions to encourage more particle aggregation. Combined with the previous results, this analysis suggests that in order to disperse mixed particles it would be optimal to reduce the lengths of the components as much as possible, or perhaps to elongate one while shortening the other. Alternatively, increasing the grafting density or increasing the NP size could also reduce ligand free volume and inhibit aggregation while also increasing electrostatic repulsion.

10.6 Conclusions

In this Chapter, we provide a first exploration of the mechanism by which charged, monolayer-protected NPs may stably aggregate, driven by the same physicochemical factors that drive bilayer insertion. The close association of two NPs can reduce the amount of exposed hydrophobic area, leading to short-range attraction due to the hydrophobic effect just as in the case of bilayer in-

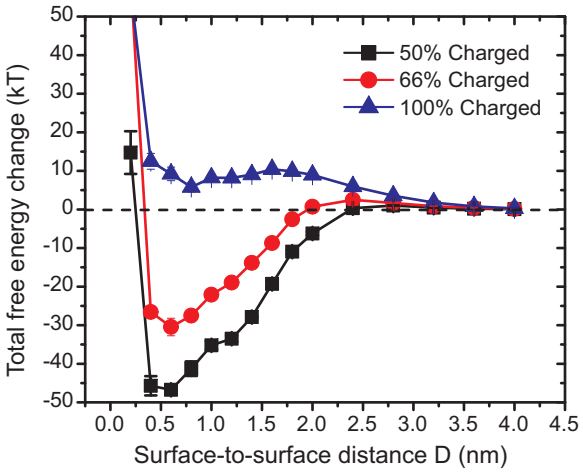

Figure 10-10: Plots of the free energy change as a function of particle separation for monolayers with 50%, 66%, and 100% charged end-functionalized ligands. All particle diameters are set to 2.0 nm, the salt concentration is 150 mM, and $\gamma = 0.0472$ kT/nm^2.

sertion. In order to optimally reduce the hydrophobic area, however, the ligands must be capable of deforming in response to the presence of the other particle which leads to a penalty due to the reduced configurational entropy of the ligands. We show that the free energy change as a function of particle separation for two monolayer-protected NPs can be modified by changing the ligand length, surrounding salt concentration, fraction of end-functionalized ligands, and particle size.

These results indicate that aggregation depends on the amount of free volume accessible to ligands, the magnitude of electrostatic interactions, and the amount of accessible hydrophobic surface area prior to aggregation. The results suggest a set of guidelines for the rational selection of system properties to control aggregation:

- Increasing NP particle size inhibits aggregation by decreasing the free volume per ligand.
- Increasing ligand lengths encourages aggregation by increasing ligand fluctuations and increasing the solvent accessible surface area.
- Increasing the relative number of hydrophobic ligands in the monolayer encourages aggregation by decreasing the magnitude of electrostatic interactions and increasing the solvent-accessible surface area.
- Increasing the solution salt concentration encourages aggregation by decreasing the magnitude of electrostatic interactions.
- Increasing the grafting density inhibits aggregation by both increasing the magnitude of electrostatic interactions and decreasing the free volume per ligand.

These guidelines may be useful in designing suspensions of NPs stable under biological conditions, or conversely may lend insight into controlling the self-assembly of NPs if desired. Moreover,

the guidelines also suggest methods for designing NPs that may still insert within bilayers while resisting aggregation. Specifically, choosing NP sizes that are below the threshold for stable insertion (Chapters 3-5) but are sufficiently large to inhibit aggregation would be optimal, leading to a reduced size range suitable for optimal NP-bilayer fusion.

This model only considers interactions between pairs of particles to show the origin of ligand-mediated attractive interactions, but in principle multiple particles could aggregate to form higher-order clusters. It is not clear whether cluster formation can be described by pair-potentials between particle dimers or requires a description of many-body interactions that are not included here, so the coagulation of a NP suspension cannot be predicted from this model alone. Despite this limitation, the phase behavior of colloidal materials with long-range repulsion but short-range attraction had been studied in detail before [318, 319, 320], and thus it may be expected that these NPs may form similar structures. Future work will concentrate on determining interactions between three and more particles in order to predict the phase behavior of higher-order aggregates in this system.

THIS PAGE INTENTIONALLY LEFT BLANK

Chapter 11

Bilayer Deformation by Embedded NPs

Work in this chapter was published in:

R. C. Van Lehn and A. Alexander-Katz, "Membrane-embedded nanoparticles induce lipid rearrangements similar to those exhibited by biological membrane proteins" – **Submitted**.

In Part I and Part II, we used a combination of simulation techniques to demonstrate that NP-bilayer fusion can be thermodynamically favorable and occurs spontaneously in the presence of lipid protrusions. These simulations were all performed in the single NP limit and ignored any possible influence of embedded NPs on each other. Previous studies of lipid rearrangements around embedded transmembrane proteins have shown that proteins can induce changes in the bilayer thickness, tail disorder, head group order, and other structural parameters [321, 74, 322]. Such perturbations of membrane structure can trigger protein aggregation [323, 324, 325], cell signaling [326, 327, 328, 329], membrane fusion [330, 331, 332], and even large scale membrane remodeling [135, 333, 334]. Given the similarity between the NPs studied here and transmembrane proteins, it is possible that NPs induce many of the same structural perturbations exhibited by proteins, but with the benefit of controllable surface properties. Additionally, while tail protrusions are rare events, previous work has established that the disruption of bilayers by fusion peptides may increase the frequency of tail protrusions [259, 284], which may also occur around embedded particles as well. Identifying how embedded NPs induce perturbations in the surrounding lipid annulus could thus lead to significant physical insight into the effects of NPs on their surroundings and in particular on how NPs may cooperatively lower the barrier to insertion or induce membrane-mediated aggregation.

In this Chapter, we use atomistic molecular dynamics simulations to gain molecular-level insight into lipid rearrangements around an embedded NP. In particular, we aim to identify how the composition of the NP monolayer affects changes in the surrounding lipid annulus. The simulations show that changing either the NP composition or NP core diameter has a significant effect on bilayer thinning near the NP-bilayer interface. We further show that the highly charged NP surface attracts surrounding lipids due to their zwitterionic head groups, condensing lipids toward the NP surface and reorienting head group dipoles. Near the NP-bilayer interface, lipid tails are disordered and correspondingly lipid tail protrusions are enhanced as was previously observed in the vicinity of fusion peptides [284]. Finally, we find that lipids can be extracted from the bilayer entirely to preferentially adsorb onto the water-exposed NP surface. Our work thus shows that embedded NPs can drastically perturb the surrounding membrane with the extent of such deformation determined in part by the monolayer composition.

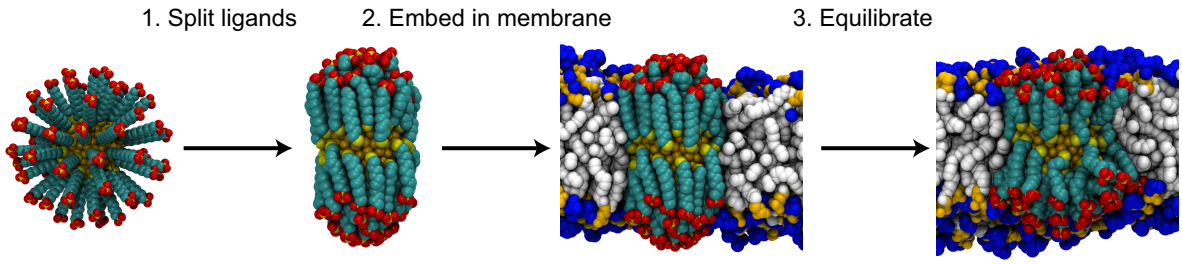

Figure 11-1: Workflow for embedding a NP in a bilayer.

11.1 Workflow for modeling bilayer deformation

Molecular dynamics simulations were conducted to simulate NPs embedded in a DOPC bilayer in a physiological (150 mM) NaCl salt concentration at 300 K following similar systems studied in previous Chapters. To probe the role of monolayer composition and particle size in determining the deformation of the surrounding bilayer, several combinations of ligand compositions and particle sizes were simulated. Following previous chapters, MUS, OT, and HDT ligands were all modeled in all-MUS, 1:1 MUS:OT, and 1:1 MUS:HDT compositions with gold core diameters of both 2 and 3 nm, yielding a total of six simulation systems.

Each NP was embedded in a lipid bilayer originally containing 512 DOPC molecules that had been pre-equilibrated for 100 ns in 150 mM salt solution. The size of the bilayer was chosen to ensure that any lipid deformations would decay before reaching the box edge. The embedding procedure followed a three step workflow as summarized in Fig. 11-1. First, the desired NP had forces applied to all MUS end groups in vacuum to split the MUS groups onto either side of the NP center, effectively elongating the NP along the z-axis. Next, the split NP was inserted into a pre-equilibrated bilayer using *g_membed*, a Gromacs tool typically used for the preparation of membrane protein systems [280]. *g_membed* works by shrinking the NP, placing it at the desired position in the middle of the bilayer, removing any occluded lipids/water/salt, then slowly "growing" the NP back to its original size while allowing surrounding lipids to relax. After this procedure, additional water was added to the system to resize the box to 10.5 nm along the z-axis (with the bilayer in the x-y plane), leading to approximately 3.5 nm of space between periodic images of the NP in the z-dimension to eliminate interactions between periodic images. Similarly, sufficient ions were added back to the system to regain a charge-neutral 150 mM NaCl solution. Finally, the system was allowed to relax for 50 ns at constant temperature and pressure using the parameters described in Appendix D.

Each NP-bilayer system was run for a total of 400 ns. The first 50 ns of each simulation were treated as equilibration time and were disregarded during analysis. All six systems were simulated twice from different initial embedded positions and different initial atom velocities to provide better statistics for the system. All simulations were performed using Gromacs version 4.6.1 [246]. Table 11.1 summarizes the components of all twelve systems. A single run of a pure bilayer with ions but no NP was also run for 400 ns as a control.

Table 11.1: Summary of simulation systems

NP type and size	Ligands	Lipids	Water	Ions (Na/Cl)	Atoms	Interface dist. [nm]
all-MUS, 2nm (1)	58	496	35,145	158/100	133,579	1.9
all-MUS, 2nm (2)	58	494	35,128	158/100	133,420	2.0
all-MUS, 3nm (1)	130	486	34,900	230/100	133,746	2.7
all-MUS, 3nm (2)	130	484	34,874	230/100	133,560	2.7
1:1 MUS:OT, 2nm (1)	58	496	35,219	129/100	133,569	1.6
1:1 MUS:OT, 2nm (2)	58	496	35,209	129/100	133,539	1.6
1:1 MUS:OT, 3nm (1)	130	490	35,062	165/100	133,569	2.4
1:1 MUS:OT, 3nm (2)	130	486	35,037	165/100	133,637	2.4
1:1 MUS:HDT, 2nm (1)	58	494	35,202	129/100	133,671	1.7
1:1 MUS:HDT, 2nm (2)	58	494	35,200	129/100	133,665	1.7
1:1 MUS:HDT, 3nm (1)	130	494	35,115	165/100	134,888	2.5
1:1 MUS:HDT, 3nm (2)	130	494	35,111	165/100	134,876	2.5
Pure bilayer, no NP	N/A	512	35,655	100/100	134,813	N/A

Given the difference in NP core size and ligand length, it is useful to scale structural parameters by the distance from the NP-bilayer interface rather than the center of the NP to facilitate comparison between NPs with varying characteristics. In general, the exact interface between the NP and bilayer is similar to a liquid-liquid interface with some lipid head groups extending farther into the general NP region than others and likewise some NP ligands protruding into the surrounding bilayer more than others. We chose to define the NP-bilayer interface as the radial distance from the center of the gold NP core where the number density of the charged phosphorus atoms in the bilayer was equivalent to the number density of the sulfur atoms in the MUS end groups of the ligands on the NP. This choice was motivated by the tendency of these atoms to be approximately co-planar. The interface was determined by first projecting the positions of these atoms into the x-y plane then calculating the radial number density of each component separately as a function of the distance from the NP center. As would be expected for a liquid-liquid interface, the density of each component has a bulk value far from the interface then decays through the interfacial region until reaching 0 (Fig. 11-2). It is clear from this plot that there is a region of finite width where the number density of both components is positive and the two components are mixed in a diffuse interface. The dashed vertical lines indicate the position where the number densities are approximately equal. This distance was calculated for all twelve systems and was nearly identical between duplicate runs of the same system and is summarized in Table 11.1.

11.2 General deformation profiles

The number densities of important system constituents were calculated around each embedded NP to first illustrate the general deformation features. The NP-bilayer system was broadly divided into three components: the ligands that comprise the monolayer of the NP, the zwitterionic head groups of the DOPC lipids, and the hydrophobic lipid tails. Fig. 11-3 plots the number densities of each of these components averaged radially around the axis of the NP, taking advantage of the

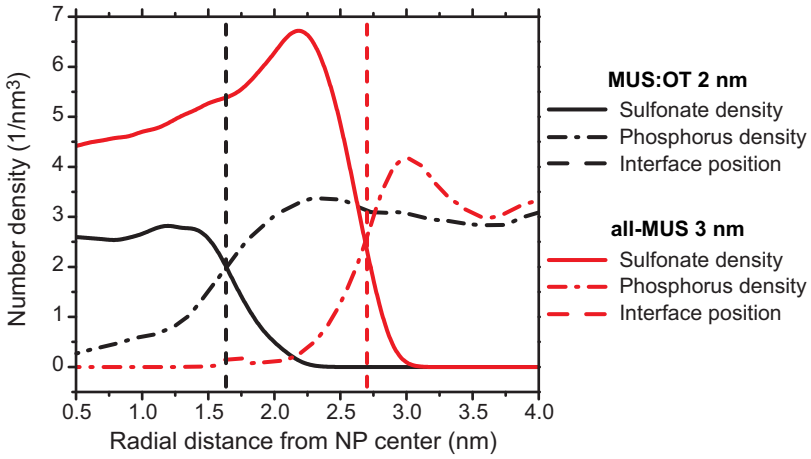

Figure 11-2: Definition of NP-bilayer interface. Examples for both a 2 nm MUS:OT NP and a 3 nm all-MUS NP are shown. The interface is defined as the intersection between the densities of the sulfonate and phosphorus beads as indicated by dashed vertical lines.

cylindrical symmetry of the system in the plane of the bilayer. Accompanying the number density profiles are representative snapshots of each NP-bilayer system. For each plot, the vertical dashed line indicates the approximate interface between the NP and bilayer used for rescaling the radial axes in measurements reported below.

Fig. 11-3 illustrates several general features. From the NP ligand densities it is apparent that the choice of monolayer composition leads to different effective NP shapes. For the all-MUS particles, the snorkeling of all charged end groups into solvent leads to an hourglass-like shape that imposes a boundary on the tilt of nearby lipids [335, 144]. For MUS:OT particles, the hydrophobic ligands can fluctuate within the hydrophobic bilayer core, creating a more uniform, cylindrical interface. Finally, the longer ligands in the MUS:HDT monolayers preferentially extend out into the hydrophobic core, inverting the hourglass shape of the all-MUS particles to create a large barrel-like boundary. The difference in these boundary conditions has been proposed to lead to attraction for hourglass-like shapes and repulsion for barrel-like shapes [335, 144], so these profiles indicate that monolayer composition may affect aggregation behavior.

For all NPs, the lipid head group densities show an apparent bilayer thinning effect in the vicinity of the NP as well as a slight enhancement of head group density near the NP-bilayer interface (slightly darker green in the color mapped density profile). The tail group densities further illustrate the thinning of the bilayer and generally match with the boundary conditions of the lipids. Notably, the lipid tails around MUS:HDT particles have a pronounced depletion effect near the region where the ligands extend into the bilayer. Another observation is a non-zero tail density in the region occupied by the NP for the 3 nm MUS:OT particle. Finally, comparing the 2 nm and 3 nm particle sizes show that the same basic features are observed for particles of the same composition, although the larger NPs lead to more pronounced deformations than the 2 nm particles (e.g. a thinner bilayer around the 3 nm all-MUS than 2 nm all-MUS particle). The origin

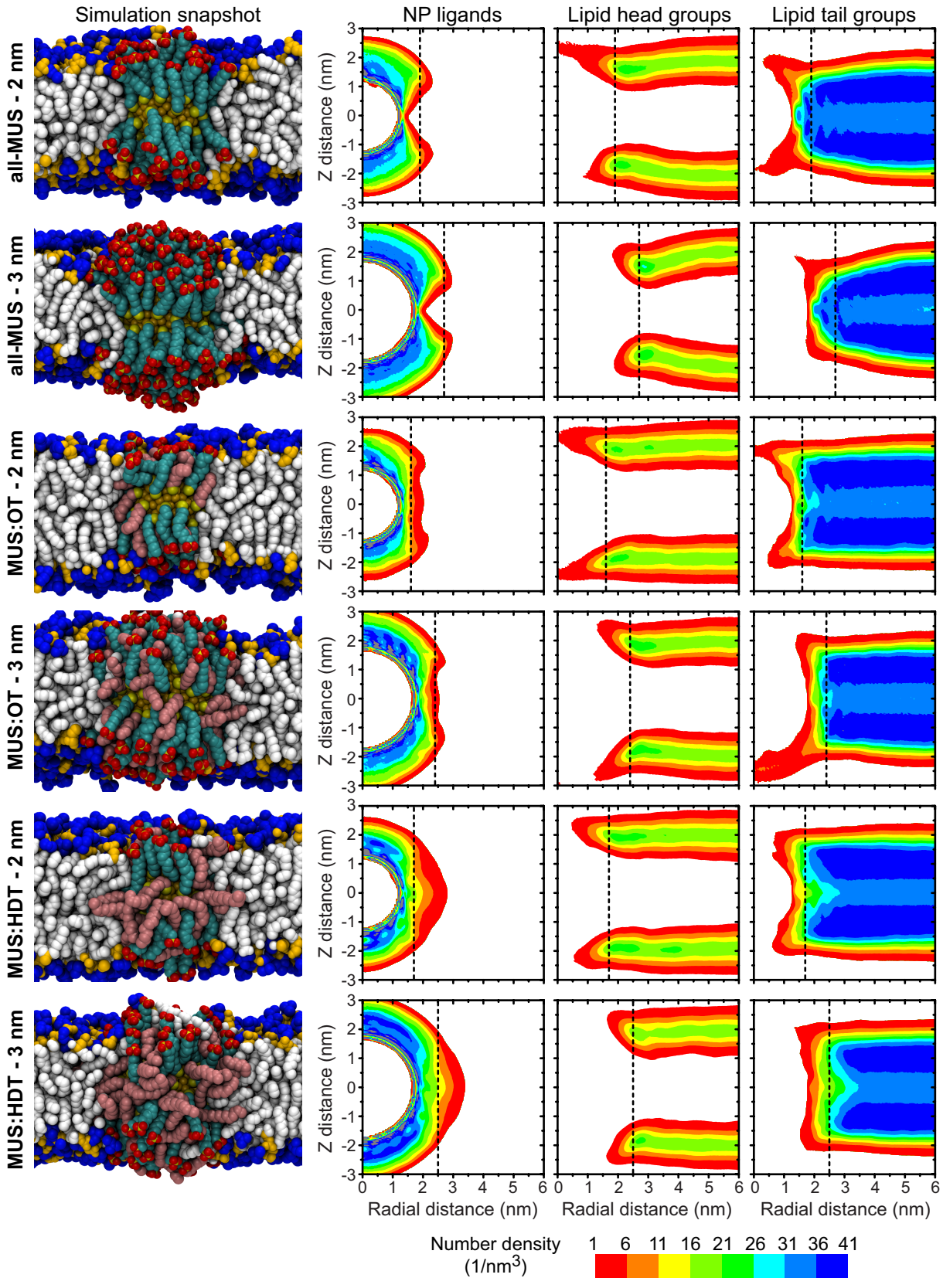

Figure 11-3: Number densities of system components, dashed lines indicate NP-bilayer interface.

of these different features will be discussed below.

11.2.1 All NPs induce negative hydrophobic mismatch

The number densities in Fig. 11-3 show that all of the NPs studied induce local bilayer thinning, a result predicted in Chapters 3 and 5 and agreeing with a recent experimental study of NPs embedded in floating bilayers [204]. To calculate structural parameters in the vicinity of the NPs more accurately, a grid-based method was developed to compute the area per lipid and bilayer thickness. For each simulation timestep, a 100 x 100 2D grid was created to span the x-y plane of the simulation box. The positions of all phosphorus atoms in the lipid head groups and all sulfur atoms in the MUS end groups were projected onto the x-y plane. The 2D distance between each grid point and all sulfur/phosphorus atoms was then calculated and the closest sulfur/phosphorus atom was assigned to each grid point for both monolayers separately. The bilayer thickness, D_{HH}, at each grid point was then defined as the distance between the z-position of the nearest phosphorus atom in the top monolayer and the z-position of the nearest phosphorus atom in the bottom monolayer; the point was disregarded if the nearest atom was sulfur in either monolayer. This method was additionally repeated for a pure bilayer without an embedded NP. Fig. 11-4 shows results for the bilayer thickness (a) and area per lipid (b) calculated for both a pure bilayer and a bilayer with a 3 nm all-MUS NP. The plots confirm the radial symmetry present in the system and illustrate the extent of deformation. Given this symmetry, the radial average was recorded by comparing the location of each grid point to the center of the NP, again projected into the x-y plane. Details of the area per lipid calculation are given below.

Fig. 11-5 shows the radial bilayer thickness profiles of the bilayer around the 2 and 3 nm NPs. All particle compositions induce significant bilayer thinning in the vicinity of the NP-bilayer interface. The MUS:HDT particles exhibit the lowest change in D_{HH} followed by MUS:OT and all-MUS, approximately following the amount of hydrophobic material present at the NP interface. A comparison between Fig. 11-5a and 11-5b further shows that increasing the NP size induces additional thinning, implying that very large particles may be unable to stably embed within the bilayer consistent with the size thresholds found in Part I. As the distance to the interface approaches 0, the bilayer thickness for all particle types increases with the MUS:OT and MUS:HDT particles causing the largest increase. This thickness increase is because lipid head groups are electrostatically attracted to the MUS end groups while lipid tail groups are also forced away from the bilayer center by steric interactions with the hydrophobic ligands that extend into the bilayer center (Fig. 11-3). Because the interfacial position is determined by the position of the MUS end groups, the hydrophobic ligands extend into the bilayer past the interface, leading to an increase for distances greater than 0. Finally, far from the NP the bilayer thickens relative to its thickness in the absence of the NP despite a plateau in D_{HH}. This effect may be due to the increase in the sodium ion concentration when a NP is added with its counterions to the system; sodium ions bind with the choline head groups of DOPC leading to enhanced electrostatic repulsion between the two bilayer leaflets and increasing the bilayer thickness [336]. The greater increase in thickness for the

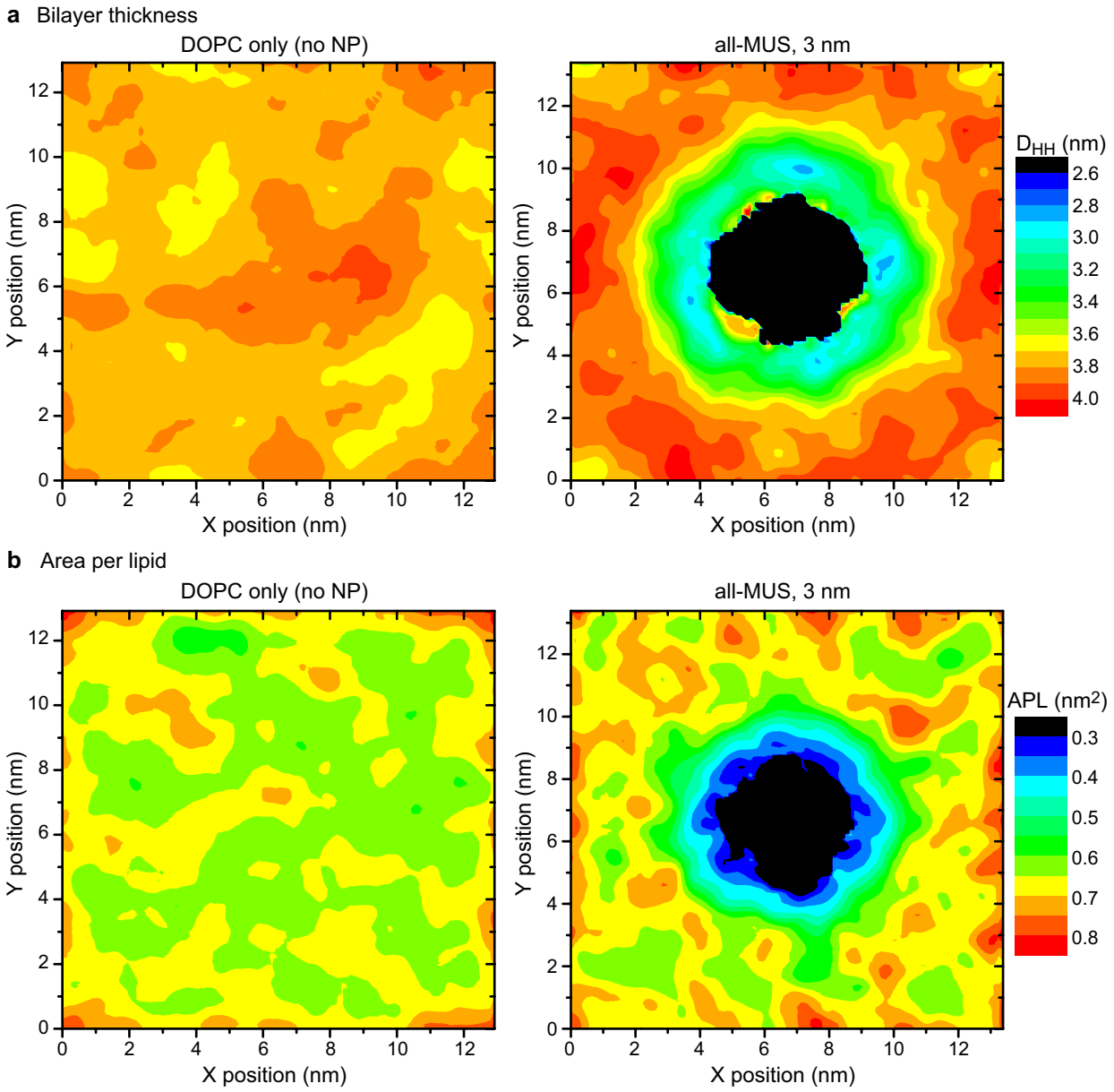

Figure 11-4: Color maps showing bilayer thickness (**a**) and area per lipid (**b**) averaged in x-y plane for pure bilayer system (left) or 3 nm all-MUS NP system (right).

3 nm all-MUS particle is due to the larger number of counterions in this system in comparison to the five others (see Table 11.1).

The change in the bilayer thickness may be attributed to the general principle of *hydrophobic mismatch* which is commonly used to describe the deformation of lipids around transmembrane proteins. Hydrophobic mismatch refers to the local modulation of bilayer thickness to shield exposed hydrophobic domains on embedded proteins from solvent [337, 321, 338, 339, 340]. The bilayer pays an energy cost for this disruption which is compensated by a reduction in the unfavorable solvation free energy of the hydrophobic surface in water. For this system, the bilayer deforms to match the

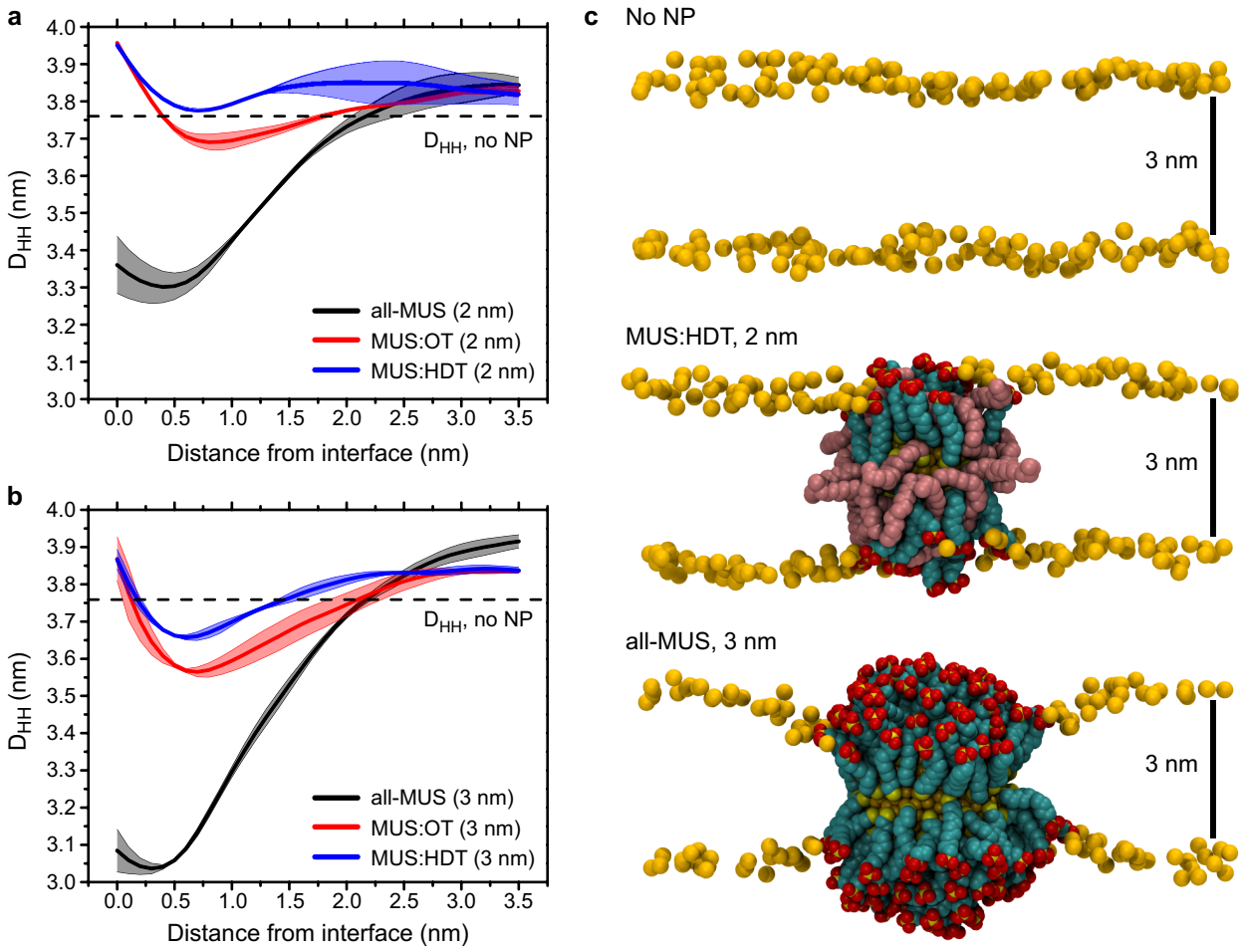

Figure 11-5: Bilayer thickness deformations around embedded NPs. **a** Thinning around 2 nm NPs of all three compositions. **b** Thinning around 3 nm NPs of all three compositions. **c** Representative snapshots of bilayer phosphorus atoms illustrating extent of deformations.

hydrophobic surface of the NP which is composed of a combination of the alkane backbones of the charged ligands and the alkane backbones of the purely hydrophobic ligands. For all systems, the bilayer thins locally and is thus under negative mismatch conditions with a thickness change of up to nearly 0.8 nm for the 3 nm all-MUS particle, an amount similar to what has been observed previously for deformations by transmembrane proteins [321, 338, 74, 38, 341]. In protein systems, hydrophobic mismatch may drive protein aggregation as the system minimizes the overall energy cost associated with deforming the surrounding bilayer [324, 325, 342]. The finding of a composition-dependent thickness profile suggests that the magnitude of this driving force for aggregation can be tuned by a choice of monolayer composition and particle size, potentially enabling tunable NP aggregation. Beyond NP aggregation, hydrophobic mismatch may have functional consequences on nearby proteins in a true cell membrane as protein function can be coupled to changes in local bilayer thickness [343, 327]. These results thus suggest that collections of NPs embedded in cell membranes may both exhibit clustering and affect nearby proteins.

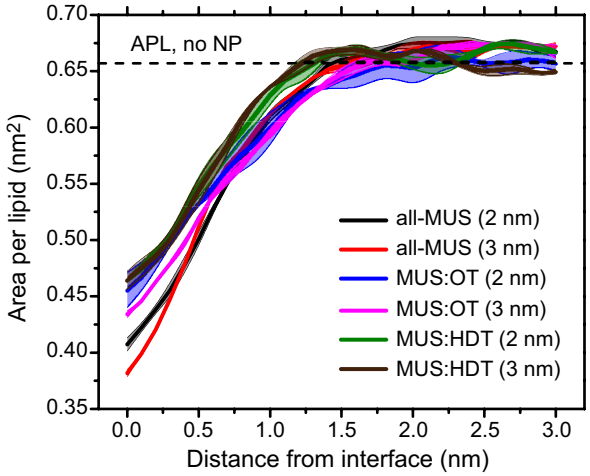

Figure 11-6: Area per lipid radially around all six NPs simulated. The dashed line indicates the APL for a pure bilayer with no NP as a control.

11.2.2 NPs condense head groups, re-orient head group dipoles

In addition to the bilayer thickness, another standard bilayer structural parameter is the area per lipid (APL) which is often used to indicate bilayer phase behavior. For example, in the gel phase, lipid head groups assume a hexagonally close-packed configuration that reduces the APL substantially from its value in the fluid phase [344]. As with the thickness, the grid method was used to calculate the APL as described previously. Based on the assignments of phosphorus/sulfur atoms to grid points, each phosphorus atom (and thus lipid) recorded the number of grid point which were assigned to that atom during the first step of the algorithm. An area per grid point was determined by dividing the box area for that simulation timestep by the fixed number of grid points and an area per lipid was then assigned to each phosphorus atom by multiplying the number of grid points assigned to that phosphorus atom by the area per grid point. In effect, this algorithm approximated the area of the Voronoi cell assigned to each phosphorus atom in the system using a discrete grid [345]. The radial average was then calculated based on the 2D distance of the phosphorus atom from the NP center. Applying this method to a pure bilayer (no NP) correctly yielded the same average area per lipid as simply dividing the box area by half the number of lipids, as expected.

Fig. 11-6 shows the APL measured radially away from the NP-bilayer interface. For all NPs, the APL decreases over approximately the same length scale and with nearly the same magnitude independent of particle type, although the two all-MUS particles show the greatest decrease throughout the entire profile. At distances far from the NP-bilayer interface, the APL returns to its baseline value for a pure bilayer, indicating no long-range disruption beyond approximately the first nanometer from the interface.

This decrease may be interpreted as a general condensing effect – the lipids are dragged closer to the surface of the NP. Interestingly, this condensing effect is achieved without thickening the bilayer,

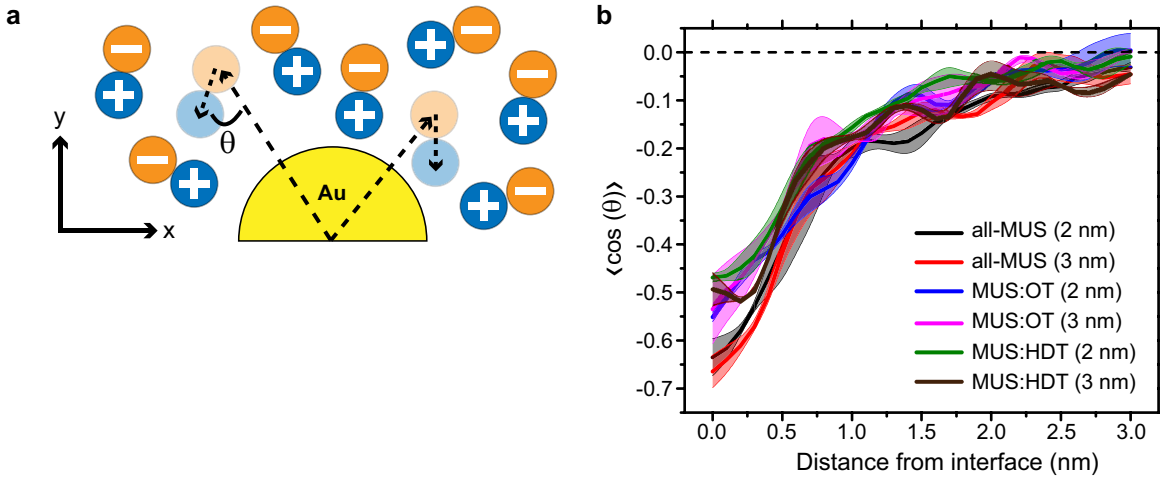

Figure 11-7: Reorientation of $P^- \rightarrow N^+$ dipoles near embedded NPs. **a** Definition of θ, the angle between the $P^- \rightarrow N^+$ vector and a reference vector to the NP center. **b** $\cos\theta$ as a function of the radial distance of lipid heads from the NP-bilayer interface.

which is the response typical of gel phase lipids [344] or lipids condensed by cholesterol [346] in which lipid tails also straighten. The observation of a locally thinner bilayer despite the dense lipid head group packing at the interface implies that lipid tails are disordering, rather than ordering, as will be discussed below. The similarity of the APL profiles for all particle types suggests that the reason for lipid condensation is due to a shared property of all the particles. One possibility is the high surface charge density of the NPs, a property not commonly associated with transmembrane proteins. The highly charged NP surfaces may attract the zwitterionic DOPC head groups leading to the preferential interaction at the interface and explaining the decay over approximately 1.0 nm, which is close to the Debye length of the system in 150 mM salt. The slightly lower APL for all-MUS particles may be due to their higher charge densities, as well.

To test whether electrostatic effects play a role in the attraction of lipid head groups to the NP surface, the orientation of the $P^- \rightarrow N^+$ vector in the lipid head groups was determined. The $P^- \rightarrow N^+$ dipole typically lies in the plane of the bilayer with no in-plane orientational preference, but in the presence of the highly charged NP it may rotate to bring the positively charged choline moieties closer to the negatively charged monolayer. To quantify the extent of rotation, the angle θ was defined as the angle between the $P^- \rightarrow N^+$ vector and a vector drawn from the center of mass of the NP core to the phosphorus atom of the lipid, with both vectors projected into the x-y plane as shown in Fig. 11-7a. In a bilayer without an embedded NP the average value of $\cos\theta$ was 0 as expected. In contrast, introducing any NP led to a decrease in $\cos\theta$ as shown in Fig. 11-7b. The decrease indicates a preferential reorientation of choline groups to face the NP with a limiting value of -1 indicating complete orientation of all $P^- \rightarrow N^+$ to face directly toward the NP center.

As with the APL results, the change in the head group dipole orientation occurs mostly over the first nanometer from the NP-bilayer interface, with $\cos\theta$ decreasing more slowly over the next two nanometers before achieving the bulk value. Head group reorientation can be attributed to

electrostatic interactions so the observation of a similar length scale between this measurement and the APL measurements implies that both observations may be related to electrostatic attraction, explaining why the same general trend is observed for all NPs. Similarly, both Fig. 11-6 and Fig. 11-7 show slightly more pronounced results for the higher charge density all-MUS particles. To the best of our knowledge, similar lipid head group reorientation has not been observed previously for lipid deformations around transmembrane proteins and thus the functional consequences of this effect are unknown. It is possible that this reorientation could influence the aggregation propensity of NPs in analogy to the thickness changes noted earlier as bringing two NPs into closer contact could minimize the number of lipids affected. A study of NP aggregation will be the focus of future work and will focus on the effect of such deformations.

11.2.3 NPs locally disorder lipid tails

Previous studies on negative hydrophobic mismatch conditions around transmembrane proteins have indicated that bilayer thinning should be accompanied by a decrease in tail order [338]. The change in tail order can be determined by calculating the deuterium order parameter, S_{CD}, for each of the methylene atoms in the lipid tails. The S_{CD} order parameter is defined as

$$S_{CD} = \frac{1}{2}\langle 3\cos^2\alpha - 1\rangle \tag{11.1}$$

where α is the angle between the $C \rightarrow D$ vector in a deuterated methlylene group and the bilayer normal. S_{CD} parameters are commonly compared to results from neutron scattering; larger values of S_{CD} are interpreted as indicating more tail order while lower values indicate disorder [347]. The order parameters were calculated according to standard methods from the literature for united atom acyl chains [347]. Since hydrogen (and thus deuterium) atoms are not explicitly represented for aliphatic groups, the S_{CD} parameter was calculated by assuming tetrahedral geometry at each methylene position. First, a new set of axes was defined relative to the methylene of interest. Denoting the central methylene as C_i, the new z-axis was defined as the vector from $C_{(i-1)}$ to $C_{(i+1)}$, the x-axis was defined as normal to the plane of $C_{(i-1)}$-C_i-$C_{(i+1)}$ (bisecting the missing hydrogen atoms), and the y-axis was taken from the cross-product of the z-axis and x-axis to ensure a right-handed coordinate system. The angles between each of these axes and the membrane normal were defined as α_x, α_y, and α_z respectively. In all simulations, the membrane normal was taken as the z-axis of the simulation box. Following these definitions, it can be shown that S_{CD} is calculated as [348]

$$S_{CD} = \frac{2}{3}S_{xx} + \frac{1}{3}S_{yy} \tag{11.2}$$

$$= \frac{2}{3}\left(\frac{\langle 3\cos^2\alpha_x - 1\rangle}{2}\right) + \frac{1}{3}\left(\frac{\langle 3\cos^2\alpha_y - 1\rangle}{2}\right) \tag{11.3}$$

Here, S_{xx} and S_{yy} are the orientational order parameters of the molecular axes relative to the

membrane normal based on the definitions above. This relationship is only valid for saturated methylene positions that have a tetrahedral geometry as the prefactors assume bond angles of approximately 109.5° [348]. DOPC is an unsaturated lipid and has two carbons joined by a double bond in each tail. For these carbons the axes were slightly redefined. The z-axis for the methylene of interest was instead drawn parallel to the double bond, the x-axis was normal to the plane created by the two carbons in the double bond and a third carbon bonded to one of these two, and the y-axis was the cross-product of the z-axis and x-axis as before. Using these new axes, S_{CD} for the unsaturated methylenes can be expressed as [348]

$$S_{CD} = \frac{1}{4}S_{zz} + \frac{3}{4}S_{yy} - \frac{\sqrt{3}}{2}S_{yz} \tag{11.4}$$

$$= \frac{1}{4}\left(\frac{\langle 3\cos^2\alpha_z - 1\rangle}{2}\right) + \frac{3}{4}\left(\frac{\langle 3\cos^2\alpha_y - 1\rangle}{2}\right) - \frac{\sqrt{3}}{2}\left(\frac{\langle 3\cos\alpha_y\cos\alpha_z - 1\rangle}{2}\right) \tag{11.5}$$

This definition was used for the C_9 and C_{10} methylene positions as defined in Fig. 11-8b. The two definitions above were implemented using a custom Gromacs tool written in-house. The order parameters were first calculated for each lipid in the simulation, then averaged over all lipids within bins a set radial distance away from the center of the NP as was done with the bilayer thickness and area per lipid measurements.

Fig. 11-8a shows the S_{CD} profiles for each of the NPs, with separate profiles shown for lipids 0-1 nm, 1-2 nm, and 2-3 nm away from each NP. Methylene positions are numbered according to the scheme in Fig. 11-8b. The all-MUS particles show significant disordering for lipids up to 2 nm away, with the lipids 2-3 nm away showing similar S_{CD} profiles to a pure bilayer. The profiles for both 2 and 3 nm NPs appear similar, implying that size is not as important as monolayer composition in determining tail group disorder. The MUS:OT particles show only a slight decrease in order for lipids up to 2 nm away while MUS:HDT particles show a decrease in order for only the lipids within 0-1 nm of the NP-bilayer interface. Unlike the all-MUS particles, only the methylene groups near the end of the tails have decreased S_{CD} values for both the MUS:OT and MUS:HDT particles while the methylene positions closer to the head group are relatively unperturbed. The tail disorder results thus roughly follow the thickness profiles from Fig. 11-5, with greater bilayer thinning corresponding to an enhanced decrease in lipid tail order. The shape of the NP boundary also likely contributes to the extent of disorder, as the cylindrical shape of the MUS:OT NP (Fig. 11-3) is commensurate with the preferred cylindrical shape of DOPC lipids, while both the hourglass-like all-MUS NPs and barrel-like MUS:HDT NPs require a perturbation of the preferred lipid structure to accommodate their interfaces. This likely explains the more significant disordering for MUS:HDT for lipids 0-1 nm from the interface compared to MUS:OT despite a smaller thickness perturbation.

To explain the origin of this disorder, the fraction of *gauche* (g^+/g^-) and *trans* (*t*) conformations assumed by rotations around dihedral angles in the acyl chains was computed. For each lipid, the dihedral angle, ϕ, of each pair of single-bonded carbon atoms in the tail was calculated. The double-bonded carbons were excluded as the rigidity of this bond prevents free rotation. Dihedral angles

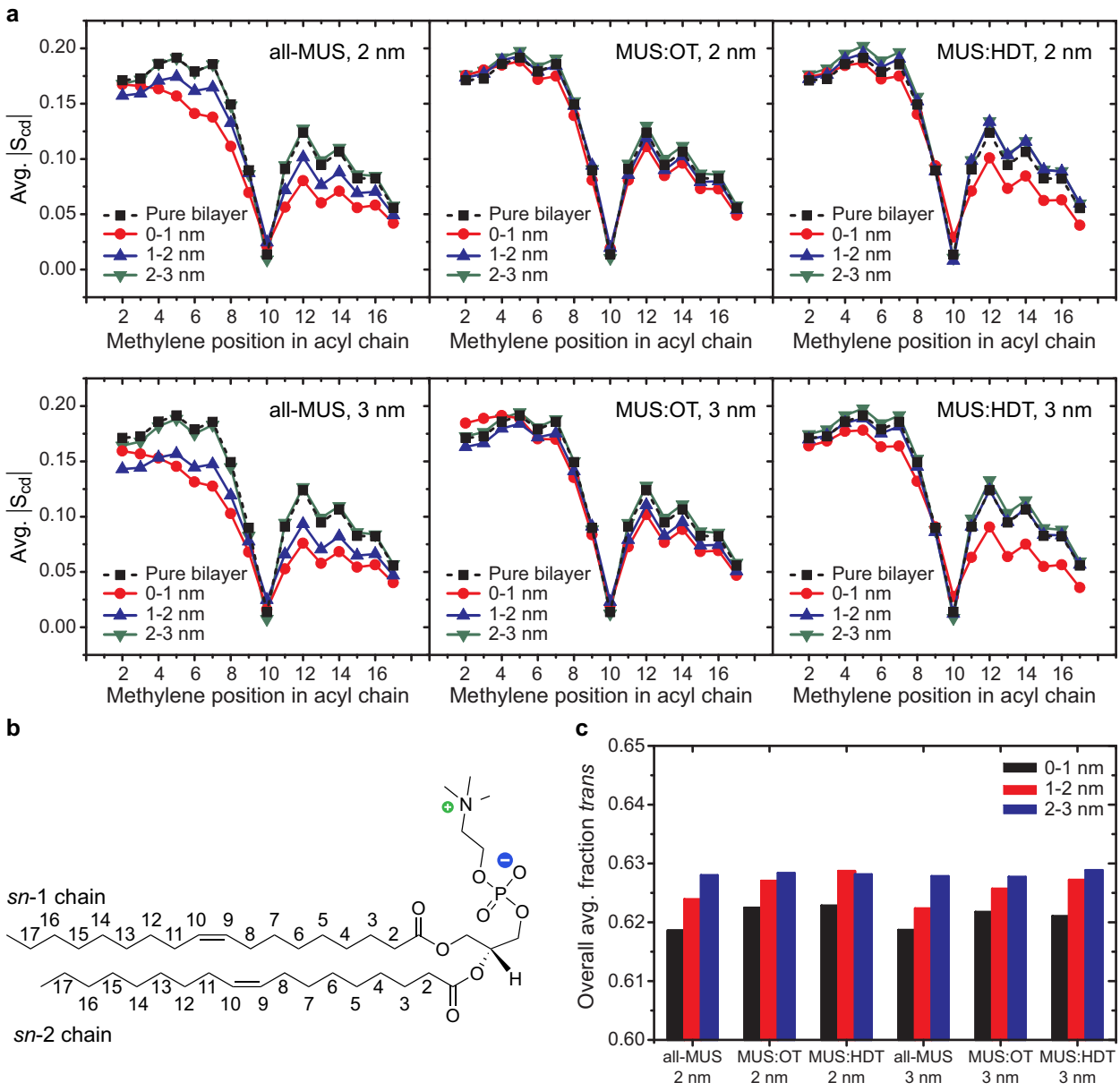

Figure 11-8: Summary of lipid tail disorder. **a** Lipid tail deuterium order parameters, S_{CD}, averaged over both the *sn*-1 and *sn*-2 tails. S_{CD} parameters are reported for each methylene position separately. Order parameters are reported separately for lipids 0-1 nm, 1-2 nm, and 2-3 nm away from the NP-bilayer interface. The order parameter for a pure bilayer with NP is shown as a black dashed line in each plot, though it is largely similar to the 2-3 nm results for all NPs. **b** Numbering scheme for methylene positions. **c** Average fraction of *trans* rotamers for each NP, sorted into same radial bins as in **a**.

were assigned as t if $\phi > 150°$ or $\phi < -150°$, g^- if $-90° \leq \phi < -30°$, and g^+ if $30° \leq \phi < 90°$. These definitions follow those of Poger et al [349, 283] and standard convention [350]. Again following the example of Poger et al, rotamer sequences were also identified after assigning a rotamer type to every pair of carbon atoms along the chain. The specific sequences identified were *eg* for *gauche* conformers of either type at the end of the chain, *gg* for a g^+g^+ or g^-g^- sequence, *gtg* for g^+tg^+ or g^-tg^- sequences, and gtg' for g^+tg^- or g^-tg^+ sequences [349, 283].Presumably, greater disorder would correlate with a larger number of *gauche* rotamers.

Fig. 11-8c shows the fraction of *trans* dihedrals for each of the different NPs for the same radial binning scheme. Surprisingly, the number of *gauche* dihedrals is only slightly affected, with the change on the order of only 1%, seemingly unable to explain the increased disorder. No clear pattern is evident for any of the particles and there is no obvious correlation with the results of Fig. 11-8a. To reconcile these differences, the average number of rotamer sequences was instead calculated as shown in Fig. 11-9. For all particles, lipids in the vicinity of the NP-bilayer interface showed a significant increase in the appearance of *gg* dihedral sequences, with the increase commensurate with the decrease in S_{CD} order shown in Fig. 11-8a. No other change in rotamer sequences was observed. The preference for *gg* sequences suggests that the change in tail direction associated with consecutive *gauche* rotamers is sufficient to disorder lipid tails even without increasing the average number of *gauche* conformations in the chain. A modified preference for particular rotamer sequences is also favorable energetically, as increasing the number of *gauche* conformations would bear an energetic cost compared to the lower energy *trans* conformations while simply switching the order of existing conformations allows lipids to accommodate the deformation with a lessened energy penalty.

The results from Figs. 11-4-11-9 show that all of the NPs induce local bilayer thinning and accompanying lipid tail disorder, while simultaneously condensing head groups toward the NP and triggering a preferential reorientation of the head group dipole due to electrostatic interactions. This combination of enhanced head group order with decreased tail group order emerges from the ability of the NPs to induce negative hydrophobic mismatch while exerting strong electrostatic forces on the zwitterionic lipid head groups.

11.3 Lipid tail protrusions enhanced in vicinity of NPs

In Chapters 7 and 8, we showed that the apparent rate-limiting step for NP insertion into the embedded state is the appearance of lipid tail protrusions. Such protrusions are typically rare in planar bilayers, but are more probable in the presence of membrane curvature [257]. Recently, it has been shown that transmembrane fusion peptides may also increase the probability of lipid tail protrusions in their vicinity by disrupting lipid tail order [259, 284], similar to the decrease in tail order described in Fig. 11-8. Based on this similarity, it is possible that lipid tail protrusions may also be more probable near embedded NPs.

Lipid tail protrusions were identified using the same criterion proposed by Larsson and Kasson

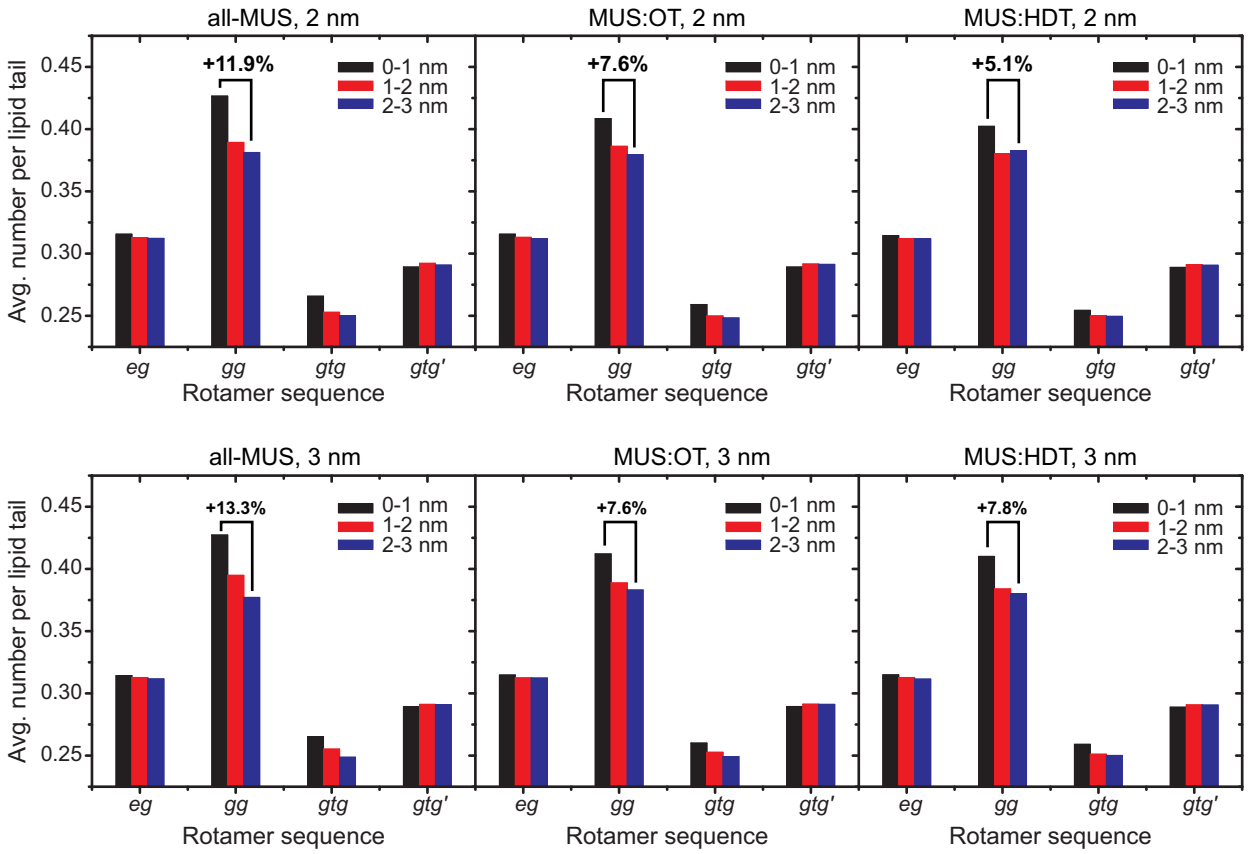

Figure 11-9: Average number of rotamer sequences per lipid for all particle types. Lipids are sorted by radial distance from the NP-bilayer interface.

[284]. For each simulation time step, the distance between every hydrophobic lipid tail atom and the nearest phosphorus atom was projected onto the membrane normal (the z-axis). If this distance was greater than 0.1 nm in the direction of the solvent (i.e. positive z-direction for the top monolayer, negative z-direction in the bottom monolayer) for any hydrophobic tail atom, the corresponding lipid was designated as protruding. Previous work has shown that protrusions identified by this definition are associated with spontaneous vesicle fusion [259] and enhanced lipid mixing [284]. Two example snapshots of spontaneous protrusion are shown in Fig. 11-10a.

Fig. 11-10b and 11-10c show the time-averaged number of protruding lipids, N_p, per lipid as a function of the radial distance from the NP-bilayer interface for 2 nm and 3 nm core diameter NPs respectively. This measurement is effectively the probability of observing a protruding lipid in the vicinity of the NP. In both plots, the dashed horizontal line indicates the probability of observing a protruding lipid in a DOPC bilayer with no NP. For both NP core diameters, there is an increase in protrusion probability in the vicinity (< 2 nm) of all NPs, with all-MUS NPs exhibiting the most significant increase. The 3 nm MUS:OT and MUS:HDT NPs have a slightly larger protrusion probability than the 2 nm NPs, while the 3 nm all-MUS NP clearly induces the highest protrusion probability. These results agree well with the lipid tail disorder shown in Fig. 11-8, where all-MUS

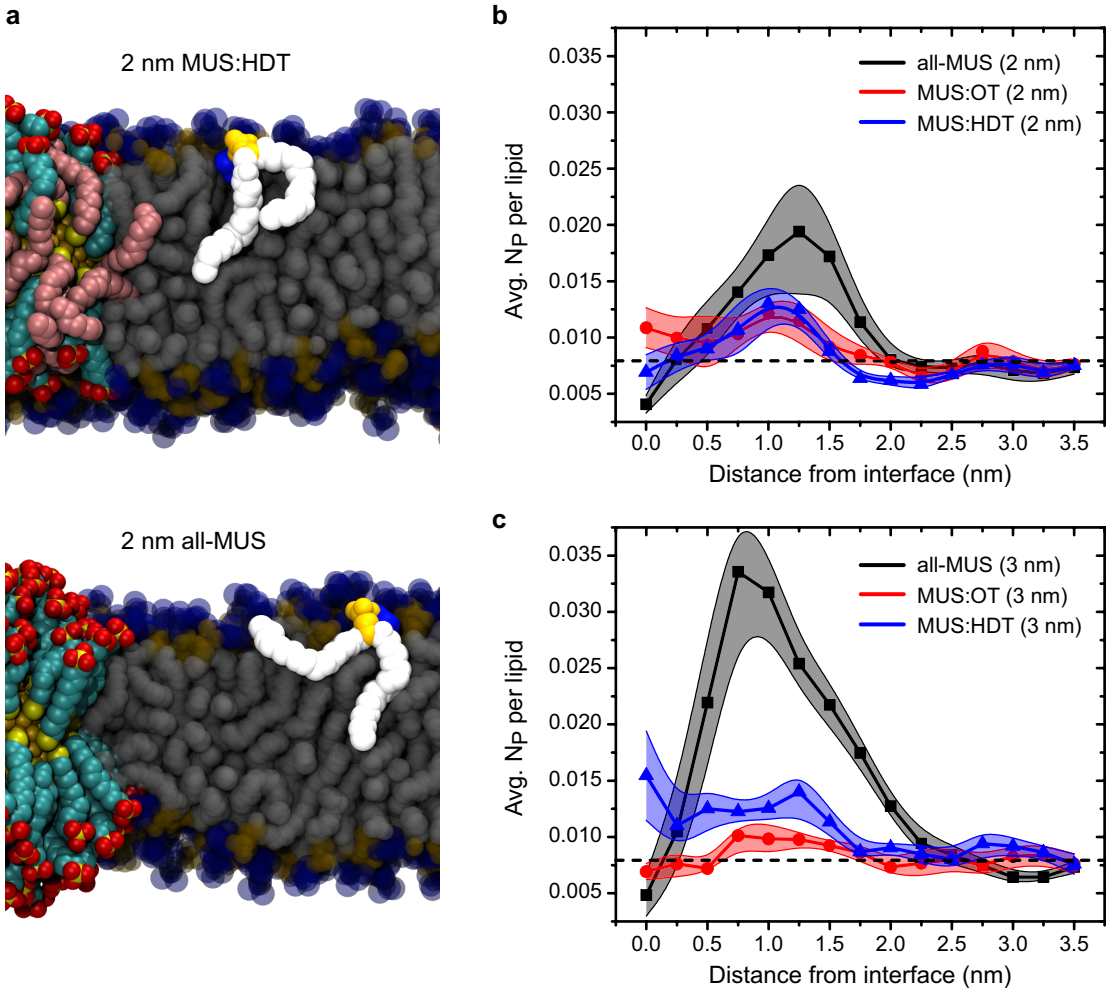

Figure 11-10: Analysis of lipid tail protrusions around embedded NPs. **a** Simulation snapshots showing example of spontaneous protrusions (highlighted lipids) near a 2 nm MUS:HDT (top) and 3 nm all-MUS (bottom) NP. **b** Average number of protruding lipids per lipid (N_p) near 2 nm NPs. **c** N_p for 3 nm NPs.

NPs disrupted lipid tails to the greatest extent. Notably, peaks in the protrusion probability occur at approximately 1.0 nm from the interface for most of the NPs. This distance is roughly where the area per lipid begins to decrease from its typical value for DOPC (Fig. 11-6). While Fig. 11-8 indicates that tails become increasingly disordered closer to the NP, the decreased area per lipid near the NP likely acts as a steric barrier to protrusions leading to the maximum enhancement in protrusion probability at the distance where the APL begins to decrease. Moreover, this steric barrier likely explains why the protrusion probability is low for 3 nm MUS:HDT NPs despite significant lipid tail disorder 0-1 nm from the interface (Fig. 11-8).

The finding that an embedded NP enhances the probability of tail protrusions suggests that the presence of an initial embedded NP may lower the barrier for the insertion of additional NPs in analogy with a nucleation-and-growth kinetic process. Moreover, the increased lipid tail disorder

and increase in tail protrusion probability in the vicinity of the embedded NPs are also effects induced by fusion peptides. In previous simulation studies, a single fusion peptide was shown to increase the probability of protrusions in its vicinity by a factor of about 4-6 [259, 284]. Here, the 3 nm all-MUS NP induces a $\approx$ 4.2x increase in protrusion probability at its peak position, commensurate with the fusion peptide results. While the other NPs only exhibit modest increases in protrusion probability, the increase in tail disorder with increasing NP size suggests that larger NPs may exhibit significantly higher protrusion probabilities. Based on our previous work, it is predicted that NPs of up to approximately 10 nm in core diameter may be able to stably embed within membranes based on the choice of surface composition. Given that the protrusion probability may be related to tail disorder, it would be likely that these larger NPs would further enhance the likelihood of observing protrusions. Similarly, for an ensemble of multiple embedded NPs the number of protrusions may be further enhanced. These findings suggest that embedded NPs can act as synthetic fusion peptide-mimicking materials that both enhance local lipid protrusions and potentially attract nearby vesicles electrostatically.

11.4 Frequent lipid extraction facilitated by similarity between NP monolayer, bilayer

In Fig. 11-3, the lipid tail density profile for the 3 nm MUS:OT particle shows a significant probability of finding lipid tails in a spatial region that overlaps with the density of NP ligands. This observation implies that lipids can be "extracted" from the bilayer entirely due to the chemical similarity between the hydrophobic lipid tails and the hydrophobic ligand backbones in the NP monolayer. Examination of the simulation trajectories led to the identification of transient lipid extraction events, in which lipids intercalated within the NP monolayer, for all of the simulations. Furthermore, it has recently been suggested in the literature that highly hydrophobic graphene sheets can extract lipids from intact bilayers in a similar process [351]. Our results suggest that such extraction events occur frequently near embedded NPs.

To explore the origin of this process, the Lennard-Jones interaction energies between a single extracted lipid and the NP, bilayer, and solvent were calculated during a 300 ns portion of a simulation run. The lipid was chosen from a 2 nm all-MUS simulation. The Lennard-Jones energies approximate van der Waals (non-polar) forces between the hydrophobic lipid tails and ligand backbones. Fig. 11-11a shows each of these energy components as well as their sum. The values are expressed as the change in the interaction energy relative to the average computed for the 100-110 ns time period. The dashed vertical lines mark the time when the lipid begins to move out of the bilayer and into the monolayer, indicating the onset of the extraction event, and the time when the lipid retracts back toward the bilayer, indicating the end of the extraction event, based on an order parameter described below. At the onset of extraction ($\approx$ 160 ns), the LJ interaction energy between the lipid and the bilayer increases but this increase is compensated by interactions with the NP. There is effectively no change in solvent interactions indicating that the lipid is shielded

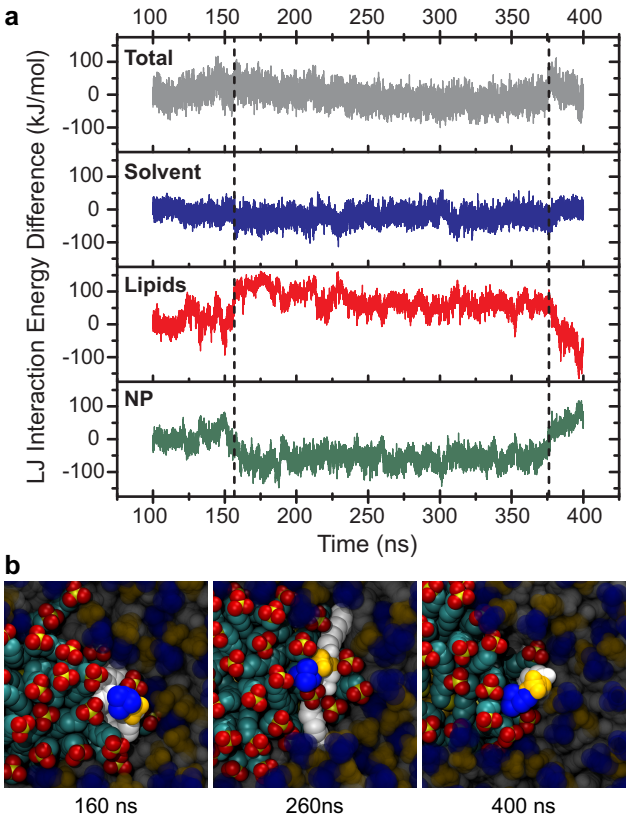

Figure 11-11: Energetics of transient lipid extraction. **a** Change in the Lennard-Jones interaction energy between the extracted lipid and system components as a function of time. The total change in energy is the sum of the solvent, lipid, and NP interactions. Dashed vertical lines indicate the start/end of extraction. **b** Top down snapshots of the extracted lipid and surrounding bilayer at the onset of extraction, 100 ns later, and after extraction.

from water when intercalated within the monolayer. The sum of all three interaction energies shows a nearly constant value throughout the entire time frame suggesting that lipid extraction occurs at approximately constant energy and lipids near the NP-bilayer interface can be freely extracted to maximize their conformational freedom. Fig. 11-11b shows top-down snapshots of the lipid at the onset of extraction, 100 ns later, and after the extraction event, illustrating how the lipid enters monolayer transiently.

To quantify the tendency of different NPs to extract lipids, a lipid tail atom was designated as extracted if no other lipid atoms were within 0.6 nm but at least one NP atom was within the same distance. A lipid was then designated as extracted if at least four atoms in either tail met these criteria. This definition was able to accurately capture lipid extraction events based on the correlation between the vertical dashed lines in Fig. 11-11 and the changes in lipid/NP interaction energies. Using this definition of lipid extraction, the number of extracted lipids per time was quantified for each NP composition. In general, lipid extraction was found to be common, with several lipids often being extracted at once. As an example, Fig. 11-12 shows the number of

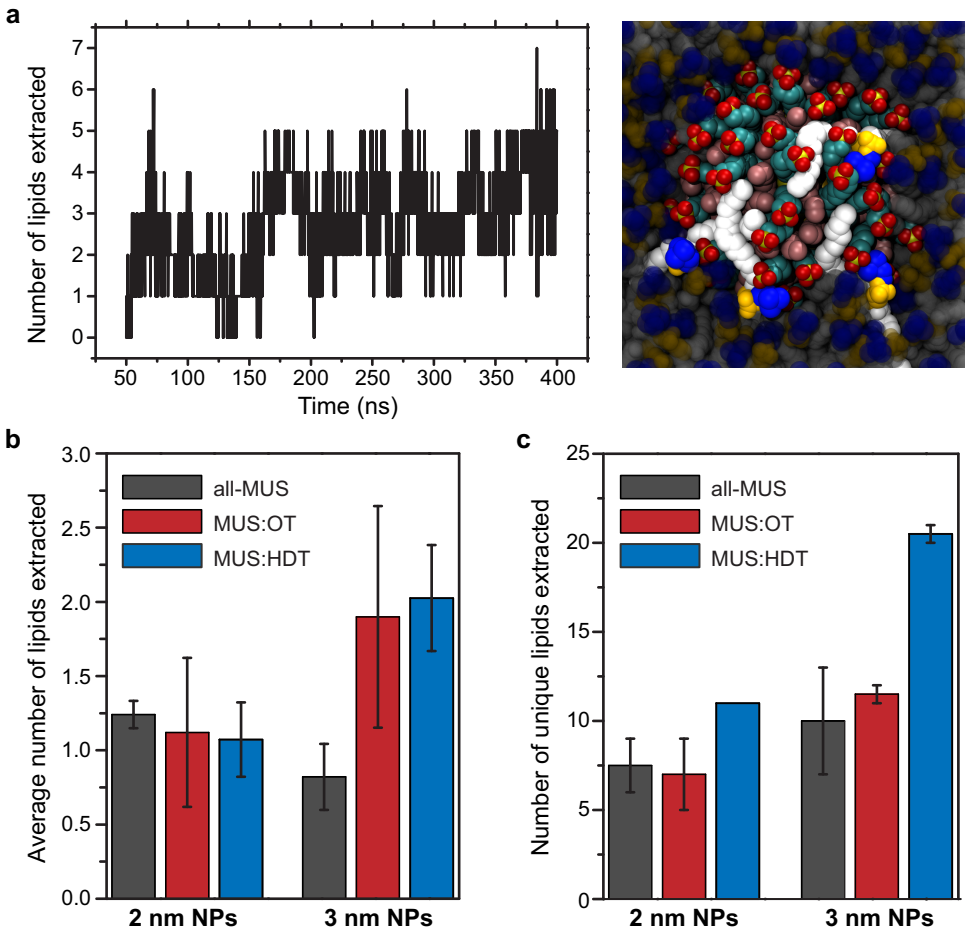

Figure 11-12: Effect of NP composition on lipid extraction. **a** Number of lipids extracted as a function of time for a 3 nm MUS:OT NP, with a single snapshot at 400 ns illustrating four lipids simultaneously extracted from a single monolayer. **b** Number of lipids extracted for all NPs, time-averaged over 350 ns for each NP. Error bars represent error between two separate simulation trajectories. **c** Number of unique lipids extracted for each NP composition over the total 350 ns trajectory.

extracted lipids as a function of time for a 3 nm MUS:OT NP and an example snapshot at 400 ns. The time plot illustrates that several lipids are consistently extracted at a time as is clearly observed in the simulation snapshot where four lipids have tails intercalating within the exposed NP monolayer. Similar results were obtained for all NPs examined.

Figure 11-12b shows the average number of lipids extracted per unit time for all NP types. For the 2 nm NPs, all three compositions showed similar tendencies to extract lipids within the error of the simulations. For 3 nm NPs, the more hydrophobic MUS:OT and MUS:HDT NPs were much more likely to extract lipids, while the all-MUS NP was even less likely to extract lipids than the 2 nm all-MUS NP. This difference is likely due to the reduced monolayer free volume in the larger all-MUS NP monolayer. For the MUS:OT and MUS:HDT particles, the removal of MUS ligands leads to a monolayer with both more free volume and more hydrophobicity, encouraging extraction

significantly relative to the all-MUS NP. The 2 nm NPs likely demonstrate similar results due to a large amount of free volume for all compositions. Because the simple time average does not distinguish between a small set of lipids that are extracted for long periods of time (e.g. the lipid in Fig. 11-11) and larger numbers of lipids that extract for smaller time periods, Fig. 11-12c plots the total number of unique lipids extracted over the 350 ns trajectories. This comparison shows that the MUS:HDT NPs extract more lipids than the other NPs which may be due to the tendency of the HDT lipids to extend into the bilayer core (c.f. Fig. 11-3), excluding volume and forcing lipid tails toward the surface where they can more easily enter the NP monolayer.

These transient lipid extraction events further illustrate the ability of embedded NPs to induce widespread disruption of the surrounding bilayer. It is yet unclear what consequences this behavior could have in a complex system with multiple NPs and multiple vesicles or bilayers. It is possible that if an embedded NP contacts another vesicle it could extract lipids from it, perhaps mediating the exchange of lipids between bilayers in a process similar to what is proposed for non-vesicular lipid transport [352]. These results thus suggest that the NPs can act as biomimetic lipid-transfer proteins in addition to mimicking fusion peptides as suggested above.

11.5 Conclusions

In this Chapter, we used atomistic molecular dynamics simulations to gain insight into the effect of embedded NPs on the surrounding lipid bilayer. We specifically sought to understand how changing the size or monolayer composition of the NPs, two tuning parameters controllable synthetically, could influence the rearrangement of lipids. Our results show that all NPs simulated locally thin the bilayer, with the extent of thinning related to the monolayer composition. This negative hydrophobic mismatch may induce clustering of NPs and potentially affect the function of nearby proteins in a cell membrane. Due to the high charge density of the exposed monolayer, electrostatic interactions attract and reorient lipid head groups toward the NP, reducing the effective area per lipid in the vicinity of the NP-bilayer interface as well as inducing a preferential reorientation of the head group dipoles. Despite this apparent ordering of lipid head groups, the lipid tail groups have decreased order due to the thinning of the bilayer. The combination of head group ordering and tail group disordering is unusual and to our knowledge has not been reported previously. The choice of monolayer composition and particle size is critical in determining both the extent of the thickness deformation and resulting decrease in tail group order.

In addition to these changes in basic structural features of the surrounding bilayer, our analysis also showed the ability of embedded NPs to lead to significant bilayer disruption due to both an enhanced probability of lipid tails protruding toward solution and the transient extraction of lipids out of the bilayer and into the NP monolayer. As the initial insertion of the NPs into the embedded state depends on similar lipid protrusions, the enhancement of protrusions near embedded NPs may imply that cooperativity between NPs may assist insertion. Furthermore, the observation of both lipid extraction and enhanced protrusions suggests that novel interactions between embedded

NPs and other lipid structures in solution, such as nearby micelles or vesicles, may be possible, including the possibility that NPs facilitate vesicle-vesicle fusion by lowering the initial barrier related to tail protrusions. This work suggests the intriguing possibility that these transmembrane NPs could be synthetic analogues to biological fusion peptides by both attracting nearby vesicles electrostatically and mediating the initial stages of membrane fusion, while having the benefit of being inserted into vesicles spontaneously in solution. The increase in protrusion probability may also enhance nearby NP-bilayer fusion, indicating that NP insertion could be a cooperative process. Moreover, the observation of lipid extraction leads to the possibility of NP-mediated lipid transfer between nearby vesicles, another process that occurs in biological membranes that is assisted by lipid-transfer proteins. Future studies will focus on understanding how embedded NPs may mediate these processes by focusing on simulations between multiple membranes in the presence of embedded NPs. This work thus shows several novel lipid rearrangements around embedded NPs and illustrates how the extent of deformation may be controlled by tuning the surface composition and size of the particle, potentially leading to design guidelines for novel nano-bio hybrid structures.

THIS PAGE INTENTIONALLY LEFT BLANK

Chapter 12

Summary and Open Questions

In this thesis, I used several novel simulation strategies to develop a comprehensive overview of interactions between amphiphilic, anionic, monolayer-protected gold nanoparticles and lipid bilayers. In Part I, I first used a highly coarse-grained representation of the NP-bilayer system to establish that spontaneous bilayer insertion can occur if the surface properties of the NP are able to dynamically rearrange in response to the presence of the hydrophobic bilayer core. While this globally-responsive model may be physically applicable to some materials systems, I next showed that a more detailed model that permitted ligand fluctuations even without grafting site diffusion could still predict stable NP-bilayer fusion. I used this implicit bilayer, implicit solvent model to calculate the free energy change for fusion using a free energy decomposition inspired by studies of transmembrane proteins. This new united atom model confirmed that ligand backbone deformations could "snorkel" charges to nearby aqueous interfaces as had been previously observed in transmembrane proteins, reducing the penalty for charge exposure and giving rise to locally-responsive surface properties. As the NP core diameter increased, the amount of free volume accessible to each ligand decreased, inhibiting the ligand's ability to snorkel charges out of the hydrophobic core and into water and leading to a large barrier to insertion. This work led to the identification of size thresholds for stable NP insertion that shifted depending on the NP composition. The prediction of fusion behavior was confirmed experimentally using confocal microscopy and TEM imaging, and moreover the predicted size thresholds were correlated with NP-bilayer interactions in synthetic black lipid membrane systems and with non-endocytic cellular uptake. The experimental results therefore suggest that the novel embedding behavior predicted may be a precursor to cell penetration.

In Part II, I studied the kinetic pathway that NPs might follow to translocate from an initial state in solution to a final state embedded in the bilayer. Using atomistic molecular dynamics simulations, I first showed that in the presence of strong membrane curvature, such as the edge of a large membrane defect, NPs could spontaneously insert into the bilayer after contact with protruding lipid tails. Over the same timescales, protrusions are unlikely to occur in planar membranes and as a result both experiments on supported lipid bilayers and simulations showed only fusion at defect sites. However, the finding of a protrusion-mediated pathway through defect edges could imply that such a mechanism would be possible in planar bilayers as well if protrusions were to occur. I showed that protrusions are rare events in planar bilayers but do occur over experimental time scales at a rate almost independent of the bilayer composition in single-component bilayers. If a NP does encounter a protrusion, it can rapidly insert into the bilayer, but is trapped in a metastable state with all charged ligands on one side of the bilayer. I finally hypothesized that ligands may gradually flip charges across the bilayer in a process similar to lipid flip-flop or protein side chain snorkeling with preliminary simulations suggesting that such a pathway is non-disruptive. Part II thus shows two possible pathways - one requiring defects, the other requiring contact with rare tail

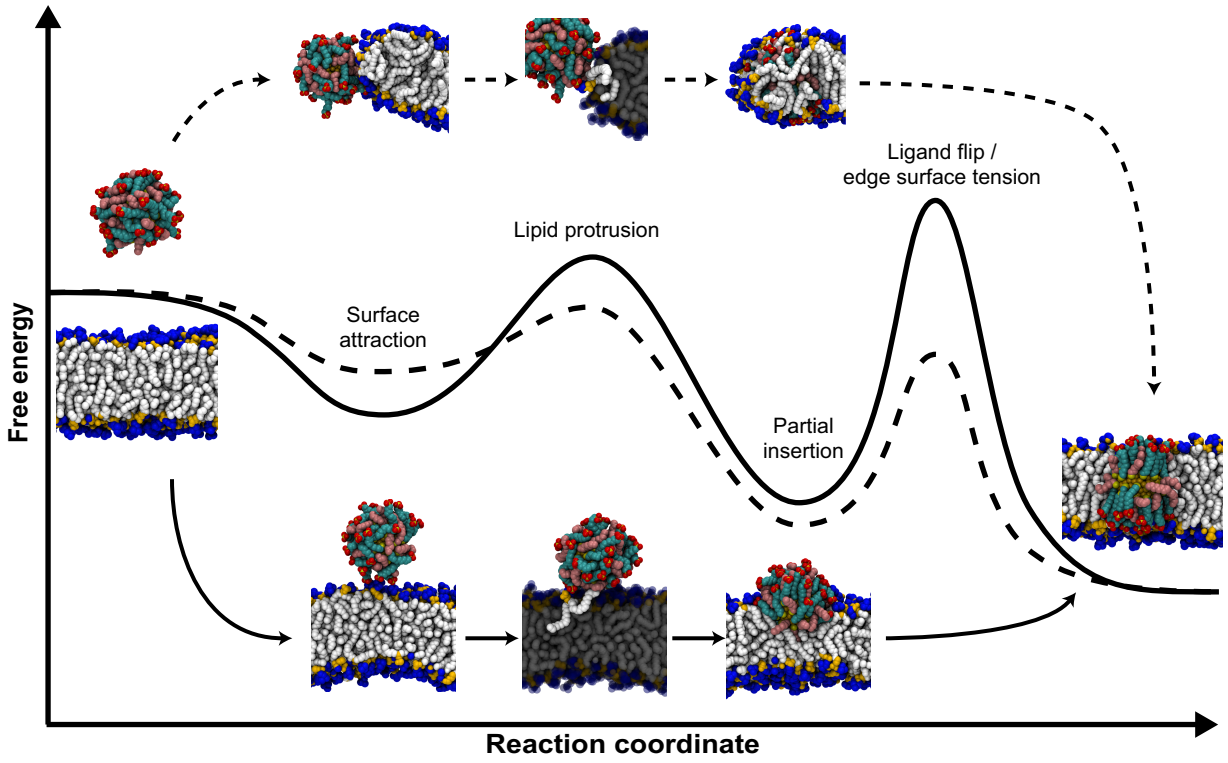

Figure 12-1: Summary of NP-bilayer fusion pathways. The NP transitions through a series of energy barriers and metastable points while inserting into a bilayer, either in the presence (dashed lines) or absence (solid lines) of defects.

protrusions - for NPs to fuse with bilayers to achieve the transmembrane configurations predicted in Part I. Fig. 12-1 summarizes these two pathways and the findings from Part I and Part II.

In Part I and II, I effectively assumed the single NP limit in studying NP-bilayer interactions which would only be achievable in highly dilute concentrations. In Part III, I performed initial studies to understand how cooperative interactions between multiple NPs might influence behavior. First, I showed that two NPs may stably aggregate in solution driven by the same factors that trigger NP-bilayer insertion. Aggregation is facilitated by the deformation of ligands to minimize hydrophobic surface area just as in the case of NP-bilayer fusion and as a result is more prominent for smaller NPs, less charged systems, and NPs with longer ligands. As aggregation may reduce the efficacy of cell penetration by effectively increasing NP size or decreasing solubility, this study puts additional constraints on NP design for suitable applications. Next, I studied how a single embedded NP can influence the surrounding environment by triggering lipid rearrangement. I found that NPs can induce significant membrane deformations similar to those exhibited by biological membrane proteins. In analogy with protein systems, it is possible that membrane-mediated interactions can trigger NP aggregation or other cooperative effects. Tuning the NP properties could influence the extent of this aggregation. Part III thus lays the groundwork for future studies of cooperative NP interactions in a biological environment.

12.1 Open questions and future work

The findings of this thesis open up many questions for future work in exploring NP bilayer interactions. Here, I will briefly summarize and hypothesize about open questions that will be addressed in future studies.

12.1.1 Collective NP behavior

Several aspects of potential cooperative NP behavior bear further study, particularly given the experimental impossibility of reaching the single NP limit assumed throughout much of this work. A first question would be how multiple NPs embedded or partially-embedded within a single vesicle/bilayer interact with each other or the surrounding system. The results of Chapter 9 suggest that partially-inserted NPs may generate significant membrane curvature, at least transiently. Previous work on curvature-generating proteins, including both peripheral proteins like the banana-shaped BAR domain [353, 64] or transmembrane proteins with wedge-like shapes [135, 327], have shown that curvature can lead to repulsive interactions between NPs or even large scale membrane-remodeling [354, 135, 333, 334]. As the generation of curvature incurs an energy penalty, these behaviors minimize the overall elastic energy stored within the bilayer [139]. However, such curvature-mediated interactions may also depend on the size of the NP as has been previously suggested [355, 356]. Membrane remodeling is particularly interesting as large collections of proteins or adsorbed NPs give rise to the formation of membrane tubules that are implicated in cellular transport [357, 358, 359, 111]. Understanding potential curvature generation and remodeling events from partially-inserted NPs could allow this behavior to be mimicked synthetically.

In Chapter 11, it was shown that fully-embedded NPs also give rise to significant membrane deformation similar to those induced by biological membrane proteins. In particular, it was shown that both the thickness of the bilayer locally and the orientation of lipid head groups were affected by embedded NPs. Thickness deformations are known to mediate protein aggregation in a similar manner to curvature deformations, so it is likely that these findings support a model of membrane-mediated NP aggregation [327, 325]. However, it is less clear how electrostatic interactions between NPs or between NPs and lipid head groups might affect such aggregation, and particularly what type of aggregates are formed. For instance, it might be assumed from the cylindrical symmetry of the thickness deformations that hexagonally close-packed NP aggregates would be preferred, but electrostatic interactions between NPs might disrupt this packing and drive line-like cluster formation instead [360]. Fig. 12-2 shows schematics of how multiple NPs might interact within a membrane environment.

Beyond NP aggregation, cooperative interactions may be important in several aspects of the kinetic pathway identified in Part II. First, the finding that an isolated NP can increase the probability of lipid tail protrusions in its vicinity (Chapter 11) implies that the insertion of a single NP can increase the likelihood for the insertion of additional NPs. However, given that protrusions are only enhanced near the embedded NP, it is possible that electrostatic repulsion between the

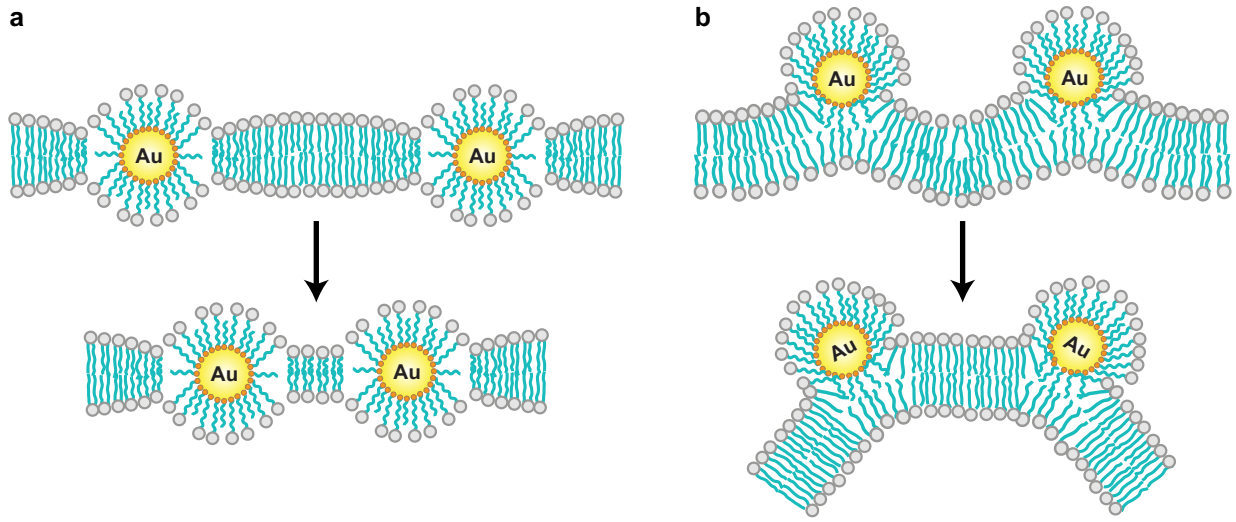

Figure 12-2: Schematic of membrane-mediated NP interactions. **a** NP aggregation triggered by minimization of bilayer thickness deformations. **b** Potential curvature generation by multiple partially-inserted NPs. Minimizing deformations around individual wedge-like NPs may induce curvature over a larger length scale.

like-charged NPs eliminates the advantage of the first NP entirely. In Chapter 9, I also showed that the flipping of charged ligands through the bilayer represents a possible pathway for NPs to transition from a partially-inserted state to a fully-embedded state over experimental timescales. This process is similar to the penetration of charged amino acid side chains through the bilayer [72]. Recent simulations have shown that the penalty for translocating charges through the hydrophobic core can be significantly reduced in the presence of other nearby proteins capable of stabilizing the necessary water defect formed during this process [73]. Similar observations were made for lipid flip-flop, another process requiring the movement of charges through the membrane [301]. An open question is then whether cooperative interactions with other NPs can lower the barrier to ligand flipping in a similar manner by stabilizing water pores [191]. It is possible that NP cooperativity could both lower the barrier for initial insertion and stabilize ligand flipping. Finally, it is possible that just as the binding of large numbers of AMPs may trigger pore formation as described in the introduction, binding several NPs may create a strong electrostatic driving force that drives NP-bilayer fusion, either by enabling ligand flipping or triggering pore formation.

12.1.2 NP-mediated bilayer interactions

One important distinction between embedded NPs and transmembrane proteins is the high charge density of the exposed NP surface. In the kinetic studies of Part II, atomistic models predict that even at biological salt concentrations of 150 mM, where the Debye length is reduced to less than a nanometer and electrostatic interactions are highly screened, small NPs are strongly attracted to the bilayer surface and are never observed to detach into solvent. This observation underscores the strong electrostatic interactions between the dipolar lipid head groups and the anionic NP surface.

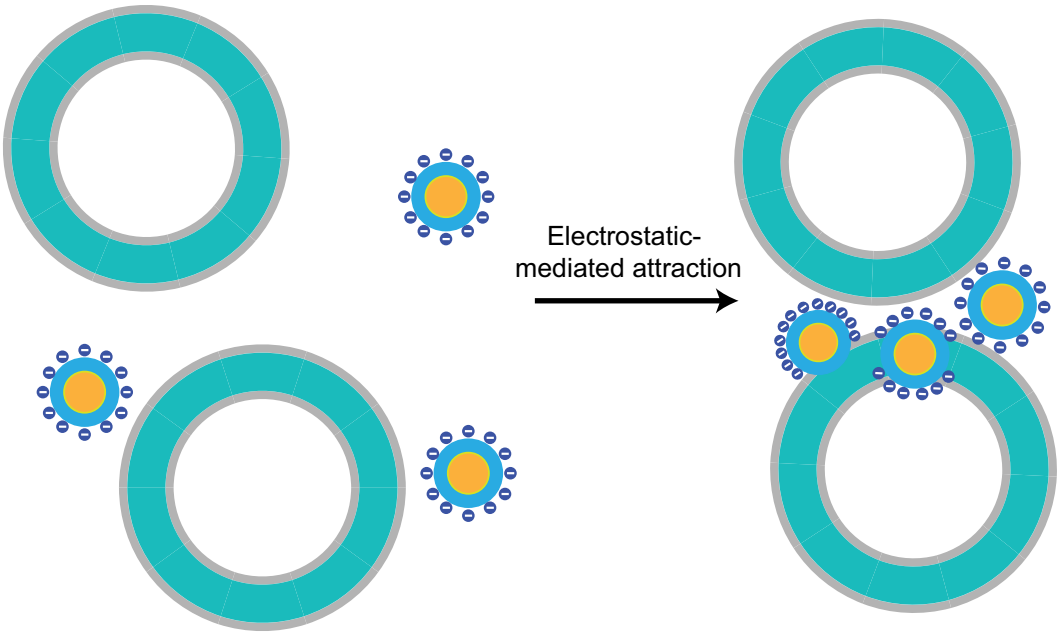

Figure 12-3: Schematic showing NP-mediated vesicle attractions. Because the charged NPs are attracted to the head groups of lipids, it is possible that embedded, partial embedded, or even adsorbed NPs may mediate vesicle-vesicle attraction through electrostatics.

However, what happens if multiple available bilayers are present in the system? It seems probable that NPs either adsorbed to the surface of a bilayer or embedded within its core could mediate attraction to other bilayers, especially if the effective local charge density is increased further by NP aggregation. This scenario might arise in both synthetic systems, such as the multilamellar vesicles studied in Chapter 4, or in biological systems given the large number of intracellular vesicles or membrane-bound cellular components. Fig. 12-3 schematically illustrates the proposed NP-mediated vesicle attraction.

If embedded NPs can indeed induce the attraction of two bilayers, then it seems even more likely that embedded NPs can mimic fusion peptides as hypothesized in Chapter 11. SNARE proteins are proposed to mediate fusion in neuronal junctions by first dehydrating the interface between two bilayers by inserting into both bilayer simultaneously [332]. The presence of the proteins provides a driving force to overcome the short-ranged repulsive hydration force between bilayers [302]. Embedded NPs could serve the same purpose using electrostatic interactions. The second function of SNARE proteins may be to destabilize the surrounding membrane, increasing the probability of tail protrusions that initiate fusion [332, 284]. Again, embedded NPs may also fulfill this role as shown in Chapter 11. Fig. 12-4 shows a summary of how an embedded NP may act as a fusion peptide mimic.

A final possible NP-mediated interaction was also suggested by results in Chapter 11 which showed that lipids can be transiently extracted from the bilayer to instead attach to the exposed NP monolayer. This finding raises the possibility that if another nearby lipid reservoir is available,

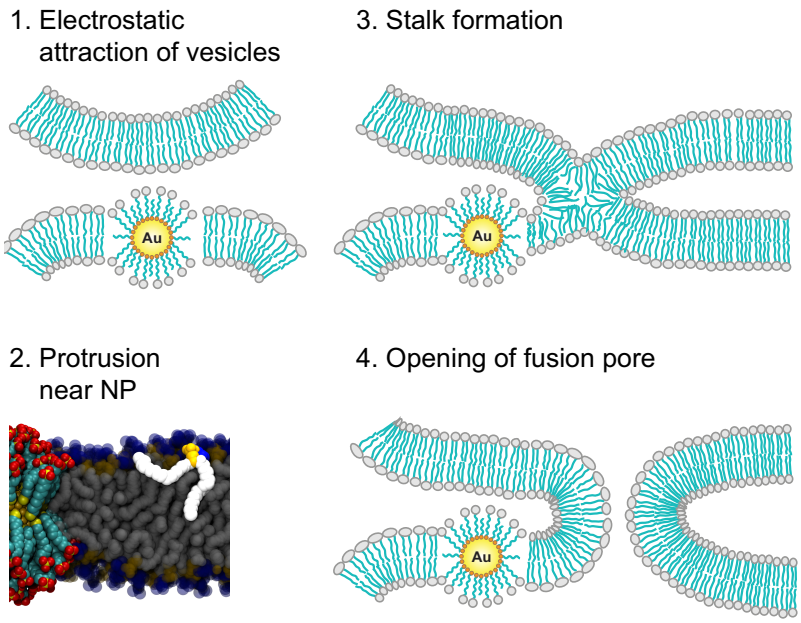

Figure 12-4: Schematic of NP facilitating vesicle fusion. The NP first mediates vesicle-vesicle attraction as in Fig. 12-3, then triggers the appearance of a lipid protrusion that mediates the onset of stalk formation. Fusion then proceeds with the opening of a fusion pore.

e.g. free lipids, micelles, or even other bilayers, then lipids may be transferred to or from the bilayer in which the NP is embedded. Such a lipid-shuttling mechanism has been proposed to occur in biological systems but has not been observed synthetically.

12.1.3 Interactions in biological settings

The focus of this thesis has been largely on determining interactions between NPs and synthetic, single-component membranes as analogues for biological membranes. The finding that predictions from these simulations can map to experiments on full cells (Chapter 4) is encouraging, yet still surprising given the significant complexity in biological systems. Several features of biological membranes could play critical roles in modulating the interactions uncovered in this thesis. For instance, the protein content of the membrane could influence electrostatic interactions with NPs in solution, the rate at which lipid protrusions appear, or even the ability of ligands to flip through the membrane as discussed above. Likewise, it is also unclear how the membrane deformations induced by embedded proteins may influence surrounding proteins, and in particular mechanosensitive proteins that may respond to bilayer perturbations [343]. Another major missing cell component is the glycocalyx, which is a negatively charged extracellular polymeric matrix [33]. Presumably, NPs would need to bypass the glycocalyx to access the bilayer itself which may be challenging given like-charge electrostatic interactions. The role of this component must be further investigated.

In addition to these missing components, the lipid composition of the bilayer in biological membranes is also much more complicated than the single-component bilayers studied throughout this

thesis. Biological membranes contain multiple different lipid species with differing compositions. Of particular importance are changes in head group charges - biological membranes can have a substantial number of anionic lipids, and due to the asymmetry between leaflets tend to have anionic lipids in the intracellular monolayer [37]. It is not clear how these anionic lipids may influence aspects of the kinetic pathway, but it may lead to an additional barrier to ligand flipping [217]. Similarly, the transmembrane potential gradient should in principle inhibit the passage of anionic ligands [361, 362]. Beyond these charge effects, the presence of cholesterol and other low melting point lipid species may give rise to stiffer, liquid-ordered bilayer regions that exhibit a lower protrusion probability, inhibiting initial NP insertion. If insertion does occur, it is also possible that NPs may preferentially recruit different lipid species to their vicinity in a manner similar to transmembrane proteins [363, 364]. Finally, it has been hypothesized that lipids may phase separate into "lipid rafts" in biological membranes that are enhanced in particular lipid species. The interfaces of these domains may exhibit enhanced permeability relative to single-component bilayers, which may imply that either membrane defects or lipid protrusions are also enhanced due to the disruption of bilayer order [365, 37]. In either case, NP insertion may be more favorable at these domain interfaces. There are thus a wide variety of considerations that must be studied in order to more fully replicate biological conditions using simulations.

12.1.4 New simulation methodologies

One of the chief findings of this thesis is the necessity of both ligand snorkeling and lipid tail protrusions to facilitate spontaneous NP insertion into bilayers. Both of these processes depend on an accurate descriptions of free volume and ligand fluctuations, requiring the detailed atomistic simulations used here. However, gaining an understanding of interactions at larger length and time scales, such as the cooperative behavior suggested above, would require significantly more computational expense. Given the success of the atomistic models, one open question would be whether a new coarse-grained methodology could be developed to accurately represent the NP-bilayer interactions described here. The most popular existing coarse-grained methodology is the MARTINI model, which combines four non-hydrogen atoms into single effective beads [113]. This level of coarse-graining is likely unsuitable to describe the detailed fluctuations used here. However, one possibility would be using an existing CG model like MARTINI and using the results of the existing simulations to inform CG simulations. For example, using the MARTINI model to represent the system but starting with NPs embedded or partially embedded in the membrane, and thus not depending on tail protrusions to mediate insertion, could be used to investigate the collective properties discussed above.

Another question is whether a more accurate model of the gold core would affect the observed results. Recently, a polarizable gold model has been developed for the CHARMM force field and was used to model protein adsorption onto a gold surface [247]. It is possible that including polarization effects could influence electrostatic interactions which may be important for NPs in biological settings when surrounded by a heterogeneous collection of proteins and other molecules.

Another aspect that is ignored is the possibility of faceting on the gold substrate. The ligands on faceted NPs have access to differing amounts of free volume if they are grafted to a planar face as opposed to the edge, which may affect structural properties [93, 183]. Finally, I introduced in Chapter 2 the possibility that ligand grafting points might diffuse across the NP surface, while for the remainder of the thesis they were assumed to be fixed. It is possible that such ligand diffusion could occur on timescales relevant to the molecular dynamics simulations and as a result may need to be considered as well [366, 367], effectively merging the globally-rearranging and locally-rearranging models proposed.

12.2 Perspective

12.2.1 Current understanding of cell penetration behavior

The primary motivation for this thesis was the finding that amphiphilic NPs could non-disruptively penetrate into cells via a non-endocytic pathway, seemingly regulated by the surface morphology of the mixed ligand monolayer [81]. In this original paper, it was acknowledged that there was minimal current understanding of how such penetration could occur, especially given the absence of biological analogues that exhibit similar behavior. The results presented in this thesis show several new findings that shine new light onto the potential penetration process.

First, the results of Part I reveal that there is a strong driving force for NP-bilayer fusion that depends critically on NP core diameter. The size threshold identified for 2:1 MUS:OT NPs was approximately 6 nm, close to the 4.5-4.9 nm particle sizes experimentally shown to penetrate into cells [81]. However, the all-MUS NPs found to not penetrate cells in the original study had a lower size threshold, approximately 3.5 nm, and thus thermodynamically would not prefer to embed within bilayers. Reducing the all-MUS NP size below the predicted threshold was found to increase cell uptake, even at 4°C when endocytosis is blocked, as discussed in Chapter 4. The agreement between the predicted fusion mechanism and actual cell internalization implies that fusion may be a precursor to cellular access. The experiments with multilamellar vesicles in Chapter 4 also demonstrate that NPs can embed within both internal and external membranes, indicating that they have the ability to cross lipid bilayers in systems that completely lack endocytic machinery. Moreover, the results of Appendix C indicate that the observation of fluorescence is due to BODIPY accessing the hydrophobic core of the bilayer and as a result is a marker for embedded NPs. These microscopy results confirm that NPs that fuse with bilayers are able to access internal membranes. Together, these results all suggest that NPs below a composition-dependent size threshold are able to fuse with bilayers and from this state access the interior of multilamellar vesicles and cells.

The primary difference between the results found for cell internalization and the predictions of fusion free energies is the role of the monolayer surface structure. The results from Chapter 3 and Chapter 5 indicate that the nanoscale arrangement of ligand grafting points has no effect on the free energy change for fusion unless the two ligand components separate into a Janus morphology. It was further demonstrated in Chapter 6 that the organization of ligands in water had no dependence

on the location of the grafting points due to the tendency of charged end groups to spread apart uniformly to minimize unfavorably electrostatic interactions. The seeming discrepancy between the importance of surface structure found experimentally and its unimportance in simulations may be attributed to the replacement of linear OT molecules with branched br-OT molecules as a means of inhibiting stripe formation experimentally [81]. While possessing seemingly similar chemical properties as linear OT, the larger side groups of br-OT may significantly inhibit the fluctuations necessary for stable fusion. Chapter 5 tested this possibility by representing the steric barrier of branched groups using larger united atom beads, which indeed did slightly reduce the size threshold for fusion and thus should reduce cell internalization. It should be noted that br-OT NPs do have a higher likelihood of entering membranes than all-MUS NPs, possibly supporting a shifted size threshold still larger than that of all-MUS NPs [81]. However, it was found in Chapter 5 that the shift in size was not large and may not solely explain the observed results. It is also possible that either morphology or the presence of branched ligands influences the kinetic pathway for NP insertion. In Part II, the initial insertion of NPs into bilayers was shown to rely on contact between protruding lipid tails and the NP monolayer. In these simulations, the influence of morphology and branching were not investigated due to computational limitations, but it is possible that both may affect the likelihood of contact between the protrusions and NP monolayer. In particular, branched ligands are known to have modified dihedral angle preferences [206] which may affect the ability to interact with protrusions. While the role of surface structure in the kinetic pathway requires further investigation, it should be noted that the ability of all-MUS NPs to penetrate cells indicates that surface structure is not absolutely necessary for cell access to occur.

12.2.2 Mechanism for cell access

Given all of the information above, the main question left to be answered is still how exactly NPs enter the cytosol of cells. The deep free energy minimum found for NP-bilayer fusion implies that NPs should prefer to stay embedded within the bilayer. While it is possible that NPs can simply detach from the membrane once in an embedded state, this event seems unlikely given the magnitude of the free energy well and the high energy barriers for ligand flipping. The question remains how to reconcile the experimental findings in light of the physical insight gained from this thesis.

One possibility is that NPs are always membrane bound but can transfer between nearby bilayers. Several pieces of evidence suggest this possibility. First, the multilamellar vesicle experiments provide strong evidence for some transfer of NPs into internal vesicles in the absence of any cellular machinery. Moreover, studies of the time-course of the transfer of fluorescence from the external to internal membranes have shown that internal membranes only display fluorescence minutes after the external membranes (personal communication with Prabhani Atukorale). Preliminary results also suggests that in cells lacking intracellular membrane-bound components, such as red blood cells, no NP internalization is found, while in contrast NPs can collect at membrane-bound components in other cell lines (unpublished). These findings suggest that NPs do strongly prefer the membrane

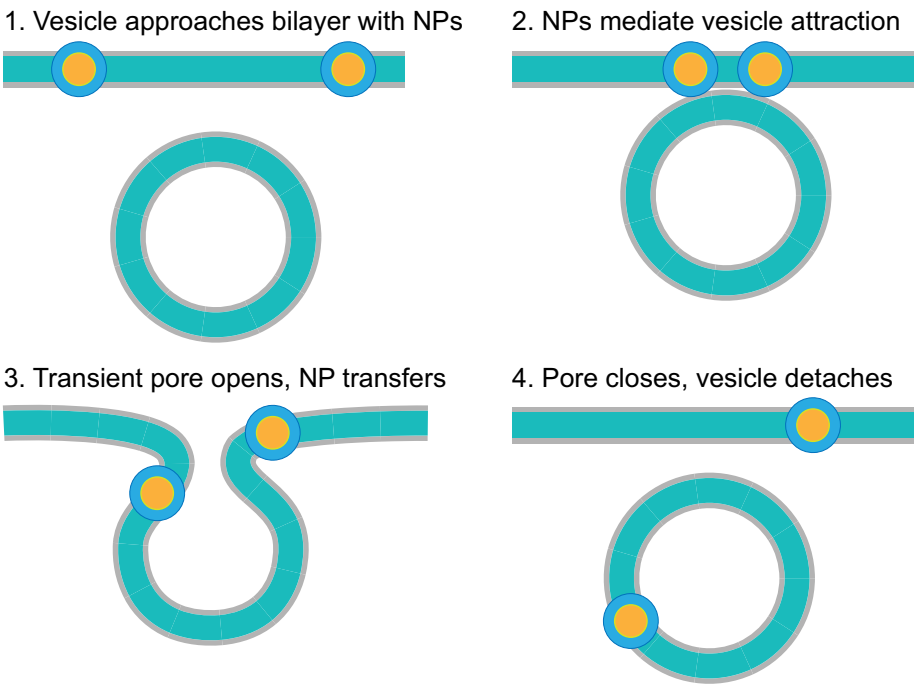

Figure 12-5: Proposed kiss-and-run mechanism for NP transfer between bilayers. Embedded NPs initiate vesicle fusion as shown in Fig. 12-4. After the opening of a transient fusion pore, a NP transfers between the two bilayers. The weak vesicle-vesicle attraction allows the fusion pore to eventually close and the vesicle to detach rather than continuing to full fusion.

and only enter cells via transfer between bilayers. A potential mechanism for such transfer may be related to the proposed facilitation of membrane fusion events by NPs discussed above. In synaptic vesicles, there are two proposed modes of fusion - *full-collapse fusion*, where two vesicles completely merge and intermix their membranes upon fusion, or *kiss-and-run fusion*, where the two vesicles transiently form a fusion pore, allowing contents to mix, but then the pore closes and the vesicles remain intact [368]. There is ongoing debate as to the importance of the kiss-and-run mode of synaptic vesicle fusion, but recent work has suggested that kiss-and-run is preferred under conditions when the two vesicles are only weakly bound together which might occur when SNARE proteins fail to undergo a conformational change [369, 370]. Interestingly, such kiss-and-run events are also believed to occur in mitochondrial membranes and provide a means for the transfer of integral membrane proteins between bilayers [371]. One potential mechanism for NP transfer between membranes would then be to mediate a kiss-and-run event, where weak, reversible electrostatic interactions between embedded NPs and lipids provides the initial vesicle-vesicle attraction, the enhanced protrusion probability in the vicinity of the NPs initiates fusion, the NP transfers from one bilayer to another upon the opening of the fusion pore, then the fusion pore closes the vesicles both remain intact. This kiss-and-run fusion mechanism would provide a non-disruptive means for membrane hopping consistent with existing evidence, and moreover would not require the action of any cellular machinery. Fig. 12-5 summarizes this proposed mechanism.

Another possibility is that upon initial NP-bilayer fusion in cells, the NP surface chemistry is modified due to the reducing intracellular environment. It has been previously shown that intracellular glutathione moieties can exchange onto the surface of NPs that are protected with thiol bonds, releasing ligands into the cytosol [372]. In principle ligands on the intracellular face of an embedded NP would be subject to such exchange which could explain intracellular observations of BODIPY fluorescence even in the absence of cytosolic entry. Moreover, removing charged ligands from the surface of the NP might reduce the barrier for flipping of other ligands while removing hydrophobic ligands might destabilize embedded NPs, driving cytosolic entry.

A final hypothesized mechanism for cytosolic entry would be through an endocytic process. It is clear that while NPs can enter cells at 4° C where endocytosis is blocked, entry is much higher at normal body temperature (see Fig. 1-6) due to endocytic uptake. Given that endosomal escape can be facilitated by incorporating fusion peptides into NPs, it is possible again that NPs act as fusion peptide mimics and facilitate endosomal escape. There are thus several plausible mechanisms by which non-disruptive cellular entry could be achieved as opposed to the disruptive mechanism typically associated with cell-penetrating or antimicrobial peptides based on the unique physical insights established in this thesis.

12.2.3 Combined design guidelines for NPs

The primary motivation for this thesis was to first understand the mechanism of non-disruptive, non-endocytic cell penetration discussed in the Introduction, then use this understanding to optimize the design of NPs to non-disruptively interact with cells. While the exact mechanism of intracellular access is still an open question as discussed above, the relationship between NP-bilayer fusion and eventual uptake indicates that it is sufficient to develop design rules to maximize bilayer insertion in order to enhance uptake. Here I can provide design rules to influence the kinetics and thermodynamics of fusion while maintaining NP solubility and preventing aggregation based on the findings of this thesis and previous work.

First, it is important to summarize the general guidelines that facilitate NP-bilayer fusion. The results of Part I suggest that NP characteristics that facilitate the snorkeling process and provide a strong hydrophobic driving force enhance fusion propensity. Modifying the NP core composition to facilitate global rearrangement may also encourage penetration. The kinetic pathways in Part II indicate that ligands that maximize initial hydrophobic contact with bilayers can trigger insertion. The findings in Chapter 10 show that NP aggregation can be prevented by either strong electrostatic interactions or inhibited ligand fluctuations. Finally, previous work has established that adding additional hydrophobic ligands decreases NP solubility [83]. Fig. 12-6 summarizes the toolbox of NP design parameters available and the three major behaviors that such parameters may influence.

From this general understanding, several guidelines emerge based on modifications to the general system properties explored so far:

- **NP size** - Fusion only occurs below a composition-dependent threshold. Small NPs may aggregate, however, so ideally the NP size is chosen to be near the threshold to maximize

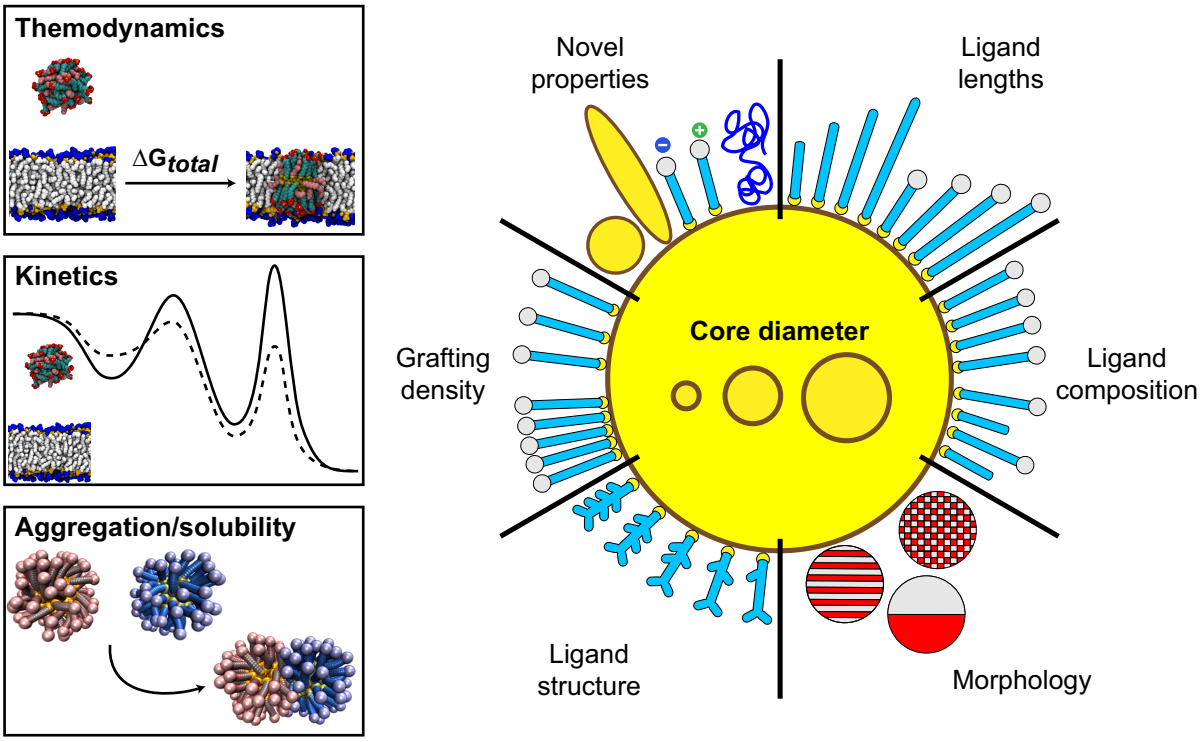

Figure 12-6: Summary of NP design toolbox. A variety of different NP parameters were tested in this thesis and shown to affect the thermodynamics, kinetics, and aggregation proposensity of NPs as summarized in the main text.

fusion while avoiding aggregation. It is also possible that small NPs form Janus morphologies that inhibit insertion [86].

- **Ligand lengths** - increasing the hydrophilic ligand length increases the ease of snorkeling, favoring fusion, while also increasing the likelihood of aggregation. Increasing the hydrophobic ligand length may not have a large increase on fusion free energy, but can increase the efficiency of initial insertion. Longer hydrophobic ligands also may reduce solubility [97]. Incorporating at least a small proportion of long hydrophobic ligands is optimal to overcome kinetic barriers.

- **Monolayer composition** - adding additional hydrophobic ligands increases the driving force for both fusion and aggregation while also reducing NP solubility [83]. The composition should be chosen to tune the size threshold while minimizing aggregation for highly hydrophobic NPs. Some fraction of hydrophobic ligands should be included to facilitate the kinetics of fusion, as end-functionalized ligands cannot extend into the bilayer to stabilize initial insertion. Incorporating only a small fraction of hydrophobic ligands would likely still provide enough electrostatic repulsion to minimize aggregation while encouraging insertion.

- **Morphology** - the thermodynamics of fusion are unaffected by nanoscale differences in morphology, although Janus particles are less likely to fuse. It is likely that similar factors apply

to the kinetics. In particular, Janus particles probably face significant kinetic barriers as electrostatic interactions should drive their charged faces to contact the bilayer first, minimizing the ability of hydrophobic ligands to anchor within the bilayer. Janus particles are also much more likely to aggregate in solution.

- **Ligand branching** - adding branched side chains to the hydrophobic ligands slightly decreased the thermodynamic driving force for fusion. While branched ligands may modify the NP morphology, this does not appear to affect the thermodynamics of insertion. It is likely that the kinetics barrier for insertion increases as the dihedral angles of branched ligands may limit NP-protrusion contact.

- **Grafting density** - increasing the grafting density decreases available monolayer free volume and as a result decreases both fusion and aggregation. It is unlikely that the grafting density would significantly affect either solubility or the kinetics of fusion.

These guidelines summarize the system changes tested explicitly during this thesis. Based on these results, an optimal NP might have a core diameter around approximately 4 nm to be below the likely size thresholds for insertion but without forming a Janus morphology, include primarily hydrophilic ligands ($\approx 80\%$) to maximize electrostatic repulsion between NPs while encouraging electrostatic attraction to the bilayer surface, and include longer hydrophobic ligands (e.g. HDT) to enhance the kinetics of insertion. However, the toolbox for NP design extends beyond just the simple linear alkanethiol ligands and gold cores studied here. For example, it may be beneficial to create NP cores with anisotropic aspect ratios (i.e. nanorods) which have been previously suggested to enhance cell uptake [107, 42, 373]. Identifying methods to increase ligand grafting site mobility to encourage globally-responsive behavior may also stabilize insertion. Finally, the ligand charge state may be of interest as well - while highly cationic ligands disrupt membranes, adding some proportion of cationic ligands to a NP may favorably interact with the transmembrane potential to enhance cellular uptake. There are thus several avenues for novel NP designs that bear future exploration and can supplement the guidelines listed above.

12.2.4 Contributed simulation methodologies

Another achievement of this thesis is the development of several novel simulation methodologies and workflows for characterizing NP-bilayer interactions. As discussed in the Introduction, previous bottlenecks in the study of NP-bilayer interactions were the use of either biased sampling methods that relied on *a priori* assumptions of NP-bilayer interactions or coarse-grained simulation models that neglect important chemical details. For example, coarse-grained dissipative particle dynamics simulations with forces applied to force bilayer penetration showed the simultaneous exposure of multiple charged groups to the bilayer core [110]. The more detailed models developed in this thesis indicate that such a process is unphysical as even the exposure of a single charge requires overcoming a significant free energy barrier as discussed in Chapter 9. Similarly, multiple studies

have used umbrella sampling methods with the coarse-grained MARTINI model to calculate the free energy for forcing NPs to cross bilayers [106, 107]. These studies find large barriers in part because they are missing the key rate-limiting step in spontaneous insertion, namely the occurrence of lipid protrusions, and thus the free energies they report do not reflect a true pathway for insertion. The coarse-grained model also likely underestimates the extent of ligand fluctuations necessary to accurately capture this process. Finally, even a recent atomistic investigation of NP-bilayer interactions failed to capture any insertion behavior by not recognizing the role of protrusions [112]. The inability of previous models to identify correct behavior due to either inaccurate representations of physical processes or the failure to overcome significant energy barriers limits their utility in designing novel NPs.

The computational methods developed during my work help overcome the limitations of these previous techniques and suggest new methodologies for approaching related bilayer interactions in the future. The development of the novel implicit bilayer, implicit solvent model used throughout Part I of the thesis was inspired in part by previous models for the folding of proteins [168] and the partitioning of transmembrane proteins [165, 180]. The success of this model in predicting experimental results illustrates the importance of recognizing the similarities between NPs and proteins, an analogy often overlooked in the literature. Similarly, the model itself is of great use in rapidly screening different NP characteristics as shown in Chapter 5, allowing for experimentally-verifiable predictions. Such coupling to experiments is one of the most important aspects of this thesis and is again often overlooked in the literature. I expect that this model may be applied for the understanding of a variety of NP systems in the future. In Part II, I further introduced a new NP parameterization for use in atomistic molecular dynamics simulations. Derived from an existing GROMOS force field, the atomistic resolution of the model exceeds the previous coarse-grained approaches, allowing for the accurate representation of both ligand and lipid fluctuations. While the parameterization itself is useful, the use of the bilayer ribbon system to identify the key transition state for spontaneous insertion without applying any system bias is particularly useful for guiding future work. By not assuming an *a priori* reaction coordinate and instead identifying the important system configuration from unbiased trajectories, I was able to maintain a physically correct representation of the system while still overcoming the significant energy barriers present in a planar system. The results and workflow developed in Chapter 9 confirmed that the NP-protrusion contact found from this approach is indeed critical for insertion into more common planar, defect-free bilayers. I believe the use of such unbiased simulations to identify important system processes will be useful for many other systems as well. Finally, the results of Chapter 9 also illustrate the potential pitfall of using fully periodic bilayer systems as is standard in most simulations. The recognition that rapid NP insertion can be inhibited by periodic boundary conditions is again important to a variety of systems and has been previously overlooked in the literature.

Taken together, the methods I have developed present a physically realistic model of NP-bilayer interactions that surpass previous methods in the simulation literature. I expect that similar approaches will be useful in examining interactions for other membrane-active systems such

as peripheral proteins, tail-anchored proteins, or viruses, extending the contribution of my thesis beyond just NP studies.

12.2.5 Potential future applications

The physical insights and design rules uncovered from this thesis will be valuable in engineering new NPs for biological applications. One possibility would be to take advantage of the non-disruptive cell internalization behavior to design new drug carriers by binding drugs (or other small molecules, such as DNA) to the NP surface. The delivery of oligonucleotides has already demonstrated that these NPs can ferry cargo into the cell [100]. Upon intracellular access, glutathione exchange could mediate the release of the cargo into the cytosol. Another possibility would be to use NPs to decorate liposomes containing the desired cargo. If the NPs embed within the liposome membrane, they may be able to induce liposome-cell fusion as discussed above as a means of triggering cargo release; such a strategy is currently being pursued (unpublished).

Beyond drug delivery, the exciting ability of these NPs to embed within synthetic membranes may lead to the development of a new class of transmembrane NPs that mimic membrane proteins. Incorporating desired receptors, dyes, or biosensors into the monolayer could allow for the molecules to be effectively embedded in the bilayer even if they are hydrophilic. The observation of monolayer-dependent membrane deformations could also be used to recruit specific lipid types to the NP surface via tuning hydrophobic mismatch. Another intriguing possibility would be to use the NPs to deliver signals to the bilayer. For example, the gold core could be excited by an electromagnetic signal to locally heat the bilayer, or iron could be incorporated into the NP core so that NPs could be actuated by an applied magnetic field to mechanically stimulate nearby proteins.

Finally, the NP-bilayer interactions described throughout this thesis depend on physicochemical forces that are certainly not unique to this class of NP, and indeed are prominent in many related biological systems. For example, high-throughput screening has recently led to the identification of peptides that can insert deeply into bilayers without overt disruption, matching the experimental results on these NPs [374]. The similarities I showed between NP-bilayer fusion and vesicle-vesicle fusion also suggest the possibility that such a fusion process is prominent in other membrane-active systems with exposed hydrophobic surface area. For example, amyloid fibers typically have significant amounts of hydrophobic and aromatic residues which could mediate bilayer interactions similar to those proposed here [375]. Peripheral proteins, antimicrobial peptides, and cell-penetrating peptides may all also exhibit interactions similar to those proposed here given the commonalities in their structure and surface properties [376]. The conclusions of this work are thus potentially far-reaching to both synthetic and biological systems and I believe my findings will be of great use in guiding future studies of interactions at the cell interface.

Appendices

Appendix A

Simulation Algorithms

In this Appendix, derivations and descriptions of several important algorithms used throughout the thesis will be described. Three different algorithms were used to sample system configurations or model system dynamics and will be described in turn. Next, the basics of free energy techniques will be described, including descriptions of the weighted-histogram analysis method and Bennett acceptance ratio method that are both employed throughout the thesis. These derivations are intended to provide the theoretical rationale for computational methodologies employed; details of the implementation of these techniques are included in relevant previous Chapters.

A.1 Metropolis Monte Carlo

In general, the goal of a simulation might be to estimate the ensemble average of a quantity which will be denoted as A. The ensemble average in the classical canonical ensemble (with the number of particles, volume, and temperature fixed) is given as:

$$\langle A \rangle = \frac{\int d\mathbf{r}^N \exp\left[-\beta U(\mathbf{r}^N)\right] A(\mathbf{r}^N)}{\int d\mathbf{r}^N \exp\left[-\beta U(\mathbf{r}^N)\right]} \tag{A.1}$$

$\mathbf{r}^N$ is an N-dimensional vector describing the entire set of atomic coordinates for N particles, $U(\mathbf{r}^N)$ is the potential energy of a particular system configuration, and $\beta = \frac{1}{kT}$ where k is Boltzmann's constant. In principle, the integrals in eq. (A.1) could be calculated in a brute force manner by determining the value of $A(\mathbf{r}^N)$ for every set of particle coordinates and integrating numerically. However, such an approach would be impossible computationally because the number of system configurations becomes effectively infinite for even a small number of particles. Moreover, it is likely that the vast majority of the system configurations would have a high energy, $U(\mathbf{r}^N) \gg kT$, and as a result the Boltzmann factor for most values of $A(\mathbf{r}^N)$ would be zero. In other words, a large portion of the phase space possible for a simulation will be inaccessible due to its high energy. Performing such a calculation would thus be not only nearly impossible, but also highly inefficient. Finally, the last thing to notice is that to calculate $\langle A \rangle$, it is not necessary to calculate the value of the integrals in both the numerator and denominator of eq. (A.1); only their ratio must be determined. Monte Carlo importance sampling using the Metropolis-Hastings scheme (referred to henceforth as Metropolis Monte Carlo) provides a means to calculate this ratio by sampling only those states of sufficiently low energy to contribute meaningfully to the integrals [377].

The method of Metropolis Monte Carlo involves first generating a configuration in phase space that has a non-zero Boltzmann factor then sampling new configurations according to their proper equilibrium distribution. New states are generated by performing a series of trial moves that attempt perturb the previous configuration. At equilibrium, the probability density for finding a

system in a configuration near $\mathbf{r}^N$ must be stationary, meaning that once equilibrium is achieved the probability density is constant. Therefore, it must be the case that the number of trial moves that generate new configurations from a particular state must be equal to the total number of trial moves from all other states that generate the original configuration. If we write the probability of transitioning from some configuration $\mathbf{r}_1$ to $\mathbf{r}_2$ (dropping the superscript for simplicity) as $\Pi(\mathbf{r}_1 \rightarrow \mathbf{r}_2)$ and the probability of being in state $\mathbf{r}_1$ as $P(\mathbf{r}_1)$, then we can fulfill the condition that $P(\mathbf{r}_1)$ is stationary by imposing the condition of *detailed balance*:

$$P(\mathbf{r}_1)\Pi(\mathbf{r}_1 \rightarrow \mathbf{r}_2) = P(\mathbf{r}_2)\Pi(\mathbf{r}_2 \rightarrow \mathbf{r}_1) \tag{A.2}$$

This condition states that the probability of being in a particular configuration and transitioning to a new one is the same as the probability of being in the new state and transitioning to the old one. It is a more stringent condition than is necessary to ensure that the equilibrium distribution is stationary. The key aspect of the Metropolis algorithm is to further divided the transition matrix, Π, into two terms - the probability of generating a particular trial configuration, $g(\mathbf{r}_1 \rightarrow \mathbf{r}_2)$, and the probability of accepting the new trial configuration, $\alpha(\mathbf{r}_1 \rightarrow \mathbf{r}_2)$:

$$\Pi(\mathbf{r}_1 \rightarrow \mathbf{r}_2) = g(\mathbf{r}_1 \rightarrow \mathbf{r}_2)\alpha(\mathbf{r}_1 \rightarrow \mathbf{r}_2) \tag{A.3}$$

Eq. (A.2) can then be rewritten as:

$$\begin{aligned} P(\mathbf{r}_1)g(\mathbf{r}_1 \rightarrow \mathbf{r}_2)\alpha(\mathbf{r}_1 \rightarrow \mathbf{r}_2) &= P(\mathbf{r}_2)g(\mathbf{r}_2 \rightarrow \mathbf{r}_1)\alpha(\mathbf{r}_2 \rightarrow \mathbf{r}_1) \\ \frac{g(\mathbf{r}_1 \rightarrow \mathbf{r}_2)\alpha(\mathbf{r}_1 \rightarrow \mathbf{r}_2)}{g(\mathbf{r}_2 \rightarrow \mathbf{r}_1)\alpha(\mathbf{r}_2 \rightarrow \mathbf{r}_1)} &= \frac{P(\mathbf{r}_2)}{P(\mathbf{r}_1)} \end{aligned} \tag{A.4}$$

Because the probability distribution $P(\mathbf{r})$ is based on Boltzmann weighting in the canonical ensemble, we can write $P(\mathbf{r}) \propto \exp\left[-\beta U(\mathbf{r})\right]$ with the partition function, Z, as a normalizing constant. Furthermore, assuming that the matrix g for generating trial moves is symmetric, then $g(\mathbf{r}_1 \rightarrow \mathbf{r}_2) = g(\mathbf{r}_2 \rightarrow \mathbf{r}_1)$ and we can write:

$$\frac{\alpha(\mathbf{r}_1 \rightarrow \mathbf{r}_2)}{\alpha(\mathbf{r}_2 \rightarrow \mathbf{r}_1)} = \exp\left\{-\beta\left[U(\mathbf{r}_2) - U(\mathbf{r}_1)\right]\right\} \tag{A.5}$$

Eq. (A.5) stipulates the conditions on the acceptance condition, $\alpha(\mathbf{r}_1 \rightarrow \mathbf{r}_2)$, that leads to correct Boltzmann-weighted sampling of configurations in the canonical ensemble. In principle several choices of the acceptance condition could fulfill this condition; the choice used in the original derivation of the Metropolis algorithm is [377]:

$$\alpha(\mathbf{r}_1 \rightarrow \mathbf{r}_2) = \min\left(1, \exp\left\{-\beta\left[U(\mathbf{r}_2) - U(\mathbf{r}_1)\right]\right\}\right) \tag{A.6}$$

This condition fulfills eq. (A.5) because if $P(\mathbf{r}_2) < P(\mathbf{r}_1)$ (i.e. $U(\mathbf{r}_2) - U(\mathbf{r}_1) > 0$) then $\alpha(\mathbf{r}_1 \rightarrow \mathbf{r}_2) = \exp\left\{-\beta\left[U(\mathbf{r}_2) - U(\mathbf{r}_1)\right]\right\}$ and $\alpha(\mathbf{r}_2 \rightarrow \mathbf{r}_1) = 1$, satisfying the desired ratio.

The Metropolis Monte Carlo algorithm for the canonical ensemble then consists of the following steps [377]:

1. Choose a starting configuration, $\mathbf{r}_0^N$.
2. Generate a trial move by perturbing $\mathbf{r}_0^N$ according to the probability $g(\mathbf{r}_0^N \rightarrow \mathbf{r}_1^N)$.
3. Accept the trial move with a probability given by eq. (A.6).
4. If the move is rejected, retain the original configuration; otherwise, update system coordinates to $\mathbf{r}_1^N$.
5. Repeat steps 2-4.

Metropolis Monte Carlo has several advantages. First, the acceptance ratio only relies on the energies of the two states, and as a result the generation rule g can be arbitrary and does not have to be physically meaningful. This feature also means that many-body potentials can be easily used to calculate system energies, which is more difficult to do in molecular dynamics simulations that require pair potentials. In addition, because all configurations are sampled according to their equilibrium probability distributions, averaging observables over simulation configurations generates ensemble averages. The downside, however, is that the algorithm is only useful for calculating equilibrium thermodynamic properties and not observing system kinetics. The Metropolis Monte Carlo technique is used in Chapters 3, 5, and 10.

A.2 Molecular Dynamics

In contrast to Metropolis Monte Carlo, molecular dynamics simulations seek to both sample configurations from the correct thermodynamic ensemble and accurately model system kinetics. In classical molecular dynamics the key assumption is that the particles in the simulation obey the laws of classical mechanics and any quantum effects or electron motion occur over time- and length-scales too small to influence the simulation. Molecular dynamics thus involves integrating Newton's laws to determine equations of motions for all particles.

The simplest molecular dynamics algorithm consists of determining the initial locations of all particles, calculating forces on all particles, then updating particle positions from the applied forces by discretizing time [377]. The method for determining forces is given by the underlying *force field* chosen for a particular simulation. Force fields stipulate both the functional form for all forces calculated during a simulation as well as any necessary parameters. Most biomolecular force fields first assume that all forces can be computed from pair-wise interactions between pairs of particles [378]. Forces can then be generally subdivided into non-bonding interactions, representing electrostatic, excluded volume, and van der Waals forces, and bonding interactions, representing covalent bonds and bond angle restrictions. For example, a typical choice of a non-bonded interaction is the Lennard-Jones potential, defined as:

$$U_{ij} = 4\epsilon \left[\left(\frac{\sigma}{d_{ij}} \right)^{12} - \left(\frac{\sigma}{d_{ij}} \right)^{6} \right] \tag{A.7}$$

This potential describes the interaction between particles i and j according to two parameters, σ and ϵ, which define a characteristic length scale and energy scale for the interaction respectively, and the scalar distance between the two particle d_{ij}. The first term is positive and represents short-ranged repulsion while the second term is negative and represents longer-ranged van der Waals attraction. The values of ϵ and σ must be defined for every pair of particles as part of the force field. Details on how forces are calculated for the GROMOS force field, used in Chapters 6-9 and 11, are provided in Appendix D.

Once a method for calculating forces has been established, particle positions must be updated by integrating the equations of motion [377]. First, we can Taylor expand the position of a particle at time t, writing:

$$\mathbf{r}(t + \Delta t) = \mathbf{r}(t) + \mathbf{v}(t)\Delta t + \frac{\mathbf{a}(t)}{2}\Delta t^2 + ... \tag{A.8}$$

$\mathbf{r}(t)$ is the position of a single particle, $\mathbf{v}(t) = \dot{\mathbf{r}}(t)$ is the velocity, and $\mathbf{a}(t) = \ddot{\mathbf{r}}(t) = \mathbf{f}(t)/m$ is the acceleration, which is related to the net force $\mathbf{f}(t)$ on the particle from Newton's second law. The increment in time Δt defines the simulation timestep. Eq. (A.8) could be used directly to calculate particle positions by calculating $\mathbf{v}(t)$ and $\mathbf{a}(t)$ for every timestep, using this to determine $\mathbf{r}(t+\Delta t)$, then advancing time by Δt and repeating. However, this approach is inefficient and leads to significant energy drift [379, 377].

An improved algorithm starts by defining the particle's position at both $\pm\Delta t$ (truncated at the Δt^2 term):

$$\begin{aligned} \mathbf{r}(t + \Delta t) &= \mathbf{r}(t) + \mathbf{v}(t)\Delta t + \frac{\mathbf{f}(t)}{2m}\Delta t^2 \\ \mathbf{r}(t - \Delta t) &= \mathbf{r}(t) - \mathbf{v}(t)\Delta t + \frac{\mathbf{f}(t)}{2m}\Delta t^2 \end{aligned}$$

Summing these two expressions yields:

$$\begin{aligned} \mathbf{r}(t + \Delta t) + \mathbf{r}(t - \Delta t) &= 2\mathbf{r}(t) + \frac{\mathbf{f}(t)}{m}\Delta t^2 \\ \mathbf{r}(t + \Delta t) &\approx 2\mathbf{r}(t) - \mathbf{r}(t - \Delta t) + \frac{\mathbf{f}(t)}{m}\Delta t^2 \end{aligned} \tag{A.9}$$

Eq. (A.9) is known as the Verlet scheme and provides a means to update particle positions without necessarily calculating velocities [379, 377].

In the leap-frog scheme, the velocity is instead determined at half-integer timesteps:

$$\mathbf{v}(t - \Delta t/2) = \frac{\mathbf{r}(t) - \mathbf{r}(t - \Delta t)}{\Delta t}$$
$$\mathbf{v}(t + \Delta t/2) = \frac{\mathbf{r}(t + \Delta t) - \mathbf{r}(t)}{\Delta t} \tag{A.10}$$

Rewriting the second equation yields:

$$\mathbf{r}(t + \Delta t) = \mathbf{r}(t) + \Delta t \mathbf{v}(t + \Delta t/2) \tag{A.11}$$

and from the Verlet scheme, eq. (A.9), we can write:

$$\mathbf{v}(t + \Delta t/2) = \mathbf{v}(t - \Delta t/2) + \Delta t \frac{\mathbf{f}(t)}{m} \tag{A.12}$$

Eqs. (A.11) and (A.12) define the leap-frog algorithm, which is the default in Gromacs and is used in Chapters 6-9 and Chapter 11 [378, 377].

If the molecular dynamics algorithm is employed as described above, then the resulting positions generated will sample the microcanonical NVE ensemble as the number of particles, volume, and total energy are all conserved. However, in most cases of interest in biomolecular systems a different ensemble will be preferred, such as the canonical NVT ensemble sampled via Monte Carlo methods or the isothermal-isobaric NPT ensemble generally applicable to laboratory conditions. The equations of motion must be updated then to include constraints on the temperature and/or pressure accordingly.

To calculate the temperature of a simulation in molecular dynamics, the kinetic energy is computed directly from the N particle velocities and related to the absolute temperature via the equipartition theorem, which states that the average kinetic energy per particle should be $1/2kT$ per degree of freedom [377]:

$$U_{kin}(t) = \frac{1}{2} \sum_{i=1}^{N} m_i \mathbf{v}_i(t)^2 = \frac{1}{2} N_{df} kT(t) \tag{A.13}$$

Here, N_{df} is the number of degrees of freedom, which is $3N$ for a system of particles with 3D translational motion and no constraints. Note that in the leap-frog algorithm $\mathbf{v}(t)$ is not calculated directly, but can be interpolated from $\mathbf{v}(t + \Delta t)$ and $\mathbf{v}(t - \Delta t)$. This equation provides the means to define temperature as a function of time from particle velocities.

To calculate the pressure of a simulation, the virial theorem is used to relate the total potential energy of the system to the average kinetic energy. The virial theorem can be stated as:

$$2\langle U_{kin} \rangle = -\sum_{i=1}^{N} \langle \mathbf{f}_i \cdot \mathbf{r}_i \rangle \tag{A.14}$$

Here, $\mathbf{f}_i$ is the total force on particle i which is located at position $\mathbf{r}_i$. The total force on a particle can be divided into two components - the first related to forces from other particles within the simulation volume (i.e. internal forces), and the second related to interactions with the walls of the simulation box (i.e. external forces). We can thus write:

$$\begin{aligned} 2\langle U_{kin}\rangle &= -\sum_{i=1}^{N}\langle(\mathbf{f}_i^{int}+\mathbf{f}_i^{ext})\cdot\mathbf{r}_i\rangle \\ &= -\sum_{i=1}^{N}\langle\mathbf{f}_i^{int}\cdot\mathbf{r}_i\rangle - \sum_{i=1}^{N}\langle\mathbf{f}_i^{ext}\cdot\mathbf{r}_i\rangle \end{aligned} \tag{A.15}$$

The first term for internal forces acting on particle i can be computed from pairwise interactions during simulations with other particles; this expression is defined as the *inner virial*. The second term can be related to external forces acting on the system; this expression will be defined as the *outer virial*, which we can now relate to the pressure. The force exerted by the wall on nearby particles will be given by the $PdA\mathbf{n}$ where n is the normal vector to the wall, P is the pressure and dA is the area element. We assume that the area element is sufficiently small that it only acts on a small set of nearby particles with roughly equivalent distances to the area element, such that all $\mathbf{r}_i = \mathbf{r}$. We can then write the contribution just from the surface element dA as:

$$\sum_{i=1}^{N}\langle\mathbf{f}_i^{ext}\cdot\mathbf{r}_i\rangle = \sum_{i=1}^{N}\langle PdA\mathbf{n}\cdot\mathbf{r}\rangle = -\int_A PdA\mathbf{n}\cdot\mathbf{r} \tag{A.16}$$

The negative sign is because the surface normal points inwards into the box volume. Integrating over the entire surface A sums contributions from all surface area elements dA on all nearby particles, and hence the integral is equivalent to the sum. Using the divergence theorem, this can be written as:

$$-\int_A PdA\mathbf{n}\cdot\mathbf{r} = -P\int_V \text{div}(\mathbf{r})\ dV = -3PV \tag{A.17}$$

Note that div r equals 3 because that is the dimensionality of the system. We can now rewrite eq. (A.14) as:

$$2\langle U_{kin}\rangle = -\sum_{i=1}^{N}\langle\mathbf{f}_i^{int}\cdot\mathbf{r}_i\rangle + 3PV \tag{A.18}$$

Substituting in the result from eq. (A.13), we thus solve for the pressure as:

$$P(t) = \frac{1}{3V}\left(N_{df}kT(t) - \sum_{i=1}^{N}\langle\mathbf{f}_i^{int}\cdot\mathbf{r}_i\rangle\right) \tag{A.19}$$

As with the temperature, we write the pressure as an instantaneous function of time while the derivation assumes ensemble averaging. This means that over sufficient timescales the average

pressure should converge to its ensemble value, but instantaneous values (which are necessary for pressure coupling) will typically fluctuate significantly. In practice, the pressure is computed as a tensor rather than as a scalar quantity to allow for box walls of differing dimensions and the contribution to the inner virial is calculated each timestep from forces acting on all particles [378].

The algorithm used to control the temperature or pressure in a simulation at constant temperature or pressure is called the thermostat or barostat respectively. Many thermostat and barostat algorithms are available with various degrees of accuracy and efficiency. An intuitively simple but effective thermostat is the velocity-rescale thermostat which is used for all simulations in Chapters 6-9 and Chapter 11 [380]. The basic principle of this thermostat is to periodically rescale the velocities of all particles in the simulation box such that the average kinetic energy correctly represents the desired ensemble. To do this, a velocity-rescale factor is defined as:

$$\alpha = \sqrt{\frac{K_t}{K(t)}} \tag{A.20}$$

Here, $K(t)$ is the instantaneous kinetic energy measured by eq. (A.13) and K_t is a target kinetic energy value drawn from the canonical distribution function:

$$P(K_t)dKt \propto K_t^{(N_{df}/2-1)} \exp(-\beta K_t) dK_t \tag{A.21}$$

The most straight-forward implementation of the velocity-rescaling algorithm consists of stochastically choosing a value of K_t from the distribution above, computing $K(t)$ (i.e. the temperature) for a particular timestep, determining α from $K(t)$ and K_t, then multiplying all particle velocities by α to establish a new system temperature. Because particle positions and velocity directions are not modified, bonding or steric constraints cannot be violated and the center-of-mass of the system remains the same. In practice, this approach leads to artifacts due to significant fluctuations in particle velocities from the rescaling step. Instead, K_t is chosen to operate under its own auxiliary dynamics to prevent significant changes in the kinetic energy upon rescaling. The stochastic term is usually chosen as:

$$dK = (K_0 - K)\frac{dt}{\tau} + 2\sqrt{\frac{K_0 K}{N_{df}}}\frac{dW}{\sqrt{\tau}} \tag{A.22}$$

where K_0 is the desired temperature, τ is a time constant controlling how tightly coupled the kinetic energy is to the reference kinetic energy, and dW is a stochastic Wiener process. This version of the velocity-rescale thermostat successfully reproduces properties of the canonical ensemble [380].

Just as thermostatting involves adjusting particle velocities to achieve the reference value of temperature, barostatting involves adjusting the simulation box volume to achieve the desired value of the pressure. A simple and effective barostat is the Berendsen algorithm which functions by periodically rescaling the box volume as well as all particle coordinates [381]. The Berendsen algorithm imposes first-order kinetic relaxation on deviations of the pressure by:

$$\frac{dP(t)}{dt} = \frac{P_0 - P(t)}{\tau_p} \tag{A.23}$$

Here $P(t)$ is the instantaneous pressured measured by from eq. (A.19), P_0 is the reference pressure, and τ_p is a time constant that controls the relaxation time scale. To enforce the pressure change, particle positions are re-scaled and the box volume is adjusted. This modifies the interparticle interactions and accordingly changes the virial, allowing eq. (A.23) to be fulfilled. Rescaling particle positions entails adding a new term to the equation of motion:

$$\frac{d\mathbf{r}}{dt} = \mathbf{v} + \alpha\mathbf{r} \tag{A.24}$$

where $\mathbf{r}$ is the particle position, $\mathbf{v}$ the velocity (calculated based on the acceleration determined from the net force on each particle) and α is a scaling constant. The corresponding change in volume is:

$$\frac{dV}{dt} = 3\alpha V \tag{A.25}$$

We can relate the change in pressure with time to the change in volume to find an expression for α. From the definition of the isothermal compressibility, B, we get:

$$\begin{aligned} B &= -\frac{1}{V}\frac{dV}{dP} \\ &= -\frac{1}{V}\frac{dV/dt}{dP/dt} \\ \frac{dP}{dt} &= -\frac{1}{BV}\frac{dV}{dt} \end{aligned} \tag{A.26}$$

Substituting eq. (A.23) and eq. (A.25) into eq. (A.26) yields the expression for α:

$$\begin{aligned} \frac{dP}{dt} = \frac{P_0 - P(t)}{\tau_p} &= -\frac{3\alpha}{B} \\ \alpha &= \frac{-B[P_0 - P(t)]}{3\tau_p} \end{aligned} \tag{A.27}$$

The modified equation of motion then reads:

$$\frac{d\mathbf{r}}{dt} = \mathbf{v} - \frac{B[P_0 - P(t)]}{3\tau_p}\mathbf{r} \tag{A.28}$$

This expression effectively scales the positions of all particles to enforce the pressure coupling. A corresponding scaling matrix, μ, can be defined in terms of Δt as:

$$\mu = 1 - \frac{B\Delta t}{3\tau_p}\left[P_0 - P(t)\right] \tag{A.29}$$

The adjusted particle position is then $\mu\mathbf{r}$ and each box vector is adjusted by a factor of μ as well.

Including the thermostat and barostat adjustments, the full algorithm for molecular dynamics becomes [381]:

1. Initialize starting particle coordinates.
2. Calculate forces on all particles according to underlying force field.
3. Evaluate the kinetic energy according to eq. (A.13) and the pressure according to eq. (A.19).
4. Compute velocities using eq. (A.12) with forces from step 2.
5. Adjust velocities according to thermostat.
6. Compute new positions according to eq. (A.11) using adjusted velocities.
7. Adjust positions according to barostat.
8. Repeat steps 2-7.

A.3 Brownian Dynamics

Molecular dynamics is a deterministic algorithm within the limits of machine precision, unless a particular thermostat or barostat is used that requires stochastic coupling. As a result, interactions with solvent molecules must be included explicitly, which can be extremely expensive computationally. In addition, many processes operate on timescales much longer than the motion of the solvent, requiring a significant amount of simulation time to be spent on modeling relatively inconsequential solvent dynamics. Ideally, studying such mesoscale processes would be accomplished without representing all solvent degrees of freedom explicitly.

Brownian dynamics is an algorithm designed for coarse-grained implicit solvent simulations by replacing the influence of the solvent with effective forces instead. As the name implies, the algorithm assumes that particles undergo Brownian motion. The general equation for motion can be written as [379]:

$$\mathbf{f}_i^{tot} = \mathbf{f}_i^{disp} + \mathbf{f}_i^{rand} + \mathbf{f}_i^{cons} \tag{A.30}$$

Here, $\mathbf{f}_i^{tot}$ is the total force acting on particle i and is decomposed into three components: $\mathbf{f}_i^{disp}$, the dissipative force, $\mathbf{f}_i^{rand}$, a stochastic force representing random collisions with solvent, and $\mathbf{f}_i^{cons}$, the sum of conservative forces from non-bonded and bonded interactions with other particles. $\mathbf{f}_i^{disp}$ and $\mathbf{f}_i^{rand}$ together account for missing interactions with solvent by representing viscous drag and Brownian motion respectively. Assuming all particles can be represented as identically-sized spheres without any hydrodynamic interactions and assuming that the unperturbed solvent velocity is the same throughout the simulation box, $\mathbf{f}_i^{disp}$ can be written following Stokes law as [379]:

$$\mathbf{f}_i^{disp} = -\zeta \frac{d\mathbf{r}_i}{dt} \tag{A.31}$$

where ζ is the friction coefficient. The stochastic force, $\mathbf{f}_i^{rand}$, represents random collisions with solvent and as a result must satisfy fluctuation-dissipation theorem. This is accomplished by establishing the conditions that:

$$\langle \mathbf{f}_i^{rand}(t) \rangle = 0 \tag{A.32}$$

$$\langle \mathbf{f}_i^{rand}(t) \mathbf{f}_j^{rand}(t+s) \rangle = 2kT\zeta\delta_{ij}\delta(s) \tag{A.33}$$

where δ_{ij} is the Kronecker delta function and $\delta(s)$ is the Dirac delta function. These relations can be satisfied by writing $\mathbf{f}_i^{rand} = \sqrt{2kT\zeta\Delta t}\mathbf{f}_r$ where $\mathbf{f}_r$ is Gaussian distributed random noise with a mean of 0 and a standard deviation of 1 [378]. Eq. (A.30) becomes:

$$\mathbf{f}_i^{tot} = -\zeta \frac{d\mathbf{r}_i}{dt} + \sqrt{2kT\zeta}\mathbf{f}_r + \mathbf{f}_i^{cons} \tag{A.34}$$

In Brownian dynamics, it is assumed that the simulation timescale is sufficiently long that the system is overdamped and no inertial effects are important. In this case, $\mathbf{f}_i^{tot} = 0$ and we can write as an equation of motion:

$$\frac{d\mathbf{r}}{dt} = \frac{1}{\zeta}\mathbf{f}_i^{cons} + \sqrt{\frac{2kT}{\zeta}}\mathbf{f}_r \tag{A.35}$$

This equation of motion is used in Chapter 2, with $\mathbf{f}_i^{cons}$ calculated using typical pair potentials and $\mathbf{f}_r$ calculated using the Gaussian distribution described above. The algorithm correctly samples the canonical ensemble and as a result no thermostatting is required [379].

A.4 Free energy calculations

The algorithms described above are suitable for sampling configurations of the simulation systems according to an underlying statistical ensemble. Equilibrium average quantities can then be calculated by averaging over system configurations, or dynamical quantities can be observed during molecular dynamics or Brownian dynamics simulations as well. However, none of the methods above give direct access to free energies which would be useful to know in many applications. If configurations are correctly sampled, however, the free energy of system process can in principle be calculated. This section derives algorithms used to perform such free energy calculations. All derivations will be performed in the canonical NVT ensemble, although extensions to constant pressure can be done as well through suitable corrections.

A.4.1 Potential of mean force

We start with the standard definition of the Helmholtz free energy, $F = -kT \ln Z$ where Z is the configurational part of the canonical partition function of the system, $Z = \int d\mathbf{r}^N \exp\left[-\beta U(\mathbf{r}^N)\right]$. We next define a collective variable $x(\mathbf{r}^N)$ as the *reaction coordinate* of the system. Example collective variables of interest might be the surface area of a bilayer, the pressure of the system, the relative position of a NP and the bilayer, etc. At equilibrium, the probability density for finding the system assuming a configuration with a particular value of the reaction coordinate $x = x'(\mathbf{r}^N)$ is then:

$$p(x) = \frac{\int d\mathbf{r}^N \exp\left[-\beta U(\mathbf{r}^N)\right] \delta(x'(\mathbf{r}^N) - x)}{Z} \tag{A.36}$$

Here, the integral in the numerator runs over all possible atomic configurations of the system and the delta function only counts states where $x = x'(\mathbf{r}^N)$, i.e. all degrees of freedom are integrated out except for configurations with the desired value of the reaction coordinate. However, we can recognize the numerator of eq. (A.36) as effectively defining a new partition function that describes the statistical properties of the system for $x = x'(\mathbf{r}^N)$, i.e. the subset of the full phase space consistent with one particular value of the reaction coordinate. We can thus write:

$$p(x) = \frac{Z_x(x)}{Z} \tag{A.37}$$

In other words, the numerator of eq. (A.36) is a new partition function ($Z_x(x)$) describing the projection of the total phase space onto a particular region that is restricted to one particular value of the reaction coordinate [377]. Now we can take the free energy associated with the new partition function:

$$F_x(x) = -kT \ln Z_x(x) = -kT \ln\left[p_x(x)\right] - kT \ln Z \tag{A.38}$$

Although we do not know the value of Z, as long as we only take *differences* in the free energy for different values of the reaction coordinate, the second term will drop out. We define these differences in the free energy as a function of the reaction coordinate as the *potential of mean force*, $W(\Delta x)$, which we can write as [382]:

$$W(x_1) - W(x_0) = -kT \ln\left[\frac{p(x_1)}{p(x_0)}\right] \tag{A.39}$$

where x_0 and x_1 are two values of the reaction coordinate of interest and the potential of mean force (PMF) calculates the free energy change associated with moving the system from a region of phase space associated with x_0 to one associated with x_1. Again the definition of $p(x)$ is:

$$p(x) = \frac{\int d\mathbf{r}^N \exp\left[-\beta U(\mathbf{r}^N)\right] \delta(x'(\mathbf{r}^N) - x)}{\int d\mathbf{r}^N \exp\left[-\beta U(\mathbf{r}^N)\right]} \tag{A.40}$$

A.4.2 Umbrella sampling

The PMF is a very useful quantity for establishing equilibrium free energy changes associated with processes that involve a well-defined reaction coordinate [382]. For example, the free energy change for bringing molecules together in solution could be computed as a function of their separation. To calculate the PMF, however, the probability densities $p(x_1)$ and $p(x_0)$ must be determined. In principle, these probability densities could be calculated by simply generating system configurations within the entire accessible phase space (using either standard molecular dynamics with correct thermostatting or via Monte Carlo sampling, for example) and seeing how frequently the desired values of the reaction coordinates are generated. However, this brute force approach is very unlikely to sample states efficiently, as the vast majority of simulation time would be spent computing configurations that do not contribute to the calculation of $p(x_1)$ or $p(x_0)$. Worse, if either value of the reaction coordinate exists in a region of phase space that is nearly inaccessible (i.e. the reaction coordinate sits at the top of a free energy barrier), then it is likely that the value may never be determined via a brute force approach.

One solution to overcome the sampling problem and facilitate the calculation of the probability densities of interest (and thus the PMF) is to apply a bias to the system dynamics. In this technique, known as *umbrella sampling*, a set of weighting functions are defined and added to the system Hamiltonian [379, 377]. Each weight function is defined to restrain the dynamics of the system such that the generated configurations are restricted to those associated with a particular value of the reaction coordinate. We define:

$$p_b(x) = \frac{\int d\mathbf{r}^N \exp\left[-\beta w(x)\right] \exp\left[-\beta U(\mathbf{r}^N)\right] \delta(x'(\mathbf{r}^N) - x)}{\int d\mathbf{r}^N \exp\left[-\beta w(x)\right] \exp\left[-\beta U(\mathbf{r}^N)\right]} \tag{A.41}$$

Here, $w(x)$ is the weight function that restrains $x'(\mathbf{r}^N)$ to a particular value x. We can now relate this biased probability density, $p_b(x)$, to the unbiased probability density $p(x)$. We can first recognize that because $w(x)$ is only a function of x, and the delta function in the integral in the numerator effectively eliminates all degrees of freedom other than x, we can take $\exp[-\beta w(x)]$ out of this integral. This gives:

$$p_b(x) = \exp\left[-\beta w(x)\right] \frac{\int d\mathbf{r}^N \exp\left[-\beta U(\mathbf{r}^N)\right] \delta(x'(\mathbf{r}^N) - x)}{\int d\mathbf{r}^N \exp\left[-\beta w(x)\right] \exp\left[-\beta U(\mathbf{r}^N)\right]} \tag{A.42}$$

We can now manipulate the second term to put the biased probability density in terms of the unbiased probability density:

$$
\begin{aligned}
p_b(x) &= \exp\left[-\beta w(x)\right] \frac{\int d\mathbf{r}^N \exp\left[-\beta U(\mathbf{r}^N)\right] \delta(x'(\mathbf{r}^N) - x)}{\int d\mathbf{r}^N \exp\left[-\beta w(x)\right] \exp\left[-\beta U(\mathbf{r}^N)\right]} \times \frac{\int d\mathbf{r}^N \exp\left[-\beta U(\mathbf{r}^N)\right]}{\int d\mathbf{r}^N \exp\left[-\beta U(\mathbf{r}^N)\right]} \\
&= \exp\left[-\beta w(x)\right] \frac{\int d\mathbf{r}^N \exp\left[-\beta U(\mathbf{r}^N)\right] \delta(x'(\mathbf{r}^N) - x)}{\int d\mathbf{r}^N \exp\left[-\beta U(\mathbf{r}^N)\right]} \times \frac{\int d\mathbf{r}^N \exp\left[-\beta U(\mathbf{r}^N)\right]}{\int d\mathbf{r}^N \exp\left[-\beta w(x)\right] \exp\left[-\beta U(\mathbf{r}^N)\right]} \\
&= \exp\left[-\beta w(x)\right] p(x) \langle \exp\left[-\beta w(x)\right] \rangle^{-1} \qquad \text{(A.43)}
\end{aligned}
$$

Here, $\langle \exp\left[-\beta w(x)\right] \rangle$ is the ensemble average of the exponential weight function for x sampled from the unbiased ensemble. We can finally write an expression for the unbiased probability density [383, 382]:

$$
p(x) = \exp\left[\beta w(x)\right] p_b(x) \langle \exp\left[-\beta w(x)\right] \rangle \qquad \text{(A.44)}
$$

The unbiased PMF for the ith value of the reaction coordinate (relative to a reference value that we assume is 0) is then:

$$
\begin{aligned}
W(x_i) &= -kT \ln\left[p(x_i)\right] \\
&= -kT \ln\left[\exp\left[\beta w(x_i)\right] p_b(x_i) \langle \exp\left[-\beta w(x_i)\right] \rangle\right] \\
&= -kT \ln\left[p_b(x_i)\right] - w(x_i) - kT \ln \langle \exp\left[-\beta w(x_i)\right] \rangle \qquad \text{(A.45)}
\end{aligned}
$$

This expression puts the PMF in terms of three contributions. The first, $-kT \ln\left[p_b(x_i)\right]$, can be estimated directly from molecular simulations because the biased Hamiltonian confines configurations to the phase space with $x'(\mathbf{r}^N) = x_i$, allowing $p_b(x_i)$ to be calculated even if this phase space is normally inaccessible. $w(x_i)$ is included analytically since the expression for the weight function is specified. This leaves the final term, $-kT \ln \langle \exp\left[-\beta w(x_i)\right] \rangle$, which we will now spend some time addressing.

A.4.3 Free energy perturbation

First, let us consider a related problem to the issue of determining the free energy along a defined reaction coordinate. As umbrella sampling involves perturbing the system Hamiltonian by incorporating weight functions, a more general question might be how to calculate the change in free energy between two states with different Hamiltonians. Finding an algorithm to accomplish this would also be useful in applications other than calculating a PMF along a reaction coordinate, such as calculating the free energy change associated with mutating the chemical identities of molecules in a simulation.

For this calculation, we will first define two partition functions, Z_0 and Z_1, corresponding to two different systems with potential energy functions $U_0(\mathbf{r}^N)$ and $U_1(\mathbf{r}^N)$. The Helmholtz free energy change for transforming from system 0 to 1 is then [379, 377]:

$$\begin{aligned}\Delta F &= F_1 - F_0 \\ &= -kT \ln Z_1/Z_0 \\ &= -kT \ln \left[\frac{\int d\mathbf{r}^N \exp\left[-\beta U_1(\mathbf{r}^N)\right]}{\int d\mathbf{r}^N \exp\left[-\beta U_0(\mathbf{r}^N)\right]} \right]\end{aligned} \tag{A.46}$$

Next, we define $p_1(\Delta U)$ as the probability density for the energy difference $\Delta U = U_1(\mathbf{r}^N) - U_0(\mathbf{r}^N)$ with configurations sampled using U_1. In other words, we can imagine generating a large number of configurations from system 1, calculating the energy of those configurations according to both U_1 and U_0, then finding the probability of identifying a particular difference ΔU. Similarly, $p_0(\Delta U)$ is the probability density for the same energy difference with configurations sampled using U_0. We then write:

$$\begin{aligned}p_1(\Delta U) &= \frac{\int d\mathbf{r}^N \exp\left[-\beta U_1(\mathbf{r}^N)\right] \delta(U_1(\mathbf{r}^N) - U_0(\mathbf{r}^N) - \Delta U)}{Z_1} \\ &= \frac{\int d\mathbf{r}^N \exp\left[-\beta (U_0(\mathbf{r}^N) + \Delta U)\right] \delta(U_1(\mathbf{r}^N) - U_0(\mathbf{r}^N) - \Delta U)}{Z_1} \\ &= \frac{\int d\mathbf{r}^N \exp\left[-\beta U_0(\mathbf{r}^N\right] \exp\left[-\beta \Delta U\right] \delta(U_1(\mathbf{r}^N) - U_0(\mathbf{r}^N) - \Delta U)}{Z_1}\end{aligned} \tag{A.47}$$

As in the previous section, here ΔU is a fixed value that is not a function of $\mathbf{r}^N$ and the delta function eliminates all other degrees of freedom, so $\exp\left[-\beta \Delta U\right]$ can be removed from the integral.

$$\begin{aligned}p_1(\Delta U) &= \exp\left[-\beta \Delta U\right] \frac{\int d\mathbf{r}^N \exp\left[-\beta U_0(\mathbf{r}^N)\right] \delta(U_1(\mathbf{r}^N) - U_0(\mathbf{r}^N) - \Delta U)}{Z_1} \\ &= \frac{Z_0}{Z_1} \exp\left[-\beta \Delta U\right] \frac{\int d\mathbf{r}^N \exp\left[-\beta U_0(\mathbf{r}^N)\right] \delta(U_1(\mathbf{r}^N) - U_0(\mathbf{r}^N) - \Delta U)}{Z_0} \\ &= \frac{Z_0}{Z_1} \exp\left[-\beta \Delta U\right] p_0(\Delta U)\end{aligned} \tag{A.48}$$

We can take the log of both sides to estimate the free energy difference using $\Delta F = -kT \ln Z_1/Z_0$:

$$\begin{aligned}\ln p_1(\Delta U) &= \ln\left[Z_0/Z_1\right] - \beta \Delta U \ln p_0(\Delta U) \\ &= \beta(\Delta F - \Delta U) \ln p_0(\Delta U)\end{aligned} \tag{A.49}$$

From this equation alone we can see that calculating the two probability densities from simulations in both ensembles would allow for the calculation of the free energy change ΔF. We can further integrate the expressions to yield a more concise expression [377]:

$$p_1(\Delta U) = p_0(\Delta U)\exp\left[\beta(\Delta F - \Delta U)\right]$$
$$\int p_1(\Delta U)d\Delta U = \int p_0(\Delta U)d\Delta U \exp\left[\beta(\Delta F - \Delta U)\right]$$

Here the integrals run over all values of ΔU and the probability densities are normalized, so:

$$\begin{aligned}
\int p_1(\Delta U)d\Delta U &= \int p_0(\Delta U)d\Delta U \exp\left[\beta(\Delta F - \Delta U)\right] \\
1 &= \exp\left[\beta\Delta F\right]\int p_0(\Delta U)d\Delta U \exp\left[-\beta\Delta U)\right] \\
1 &= \exp\left[\beta\Delta F\right]\langle\exp\left[-\beta\Delta U\right]\rangle_0 \\
\exp\left[-\beta\Delta F\right] &= \langle\exp\left[-\beta\Delta U\right]\rangle_0
\end{aligned} \tag{A.50}$$

The final expression relates the free energy change for transforming from system 0 to system 1 to the ensemble average of the energy change for this transformation for configurations sampled from Z_0. This expression is often referred to as *free energy perturbation* and can be used directly in molecular simulations by defining system 0 and 1, generating configurations according to the Hamiltonian of system 0, calculating the energy of the same configuration calculated using both U_1 and U_0, then averaging $U_1 - U_0$ to get ΔF according to eq. (A.50). However, in practice this method is limited because it is likely that $p_0(\Delta U)$ is very small in regions where $\exp(-\beta\Delta U)$ is very large, so it is likely that large contributors to the ensemble average will not be sampled in a typical simulation. This problem can be ameliorated if there is significant overlap in the phase space of Z_1 and Z_0, meaning that the configurations generated from one partition function will still be probable in the other, but this is a severe limitation of the technique. The derivation of the Bennett acceptance ratio method given below will demonstrate how this problem can be circumvented even in cases where there is minimal phase space overlap.

A.4.4 Weighted-Histogram Analysis Method (WHAM)

The equation for umbrella sampling, eq. (A.45), expresses the PMF in terms of a biased probability density, the weighting functions, and an as-yet undiscussed term related to the weighting functions, $-kT\ln\langle\exp\left[-\beta w(x)\right]\rangle$. However, comparing this term with eq. (A.50) and eq. (A.45) shows that this term can be interpreted as the free energy change associated with introducing the weighting function for the ith value of the reaction coordinate into the unbiased Hamiltonian:

$$-kT\ln\langle\exp\left[-\beta w(x_i)\right]\rangle \equiv F_i \tag{A.51}$$

The umbrella sampling equation can then be rewritten as:

$$W(x_i) = -kT \ln [p_b(x_i)] - w(x_i) + F_i \tag{A.52}$$

To find differences in the PMF (i.e. $W(x_1) - W(x_0)$), there needs to be a means for efficiently calculating the set of F_i, as the value of each F_i will differ as the system is restrained to different values of the reaction coordinate. In principle, F_i could be determined by calculating $W(x_i)$ for a series of simulations such that there is significant overlap in the phase space sampled between different regions (e.g. by setting constraints with weak harmonic springs to allow systems constrained to one value of x_i to still sample other similar values of x_i). In this case, the value of $W(x_i)$ would have to be identical in regions of overlap independent of the set of weights used and F_i could be determined by enforcing this equivalence [382]. However, such an approach would require significant phase space overlap for the estimates of the F_i to converge and is thus computationally inefficient. Instead, a more efficient method must be identified to calculate the set of F_i and thus the PMF.

One popular method for calculating the set of F_i efficiently is known as the weighted-histogram analysis method, or WHAM [383]. WHAM is a method derived to optimally determine the values of the set of F_i based on the results of a series of umbrella sampling simulations by apportioning simulation results into histograms for post-simulation analysis. Assuming that R simulations have been run to restrain the system to R different values of the reaction coordinate, the idea of WHAM is to optimally estimate the unbiased probability density, $p(x_i)$, for a particular value of the reaction coordinate by weighting the estimates of $p(x_i)$ from all R simulations. With knowledge of $p(x_i)$, the values of F_i can be calculated from eq. (A.51) since:

$$\exp [-\beta F_i] = \langle \exp [-\beta w(x_i)] \rangle = \int p(x_i) \exp [-\beta w(x_i)] \, dx_i \tag{A.53}$$

The algorithm consists of first running the R simulations, periodically calculating the value of the reaction coordinate, x, and binning each recorded value into a histogram. First, we can combine eq. (A.44) and (A.51) to write:

$$p(x_i) = p_b(x_i) \exp[\beta(w(x_i) - F_i)] \tag{A.54}$$

From the set of R histograms, one per simulation, we can define $\Omega_j(x_i)$ as the estimate of $p(x_i)$ from simulation j. This quantity can be determined for each individual simulation as:

$$\Omega_j(x_i) = \frac{n_j(x_i)}{N_j} \exp[\beta(w_j(x_i) - F_j)] \tag{A.55}$$

$n_j(x_i)$ is the the number of values in the bin corresponding to x_i from simulation j, N_j is the total number of values recorded, and thus $n_j(x_i)/N_j$ is an estimate for the biased probability $p_b(x_i)$ subject to the constraints $w_j(x_i)$ for simulation j. Note that here the free energy F_j is for the simulation that is run since it is the free energy change for introducing a bias into that simulation's Hamiltonian. The optimal value of $p(x_i)$ can be written as a weighted sum of the estimates from all R simulations:

$$p(x_i) = \sum_{j=1}^{R} \lambda_j \Omega_j(x_i) \tag{A.56}$$

λ_j is the weight on simulation j such that $\sum_{j=1}^{R} \lambda_j = 1$. The WHAM equations are found by minimizing the error in $p(x_i)$ with respect to changes to λ_j subject to the constraint that the sum of the weights is 1. It can be shown that the optimal selection of weights is [383, 382]:

$$\lambda_j = \frac{N_j \exp[-\beta(w_j(x) - F_j)]}{\sum_{k=1}^{R} N_k \exp[-\beta(w_k(x) - F_k)]} \tag{A.57}$$

Substituting this expression with eq. (A.55) into eq. (A.56) yields:

$$p(x_i) = \frac{\sum_{j=1}^{R} n_j(x_i)}{\sum_{k=1}^{R} N_k \exp[-\beta(w_k(x) - F_k)]} \tag{A.58}$$

From eq. (A.58) and eq. (A.53), the probability densities $p(x_i)$ and the free energies F_i can be solved for self-consistently. The set of F_i along with the optimal estimates of $p(x_i)$ can then be used with eq. (A.54) and eq. (A.52) to calculate the PMF.

A full workflow for calculating the PMF along a particular reaction coordinate thus consists of the following steps:

1. Run an initial (biased) simulation to generate R starting configurations near the desired set of R values of the reaction coordinate, x.

2. Define a set of weight functions $w(x_i)$, to restrain the system near desired values of the reaction coordinate. Typically restraints are enforced by applying harmonic springs.

3. Launch R biased simulations with the restraints in place.

4. For each simulation, bin values of the reaction coordinates into a histogram (i.e. generate $n_j(x)$ for each value of x). Note that the number of bins in general will be much larger than R, the number of simulations run.

5. After the conclusion of the simulations, iteratively solve eq. (A.58) and eq. (A.53) using the set of $n_j(x)$ to find F_i, then obtain the PMF from eq. (A.52).

The PMFs in Chapter 8 and Appendix C were all generated using umbrella sampling and WHAM following this approach.

A.4.5 Bennett acceptance ratio

The PMF is an excellent approach for determining free energy changes along a particular path through phase space. However, this procedure can be computationally demanding given the necessity of sampling both large numbers of configurations and large numbers of windows to properly

calculate the PMF along the reaction coordinate. In some cases, it may be desirable to just know the change in free energy between two points in phase space, or the free energy change between two different ensembles entirely (these are equivalent calculations since different regions of phase space along a reaction coordinate have different ensembles, c.f. eq. (A.37)). One method for such a computation - free energy perturbation (FEP) - was derived above. In FEP, the free energy change between two ensembles is computed from the change in energy between the two ensembles calculated for configurations sampled from only one ensemble. This method has significant drawbacks if there is minimal overlap in the accessible phase space of both systems; in this case, configurations for which ΔU is small will be only sampled very rarely, even though small values of ΔU would dominate the exponential averaging. An improved method would rely on generating configurations from both ensembles and optimally identifying the free energy change.

The Bennett acceptance ratio (BAR) method provides an optimally efficient method for calculating this two-state free energy change. The basic idea of BAR is based on the following identity [377]:

$$\begin{aligned}
\frac{Z_0}{Z_1} &= \frac{Z_0}{Z_1}\frac{\int d\mathbf{r}^N \omega(\mathbf{r}^N)\exp[-\beta(U_0(\mathbf{r}^N)+U_1(\mathbf{r}^N))]}{\int d\mathbf{r}^N \omega(\mathbf{r}^N)\exp[-\beta(U_0(\mathbf{r}^N)+U_1(\mathbf{r}^N))]} \\
&= \frac{Z_0}{\int d\mathbf{r}^N \omega(\mathbf{r}^N)\exp[-\beta(U_0(\mathbf{r}^N)+U_1(\mathbf{r}^N))]}\frac{\int d\mathbf{r}^N \omega(\mathbf{r}^N)\exp[-\beta(U_0(\mathbf{r}^N)+U_1(\mathbf{r}^N))]}{Z_1} \\
&= \frac{\langle \omega(\mathbf{r}^N)\exp[-\beta U_0(\mathbf{r}^N)]\rangle_1}{\langle \omega(\mathbf{r}^N)\exp[-\beta U_1(\mathbf{r}^N)]\rangle_0}
\end{aligned} \tag{A.59}$$

The subscripts on the ensemble averages indicate configurations generated using the Hamiltonian of system 0 or 1 respectively. The free energy change is then:

$$\beta\Delta F = \ln Z_0/Z_1 = \ln\langle \omega(\mathbf{r}^N)\exp(-\beta U_0(\mathbf{r}^N))\rangle_1 - \ln\langle \omega(\mathbf{r}^N)\exp(-\beta U_1(\mathbf{r}^N))\rangle_0 \tag{A.60}$$

This simple relationship provides the essence of the BAR approach - by choosing a function $\omega(\mathbf{r}^N)$ to weight system energies, the free energy change can be computed by running a single simulation of system 0 and a single simulation of system 1 and computing the energy of configurations calculated with the other system's Hamiltonian. The question is then how to optimally choose $\omega(\mathbf{r}^N)$. By minimizing the variance in the free energy, Bennett showed that the optimal choice is [194]:

$$\omega = \frac{c}{Z_0\exp(-\beta U_1(\mathbf{r}^N)) + Z_1\exp(-\beta U_0(\mathbf{r}^N))} \tag{A.61}$$

where c is a constant. We can now substitute this equation back into eq. (A.59):

$$
\begin{aligned}
\frac{Z_0}{Z_1} &= \frac{\langle \omega(\mathbf{r}^N) \exp[-\beta U_0(\mathbf{r}^N)] \rangle_1}{\langle \omega(\mathbf{r}^N) \exp[-\beta U_1(\mathbf{r}^N)] \rangle_0} \\
&= \left\langle \frac{c \exp[-\beta U_0(\mathbf{r}^N)]}{Z_0 \exp(-\beta U_1(\mathbf{r}^N)) + Z_1 \exp(-\beta U_0(\mathbf{r}^N))} \right\rangle_1 \left\langle \frac{Z_0 \exp(-\beta U_1(\mathbf{r}^N)) + Z_1 \exp(-\beta U_0(\mathbf{r}^N))}{c \exp[-\beta U_1(\mathbf{r}^N)]} \right\rangle_0 \\
&= \frac{\left\langle Z_0 + Z_1 \exp[\beta(U_1(\mathbf{r}^N) - U_0(\mathbf{r}^N))] \right\rangle_0}{\left\langle Z_1 + Z_0 \exp[\beta(U_0(\mathbf{r}^N) - U_1(\mathbf{r}^N))] \right\rangle_1} \\
&= \frac{\left\langle 1 + Z_1/Z_0 \exp[\beta(U_1(\mathbf{r}^N) - U_0(\mathbf{r}^N))] \right\rangle_0}{\left\langle 1 + Z_0/Z_1 \exp[\beta(U_0(\mathbf{r}^N) - U_1(\mathbf{r}^N))] \right\rangle_1} \frac{Z_0}{Z_1} \\
&= \frac{\left\langle 1 + \exp[\beta(U_1(\mathbf{r}^N) - U_0(\mathbf{r}^N) - C)] \right\rangle_0}{\left\langle 1 + \exp[\beta(U_0(\mathbf{r}^N) - U_1(\mathbf{r}^N) + C)] \right\rangle_1} \exp(\beta C)
\end{aligned} \tag{A.62}
$$

Here, $\exp(\beta C) = Z_0/Z_1$ is a constant and is equivalent to the free energy change, $C = \Delta F$. It is assumed for this derivation that the number of samples drawn from each simulation is identical. Eq. (A.62) can be more conveniently expressed in terms of the Fermi function, $f(x) = 1/(1+\exp(\beta x))$:

$$
\frac{Z_0}{Z_1} = \frac{\langle f(U_0(\mathbf{r}^N) - U_1(\mathbf{r}^N) + C) \rangle_1}{\langle f(U_1(\mathbf{r}^N) - U_0(\mathbf{r}^N) - C) \rangle_0} \exp(\beta C) \tag{A.63}
$$

Since $C = \Delta F = \ln Z_0/Z_1$, eq. (A.63) is only satisfied if:

$$
\langle f(U_0(\mathbf{r}^N) - U_1(\mathbf{r}^N) + C) \rangle_1 = \langle f(U_1(\mathbf{r}^N) - U_0(\mathbf{r}^N) - C) \rangle_0 \tag{A.64}
$$

C can thus be calculated by sampling configurations from both system 0 and system 1, storing the energy difference $U_0(\mathbf{r}^N) - U_1(\mathbf{r}^N)$ for configurations sampled from system 1 and $U_1(\mathbf{r}^N) - U_0(\mathbf{r}^N)$ for configurations sampled from system 0, then self-consistently solving the equation:

$$
\sum_1 f(U_0(\mathbf{r}^N) - U_1(\mathbf{r}^N) + C) = \sum_0 f(U_1(\mathbf{r}^N) - U_0(\mathbf{r}^N) - C) \tag{A.65}
$$

by adjusting C until convergence. The final value of C is thus the free energy change. This algorithm was used to compute free energy changes in Chapters 3, 5, and 10; a slightly modified algorithm known as the multi-state Bennett acceptance ratio method was used in Chapter 10.

THIS PAGE INTENTIONALLY LEFT BLANK

Appendix B

Generation of Surface Morphologies

Work in this chapter was published in:

R. C. Van Lehn and A. Alexander-Katz, "Lateral phase separation of mixed polymer brushes physisorbed on planar substrates" *Journal of Chemical Physics*, **135**, pp. 141106, 2011, DOI: 10.1063/1.3653937.

Reproduced in part with permission from the American Institute of Physics.

One of the major questions addressed in this thesis is the role of surface morphology in determining the interactions between NPs and bilayers. In particular, we studied how slight variations between nanoscale random, mixed, and striped morphologies affected NP-bilayer fusion. In this Appendix, we explain the algorithm used to self-assemble various nanoscale morphologies in order to accurately model the features of these patterns. We developed a new model inspired by mixed polymer brushes, a qualitatively similar system to the oligomers used experimentally [84, 85], and used it to both explore polymer brush phase behavior on planar surfaces and map the same model to the generation of morphologies on curved surfaces. These morphologies were then used in the main simulations performed in the thesis.

B.1 Lateral phase separation of mixed polymer brushes

Polymer brushes are an important class of soft materials composed of polymers tethered to a surface. The grafting points may be fixed, as in the case of polymers covalently bound to the surface, or mobile, as in the case of physisorbed brushes. If the grafting density is sufficiently high, the tethered polymers will extend away from the surface to minimize steric overlap, forming the characteristic brush morphology [384]. When two (or more) polymer species are tethered to the same surface, the resulting system is referred to as a mixed polymer brush. The interaction between these two species, along with the interactions between each species and the solvent, gives rise to a range of possible surface morphologies. Depending on the difference in chain lengths, the mixed brush can undergo either lateral phase separation, where both species are exposed to solvent but develop ordered morphologies in the plane, or vertical phase separation, where a single species preferentially interacts with solvent while the other collapses near the surface. These morphologies also depend on structural factors including the grafting density, phase fraction of each species, molecular weight, and chain lengths of the polymers.

The behavior of polymer brushes has been studied in detail theoretically, beginning with the pioneering work of Alexander [385] and de Gennes [386] that resulted in an eponymous scaling

theory for the free energy and height of the brush layer. Their scaling approach characterizes each polymer in the brush as a series of blobs with a uniform size determined by the confinement of surrounding chains [387]. This confinement and the influence of a good solvent leads the chains to strongly stretch away from the surface. The free energy of the brush is a function of the number of blobs, which are assumed to have an energy on the order of kT, and an elastic term characterizing this chain stretching. The physics behind the chain elongation, namely steric confinement due to other chains, is thus similar in nature to the proposed physics of stripe formation for mixed oligomeric alkanethiol monolayers [91]. In the work by Singh et al, it was proposed that stripe formation is related to the length difference between the oligomeric ligands, as the entropy of the longer chains will be maximized when next to shorter neighbors due to a larger amount of free volume [91]. This driving force is qualitatively similar to what drives lateral phase separation in mixed brushes and we expect similar morphologies would be formed in a mixed brush system. As a result, we present a novel model combining Flory-Huggins and Alexander-de Gennes theory to simulate the lateral phase separation of mixed polymer brushes with mobile grafting points.

We consider a system composed of two polymer species grafted to a planar surface at a density in the brush regime and exposed to a non-selective good solvent. The polymers are allowed to rearrange across the surface to minimize the system free energy. The two species are assumed to have different chain lengths leading to the formation of two brush layers. The first layer is uniformly thick and consists of all the "short" polymer chains and part of the "long" polymer chains, while the second layer is formed from the ends of the long polymers that extend farther into the solvent. In both layers, strong stretching consistent with the Alexander-de Gennes approach is assumed. Fig. B-1 illustrates a schematic drawing of the system for both a planar and curved substrate. There is a competition between the entropy of mixing of the two species due the mobility of grafting points, enthalpic Flory-Huggins interactions, and the entropic/elastic contribution arising from strong stretching of the longer chains. This competition gives rise to rich phase behavior, including the possible formation of mixed, macrophase separated, and microphase separated states at large values of the enthalpic parameter where macrophase separation alone would typically be expected. Similar morphologies have been predicted for the NP systems, again furthering this analogy [91, 86, 92, 94, 93].

We will first describe the model for mixed polymer brushes in the limit of a perfectly planar substrate to investigate potential phase behavior before extending the model to spherical substrates appropriate for modeling the NP system. The first interaction considered in the model is a pair-potential for the enthalpic interaction between chain i and neighboring chains:

$$U_i^{F-H} = kT\chi \sum_{j \in n(i)} b_{ij} \tag{B.1}$$

$$b_{ij} = \begin{cases} 0 & \text{if } i,\ j \text{ both short or both long} \\ 1 & \text{if } i,\ j \text{ are different} \end{cases}$$

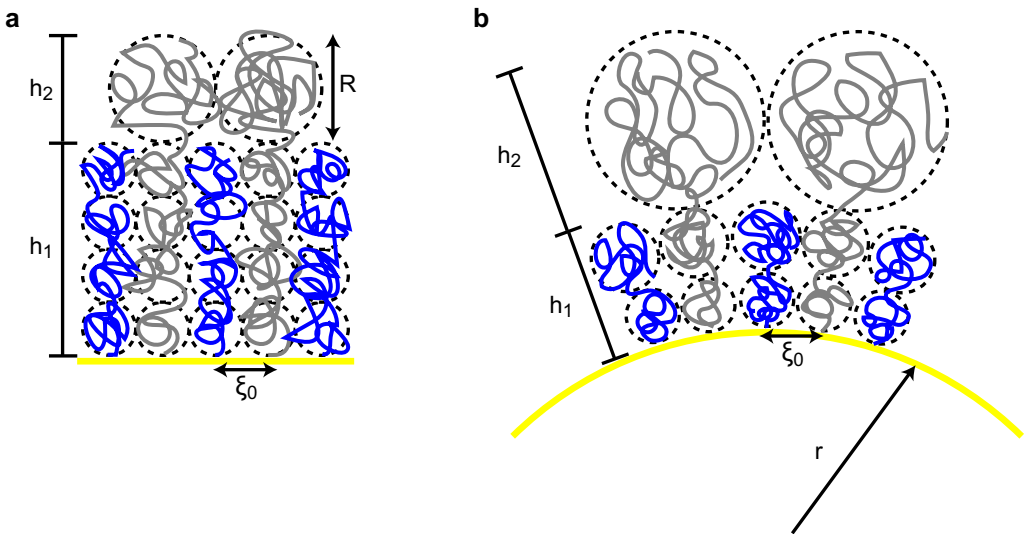

Figure B-1: Schematic of mixed polymer brush system. **a** Mixed polymer brushes of different lengths grafted to a planar substrate. Dashed lines indicate blobs within the Alexander-de Gennes model. **b** Mixed polymer brushes grafted to a spherical substrate.

Here, $n(i)$ is the set of nearest-neighbors for chain i, reflecting the assumption of densely grafted polymers that only interact with a small subset of surrounding chains. The key parameter is χ, which is typically positive and can be interpreted as the degree of miscibility between the two polymer species. This χ parameter can be thought of as qualitatively and effectively similar to χN, the Flory-Huggins miscibility parameter commonly used to describe polymer blends [388]. We drop the parameter N to maintain generality.

The second interaction is a mean-field, many-body interaction to model the free energy of chain overlap between long polymer ends in the second brush layer. This "blob" interaction depends on the local density of long polymers which determines the size and number of blobs in the brush and thus the free energy. To calculate an approximate form for this interaction, we use equations originally derived by Komura and Safran [389] which in turn follow from the Alexander-de Gennes model. It is assumed that the long polymer ends are dense enough to overlap and can be described as a series of blobs. The size of the blobs, R_i, for chain i is related to the local density ϕ_i of long polymer ends around the chain and the grafting length in the bottom layer ξ_0 by $R_i(\phi_i) = \xi_0/\phi_i^{1/2}$. The free energy of the brush layer is proportional to the number of blobs in the system, which from geometry is h_2/R_i where h_2 is the height of the second brush layer. Finally, h_2 is also a function of the number of statistical segments of the short polymer N_S and long polymer N_L, the grafting length ξ_0, the segment length of the polymer chain a, and a solvent quality scaling exponent ν. The lateral length scale is set by the grafting length ξ_0, since this parameter both affects the size of the blobs and sets a length scale for nearest-neighbor enthalpic interactions. A detailed derivation is given by Komura and Safran with a final result of:

$$U_i^{blob}(\phi_i) \approx kT\frac{h_2}{R} \approx kT(N_L - N_S)a^{1/\nu}\xi_0^{-1/\nu}\phi_i^{1/2\nu}$$
$$\approx kT\kappa\phi_i^{1/2\nu} \tag{B.2}$$

where $\kappa = (N_L - N_S)a^{1/\nu}\xi_0^{-1/\nu}$ is a dimensionless parameter combining all spatially uniform parameters. In the original work by Komura and Safran, it was assumed that the surface coverage was uniform and thus ϕ_i was identical for each chain i in the second brush layer. However, by allowing ϕ_i to vary for each i, ϕ_i instead reflects the *local* confinement of each long polymer chain and depends on the morphology of surface. The competition of enthalpic interactions between the short and long polymers, blob interactions between long polymers, and the mixing entropy of the system gives rise to a range of lateral morphologies.

B.1.1 Monte Carlo methodology

Monte Carlo simulations were used to find equilibrium system morphologies based on these two interactions. To simplify the calculations, the polymers were assumed to be tethered to a hexagonally close-packed lattice such that every lattice point represented either a long or short polymer. The distance between lattice points was again given by the grafting length ξ_0. For each Monte Carlo timestep, two neighboring lattice points containing polymers of opposite type were selected and the change in system energy for switching their positions was calculated. Following the Metropolis algorithm, the switch was accepted with a probability of

$$P_{12} = \min\left(1, e^{-\Delta U_{12}/kT}\right) \tag{B.3}$$

where $\Delta U_{12} = \Delta U_{12}^{F-H} + \Delta U_{12}^{blob}$ is the change in the total energy of the system for switching the positions of chains 1 and 2. Due to the lattice simplification, eq. (B.1) was applied directly to calculate U_i^{F-H} for each chain in their positions before and after the proposed switch, where the set of near-neighbors for each is defined by the lattice. To calculate $U_i^{blob}(\phi_i)$, we invoked a mean-field approximation where the phase fraction ϕ_i was given by the average density of *long* polymer chains around i, if i itself was a long polymer. In the lattice approximation, the average density was the fraction of sites occupied by long chains among the second nearest-neighbor sites of chain i. Short polymers were ignored in the calculation of the blob energy change because the density of polymers in the first brush layer was uniform.

Each simulation was run for 200,000 timesteps per site on a lattice with 1,600 points and periodic boundary conditions. The initial state of the lattice was generated by randomly determining whether each site was a long or short chain, subject to the constraint of a fixed overall phase fraction f of long chains. Because each Monte Carlo step involved switching the polymer type on adjacent sites but not changing the relative proportion of each type, f was conserved throughout each simulation. There was no restriction on chain positions in the system, such that the initial random

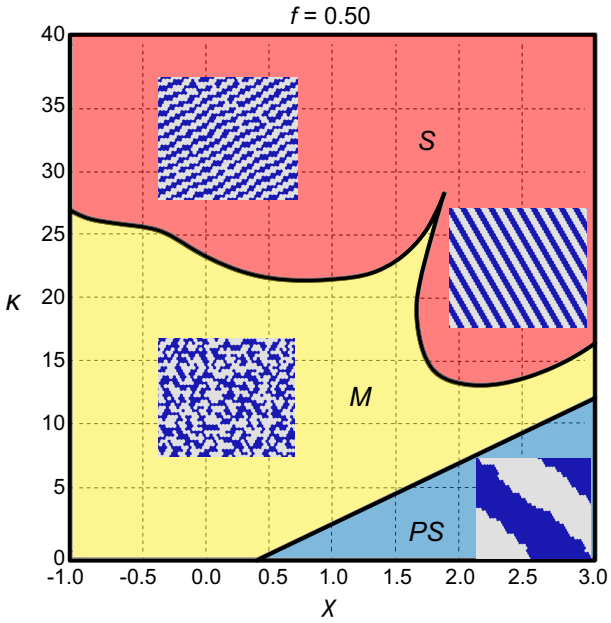

Figure B-2: Phase behavior for fixed 0.5 phase fraction, f. Three morphologies are identified as a function of the tuning parameters κ and χ.

configuration had no bearing on the final morphology and macrophase separation was allowed.

B.2 Morphologies on planar substrate

Phase diagrams were generated using the results of over 6,000 simulations each to define accurate phase boundaries. The heat capacity of the system was obtained from measuring energy fluctuations, with a peak in the heat capacity indicating a phase transition [138]. Fig. B-2 shows a phase diagram and simulation snapshots of the system for a fixed phase fraction $f = 0.50$. Different phases are indicated as a function of the key parameters χ and κ from eqs. (B.1) and (B.2). Phase transitions are indicated with black lines, with transitions identified by peaks in the heat capacity as well as visual inspection. All simulations were performed with $\nu = 3/5$ to represent a non-selective good solvent. In addition to typical cases where $\chi > 0$, the phase diagram additionally extends χ to negative values, representing polymers that are highly miscible due to hydrogen bonding, electrostatic, or other attractive interactions [390].

The phase diagram successfully reproduces several established morphologies of polymer brush systems. A trivial example is $\kappa = 0$, implying that $N_L = N_S$ and there is no length difference between the two polymers in the system. In this case, the model correctly predicts phase separation (marked as PS in Fig. B-2) if the value of χ is sufficiently positive to overcome the entropy of mixing, and complete mixing (M) for lower values of χ. For $\kappa > 0$, the blob interaction penalizes long polymers that are close together on the lattice, encouraging mixing and thus increasing the value of χ necessary for phase separation. As κ further increases, the system transitions into a striped, or

ripple, phase (S) that has been previously reported in the literature [391, 392]. Interestingly, this stripe morphology was itself tunable - at low values of χ, the stripes were largely disordered with noticeable defects, but as χ increased the enthalpic contribution from χ dominated over thermal fluctuations, leading to perfectly aligned stripes.

Fig. B-3 shows a phase diagram for fixed $\chi = 1.5$ while f and κ are allowed to vary. As in fig. B-2, phase separated (PS) mixed (M), and striped (S) phases are observed; however, for certain phase fractions an additional "dimple" phase (D) is predicted. This phase consists of an ordered arrangement of clusters of the minority component surrounded by the majority component, and has also been previously identified in the literature [393, 392]. Notably, the transition to the dimple phase as κ increases is asymmetric with respect to f, consistent with the application of the blob interaction to only long polymers in the model. The value of κ necessary to induce a phase transition is higher for larger values of f because the greater surface coverage of long polymer chains yields larger values of ϕ_i on average across the lattice. For a typical value in good solvent of $\nu = 3/5$, eq. (B.2) shows that $U_i^{blob}(\phi_i) \propto \phi^{5/6}$, and hence changing the local density of long chains leads to a lower change in blob energy if ϕ_i is higher on average. The magnitude of the change ΔU_{12}^{blob} thus tends to be smaller than for higher values of f, requiring a greater value of κ for ordering to be thermodynamically preferred.

These phase diagrams show that a key tuning parameter to control phase behavior is κ. To put this parameter in some context, consider a system with $N_S = 200$, $N_L = 350$, $a = 1.0$, $\xi_0 = 3.0$, and $\nu = 3/5$, where a sets the length scale. Under these conditions, the radius of gyration R_G of the free short polymer is $R_G \approx \frac{1}{6} N_S^{3/5} a \approx 4.0$, which is greater than ξ_0 so that the system is in the brush regime [384]. Evaluating κ with these values from eq. (B.2) gives a value of $\kappa \approx 24.0$. For this κ, the phase diagram in Fig. B-2 predicts that if the amount of each polymer species is equal, a striped or disordered morphology can be obtained by modifying χ, with stripes preferred for most values of $\chi > 0$. Alternatively, the phase diagrams in Fig. B-3 show that if χ is fixed at 1.5, the system can transition into a dimple morphology if the fraction of long polymer is reduced below ≈ 0.45 or increased near ≈ 0.65. In principle, χ and κ can be tuned by chemical modification of the polymer chains, control of the grafting density, or choosing an appropriate chain length difference. This simple example illustrates the utility of the model in making quantitative predictions of use to experimentalists interested in self-assembling polymer brushes on surfaces with specific morphologies.

B.3 Adaptation to spherical substrate

The results from the planar substrate calculations indicate a series of morphologies that are qualitatively identical to what would be expected for the NP morphologies. In particular, the striped morphology, dimple morphology, mixed morphology, and phase separated morphologies resemble the striped, mixed/checkerboard, random, and Janus morphologies used in Parts I-III. To adapt this model to a spherical model, the derivations of Komura and Safran were again followed, which

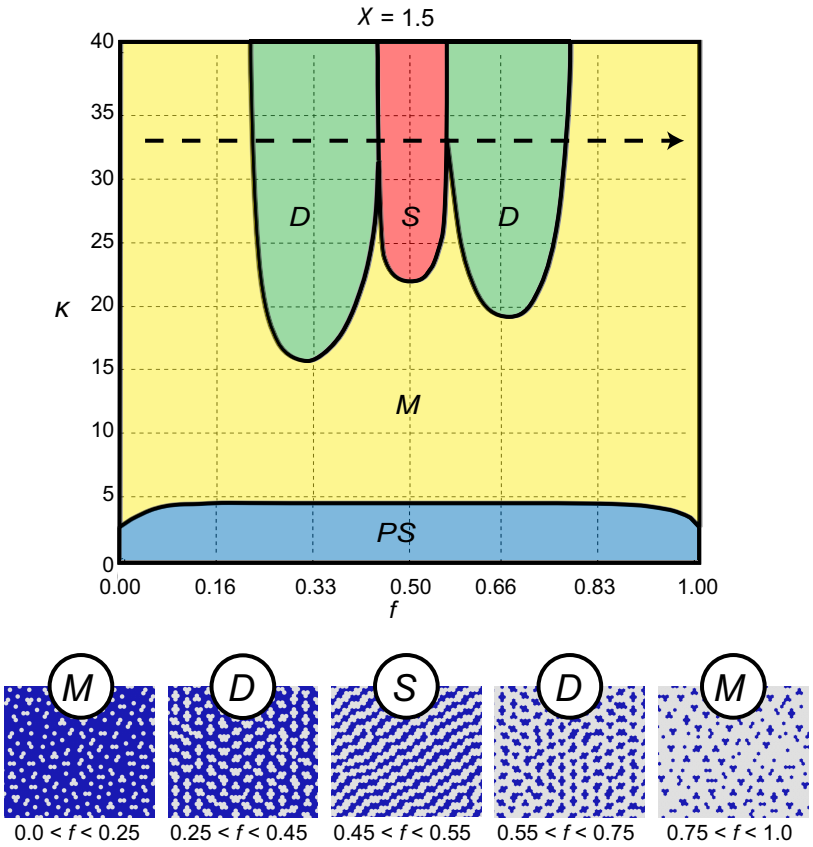

Figure B-3: Phase behavior for a fixed $\chi = 1.5$. Several morphologies are identified as a function of the phase fraction, f, and the tuning parameter κ.

invoke assumptions from the Daoud-Cotton model for the scaling relations of polymer brushes on spherical substrates. The enthalpic interactions are assumed to be unchanged by the curvature of the substrate, and only the entropic, blob term was modified to yield

$$U_i^{blob}(\phi_i, r) \approx \lambda \frac{\nu r}{2\epsilon_0} \phi^{1/2} \ln\left(1 + \frac{h_1 \alpha \phi^{(1-\nu)/2\nu}}{h_1 + 2\nu}\right) \tag{B.4}$$

Here, r is the radius of the spherical substrate as shown in Fig. B-1. In the Monte Carlo model, the change to a spherical substrate was accomplished by forming an approximately spherical lattice of the desired radius, setting an appropriate χ value, and then scaling eq. (B.4) by the constant λ to achieve the desired phase behavior, guided by the values used in the planar case. Fig. B-4 shows snapshots of the morphologies generated and the representative values of λ and χ. All other parameters were set identically as in the planar case and $r = 2.5$ nm. Random morphologies were created by randomly assigning bead positions. As shown in Fig. B-3, the 0.50 phase fraction simulations favored striped arrangements while the 0.66 phase fraction simulations favored dimple/checkerboard morphologies, with similar results found for the spherical substrate

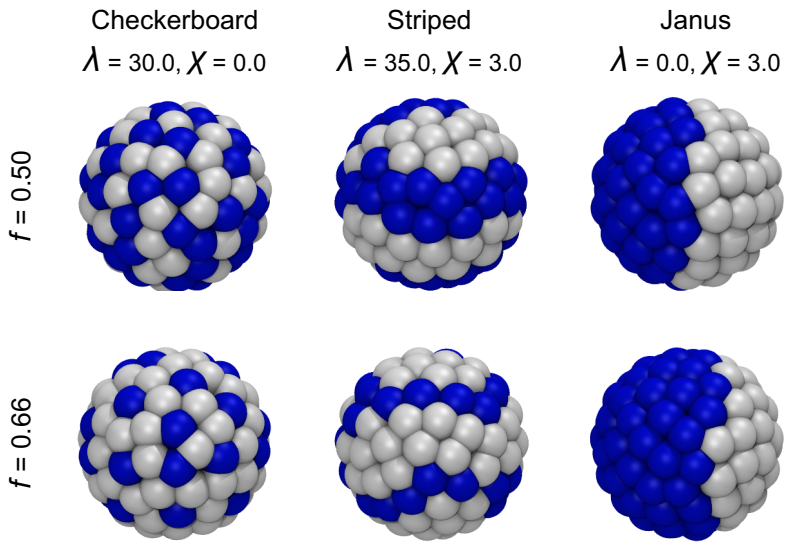

Figure B-4: Morphologies for two phase fractions f with corresponding values of λ and χ listed. The $f = 0.66$ striped and $f = 0.50$ checkerboard morphologies were created by modifying the $f = 0.50$ striped and $f = 0.66$ checkerboard morphologies respectively.

as well. Because we sought to model all morphologies for both 0.50 and 0.66 phase fractions in the NP-bilayer simulations, the 0.50 checkerboard and 0.66 striped morphologies were created by manually switching beads in the 0.66 checkerboard and 0.50 striped morphologies to retain the same morphology in the new phase fraction.

The results presented here demonstrate that combining the Flory-Huggins treatment of enthalpic interactions with an Alexander-de Gennes model for chain overlap is suitable for describing the lateral phase separation of mixed polymer brushes with mobile grafting points. The rich phase behavior identified agrees well with morphologies exhibited by NPs with mixed alkanethiol monolayers, indicating that this method is suitable for generating NP morphologies due to the similarity in the physics of phase separation. Given the generality of the model, it may also be used to model block copolymers or other tethered polymer systems that have been described by Alexander-de Gennes theory [384].

Appendix C

BODIPY as Sensor of Membrane Insertion

In Chapter 4, NPs were added in salt solution to multilamellar vesicles to study NP-bilayer interactions in a synthetic bilayer system. The NPs were labeled with a fluorescent dye, BODIPY, to identify NP positions using confocal microscopy. The images of the BODIPY-labeled NPs indicate that BODIPY fluorescence colocalizes with available membranes, implying that the NPs interact with bilayers. However, very little background fluorescence was observed from particles in solution, as opposed to significant background fluorescence in the case of free BODIPY. The image in Fig. C-1a shows a confocal microscopy image of a vesicle sample in the complete absence of BODIPY, where only faint autofluorescence from vesicles is visible (experiments performed by Prabhani U. Atukorale under the supervision of Prof. Darrell J. Irvine). Similarly, the image in Fig. C-1b shows a confocal microscopy image of BODIPY-labeled NPs in solution with anionic vesicles as previously shown in Chapter 4. As these NPs do not interact with the vesicles due to electrostatic repulsion, the expectation would be that the BODIPY on the surface would still fluoresce; however, the image appears almost identical to the untreated sample. In contrast, Fig. C-1c shows strong fluorescence from completely free BODIPY. These observations indicate that grafted BODIPY does not exhibit strong background fluorescence when NPs are in solution. In this Appendix, we hypothesize that these observations may be explained by the quenching of BODIPY by the gold core in solution, but not when embedded in the bilayer. If true, then the observation of BODIPY fluorescence near membranes strongly suggests that NPs are embedded in the bilayer, not merely absorbed to the bilayer surface.

The lack of background fluorescence may be attributed to the known ability of gold to quench the fluorescence of nearby dyes in a process often referred to as nanosurface energy transfer (NSET) when observed in a metal-fluorophore system [394, 395, 396]. NSET has been studied as a quenching mechanism for gold NPs by grafting fluorophores a specified distance away from the gold surface using double-stranded DNA, demonstrating that quenching is in fact distance dependent [395, 396, 397, 398]. In this system, the observation of fluorescence from NPs interacting with membranes but not from NPs in solution may indicate an increase in the distance of the fluorophore from the gold surface and a corresponding decrease in the quenching efficiency. To test whether there is a change in the preferred separation between BODIPY and the gold surface upon membrane embedding, we use molecular dynamics simulations to calculate the thermodynamically preferred equilibrium separation of the dye in solution and in the bilayer.

C.1 Parameterization of BODIPY dye

The NP and bilayer were modeled with the same force field described in Part II. The BODIPY 630/650 dye was parameterized using a "building block" approach as previously recommended for

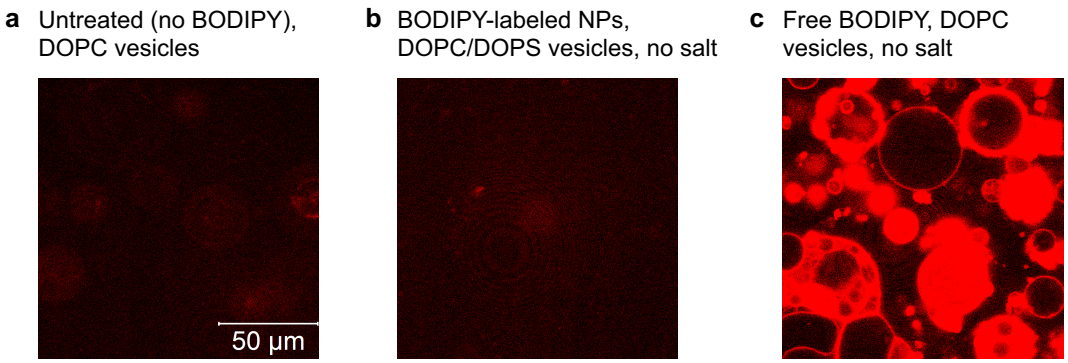

Figure C-1: Comparison of BODIPY fluorescence. **a** Untreated control of vesicles in the absence of NPs. **b** BODIPY-labeled NPs in presence of anionic vesicles with no salt. **c** Free BODIPY dye in presence of zwitterionic vesicles with no salt. All experiments were conducted by Prabhani U. Atukorale.

the GROMOS force field [223, 399, 226]. While servers such as PRODRG [400] and the ATB [226] exist to aid in the parameterization of novel ligands, the unreliability of PRODRG parameters [399] and the inability of ATB to model ligands with boron made these resources unsuitable. Instead, we chose parameters to mimic molecules within the existing GROMOS library as closely as possible, relying on quantum chemical calculations to fill in missing parameters. Atom types were selected according to standard GROMOS convention [223] so only bonding parameters and charges were selected. Specifically, we used parameters from HEME due to the similarity to the main BODIPY ring, parameters from thiophene generated by the ATB, and amino acid parameters for the peptide linkers from the standard GROMOS 54a7 force field [222]. Finally, a recent CHARMM parameterization of BODIPY used charges derived at the HF/G-31G* level of theory [401]; these charges have been used for the BODIPY center. The initial structure of BODIPY 630/650 was generated using Gaussian 03 optimized at the AM1 level of theory. These results also served as a comparison to ensure that the parameters adapted from pre-existing residues correctly mapped to the molecule's geometry. Boron is not included in the standard GROMOS force field, so sulfur non-bonded parameters were used instead following the example of previous CHARMM studies [401]. Fig. C-2 summarizes the BODIPY parameterization. Fig. C-1a shows the simulation representation, Fig. C-2b shows the partial charges assigned to each atom color-coded by the charge magnitude, q, and Fig. C-3c colors the overall structure according to its hydrophobicity. While there may be some quantitative differences between this parameterization and a more precise description of BODIPY, our model does capture the key physicochemical properties of the molecule including the hydrophobicity and rigidity of the BODIPY rings and flexibility of the linker segment. Our model is thus suitable for detecting trends in the position of the BODIPY center.

Two different types of simulations were run to estimate the potential of mean force (PMF) associated with moving the BODIPY fluorophore away from the gold surface when the NP is in solution and when it is embedded in the bilayer. All simulations used a NP with a gold core diameter of 2.0 nm and a 2:1 ratio of MUS:OT ligands on the surface, a NP composition representative of the

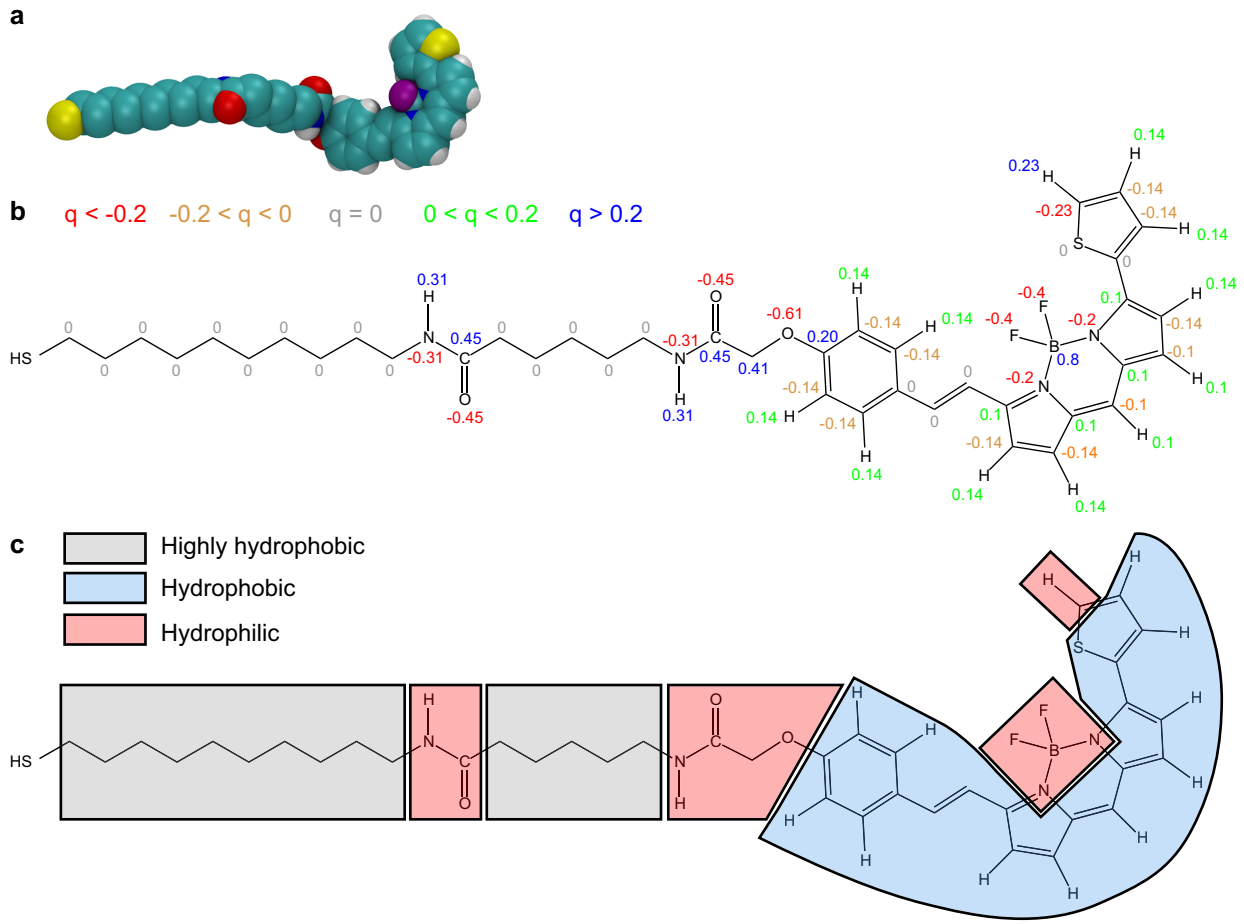

Figure C-2: Summary of BODIPY parameterization. **a** Simulation snapshot of BODIPY molecule. **b** Assigned charges, color-coded as shown in the label by the magnitude of the charge, q. **c** BODIPY structure color-coded by approximate hydrophobicity on the basis of the partial charges and atom types assigned.

experiments in Chapter 4. One of the MUS ligands was randomly replaced by a BODIPY molecule to yield a final monolayer composition of 38 MUS ligands, 20 OT ligands, and 1 BODIPY fluorophore. The ligands were arranged on the surface in a "checkerboard" like morphology following similar simulations in Part II. Simulation parameters are detailed in Appendix D. All simulations were performed using Gromacs version 4.6.1 [246].

In the first set of simulations, the NP was simulated in aqueous solution with only sufficient sodium counterions to neutralize the MUS ligands. A NP with all ligands in an initial all-*trans* configuration was placed in a rhombic dodecahedral box with an initial distance of 1.5 nm from the box walls to the nearest atom in the NP to ensure no interactions between periodic images of the NP. The box was filled with 26,752 water molecules to yield a total system size of 81,312 atoms. Umbrella sampling was then performed using the distance between the boron atom in the BODIPY fluorophore and the center of mass of the gold NP as a reaction coordinate. 12 windows with a

range of 1.4 nm to 2.5 nm and separated by 0.1 nm were chosen. For each window, the boron atom was constrained using a harmonic biasing potential with a spring constant of 500 kJ mol^{-1} nm^{-2} for an initial 5 ns equilibration and a spring constant of 3000 kJ mol^{-1} nm^{-2} for an addition 75 ns. The initial configurations for each window were generated from a corresponding pulling simulation. The weighted histogram analysis method (WHAM) was used unbias the umbrella sampling results and calculate the corresponding PMF [383, 382]. The WHAM equations were applied using the Gromacs tool *g_wham* [288], using only the last 70 ns of the umbrella sampling simulations which was sufficient to observe convergence of the PMF. The standard error of the PMF was calculated by repeating the entire simulation procedure again for a second NP in solution and computing the error between the two different PMF calculations.

In the second set of simulations, the PMF was calculated for extending BODIPY into the hydrophobic core region of the bilayer for an embedded NP. A bilayer with 392 lipids was created by duplicating the pre-equilibrated bilayer provided by Poger and Mark [349] and adjusting the number of lipids, then equilibrating again for 100 ns. The NP was embedded in the bilayer following the methodology in Chapter 11 (see Fig. 11-1). Sufficient water to ensure a 1.5 nm separation between the top of the NP and the box was then added along with counterions to neutralize the system, yielding a total system size of 98,736 atoms. The longer equilibration time was necessary due to the slower degrees of freedom associated with the bilayer. Umbrella sampling was then performed using the same reaction coordinate as in the solution case. 13 windows with a range of 1.8 nm to 4.0 nm were used with a separation of 0.2 nm. For each window, the boron atom was constrained using a harmonic biasing potential with a spring constant of 500 kJ mol^{-1} nm^{-2} for an initial 5 ns equilibration and a spring constant of 2000 kJ mol^{-1} nm^{-2} for an additional 80 ns. A weaker spring was used due to the larger separation between windows. As before, the initial configurations for each window were generated from a corresponding pulling simulation. The PMF was again calculated using *g_wham*, ignoring the first 5 ns of the umbrella sampling trajectories, and again the standard error was calculated by repeating the entire simulation methodology, including re-embedding the NP in a different position in the bilayer. All simulations were performed at 300 K.

C.2 Potential of mean force for BODIPY in solution

To understand how the distance between the fluorophore and the gold surface might change when a NP embeds within a lipid bilayer, we calculated the PMF associated with moving the BODIPY molecule away from the particle surface for a NP in solution and for a NP embedded in a DOPC bilayer. In the simulations, we chose the distance between the boron atom in the BODIPY molecule and the gold surface as the generalized coordinate of interest. The minimum in the PMF thus shows the preferred distance between the fluorophore and gold surface and the magnitude of the free energy well around that minimum.

Fig. C-3a shows the PMFs for BODIPY attached to a particle in solution and embedded in the

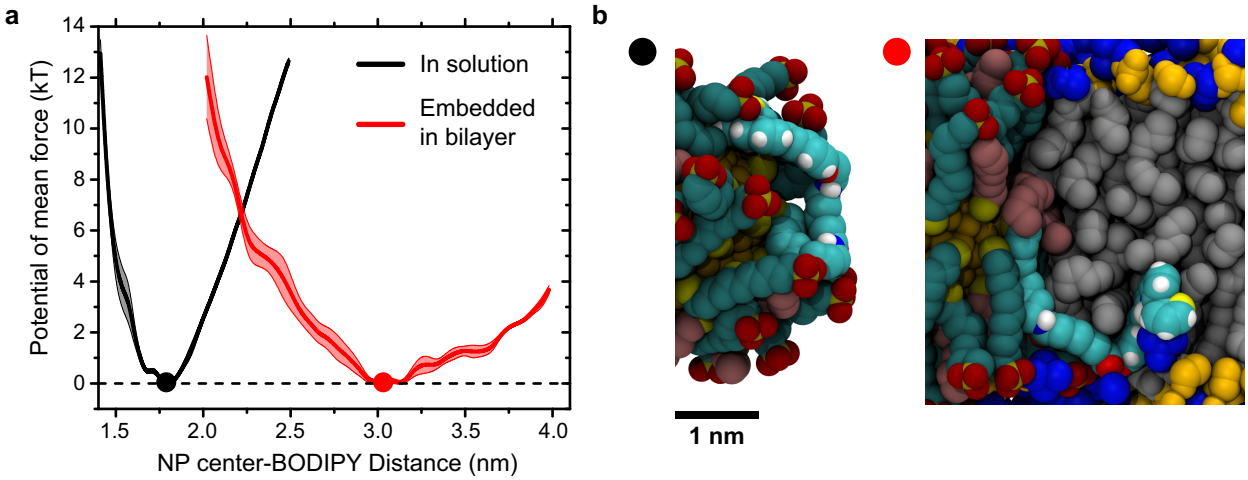

Figure C-3: PMFs of for NP-BODIPY separation in solution and embedded. **a** PMFs for both NPs in solution and embedded as a function of the distance between BODIPY and the center of the NP. The PMFs are rescaled to have their minima set to 0 kT. **b** Snapshots of the preferred system configurations. The BODIPY molecule is highlighted in both cases.

bilayer along with representative snapshots of the PMF minima. The PMFs are both rescaled such that the energy is 0 at the minimum. Fig. C-3b shows snapshots from the simulations of the system at the minimum of the PMF, i.e. the preferred equilibrium configuration. The snapshot of the NP in solution shows that BODIPY tends to "bend" toward the gold surface, avoiding exposure of the hydrophobic aromatic ring structures to water. The bending is facilitated by the flexible alkyl linker segment and is similar to behavior exhibited by long hydrophobic ligands (see Chapter 6). By sequestering the hydrophobic rings within the monolayer, the system reduces the free energy cost associated with unfavorable hydrophobic hydration [162] and in the process brings the fluorophore very close to the gold surface. The close distance between the fluorophore and gold would explain the quenching observed in solution as calculations based on NSET would predict nearly 100% quenching efficiency under these conditions [395, 398]. The PMF is also sharply peaked around its minimum due to the high free energy cost for attempting to extend the BODIPY rings into water, which not only increases the amount of hydrophobic surface exposed to water but also leads to a deformation of the entire monolayer.

In contrast to the NP in solution, the PMF of the NP embedded in the bilayer shows a minimum value approximately 1.3 nm farther from the NP surface, indicating that BODIPY prefers to extend into the hydrophobic core of the bilayer. Due to the hydrophobic environment, this extension is not penalized energetically and is instead favorable entropically as the fluorophore can explore a greater conformational space than it could in solution. Similar observations have been made for long hydrophobic ligands bound to embedded NPs in Chapter 11. The snapshots show a general preference for the fluorophore to occupy a region near the head groups. This conformation allows limited access of water to hydrophilic groups in the aromatic ring and the nitrogen and oxygen atoms of the linker, consistent with other studies of aromatic peptides that lie just

below the headgroup region [70, 402]. Furthermore, the general preference of BODIPY to reside just below the headgroup region is consistent with studies of lipid-bound BODIPY which has been shown to prefer the membrane-water interface studies [403, 404]. The simulations thus agree with expectations that BODIPY should be able to more freely extend away from the gold surface within the hydrophobic bilayer core than in solution, decreasing the quenching efficiency due to the increased distance between the fluorophore and gold. The increase in the fluorescence intensity could further be related to the known distance-dependent fluorescence enhancement near gold [405, 406] or potentially from the change in the surrounding solvent medium. While the simulations are not able to elucidate the exact mechanism of fluorescence enhancement, the observation of an increased gold-BODIPY distance indicates that the spatial colocalization of fluorescence with vesicles observed experimentally is indicative of BODIPY-labeled particles embedding within bilayers, and the absence of background fluorescence is due to the shielding of the hydrophobic BODIPY within the monolayer. The simulations also imply that fluorescence microscopy may be better than cryo-EM at distinguishing between NPs adsorbed to the bilayer surface, where the BODIPY would not have access to the hydrophobic core and thus would remain quenched, and embedded particles. Finally, one interesting possibility is that the preference of BODIPY for the hydrocarbon region of the bilayer may actually assist in the initial NP-bilayer insertion process, especially given the finding from Chapter 9 that longer ligands enhance the probability of insertion.

Appendix D
Overview of GROMOS Force Field

In Part II and Part III of this thesis, a modified version of the GROMOS 54a7 force field was used for molecular dynamics simulations. In this Appendix, we will briefly summarize the functional forms and parameterization strategy behind the GROMOS force field so that its utilization in simulations can be understood.

D.1 General GROMOS features

GROMOS is a united atom force field designed for modeling biomolecular systems [223] with the 54a7 version specifically re-parameterized to improve the representation of lipids [222]. In the united atom representation, the hydrogen atoms bonded to all aliphatic carbon atoms are not represented explicitly and are instead combined with the carbon atom as a single effective bead. This choice saves considerable computational expense; for example, this eliminates 84 atoms (60%) from the representation of the lipid DOPC while still modeling lipid properties with similar accuracy [267, 407].

Starting with the GROMOS 53a6 parameter set, the parameterization strategy for the force field has been to establish a consistent set of parameters that describe the thermodynamic properties of a variety of small molecules, use these parameters to calculate the free energy of solvation for amino acid analogues, then use this combined set of parameters to determine interactions in larger molecules based on similarities to moieties within the test set [223]. This "building-block" approach is simple and intuitive, and more importantly is designed to replicate thermodynamic parameters of importance to protein folding and other biological processes. This parameterization strategy makes GROMOS ideally suited for investigating spontaneous system behavior since the force field makes a concerted effort to accurately represent system thermodynamics.

D.2 Bonded interactions

Interactions in the GROMOS force field are divided into bonding interactions and non-bonded interactions. Fig. D-1 schematically illustrates different bonding interactions. Covalent bonds between a pair of atoms are represented by the potential:

$$U_{bond} = \frac{1}{4} K_{bond} (b^2 - b_0^2)^2 \tag{D.1}$$

$b = |r_{ij}|$ is the distance between two atoms, K_{bond} is tuning parameter controlling bond strength, and b_0 is the equilibrium bond distance [223]. In practice, constraints may instead be used to enforce the equilibrium bond separation [408]. Constraints are preferred to enable a longer simulation

timestep by eliminating bond vibrations which serve minimal functional purpose in most cases. The set of b_0 between different atom types was determined from X-ray diffraction data [409]. Fig. D-1a illustrates how bonding interactions and relevant parameters are defined.

Bond angles are enforced by the following potential:

$$U_{angle} = \frac{1}{2} K_{angle} (\cos\theta - \cos\theta_0)^2 \tag{D.2}$$

θ is the angle measured between three atoms and θ_0 is the equilibrium bond angle [223]. K_{angle} is an effective spring constant that penalizes the deviation from the equilibrium average. K_{angle} is determined for each angle from spectroscopic data while θ_0 is determined from X-ray scattering data.

Improper dihedral angles, which are used to maintain the planarity of aromatic or double bonded atoms or maintain the tetrahedral arrangement of united atom carbons (that lack hydrogen atoms necessary to maintain tetrahedrality), are enforced using a harmonic potential:

$$U_{improper} = \frac{1}{2} K_{improper} (\psi - \psi_0)^2 \tag{D.3}$$

$K_{improper}$ and ψ_0 are chosen to enforce the geometry and are not based on experimental parameters; as a result only two improper dihedral types are defined independent of the chemical identity of the atoms involved [223]. Fig. D-1b shows examples of when improper dihedrals should be used.

Proper dihedral angles are used to control torsional rotations around bonds and are specified for groups of four atoms. The form of the potential for proper dihedrals is:

$$U_{dihed} = K_{dihed} \left[1 + \cos(\delta)\cos(m\psi)\right] \tag{D.4}$$

K_{dihed} controls the strength of the potential, δ is the phase shift which is either 0 or π, m is the multiplicity which is between 1-6, and ψ is the measured dihedral angle [223]. The form of this potential is important as it is just a cosine with the multiplicity controlling the period and the phase shift shifting the value relative to the origin. However, real torsional potentials are not perfectly periodic. For example, in alkane chains rotamers are distinguished between the lowest energy *trans* conformations ($\psi = 0$) and two higher energy *gauche* conformations ($\psi = \pm 2\pi/3$), with all other angles at high energy [350]. The *gauche* conformations are higher energy than the *trans* conformation because atoms are brought into slightly closer contact, leading to a steric penalty. With the potential in eq. (D.4), setting the multiplicity $m = 3$ would yield three different lowest-energy states in the potential, but there would be no distinction between the *trans* and *gauche* conformers. This discrepancy is because non-bonded interactions between atoms also affect the torsional freedom of the atoms, reflecting the underlying physical reason for the difference between the *gauche* and *trans* states. In other words, while the dihedral potential may treat both rotamers identically, non-bonded interactions between the first and fourth atoms will be different in the two states, changing the relative energy of the two conformations. The dihedral angles are thus parameterized in conjunction with these 1-4 non-bonded interactions to correctly represent

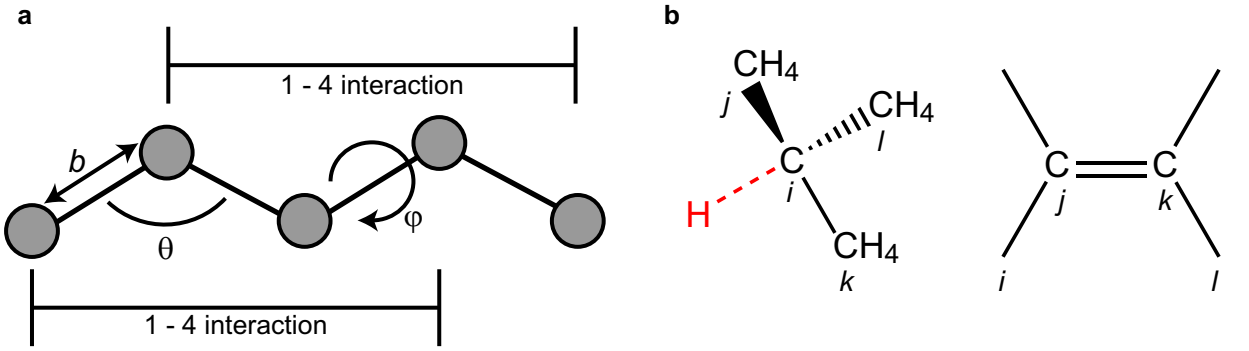

Figure D-1: Schematic of GROMOS bonded interactions. **a** Illustration of bonded, bond angle, proper dihedral, and 1-4 interactions. **b** Two cases in which improper dihedrals would be applied. The first is to maintain tetrahedrality in united atom carbons lacking a hydrogen atom (in red). The second is to maintain planarity in aromatic rings/multiply-bonded atoms. In both cases the improper dihedral is defined between atoms *i-j-k-l*.

torsional parameters and are fit to quantum mechanical measurements.

D.3 Non-bonded interactions

Non-bonded interactions between all atoms can be separated into contributions from van der Waals interactions and electrostatic interactions. The van der Waals interactions are incorporated through the use of the Lennard-Jones potential:

$$U_{LJ} = \left(\frac{C12_{ij}}{r_{ij}^{12}} - \frac{C6_{ij}}{r_{ij}^{6}} \right) \tag{D.5}$$

$C12_{ij}$ determines short-ranged repulsive interactions between atoms i and j and $C6_{ij}$ determines attractive interactions. The method for determining the value of $C12_{ij}$ and $C6_{ij}$ for a pair of particles is given by the geometric mean combination rules:

$$C12_{ij} = \sqrt{C12_{ii} C12_{jj}} \tag{D.6}$$

$$C6_{ij} = \sqrt{C6_{ii} C6_{jj}} \tag{D.7}$$

Several exceptions to these general combination rules are included by defining multiple values of $C12$ depending on the exact interaction. For atoms involved in polar or ionic interactions, $C12$ is increased slightly to ensure stable electrostatic interactions, and similarly $C12$ is increased farther for interactions between fully charged groups of opposite sign, such as ions, to ensure the atoms do not collapse on top of each other [223]. Finally, separate 1-4 interactions are specified separately to correctly represent torsional angles as noted above. Note that for all of these cases, the $C6$ interactions are left fixed, as this attractive component for the van der Waals interaction is physically

related to atomic polarizabilities. To determine the full set of possible van der Waals interactions, 54 different atom types (in GROMOS 54a7, 53 in GROMOS 53a6) are defined, representing a full set of atoms and united atom moieties relevant to biomolecular systems [222].

Electrostatic interactions are determined by assigning a partial charge to every atom in the system. In general, the partial charge of an atom is independent of its atom type (i.e. its van der Waals interaction). For example, the united atom CH_3 groups in the choline head groups of DOPC are assigned positive partial charges while the same CH_3 groups in alkane chains have no partial charge. The use of partial charges in conjunction with the van der Waals terms models polar and hydrogen bonding interactions while larger integer charges are assigned to ions or atoms engaging in ionic interactions. Polarization effects are not included in the GROMOS force field other than being effectively represented through the $C6$ attractive terms in the Lennard-Jones potentials, so partial charges are fixed throughout the course of a simulation and do not fluctuate.

In the original formulation of the GROMOS force field, electrostatic interactions were calculated using three contributions - one from direct Coulombic interactions between atoms within a 1.4 nm cutoff distance, one from a reaction-field contribution representing interactions between a charge and induced fields within a dielectric medium at a distance in excess of 1.4 nm, and a third distance-independent reaction field contribution used to ensure that the potential energy at the 1.4 nm cutoff is also zero [223]. In recent years the growth in computational power and improvements in parallelization have led to the adoption of improved electrostatic methods that do not require long-range cutoffs or effective treatments of dielectric media [377]. Capturing long-range electrostatic interactions is extremely important in most simulations and in particular for lipid simulations given the contribution of electrostatic interactions between head groups and solvent to bilayer properties [267]. The most popular method for modeling electrostatic interactions in biomolecular simulations is the Particle Mesh Ewald (PME) method that takes advantage of the translational periodicity of typical simulations to quickly compute a summation of interaction energies in Fourier space. The basic idea of the Ewald sum approach is to imagine that each point charge (i.e. charged atom) in the simulation is surrounded by a compensating cloud of charge that is collectively of opposite sign and magnitude to cancel out the charge on the atom itself. At distances far from the atom, the original point charge now appears screened due to the compensating diffuse charge distribution and as a result its contribution to the electrostatic potential decays quickly. We can thus think of the electrostatic potential due to a single point charge as consisting of three components - one due to the screened interaction with the charge itself, one due to the compensating diffuse charge distribution, and one due to a compensating charge cloud that must be added to ensure electrostatic neutrality. The essence of the Ewald sum method is recognizing that because of periodic boundary conditions, the compensating charge cloud is translationally periodic and can be easily computed in Fourier space while the rapidly-decaying interactions with the screened charges can be computed in real-space. Detailed derivations of this method and the implementation of the Particle Mesh Ewald method are given elsewhere [377].

As noted above, GROMOS employs cutoffs to minimize computational expense associated with

calculating non-bonded interactions over distances where their contribution would be small. The original force field calculates non-bonded interactions for atoms within 0.8 nm of each other every 2 fs timestep while interactions between atoms within 0.8-1.4 nm of each other were calculated every 10 fs. However, the use of PME necessitates a change of cut-off definition reflecting a proper treatment of long-range electrostatic interactions. Throughout this thesis, we instead use a single cutoff distance of 1.0 nm, updated every 2 fs, to calculate both van der Waals interactions and the short-range contribution to electrostatic interactions. This choice was found to be suitable for bilayer simulations and the use of PME leads to overall improvement in bilayer properties [267]. The one exception is the exclusion of non-bonded interactions between atoms within the same molecule that are either bonded together or within two bonds of each other. These exclusions are used to prevent interference with the bonding and bond angle interactions defined in the previous section. Again, atoms three bonds apart are treated using a special set of 1-4 interactions for the van der Waals terms but interact normally via electrostatic interactions.

The parameterization of GROMOS 53a5 and 53a6 involved modifying the set of $C12$ interactions and atomic charges based on the calculated free energies of solvation for a diverse set of small molecules. The difference between the 53a5 and 53a6 parameter sets is the choice of solvent for the free energy calculations - 53a5 was parameterized using cyclohexane to represent a non-polar environment while 53a6 was parameterized in SPC water to represent typical aqueous environments. Only the partial charges were modified between the two parameter sets; all Lennard-Jones interacts were identical. Following the building-block philosophy described above, these non-bonded parameters were chosen to try to be as consistent as possible for describing equivalent atoms within different chemical moieties to facilitate the parameterization of new molecules.

The non-bonded parameters were first chosen to reproduce the densities and heats of vaporization for a set of 28 small molecule liquids of varying polarity and chemical structure. These small molecules form the building blocks of the force field. Next, the parameters from these 28 molecules were used to generate parameters for 14 amino acid analogues by matching similar functional groups. The free energy of solvation for these 14 amino acids was calculated in cyclohexane and used to adjust the charges and $C12$ parameters accordingly by matching to experimental solvation free energies, producing the 53a5 parameter set. Using the same set of $C12$ parameters, the partial charges were then re-parameterized to fit the free energy of solvation in SPC water to experimental measurements, yielding the 53a6 parameter set. The final amino acid parameterizations led to solvation free enthalpies in water that were all within 2 kJ/mol of the experiments and correctly reproduced partitioning between aqueous and hydrophobic environments [223].

The parameterization of a novel molecule within the GROMOS force field thus consists of first matching moieties within the molecule to the existing set of small molecules to obtain atom types then re-parameterizing charges based on either hydration free energies (if experimental data is available) or quantum mechanical measurements [399]. Automated approaches for this process now exist as well [226]. This basic parameterization strategy was used to parameterize lipids, where it was found that the 53a6 force field did not suitably model choline repulsion in PC head

groups. A reparameterization of this atom type along with torsional angles in helical peptides resulted in the GROMOS 54a7 force field used throughout this thesis [349, 222]. The 54a7 force field represents one of the only force fields that includes a full, accurate set of lipid parameters, a straight-forward parameterization strategy for novel molecules, and an accurate representation of thermodynamic properties, making it ideal for studying spontaneous NP partitioning between aqueous and hydrophobic environments.

D.4 Parameters used in simulations

Similar parameters were used for the simulations in Chapters 6-9, Chapter 11, and Appendix C, and will be listed here for brevity.

The temperature was controlled in all simulations using a velocity-rescale thermostat with a time constant of 0.1 ps. Multiple temperature-coupling groups were defined depending on the system - typically the lipid bilayer, water and ions, and NP were all assigned independent temperature-coupling groups. The pressure was controlled using either a Berendsen barostat or Parrinello-Rahman barostat. The Berendsen barostat was used for equilibrating systems while Parrinello-Rahman was preferred for production runs. The exception is in systems with a lipid ribbon (Chapter 7/9) in which case the Berendsen barostat was consistently used. For isotropic systems, the pressure coupling was performed with a time constant of 2.0 ps, a reference pressure of 1 bar, and an isothermal compressibility of 4.5 $\times 10^{-5}$ bar^{-1}. Similar parameters were used with a semi-isotropic barostat for box-spanning bilayer systems. For the anisotropic ribbon systems, the time constant was instead set to 5.0 ps and the reference pressure compressibility were set to 0 in the y-dimension to eliminate box motion while allowing box motion in the x/z dimensions.

Bond lengths were constrained using the LINCS algorithm [408]. The simple point charge water model was used with the water geometry constrained via the SETTLE algorithm [410]. The simulation timestep was set to 2 fs with a molecular dynamics leap-frog integrator. Electrostatic interactions were calculated using the smooth particle mesh Ewald method with a real-space cutoff of 1.0 nm, a grid spacing of 0.12 nm, and fourth-order interpolation [267]. The van der Waals and neighbor list cutoffs were also both set to 1.0 nm in accordance with recent simulations of lipid bilayers using PME and the GROMOS 54a7 parameter set [267].

Bibliography

[1] M. Vert, Y. Doi, K.-H. Hellwich, M. Hess, P. Hodge, P. Kubisa, M. Rinaudo, F. Schué. Terminology for biorelated polymers and applications (IUPAC Recommendations 2012). *Pure Appl. Chem.* **2012**, *84*, 377410.

[2] P. Sharma, S. Brown, G. Walter, S. Santra, B. Moudgil. Nanoparticles for bioimaging. *Adv. Colloid Interface Sci.* **2006**, *123126*, 471–485.

[3] P. K. Jain, X. Huang, I. H. El-Sayed, M. A. El-Sayed. Noble metals on the nanoscale: Optical and photothermal properties and some applications in imaging, sensing, biology, and medicine. *Acc. Chem. Res.* **2008**, *41*, 1578–1586.

[4] S. T. Selvan, T. T. Y. Tan, D. K. Yi, N. R. Jana. Functional and multifunctional nanoparticles for bioimaging and biosensing. *Langmuir* **2010**, *26*, 11631–11641.

[5] Z. Wang, L. Ma. Gold nanoparticle probes. *Coord. Chem. Rev.* **2009**, *253*, 1607–1618.

[6] S. Jiang, K. Y. Win, S. Liu, C. P. Teng, Y. Zheng, M.-Y. Han. Surface-functionalized nanoparticles for biosensing and imaging-guided therapeutics. *Nanoscale* **2013**, *5*, 3127–3148.

[7] K. Cho, X. Wang, S. Nie, Z. G. Chen, D. M. Shin. Therapeutic nanoparticles for drug delivery in cancer. *Clin. Cancer Res.* **2008**, *14*, 1310–1316.

[8] P. Ghosh, G. Han, M. De, C. K. Kim, V. M. Rotello. Gold nanoparticles in delivery applications. *Adv. Drug Deliv. Rev.* **2008**, *60*, 1307–1315.

[9] A. Kumari, S. K. Yadav, S. C. Yadav. Biodegradable polymeric nanoparticles based drug delivery systems. *Colloids Surf., B* **2010**, *75*, 1–18.

[10] J. M. Chan, P. M. Valencia, L. Zhang, R. Langer, O. C. Farokhzad. Polymeric nanoparticles for drug delivery. *Methods Mol. Biol.* **2010**, *624*, 163–175.

[11] J. P. Rao, K. E. Geckeler. Polymer nanoparticles: Preparation techniques and size-control parameters. *Prog. Polym. Sci.* **2011**, *36*, 887–913.

[12] D. D. Lasic, D. Needham. The "stealth" liposome: a prototypical biomaterial. *Chem. Rev.* **1995**, *95*, 2601–2628.

[13] V. P. Torchilin. Recent advances with liposomes as pharmaceutical carriers. *Nat. Rev. Drug Discovery* **2005**, *4*, 145–160.

[14] A. Puri, K. Loomis, B. Smith, J.-H. Lee, A. Yavlovich, E. Heldman, R. Blumenthal. Lipid-based nanoparticles as pharmaceutical drug carriers: from concepts to clinic. *Crit. Rev. Ther. Drug Carrier Syst.* **2009**, *26*, 523–580.

[15] M. De, P. S. Ghosh, V. M. Rotello. Applications of nanoparticles in biology. *Adv. Mater.* **2008**, *20*, 4225–4241.

[16] Y.-C. Yeh, B. Creran, V. M. Rotello. Gold nanoparticles: Preparation, properties, and applications in bionanotechnology. *Nanoscale* **2012**, *4*, 1871–1880.

[17] X. Michalet, F. F. Pinaud, L. A. Bentolila, J. M. Tsay, S. Doose, J. J. Li, G. Sundaresan, A. M. Wu, S. S. Gambhir, S. Weiss. Quantum dots for live cells, in vivo imaging, and diagnostics. *Science* **2005**, *307*, 538–544.

[18] B. A. Kairdolf, A. M. Smith, T. H. Stokes, M. D. Wang, A. N. Young, S. Nie. Semiconductor quantum dots for bioimaging and biodiagnostic applications. *Annu. Rev. Anal. Chem.* **2013**, *6*, 143–162.

[19] C. Sun, J. S. H. Lee, M. Zhang. Magnetic nanoparticles in MR imaging and drug delivery. *Adv. Drug Deliv. Rev.* **2008**, *60*, 1252–1265.

[20] T. Kobayashi. Cancer hyperthermia using magnetic nanoparticles. *Biotechnol. J.* **2011**, *6*, 1342–1347.

[21] W. Yang, P. Thordarson, J. J. Gooding, S. P. Ringer, F. Braet. Carbon nanotubes for biological and biomedical applications. *Nanotechnology* **2007**, *18*, 412001.

[22] M. E. Davis, Z. G. Chen, D. M. Shin. Nanoparticle therapeutics: an emerging treatment modality for cancer. *Nat. Rev. Drug Discov.* **2008**, *7*, 771–782.

[23] L. Y. T. Chou, K. Ming, W. C. W. Chan. Strategies for the intracellular delivery of nanoparticles. *Chem. Soc. Rev.* **2010**, *40*, 233–245.

[24] S. Naahidi, M. Jafari, F. Edalat, K. Raymond, A. Khademhosseini, P. Chen. Biocompatibility of engineered nanoparticles for drug delivery. *J. Controlled Release* **2013**, *166*, 182–194.

[25] E. Ruoslahti, S. N. Bhatia, M. J. Sailor. Targeting of drugs and nanoparticles to tumors. *J. Cell Biol.* **2010**, *188*, 759–768.

[26] B. S. Zolnik, A. Gonzlez-Fernández, N. Sadrieh, M. A. Dobrovolskaia. Nanoparticles and the immune system. *Endocrinology* **2010**, *151*, 458–465.

[27] A. E. Nel, L. Mädler, D. Velegol, T. Xia, E. M. V. Hoek, P. Somasundaran, F. Klaessig, V. Castranova, M. Thompson. Understanding biophysicochemical interactions at the nano–bio interface. *Nat. Mater.* **2009**, *8*, 543–557.

[28] A. Verma, F. Stellacci. Effect of surface properties on nanoparticle-cell interactions. *Small* **2009**, *6*, 12–21.

[29] C.-C. You, M. De, V. M. Rotello. Monolayer-protected nanoparticle-protein interactions. *Curr. Opin. Chem. Biol.* **2005**, *9*, 639–646.

[30] D. F. Moyano, V. M. Rotello. Nano meets biology: Structure and function at the nanoparticle interface. *Langmuir* **2011**, *27*, 10376–10385.

[31] K. E. Sapsford, W. R. Algar, L. Berti, K. B. Gemmill, B. J. Casey, E. Oh, M. H. Stewart, I. L. Medintz. Functionalizing nanoparticles with biological molecules: developing chemistries that facilitate nanotechnology. *Chem. Rev.* **2013**, *113*, 1904–2074.

[32] I. C. Pons-Siepermann, S. C. Glotzer. Design of patchy particles using quaternary self-assembled monolayers. *ACS Nano* **2012**, *6*, 3919–3924.

[33] H. Lodish, A. Berk, S. L. Zipursky, P. Matsudaira, D. Baltimore, J. Darnell, *Molecular Cell Biology 4th ed.*, W. H. Freeman, **2000**.

[34] G. van Meer, D. R. Voelker, G. W. Feigenson. Membrane lipids: where they are and how they behave. *Nat. Rev. Mol. Cell Biol.* **2008**, *9*, 112–124.

[35] G. E. Tusnády, I. Simon. Principles governing amino acid composition of integral membrane proteins: application to topology prediction. *J. Mol. Biol.* **1998**, *283*, 489–506.

[36] S. J. Singer, G. L. Nicolson. The fluid mosaic model of the structure of cell membranes. *Science* **1972**, *175*, 720–731.

[37] T. Heimburg, *Thermal Biophysics of Membranes*, John Wiley & Sons, **2008**.

[38] O. S. Andersen, R. E. Koeppe. Bilayer thickness and membrane protein function: an energetic perspective. *Annu. Rev. Biophys. Biomol. Struct.* **2007**, *36*, 107–130.

[39] D. W. Deamer, J. Bramhall. Permeability of lipid bilayers to water and ionic solutes. *Chem. Phys. Lipids* **1986**, *40*, 167–188.

[40] G. J. Doherty, H. T. McMahon. Mechanisms of endocytosis. *Annu. Rev. Biochem.* **2009**, *78*, 857–902.

[41] J. Rejman, V. Oberle, I. S. Zuhorn, D. Hoekstra. Size-dependent internalization of particles via the pathways of clathrin- and caveolae-mediated endocytosis. *Biochem. J.* **2004**, *377*, 159–169.

[42] C. Huang, Y. Zhang, H. Yuan, H. Gao, S. Zhang. Role of nanoparticle geometry in endocytosis: Laying down to stand up. *Nano Lett.* **2013**, *13*, 4546–4550.

[43] M. Lindgren, M. Hllbrink, A. Prochiantz, l. Langel. Cell-penetrating peptides. *Trends Pharmacol. Sci.* **2000**, *21*, 99–103.

[44] H. D. Herce, A. E. Garcia. Cell penetrating peptides: How do they do it? *J. Biol. Phys.* **2007**, *33*, 345–356.

[45] P. Säälik, A. Niinep, J. Pae, M. Hansen, D. Lubenets, U. Langel, M. Pooga. Penetration without cells: Membrane translocation of cell-penetrating peptides in the model giant plasma membrane vesicles. *J. Controlled Release* **2011**, *153*, 117–125.

[46] J. P. Richard, K. Melikov, E. Vives, C. Ramos, B. Verbeure, M. J. Gait, L. V. Chernomordik, B. Lebleu. Cell-penetrating peptides: a reevaluation of the mechanism of cellular uptake. *J. Biol. Chem.* **2003**, *278*, 585–590.

[47] M. Zorko, U. Langel. Cell-penetrating peptides: mechanism and kinetics of cargo delivery. *Adv. Drug Deliv. Rev.* **2005**, *57*, 529–545.

[48] S.-T. Yang, E. Zaitseva, L. V. Chernomordik, K. Melikov. Cell-penetrating peptide induces leaky fusion of liposomes containing late endosome-specific anionic lipid. *Biophys. J.* **2010**, *99*, 2525–2533.

[49] E. Vivès, J.-P. Richard, C. Rispal, B. Lebleu. TAT peptide internalization: seeking the mechanism of entry. *Curr. Protein Pept. Sci* **2003**, *4*, 125–132.

[50] S. Kawamoto, M. Takasu, T. Miyakawa, R. Morikawa, T. Oda, S. Futaki, H. Nagao. Inverted micelle formation of cell-penetrating peptide studied by coarse-grained simulation: Importance of attractive force between cell-penetrating peptides and lipid head group. *J. Chem. Phys.* **2011**, *134*, 095103.

[51] S. Yesylevskyy, S.-J. Marrink, A. E. Mark. Alternative mechanisms for the interaction of the cell-penetrating peptides penetratin and the TAT peptide with lipid bilayers. *Biophys. J.* **2009**, *97*, 40–49.

[52] K. Saar, M. Lindgren, M. Hansen, E. Eiríksdóttir, Y. Jiang, K. Rosenthal-Aizman, M. Sassian, U. Langel. Cell-penetrating peptides: a comparative membrane toxicity study. *Anal. Biochem.* **2005**, *345*, 55–65.

[53] K. Huang, A. E. García. Free energy of translocating an arginine-rich cell-penetrating peptide across a lipid bilayer suggests pore formation. *Biophys. J.* **2013**, *104*, 412–420.

[54] J. Lin, A. Alexander-Katz. Cell membranes open "doors" for cationic nanoparticles/biomolecules: Insights into uptake kinetics. *ACS Nano* **2013**, *7*, 10799–10808.

[55] S. A. Wheaten, F. D. O. Ablan, B. L. Spaller, J. M. Trieu, P. F. Almeida. Translocation of cationic amphipathic peptides across the membranes of pure phospholipid giant vesicles. *J. Am. Chem. Soc.* **2013**, *135*, 16517–16525.

[56] R. M. Epand, H. J. Vogel. Diversity of antimicrobial peptides and their mechanisms of action. *BBA-Biomembranes* **1999**, *1462*, 11–28.

[57] K. A. Brogden. Antimicrobial peptides: pore formers or metabolic inhibitors in bacteria? *Nat. Rev. Microbiol.* **2005**, *3*, 238–250.

[58] P. F. Almeida, A. Pokorny. Mechanisms of antimicrobial, cytolytic, and cell-penetrating peptides: From kinetics to thermodynamics. *Biochemistry* **2009**, *48*, 8083–8093.

[59] R. M. Epand. Fusion peptides and the mechanism of viral fusion. *Biochim. Biophys. Acta* **2003**, *1614*, 116–121.

[60] H. T. McMahon, M. M. Kozlov, S. Martens. Membrane curvature in synaptic vesicle fusion and beyond. *Cell* **2010**, *140*, 601–605.

[61] M. Fuhrmans, S. J. Marrink. Molecular view of the role of fusion peptides in promoting positive membrane curvature. *J. Am. Chem. Soc.* **2012**, *134*, 1543–1552.

[62] L. V. Chernomordik, M. M. Kozlov. Mechanics of membrane fusion. *Nat. Struct. Mol. Biol.* **2008**, *15*, 675–683.

[63] J. L. Nieva, S. Nir, A. Muga, F. M. Goni, J. Wilschut. Interaction of the HIV-1 fusion peptide with phospholipid vesicles: different structural requirements for fusion and leakage. *Biochemistry* **1994**, *33*, 3201–3209.

[64] H. Cui, G. S. Ayton, G. A. Voth. Membrane binding by the endophilin N-BAR domain. *Biophys. J.* **2009**, *97*, 2746–2753.

[65] T. Heimburg, B. Angerstein, D. Marsh. Binding of peripheral proteins to mixed lipid membranes: effect of lipid demixing upon binding. *Biophys. J.* **1999**, *76*, 2575–2586.

[66] W. C. Wimley, S. H. White. Experimentally determined hydrophobicity scale for proteins at membrane interfaces. *Nat. Struct. Mol. Biol.* **1996**, *3*, 842–848.

[67] T. Hessa, H. Kim, K. Bihlmaier, C. Lundin, J. Boekel, H. Andersson, I. Nilsson, S. H. White, G. von Heijne. Recognition of transmembrane helices by the endoplasmic reticulum translocon. *Nature* **2005**, *433*, 377–381.

[68] T. Hessa, N. M. Meindl-Beinker, A. Bernsel, H. Kim, Y. Sato, M. Lerch-Bader, I. Nilsson, S. H. White, G. von Heijne. Molecular code for transmembrane-helix recognition by the Sec61 translocon. *Nature* **2007**, *450*, 1026–1030.

[69] C. P. Moon, K. G. Fleming. Side-chain hydrophobicity scale derived from transmembrane protein folding into lipid bilayers. *Proc. Natl. Acad. Sci. U.S.A.* **2011**, *108*, 10174–10177.

[70] J. A. Killian, G. von Heijne. How proteins adapt to a membrane-water interface. *Trends Biochem. Sci.* **2000**, *25*, 429–434.

[71] E. V. Schow, J. A. Freites, P. Cheng, A. Bernsel, G. von Heijne, S. H. White, D. J. Tobias. Arginine in membranes: the connection between molecular dynamics simulations and translocon-mediated insertion experiments. *J. Mem. Biol.* **2011**, *239*, 35–48.

[72] S. Dorairaj, T. W. Allen. On the thermodynamic stability of a charged arginine side chain in a transmembrane helix. *Proc. Natl. Acad. Sci. U.S.A.* **2007**, *104*, 4943–4948.

[73] A. C. V. Johansson, E. Lindahl. Protein contents in biological membranes can explain abnormal solvation of charged and polar residues. *Proc. Natl. Acad. Sci. USA* **2009**, *106*, 15684–15689.

[74] P. J. Bond, M. S. P. Sansom. Bilayer deformation by the Kv channel voltage sensor domain revealed by self-assembly simulations. *Proc. Natl. Acad. Sci. USA* **2007**, *104*, 2631–2636.

[75] J. Gumbart, B. Roux. Determination of membrane-insertion free energies by molecular dynamics simulations. *Biophys. J.* **2012**, *102*, 795–801.

[76] P. R. Leroueil, S. A. Berry, K. Duthie, G. Han, V. M. Rotello, D. Q. McNerny, Baker, B. G. Orr, M. M. Banaszak Holl. Wide varieties of cationic nanoparticles induce defects in supported lipid bilayers. *Nano Lett.* **2008**, *8*, 420–424.

[77] J. Chen, J. A. Hessler, K. Putchakayala, B. K. Panama, D. P. Khan, S. Hong, D. G. Mullen, S. C. DiMaggio, A. Som, G. N. Tew, A. N. Lopatin, J. R. Baker, M. M. B. Holl, B. G. Orr. Cationic nanoparticles induce nanoscale disruption in living cell plasma membranes. *J. Phys. Chem. B* **2009**, *113*, 11179–11185.

[78] S. Li, N. Malmstadt. Deformation and poration of lipid bilayer membranes by cationic nanoparticles. *Soft Matter* **2013**, *9*, 4969–4976.

[79] S. T. Kim, K. Saha, C. Kim, V. M. Rotello. The role of surface functionality in determining nanoparticle cytotoxicity. *Acc. Chem. Res.* **2013**, *46*, 681–691.

[80] A. K. Varkouhi, M. Scholte, G. Storm, H. J. Haisma. Endosomal escape pathways for delivery of biologicals. *J. Controlled Release* **2011**, *151*, 220–228.

[81] A. Verma, O. Uzun, Y. Hu, Y. Hu, H.-S. Han, N. Watson, S. Chen, D. J. Irvine, F. Stellacci. Surface-structure-regulated cell-membrane penetration by monolayer-protected nanoparticles. *Nat. Mater.* **2008**, *7*, 588–595.

[82] H. Häkkinen. The gold-sulfur interface at the nanoscale. *Nat. Chem.* **2012**, *4*, 443–455.

[83] O. Uzun, Y. Hu, A. Verma, S. Chen, A. Centrone, F. Stellacci. Water-soluble amphiphilic gold nanoparticles with structured ligand shells. *Chem. Commun.* **2008**, 196.

[84] A. M. Jackson, J. W. Myerson, F. Stellacci. Spontaneous assembly of subnanometre-ordered domains in the ligand shell of monolayer-protected nanoparticles. *Nat. Mater.* **2004**, *3*, 330–336.

[85] A. M. Jackson, Y. Hu, P. J. Silva, F. Stellacci. From homoligand- to mixed-ligand- monolayer-protected metal nanoparticles: a scanning tunneling microscopy investigation. *J. Am. Chem. Soc.* **2006**, *128*, 11135–11149.

[86] R. P. Carney, G. A. DeVries, C. Dubois, H. Kim, J. Y. Kim, C. Singh, P. K. Ghorai, J. B. Tracy, R. L. Stiles, R. W. Murray, S. C. Glotzer, F. Stellacci. Size limitations for the formation of ordered striped nanoparticles. *J. Am. Chem. Soc.* **2007**, *130*, 798–799.

[87] X. Liu, M. Yu, H. Kim, M. Mameli, F. Stellacci. Determination of monolayer-protected gold nanoparticle ligandshell morphology using NMR. *Nat. Commun.* **2012**, *3*, 1182.

[88] F. Biscarini, Q. K. Ong, C. Albonetti, F. Liscio, M. Longobardi, K. S. Mali, A. Ciesielski, J. Reguera, C. Renner, S. De Feyter, P. Samor, F. Stellacci. Quantitative analysis of scanning tunneling microscopy images of mixed-ligand-functionalized nanoparticles. *Langmuir* **2013**, *29*, 13723–13734.

[89] Q. K. Ong, J. Reguera, P. J. Silva, M. Moglianetti, K. Harkness, M. Longobardi, K. S. Mali, C. Renner, S. De Feyter, F. Stellacci. High-resolution scanning tunneling microscopy characterization of mixed monolayer protected gold nanoparticles. *ACS Nano* **2013**, *7*, 8529–8539.

[90] M. Moglianetti, Q. K. Ong, J. Reguera, K. M. Harkness, M. Mameli, A. Radulescu, J. Kohlbrecher, C. Jud, D. I. Svergun, F. Stellacci. Scanning tunneling microscopy and small angle neutron scattering study of mixed monolayer protected gold nanoparticles in organic solvents. *Chem. Sci.* **2014**, *5*, 1232–1240.

[91] C. Singh, P. K. Ghorai, M. A. Horsch, A. M. Jackson, R. G. Larson, F. Stellacci, S. C. Glotzer. Entropy-mediated patterning of surfactant-coated nanoparticles and surfaces. *Phys. Rev. Lett.* **2007**, *99*, 226106.

[92] C. Singh, Y. Hu, B. P. Khanal, E. R. Zubarev, F. Stellacci, S. C. Glotzer. Striped nanowires and nanorods from mixed SAMS. *Nanoscale* **2011**, *3*, 3244–3250.

[93] A. Santos, J. A. Millan, S. C. Glotzer. Facetted patchy particles through entropy-driven patterning of mixed ligand SAMS. *Nanoscale* **2012**, *4*, 2640–2650.

[94] W. L. Miller, B. Bozorgui, K. Klymko, A. Cacciuto. Free energy of alternating two-component polymer brushes on cylindrical templates. *J. Chem. Phys.* **2011**, *135*, 244902.

[95] C. M. Goodman, C. D. McCusker, T. Yilmaz, V. M. Rotello. Toxicity of gold nanoparticles functionalized with cationic and anionic side chains. *Bioconjugate Chem.* **2004**, *15*, 897–900.

[96] R. R. Arvizo, O. R. Miranda, M. A. Thompson, C. M. Pabelick, R. Bhattacharya, J. D. Robertson, V. M. Rotello, Y. S. Prakash, P. Mukherjee. Effect of Nanoparticle Surface Charge at the Plasma Membrane and Beyond. *Nano Lett.* **2010**, *10*, 2543–2548.

[97] K. K. Sandhu, C. M. McIntosh, J. M. Simard, S. W. Smith, V. M. Rotello. Gold Nanoparticle-Mediated Transfection of Mammalian Cells. *Bioconjugate Chem.* **2002**, *13*, 3–6.

[98] B. D. Chithrani, A. A. Ghazani, W. C. W. Chan. Determining the Size and Shape Dependence of Gold Nanoparticle Uptake into Mammalian Cells. *Nano Lett.* **2006**, *6*, 662–668.

[99] W. Jiang, B. Y. S. Kim, J. T. Rutka, W. C. W. Chan. Nanoparticle-mediated cellular response is size-dependent. *Nat. Nanotechnol.* **2008**, *3*, 145–150.

[100] C. M. Jewell, J.-M. Jung, P. U. Atukorale, R. P. Carney, F. Stellacci, D. J. Irvine. Oligonucleotide delivery by cell-penetrating "striped" nanoparticles. *Angew. Chem. Int. Edit.* **2011**, *50*, 12312–12315.

[101] C. Leduc, J.-M. Jung, R. R. Carney, F. Stellacci, B. Lounis. Direct investigation of intracellular presence of gold nanoparticles via photothermal heterodyne imaging. *ACS Nano* **2011**, *5*, 2587–2592.

[102] M. Karplus, J. A. McCammon. Molecular dynamics simulations of biomolecules. *Nat. Struct. Mol. Biol.* **2002**, *9*, 646–652.

[103] R. O. Dror, R. M. Dirks, J. P. Grossman, H. Xu, D. E. Shaw. Biomolecular simulation: a computational microscope for molecular biology. *Annu. Rev. Biophys. Biomol. Struct.* **2012**, *41*, 429–452.

[104] J. Wong-Ekkabut, S. Baoukina, W. Triampo, I.-M. Tang, D. P. Tieleman, L. Monticelli. Computer simulation study of fullerene translocation through lipid membranes. *Nat. Nanotechnol.* **2008**, *3*, 363–368.

[105] K. Yang, Y. Q. Ma. Computer simulation of the translocation of nanoparticles with different shapes across a lipid bilayer. *Nat. Nanotechnol.* **2010**, *5*, 579–583.

[106] J. Q. Lin, H. W. Zhang, Z. Chen, Y. G. Zheng. Penetration of lipid membranes by gold nanoparticles: Insights into cellular uptake, cytotoxicity, and their relationship. *ACS Nano* **2010**, *4*, 5421–5429.

[107] S. Nangia, R. Sureshkumar. Effects of nanoparticle charge and shape anisotropy on translocation through cell membranes. *Langmuir* **2012**, *28*, 17666–17671.

[108] H.-M. Ding, Y.-Q. Ma. Interactions between Janus particles and membranes. *Nanoscale* **2012**, *4*, 1116–1122.

[109] R. Vcha, F. J. Martinez-Veracoechea, D. Frenkel. Receptor-mediated endocytosis of nanoparticles of various shapes. *Nano Lett.* **2011**, *11*, 5391–5395.

[110] Y. Li, X. Li, Z. Li, H. Gao. Surface-structure-regulated penetration of nanoparticles across a cell membrane. *Nanoscale* **2012**, *4*, 3768–3775.

[111] T. Yue, X. Zhang, F. Huang. Molecular modeling of membrane tube pearling and the effect of nanoparticle adsorption. *Phys. Chem. Chem. Phys.* **2014**, *16*, 10799–10809.

[112] E. Heikkilä, H. Martinez-Seara, A. A. Gurtovenko, M. Javanainen, H. Häkkinen, I. Vattulainen, J. Akola. Cationic Au nanoparticle binding with plasma membrane-like lipid bilayers: Potential mechanism for spontaneous permeation to cells revealed by atomistic simulations. *J. Phys. Chem. C* **2014**, *118*, 11131–11141.

[113] S. J. Marrink, H. J. Risselada, S. Yefimov, D. P. Tieleman, A. H. de Vries. The MARTINI force field: coarse grained model for biomolecular simulations. *J. Phys. Chem. B* **2007**, *111*, 7812–7824.

[114] J.-Q. Lin, H.-W. Zhang, Z. Chen, Y.-G. Zheng, Z.-Q. Zhang, H.-F. Ye. Simulation study of aggregations of monolayer-protected gold nanoparticles in solvents. *J. Phys. Chem. C* **2011**, *115*, 18991–18998.

[115] W.-d. Tian, Y.-q. Ma. Insights into the endosomal escape mechanism via investigation of dendrimermembrane interactions. *Soft Matter* **2012**, *8*, 6378–6384.

[116] Z.-l. Li, H.-m. Ding, Y.-q. Ma. Translocation of polyarginines and conjugated nanoparticles across asymmetric membranes. *Soft Matter* **2012**, *9*, 1281–1286.

[117] P. Gkeka, L. Sarkisov, P. Angelikopoulos. Homogeneous hydrophobichydrophilic surface patterns enhance permeation of nanoparticles through lipid membranes. *J. Phys. Chem. Lett.* **2013**, *4*, 1907–1912.

[118] C. L. Ting, Z.-G. Wang. Minimum free energy paths for a nanoparticle crossing the lipid membrane. *Soft Matter* **2012**, *8*, 12066–12071.

[119] C. L. Ting, Z. G. Wang. Interactions of a charged nanoparticle with a lipid membrane: Implications for gene delivery. *Biophys. J.* **2011**, *100*, 1288–1297.

[120] S. Pogodin, M. Werner, J.-U. Sommer, V. A. Baulin. Nanoparticle-induced permeability of lipid membranes. *ACS Nano* **2012**, *6*, 10555–10561.

[121] S. O. Yesylevskyy, L. V. Schäfer, D. Sengupta, S. J. Marrink. Polarizable water model for the coarse-grained MARTINI force field. *PLoS Comput. Biol.* **2010**, *6*, e1000810.

[122] S. V. Atre, B. Liedberg, D. L. Allara. Chain-length dependence of the structure and wetting properties in binary composition monolayers of OH-terminated and CH3-terminated alkanethiolates on gold. *Langmuir* **1995**, *11*, 3882–3893.

[123] J. P. Folkers, P. E. Laibinis, G. M. Whitesides, J. Deutch. Phase-behavior of 2-component self-assembled monolayers of alkanethiolates on gold. *J. Phys. Chem.* **1994**, *98*, 563–571.

[124] S. J. Stranick, A. N. Parikh, Y. T. Tao, D. L. Allara, P. S. Weiss. Phase-separation of mixed-composition self-assembled monolayers into nanometer-scale molecular domains. *J. Phys. Chem.* **1994**, *98*, 7636–7646.

[125] A. V. Shevade, J. Zhou, M. T. Zin, S. Y. Jiang. Phase behavior of mixed self-assembled monolayers of alkanethiols on Au(111): A configurational-bias Monte Carlo simulation study. *Langmuir* **2001**, *17*, 7566–7572.

[126] K. Tamada, M. Hara, H. Sasabe, W. Knoll. Surface phase behavior of n-alkanethiol self-assembled monolayers adsorbed on Au(111): An atomic force microscope study. *Langmuir* **1997**, *13*, 1558–1566.

[127] C. Munuera, C. Ocal. Real time scanning force microscopy observation of a structural phase transition in self-assembled alkanethiols. *J. Chem. Phys.* **2006**, *124*, 1–5.

[128] F. Schreiber. Structure and growth of self-assembling monolayers. *Prog. Surf. Sci.* **2000**, *65*, 151–256.

[129] M. Wojcik, M. Kolpaczynska, D. Pociecha, J. Mieczkowski, E. Gorecka. Multidimensional structures made by gold nanoparticles with shape-adaptive grafting layers. *Soft Matter* **2010**, *6*, 5397–5400.

[130] V. Sashuk, R. Hołlyst, T. Wojciechowski, M. Fiałkowski. Close-packed monolayers of charged Janus-type nanoparticles at the air-water interface. *J. Colloid Interface Sci.* **2012**, *375*, 180–186.

[131] J. Paczesny, M. Wójcik, K. Sozański, K. Nikiforov, C. Tschierske, A. Lehmann, E. Górecka, J. Mieczkowski, R. Hołyst. Self-assembly of gold nanoparticles into 2D arrays induced by bolaamphiphilic ligands. *J. Phys. Chem. C* **2013**, *117*, 24056–24062.

[132] I. R. Cooke, M. Deserno. Solvent-free model for self-assembling fluid bilayer membranes: Stabilization of the fluid phase based on broad attractive tail potentials. *J. Chem. Phys.* **2005**, *123*, 320–323.

[133] I. R. Cooke, K. Kremer, M. Deserno. Tunable generic model for fluid bilayer membranes. *Phys. Rev. E.* **2005**, *72*, 1–4.

[134] G. Illya, M. Deserno. Coarse-grained simulation studies of peptide-induced pore formation. *Biophys. J.* **2008**, *95*, 4163–4173.

[135] B. J. Reynwar, G. Illya, V. A. Harmandaris, M. M. Muller, K. Kremer, M. Deserno. Aggregation and vesiculation of membrane proteins by curvature-mediated interactions. *Nature* **2007**, *447*, 461–464.

[136] S. V. Bennun, M. I. Hoopes, C. Y. Xing, R. Faller. Coarse-grained modeling of lipids. *Chem. Phys. Lipids* **2009**, *159*, 59–66.

[137] C. Tanford. Interfacial free-energy and the hydrophobic effect. *Proc. Natl. Acad. Sci. USA* **1979**, *76*, 4175–4176.

[138] D. A. McQuarrie, *Statistical Mechanics*, University Science Books, Sausalito, Calif., **2000**.

[139] J. Zimmerberg, M. M. Kozlov. How proteins produce cellular membrane curvature. *Nat. Rev. Mol. Cell Biol.* **2006**, *7*, 9–19.

[140] A. Alexeev, W. E. Uspal, A. C. Balazs. Harnessing Janus nanoparticles to create controllable pores in membranes. *ACS Nano* **2008**, *2*, 1117–1122.

[141] M. Deserno, T. Bickel. Wrapping of a spherical colloid by a fluid membrane. *Europhys. Lett.* **2003**, *62*, 767–773.

[142] C. Nielsen, M. Goulian, O. S. Anderson. Energetics of membrane deformation in systems with non-zero monolayer curvature. *Biophys. J.* **1998**, *74*, A309–A309.

[143] C. Nielsen, O. S. Andersen. Inclusion-induced bilayer deformations: Effects of monolayer equilibrium curvature. *Biophys. J.* **2000**, *79*, 2583–2604.

[144] S. May. Theories on structural perturbations of lipid bilayers. *Curr. Opin. Colloid Interface Sci.* **2000**, *5*, 244–249.

[145] J. M. D. Lane, G. S. Grest. Spontaneous asymmetry of coated spherical nanoparticles in solution and at liquid-vapor interfaces. *Phys. Rev. Lett.* **2010**, *104*, 235501.

[146] S. L. Zhang, J. Li, G. Lykotrafitis, G. Bao, S. Suresh. Size-dependent endocytosis of nanoparticles. *Adv. Mater.* **2009**, *21*, 419–424.

[147] S. Berger, A. Synytska, L. Ionov, K. J. Eichhorn, M. Stamm. Stimuli-responsive bicomponent polymer janus particles by "grafting from"/"grafting to" approaches. *Macromolecules* **2008**, *41*, 9669–9676.

[148] Y. Guo, M. G. Moffitt. Semiconductor quantum dots with environmentally responsive mixed polystyrene/poly(methyl methacrylate) brush layers. *Macromolecules* **2007**, *40*, 5868–5878.

[149] D. Li, X. Sheng, B. Zhao. Environmentally responsive "hairy" nanoparticles: Mixed homopolymer brushes on silica nanoparticles synthesized by living radical polymerization techniques. *J. Am. Chem. Soc.* **2005**, *127*, 6248–6256.

[150] B. Zhao, L. Zhu. Mixed polymer brush-grafted particles: a new class of environmentally responsive nanostructured materials. *Macromolecules* **2009**, *42*, 9369–9383.

[151] E. W. Edwards, M. Chanana, D. Wang, H. Mohwald. Stimuli-responsive reversible transport of nanoparticles across water/oil interfaces. *Angew. Chem. Int. Edit.* **2008**, *47*, 320–323.

[152] K. S. Iyer, B. Zdyrko, S. Malynych, G. Chumanov, I. Luzinov. Reversible submergence of nanoparticles into ultrathin block copolymer films. *Soft Matter* **2011**, *7*, 2538–2542.

[153] B. J. Kim, G. H. Fredrickson, C. J. Hawker, E. J. Kramer. Nanoparticle surfactants as a route to bicontinuous block copolymer morphologies. *Langmuir* **2007**, *23*, 7804–7809.

[154] D. J. Li, B. Zhao. Temperature-induced transport of thermosensitive hairy hybrid nanoparticles between aqueous and organic phases. *Langmuir* **2007**, *23*, 2208–2217.

[155] A. Walther, A. H. E. Müller. Janus particles. *Soft Matter* **2008**, *4*, 663–668.

[156] A. Walther, C. Barner-Kowollik, A. H. E. Muller. Mixed, multicompartment, or janus micelles? A systematic study of thermoresponsive bis-hydrophilic block terpolymers. *Langmuir* **2010**, *26*, 12237–12246.

[157] C. LoPresti, M. Massignani, C. Fernyhough, A. Blanazs, A. J. Ryan, J. Madsen, N. J. Warren, S. P. Armes, A. L. Lewis, S. Chirasatitsin, A. J. Engler, G. Battaglia. Controlling polymersome surface topology at the nanoscale by membrane confined polymer/polymer phase separation. *ACS Nano* **2011**, *5*, 1775–1784.

[158] K. L. Genson, J. Holzmueller, C. Y. Jiang, J. Xu, J. D. Gibson, E. R. Zubarev, V. V. Tsukruk. Langmuir-Blodgett monolayers of gold nanoparticles with amphiphilic shells from V-shaped binary polymer arms. *Langmuir* **2006**, *22*, 7011–7015.

[159] E. R. Zubarev, J. Xu, A. Sayyad, J. D. Gibson. Amphiphilic gold nanoparticles with V-shaped arms. *J. Am. Chem. Soc.* **2006**, *128*, 4958–4959.

[160] S. Sekiguchi, K. Niikura, Y. Matsuo, K. Ijiro. Hydrophilic gold nanoparticles adaptable for hydrophobic solvents. *Langmuir* **2012**, *28*, 5503–5507.

[161] R. A. Petros, J. M. DeSimone. Strategies in the design of nanoparticles for therapeutic applications. *Nat. Rev. Drug Discov.* **2010**, *9*, 615–627.

[162] D. Chandler. Interfaces and the driving force of hydrophobic assembly. *Nature* **2005**, *437*, 640–647.

[163] E. Strandberg, J. A. Killian. Snorkeling of lysine side chains in transmembrane helices: how easy can it get? *FEBS Lett.* **2003**, *544*, 69–73.

[164] N. Ben-Tal, A. Ben-Shaul, A. Nicholls, B. Honig. Free-energy determinants of alpha-helix insertion into lipid bilayers. *Biophys. J.* **1996**, *70*, 1803–1812.

[165] S. H. White, W. C. Wimley. Membrane protein folding and stability: Physical principles. *Annu. Rev. Biophys. Biomol. Struct.* **1999**, *28*, 319–365.

[166] C. Chothia. Hydrophobic bonding and accessible surface area in proteins. *Nature* **1974**, *248*, 338–339.

[167] T. Ooi, M. Oobatake, G. Némethy, H. A. Scheraga. Accessible surface areas as a measure of the thermodynamic parameters of hydration of peptides. *Proc. Natl. Acad. Sci. U.S.A.* **1987**, *84*, 3086–3090.

[168] J. R. Livingstone, R. S. Spolar, M. T. Record. Contribution to the thermodynamics of protein folding from the reduction in water-accessible nonpolar surface area. *Biochemistry* **1991**, *30*, 4237–4244.

[169] K. A. Sharp, A. Nicholls, R. F. Fine, B. Honig. Reconciling the magnitude of the microscopic and macroscopic hydrophobic effects. *Science* **1991**, *252*, 106–109.

[170] D. Sitkoff, N. Ben-Tal, B. Honig. Calculation of alkane to water solvation free energies using continuum solvent models. *J. Phys. Chem.* **1996**, *100*, 2744–2752.

[171] J. A. Wagoner, N. A. Baker. Assessing implicit models for nonpolar mean solvation forces: The importance of dispersion and volume terms. *Proc. Natl. Acad. Sci. USA* **2006**, *103*, 8331–8336.

[172] S. Choe, K. A. Hecht, M. Grabe. A continuum method for determining membrane protein insertion energies and the problem of charged residues. *J. Gen. Physiol.* **2008**, *131*, 563–573.

[173] S. Mondal, G. Khelashvili, J. Shan, O. S. Andersen, H. Weinstein. Quantitative modeling of membrane deformations by multihelical membrane proteins: application to G-protein coupled receptors. *Biophys. J.* **2011**, *101*, 2092–2101.

[174] K. Öjemalm, T. Higuchi, Y. Jiang, U. Langel, I. Nilsson, S. H. White, H. Suga, G. von Heijne. Apolar surface area determines the efficiency of translocon-mediated membrane-protein integration into the endoplasmic reticulum. *Proc. Natl. Acad. Sci. USA* **2011**, *108*, E359–E364.

[175] A. Nicholls, K. A. Sharp, B. Honig. Protein folding and association: Insights from the interfacial and thermodynamic properties of hydrocarbons. *Proteins* **1991**, *11*, 281–296.

[176] R. Qiao, A. P. Roberts, A. S. Mount, S. J. Klaine, P. C. Ke. Translocation of C-60 and its derivatives across a lipid bilayer. *Nano Lett.* **2007**, *7*, 614–619.

[177] D. Bedrov, G. D. Smith, H. Davande, L. Li. Passive transport of C60 fullerenes through a lipid membrane: A molecular dynamics simulation study. *J. Phys. Chem. B.* **2008**, *112*, 2078–2084.

[178] A. Jusufi, R. H. DeVane, W. Shinoda, M. L. Klein. Nanoscale carbon particles and the stability of lipid bilayers. *Soft Matter* **2011**, *7*, 1139–1146.

[179] M. Feig, C. L. Brooks III. Recent advances in the development and application of implicit solvent models in biomolecule simulations. *Curr. Opin. Struct. Biol.* **2004**, *14*, 217–224.

[180] M. B. Ulmschneider, J. P. Ulmschneider, M. S. P. Sansom, A. Di Nola. A generalized born implicit-membrane representation compared to experimental insertion free energies. *Biophys. J.* **2007**, *92*, 2338–2349.

[181] J. L. MacCallum, W. F. D. Bennett, D. P. Tieleman. Partitioning of amino acid side chains into lipid bilayers: results from computer simulations and comparison to experiment. *J. Gen. Physiol.* **2007**, *129*, 371–377.

[182] J. L. MacCallum, W. F. D. Bennett, D. P. Tieleman. Distribution of amino acids in a lipid bilayer from computer simulations. *Biophys. J.* **2008**, *94*, 3393–3404.

[183] P. Guo, R. Sknepnek, M. Olvera de la Cruz. Electrostatic-driven ridge formation on nanoparticles coated with charged end-group ligands. *J. Phys. Chem. C* **2011**, *115*, 6484–6490.

[184] E. Heikkilä, A. A. Gurtovenko, H. Martinez-Seara, H. Häkkinen, I. Vattulainen, J. Akola. Atomistic simulations of functional Au144(SR)60 gold nanoparticles in aqueous environment. *J. Phys. Chem. C* **2012**, *116*, 9805–9815.

[185] M. J. Zimmer, T. Geyer. Do we have to explicitly model the ions in brownian dynamics simulations of proteins? *J. Chem. Phys.* **2012**, *136*, 125102.

[186] C. Nielsen, M. Goulian, O. S. Andersen. Energetics of inclusion-induced bilayer deformations. *Biophys. J.* **1998**, *74*, 1966–1983.

[187] R. P. Carney, T. M. Carney, M. Mueller, F. Stellacci. Dynamic cellular uptake of mixed-monolayer protected nanoparticles. *Biointerphases* **2012**, *7*, 17.

[188] A. Bondi. van der Waals volumes and radii. *J. Phys. Chem.* **1964**, *68*, 441–451.

[189] S. Tristram-Nagle, H. I. Petrache, J. F. Nagle. Structure and interactions of fully hydrated dioleoylphosphatidylcholine bilayers. *Biophys. J.* **1998**, *75*, 917–925.

[190] A. Shrake, J. Rupley. Environment and exposure to solvent of protein atoms. Lysozyme and insulin. *J. Mol. Biol.* **1973**, *79*, 351–371.

[191] J. L. MacCallum, W. F. D. Bennett, D. P. Tieleman. Transfer of arginine into lipid bilayers is nonadditive. *Biophys. J.* **2011**, *101*, 110–117.

[192] K. E. Forsten, R. E. Kozack, D. A. Lauffenburger, S. Subramaniam. Numerical solution of the nonlinear poisson-boltzmann equation for a membrane-electrolyte system. *J. Phys. Chem.* **1994**, *98*, 5580–5586.

[193] V. B. Arakelian, D. Walther, E. Donath. Electric potential distributions around discrete charges in a dielectric membrane-electrolyte solution system. *Colloid Polym. Sci.* **1993**, *271*, 268–276.

[194] C. H. Bennett. Efficient estimation of free energy differences from Monte Carlo data. *J. Comput. Phys.* **1976**, *22*, 245–268.

[195] G. König, S. Bruckner, S. Boresch. Unorthodox uses of Bennett's acceptance ratio method. *J. Comput. Chem.* **2009**, *30*, 1712–1718.

[196] W. H. Press, S. A. Teukolsky, W. T. Vetterling, B. P. Flannery, *Numerical Recipes In C (2nd Ed.): The Art Of Scientific Computing*, Cambridge University Press, New York, NY, USA, **1992**.

[197] R. P. Carney, Y. Astier, T. M. Carney, K. Voïtchovsky, P. H. Jacob Silva, F. Stellacci. Electrical method to quantify nanoparticle interaction with lipid bilayers. *ACS Nano* **2013**, *7*, 932.

[198] R. P. Carney, J. Y. Kim, H. Qian, R. Jin, H. Mehenni, F. Stellacci, O. M. Bakr. Determination of nanoparticle size distribution together with density or molecular weight by 2d analytical ultracentrifugation. *Nat. Commun.* **2011**, *2*, 335.

[199] B. Wang, L. Zhang, S. C. Bae, S. Granick. Nanoparticle-induced surface reconstruction of phospholipid membranes. *Proc. Natl. Acad. Sci. U.S.A.* **2008**, *105*, 18171–18175.

[200] G. Von White, Y. Chen, J. Roder-Hanna, G. D. Bothun, C. L. Kitchens. Structural and thermal analysis of lipid vesicles encapsulating hydrophobic gold nanoparticles. *ACS Nano* **2012**, *6*, 4678–4685.

[201] Y. Mai, A. Eisenberg. Controlled incorporation of particles into the central portion of vesicle walls. *J. Am. Chem. Soc.* **2010**, *132*, 10078–10084.

[202] H.-Y. Lee, S. H. R. Shin, L. L. Abezgauz, S. A. Lewis, A. M. Chirsan, D. D. Danino, K. J. M. Bishop. Integration of gold nanoparticles into bilayer structures via adaptive surface chemistry. *J. Am. Chem. Soc.* **2013**, *135*, 5950–5953.

[203] P. Andreozzi, C. Martinelli, R. P. Carney, T. M. Carney, F. Stellacci. Erythrocyte incubation as a method for free-dye presence determination in fluorescently labeled nanoparticles. *Mol. Pharmaceutics* **2013**, *10*, 875–882.

[204] S. Tatur, M. Maccarini, R. Barker, A. Nelson, G. Fragneto. Effect of functionalized gold nanoparticles on floating lipid bilayers. *Langmuir* **2013**, *29*, 6606–6614.

[205] G. J. Gordillo, Z. Krpetić, M. Brust. Interactions of gold nanoparticles with a phospholipid monolayer membrane on mercury. *ACS Nano* **2014**, *8*, 6074–6080.

[206] M. Mondello, G. S. Grest. Molecular dynamics of linear and branched alkanes. *J. Chem. Phys.* **1995**, *103*, 7156.

[207] A. Badia, R. B. Lennox, L. Reven. A dynamic view of self-assembled monolayers. *Acc. Chem. Res.* **2000**, *33*, 475–481.

[208] L. Ramin, A. Jabbarzadeh. Odd-even effects on the structure, stability, and phase transition of alkanethiol self-assembled monolayers. *Langmuir* **2011**, *27*, 9748–9759.

[209] R. J. B. Kalescky, W. Shinoda, P. B. Moore, S. O. Nielsen. Area per ligand as a function of nanoparticle radius: A theoretical and computer simulation approach. *Langmuir* **2009**, *25*, 1352–1359.

[210] A. Jiménez, A. Sarsa, M. Blázquez, T. Pineda. A molecular dynamics study of the surfactant surface density of alkanethiol self-assembled monolayers on gold nanoparticles as a function of the radius. *J. Phys. Chem. C* **2010**, *114*, 21309–21314.

[211] P. K. Ghorai, S. C. Glotzer. Molecular dynamics simulation study of self-assembled monolayers of alkanethiol surfactants on spherical gold nanoparticles. *J. Phys. Chem. C* **2007**, *111*, 15857–15862.

[212] S. M. Chabane Sari, P. J. Debouttiére, R. Lamartine, F. Vocanson, C. Dujardin, G. Ledoux, S. Roux, O. Tillement, P. Perriat. Grafting of colloidal stable gold nanoparticles with lissamine rhodamine B: an original procedure for counting the number of dye molecules attached to the particles. *J. Mater. Chem.* **2004**, *14*, 402.

[213] N. L. Rosi, D. A. Giljohann, C. S. Thaxton, A. K. R. Lytton-Jean, M. S. Han, C. A. Mirkin. Oligonucleotide-modified gold nanoparticles for intracellular gene regulation. *Science* **2006**, *312*, 1027–1030.

[214] T. Lund, M. F. Callaghan, P. Williams, M. Turmaine, C. Bachmann, T. Rademacher, I. M. Roitt, R. Bayford. The influence of ligand organization on the rate of uptake of gold nanoparticles by colorectal cancer cells. *Biomaterials* **2011**, *32*, 9776–9784.

[215] H. Lee, R. G. Larson. Multiscale modeling of dendrimers and their interactions with bilayers and polyelectrolytes. *Molecules* **2009**, *14*, 423–438.

[216] A. J. Makarucha, N. Todorova, I. Yarovsky. Nanomaterials in biological environment: a review of computer modelling studies. *Eur. Biophys. J.* **2011**, *40*, 103–115.

[217] H.-M. Ding, W.-d. Tian, Y.-Q. Ma. Designing nanoparticle translocation through membranes by computer simulations. *ACS Nano* **2012**, *6*, 1230–1238.

[218] J. P. Prates Ramalho, P. Gkeka, L. Sarkisov. Structure and phase transformations of DPPC lipid bilayers in the presence of nanoparticles: insights from coarse-grained molecular dynamics simulations. *Langmuir* **2011**, *27*, 3723–30.

[219] J. J. Kuna, K. Voïtchovsky, C. Singh, H. Jiang, S. Mwenifumbo, P. K. Ghorai, M. M. Stevens, S. C. Glotzer, F. Stellacci. The effect of nanometre-scale structure on interfacial energy. *Nat. Mater.* **2009**, *8*, 837–842.

[220] A.-C. Yang, C.-I. Weng. Structural and dynamic properties of water near monolayer-protected gold clusters with various alkanethiol tail groups. *J. Phys. Chem. C* **2010**, *114*, 8697–8709.

[221] Y. Li, Z. Yang, N. Hu, R. Zhou, X. Chen. Insights into hydrogen bond dynamics at the interface of the charged monolayer-protected Au nanoparticle from molecular dynamics simulation. *J. Chem. Phys.* **2013**, *138*, 184703–184703–9.

[222] N. Schmid, A. P. Eichenberger, A. Choutko, S. Riniker, M. Winger, A. E. Mark, W. F. van Gunsteren. Definition and testing of the GROMOS force-field versions 54a7 and 54b7. *Eur. Biophys. J.* **2011**, *40*, 843–856.

[223] C. Oostenbrink, A. Villa, A. E. Mark, W. F. van Gunsteren. A biomolecular force field based on the free enthalpy of hydration and solvation: The GROMOS force-field parameter sets 53a5 and 53a6. *J. Comput. Chem.* **2004**, *25*, 1656–1676.

[224] M. J. Hinner, S.-J. Marrink, A. H. de Vries. Location, tilt, and binding: a molecular dynamics study of voltage-sensitive dyes in biomembranes. *J. Phys. Chem. B* **2009**, *113*, 15807–15819.

[225] J. N. C. Lopes, A. A. H. Pádua, K. Shimizu. Molecular force field for ionic liquids IV: Trialkylimidazolium and alkoxycarbonyl-imidazolium cations; alkylsulfonate and alkylsulfate anions. *J. Phys. Chem. B* **2008**, *112*, 5039–5046.

[226] A. K. Malde, L. Zuo, M. Breeze, M. Stroet, D. Poger, P. C. Nair, C. Oostenbrink, A. E. Mark. An automated force field topology builder (ATB) and repository: version 1.0. *J. Chem. Theory Comput.* **2011**, *7*, 4026–4037.

[227] J. Hautman, M. L. Klein. Simulation of monolayer of alkyl thiol chains. *J. Chem. Phys* **1989**, *91*, 4994.

[228] W. Mar, M. L. Klein. Molecular dynamics study of the self-assembled monolayer composed of S(CH2)14CH3 molecules using an all-atoms model. *Langmuir* **1994**, *10*, 188–196.

[229] K. J. Tupper, D. W. Brenner. Compression-induced structural transition in a self-assembled monolayer. *Langmuir* **1994**, *10*, 2335–2338.

[230] R. Mahaffy, R. Bhatia, B. J. Garrison. Diffusion of a butanethiolate molecule on a Au{111} surface. *J. Phys. Chem. B* **1997**, *101*, 771–773.

[231] A. K. Rappe, C. J. Casewit, K. S. Colwell, W. A. Goddard, W. M. Skiff. UFF, a full periodic table force field for molecular mechanics and molecular dynamics simulations. *J. Am. Chem. Soc.* **1992**, *114*, 10024–10035.

[232] T.-H. Fang, W.-Y. Chang, S.-J. Lin, C.-N. Fang. Interface dynamics and mechanisms of nanoindented alkanethiol self-assembled monolayers using molecular simulations. *J. Colloid Interface Sci.* **2010**, *345*, 19–26.

[233] O. Lopez-Acevedo, J. Akola, R. L. Whetten, H. Grönbeck, H. Häkkinen. Structure and bonding in the ubiquitous icosahedral metallic gold cluster Au144(SR)60. *J. Phys. Chem. C* **2009**, *113*, 5035–5038.

[234] D. Zanchet, B. D. Hall, D. Ugarte. Structure population in thiol-passivated gold nanoparticles. *J. Phys. Chem. B* **2000**, *104*, 11013–11018.

[235] E. Pensa, E. Cortés, G. Corthey, P. Carro, C. Vericat, M. H. Fonticelli, G. Benítez, A. A. Rubert, R. C. Salvarezza. The chemistry of the sulfur-gold interface: In search of a unified model. *Acc. Chem. Res.* **2012**, *45*, 1183–1192.

[236] A. Patriksson, E. Marklund, D. van der Spoel. Protein structures under electrospray conditions. *Biochemistry* **2007**, *46*, 933–945.

[237] E. G. Marklund, D. S. D. Larsson, D. v. d. Spoel, A. Patriksson, C. Caleman. Structural stability of electrosprayed proteins: temperature and hydration effects. *Phys. Chem. Chem. Phys.* **2009**, *11*, 8069–8078.

[238] S. W. I. Siu, K. Pluhackova, R. A. Bckmann. Optimization of the OPLS-AA force field for long hydrocarbons. *J. Chem. Theory Comput.* **2012**, *8*, 1459–1470.

[239] A. P. Kaushik, P. Clancy. Explicit all-atom modeling of realistically sized ligand-capped nanocrystals. *J. Chem. Phys.* **2012**, *136*, 114702.

[240] W. D. Luedtke, U. Landman. Structure and thermodynamics of self-assembled monolayers on gold nanocrystallites. *J. Phys. Chem. B* **1998**, *102*, 6566–6572.

[241] A. Badia, S. Singh, L. Demers, L. Cuccia, G. R. Brown, R. B. Lennox. Self-assembled monolayers on gold nanoparticles. *Chem. Eur. J.* **1996**, *2*, 359–363.

[242] A. Badia, L. Cuccia, L. Demers, F. Morin, R. B. Lennox. Structure and dynamics in alkanethiolate monolayers self-assembled on gold nanoparticles: A DSC, FT-IR, and deuterium NMR study. *J. Am. Chem. Soc.* **1997**, *119*, 2682–2692.

[243] M. J. Hostetler, J. E. Wingate, C.-J. Zhong, J. E. Harris, R. W. Vachet, M. R. Clark, J. D. Londono, S. J. Green, J. J. Stokes, G. D. Wignall, G. L. Glish, M. D. Porter, N. D. Evans, R. W. Murray. Alkanethiolate gold cluster molecules with core diameters from 1.5 to 5.2 nm: Core and monolayer properties as a function of core size. *Langmuir* **1998**, *14*, 17–30.

[244] C. Weeraman, A. K. Yatawara, A. N. Bordenyuk, A. V. Benderskii. Effect of nanoscale geometry on molecular conformation:Vibrational sum-frequency generation of alkanethiols on gold nanoparticles. *J. Am. Chem. Soc.* **2006**, *128*, 14244–14245.

[245] A. N. Bordenyuk, C. Weeraman, A. Yatawara, H. D. Jayathilake, I. Stiopkin, Y. Liu, A. V. Benderskii. Vibrational sum frequency generation spectroscopy of dodecanethiol on metal nanoparticles. *J. Phys. Chem. C* **2007**, *111*, 8925–8933.

[246] B. Hess, C. Kutzner, D. van der Spoel, E. Lindahl. GROMACS 4: Algorithms for highly efficient, load-balanced, and scalable molecular simulation. *J. Chem. Theory Comput.* **2008**, *4*, 435–447.

[247] L. B. Wright, P. M. Rodger, S. Corni, T. R. Walsh. GolP-CHARMM: first-principles based force fields for the interaction of proteins with Au(111) and Au(100). *J. Chem. Theory Comput.* **2013**, *9*, 1616–1630.

[248] J. Qian, R. Hentschke, W. Knoll. Superstructures of cyclodextrin derivatives on Au(111): a combined random plantingmolecular dynamics approach. *Langmuir* **1997**, *13*, 7092–7098.

[249] J. C. Shelley, G. N. Patey, D. R. Bérard, G. M. Torrie. Modeling and structure of mercury-water interfaces. *J. Chem. Phys.* **1997**, *107*, 2122–2141.

[250] J. C. Shelley, D. R. Bérard, *Computer simulation of water physisorption at metal-water interfaces* in *Reviews in Computational Chemistry*, K. B. Lipkowitz, D. B. Boyd (Eds.), John Wiley & Sons, Inc., **1998**, pp. 137–205.

[251] F. Iori, S. Corni. Including image charge effects in the molecular dynamics simulations of molecules on metal surfaces. *J. Comput. Chem.* **2008**, *29*, 1656–1666.

[252] R. M. Venable, Y. Luo, K. Gawrisch, B. Roux, R. W. Pastor. Simulations of anionic lipid membranes: development of interaction-specific ion parameters and validation using nmr data. *J. Phys. Chem. B* **2013**, *117*, 10183–10192.

[253] P. E. Smith, W. F. v. Gunsteren. Consistent dielectric properties of the simple point charge and extended simple point charge water models at 277 and 300 K. *J. Chem. Phys.* **1994**, *100*, 3169–3174.

[254] R. Huang, R. P. Carney, F. Stellacci, B. L. T. Lau. Colloidal stability of self-assembled monolayer-coated gold nanoparticles: The effects of surface compositional and structural heterogeneity. *Langmuir* **2013**, *29*, 11560–11566.

[255] R. Huang, R. P. Carney, F. Stellacci, B. L. T. Lau. Protein-nanoparticle interactions: The effects of surface compositional and structural heterogeneity are scale dependent. *Nanoscale* **2013**, *5*, 6928–6935.

[256] S. Vanni, L. Vamparys, R. Gautier, G. Drin, C. Etchebest, P. F. J. Fuchs, B. Antonny. Amphipathic lipid packing sensor motifs: probing bilayer defects with hydrophobic residues. *Biophys. J.* **2013**, *104*, 575–584.

[257] D. Mirjanian, A. N. Dickey, J. H. Hoh, T. B. Woolf, M. J. Stevens. Splaying of aliphatic tails plays a central role in barrier crossing during liposome fusion. *J. Phys. Chem. B* **2010**, *114*, 11061–11068.

[258] M. J. Stevens, J. H. Hoh, T. B. Woolf. Insights into the molecular mechanism of membrane fusion from simulation: evidence for the association of splayed tails. *Phys. Rev. Lett.* **2003**, *91*, 188102.

[259] P. M. Kasson, E. Lindahl, V. S. Pande. Atomic-resolution simulations predict a transition state for vesicle fusion defined by contact of a few lipid tails. *PLoS Comput. Biol.* **2010**, *6*, e1000829.

[260] V. Knecht, S.-J. Marrink. Molecular dynamics simulations of lipid vesicle fusion in atomic detail. *Biophys. J.* **2007**, *92*, 4254–4261.

[261] Y. G. Smirnova, S.-J. Marrink, R. Lipowsky, V. Knecht. Solvent-exposed tails as prestalk transition states for membrane fusion at low hydration. *J. Am. Chem. Soc.* **2010**, *132*, 6710–6718.

[262] H. Cui, E. Lyman, G. A. Voth. Mechanism of membrane curvature sensing by amphipathic helix containing proteins. *Biophys. J.* **2011**, *100*, 1271–1279.

[263] L. Vamparys, R. Gautier, S. Vanni, W. F. D. Bennett, D. P. Tieleman, B. Antonny, C. Etchebest, P. J. Fuchs. Conical lipids in flat bilayers induce packing defects similar to that induced by positive curvature. *Biophys. J.* **2013**, *104*, 585–593.

[264] R. Du, V. S. Pande, A. Y. Grosberg, T. Tanaka, E. S. Shakhnovich. On the transition coordinate for protein folding. *J. Chem. Phys.* **1998**, *108*, 334–350.

[265] P. G. Bolhuis, D. Chandler, C. Dellago, P. L. Geissler. Transition path sampling: Throwing ropes over rough mountain passes, in the dark. *Annu. Rev. Phys. Chem.* **2002**, *53*, 291–318.

[266] A. West, K. Ma, J. L. Chung, J. T. Kindt. Simulation studies of structure and edge tension of lipid bilayer edges: effects of tail structure and force-field. *J. Phys. Chem. A* **2013**, *117*, 7114–7123.

[267] D. Poger, A. E. Mark. Lipid bilayers: The effect of force field on ordering and dynamics. *J. Chem. Theory Comput.* **2012**, *8*, 4807–4817.

[268] N. Zheng, J. Fan, G. D. Stucky. One-step one-phase synthesis of monodisperse noble-metallic nanoparticles and their colloidal crystals. *J. Am. Chem. Soc.* **2006**, *128*, 6550–6551.

[269] R. Richter, A. Mukhopadhyay, A. Brisson. Pathways of lipid vesicle deposition on solid surfaces: a combined QCM-D and AFM study. *Biophys. J.* **2003**, *85*, 3035–3047.

[270] R. P. Richter, A. R. Brisson. Following the formation of supported lipid bilayers on mica: a study combining AFM, QCM-D, and ellipsometry. *Biophys. J.* **2005**, *88*, 3422–3433.

[271] P. M. Kasson, V. S. Pande. Control of membrane fusion mechanism by lipid composition: predictions from ensemble molecular dynamics. *PLoS Comput. Biol.* **2007**, *3*, e220.

[272] H. Chakraborty, P. K. Tarafdar, M. J. Bruno, T. Sengupta, B. R. Lentz. Activation thermodynamics of poly(ethylene glycol)-mediated model membrane fusion support mechanistic models of stalk and pore formation. *Biophys. J.* **2012**, *102*, 2751–2760.

[273] W. A. Talbot, L. X. Zheng, B. R. Lentz. Acyl chain unsaturation and vesicle curvature alter outer leaflet packing and promote poly(ethylene glycol)-mediated membrane fusion. *Biochemistry* **1997**, *36*, 5827–5836.

[274] J. Lee, B. R. Lentz. Outer leaflet-packing defects promote poly(ethylene glycol)-mediated fusion of large unilamellar vesicles. *Biochemistry* **1997**, *36*, 421–431.

[275] S. Aeffner, T. Reusch, B. Weinhausen, T. Salditt. Energetics of stalk intermediates in membrane fusion are controlled by lipid composition. *Proc. Natl. Acad. Sci. U.S.A.* **2012**, *109*, E1609–E1618.

[276] C. Scomparin, S. Lecuyer, M. Ferreira, T. Charitat, B. Tinland. Diffusion in supported lipid bilayers: influence of substrate and preparation technique on the internal dynamics. *Eur. Phys. J. E Soft Matter* **2009**, *28*, 211–220.

[277] H. M. Seeger, A. D. Cerbo, A. Alessandrini, P. Facci. Supported lipid bilayers on mica and silicon oxide: Comparison of the main phase transition behavior. *J. Phys. Chem. B* **2010**, *114*, 8926–8933.

[278] M. H. Abdulreda, V. T. Moy. Atomic force microscope studies of the fusion of floating lipid bilayers. *Biophys. J.* **2007**, *92*, 4369–4378.

[279] F. Eisenhaber, P. Lijnzaad, P. Argos, C. Sander, M. Scharf. The double cubic lattice method: Efficient approaches to numerical integration of surface area and volume and to dot surface contouring of molecular assemblies. *J. Comput. Chem.* **1995**, *16*, 273–284.

[280] M. G. Wolf, M. Hoefling, C. Aponte-Santamaría, H. Grubmüller, G. Groenhof. g_membed: Efficient insertion of a membrane protein into an equilibrated lipid bilayer with minimal perturbation. *J. Comput. Chem.* **2010**, *31*, 2169–2174.

[281] J. Zhou, J. Ralston, R. Sedev, D. A. Beattie. Functionalized gold nanoparticles: synthesis, structure and colloid stability. *J. Colloid Interface Sci.* **2009**, *331*, 251–262.

[282] X. Liu, H. Huang, Q. Jin, J. Ji. Mixed charged zwitterionic self-assembled monolayers as a facile way to stabilize large gold nanoparticles. *Langmuir* **2011**, *27*, 5242–5251.

[283] D. Poger, A. E. Mark. On the validation of molecular dynamics simulations of saturated and cis-monounsaturated phosphatidylcholine lipid bilayers: A comparison with experiment. *J. Chem. Theory Comput.* **2010**, *6*, 325–336.

[284] P. Larsson, P. M. Kasson. Lipid tail protrusion in simulations predicts fusogenic activity of influenza fusion peptide mutants and conformational models. *PLoS Comput. Biol.* **2013**, *9*, e1002950.

[285] L. V. Chernomordik, M. M. Kozlov, G. B. Melikyan, I. G. Abidor, V. S. Markin, Y. A. Chizmadzhev. The shape of lipid molecules and monolayer membrane fusion. *BBA-Biomembranes* **1985**, *812*, 643–655.

[286] D. P. Tieleman, S.-J. Marrink. Lipids out of equilibrium: Energetics of desorption and pore mediated flip-flop. *J. Am. Chem. Soc.* **2006**, *128*, 12462–12467.

[287] N. Sapay, W. F. D. Bennett, D. P. Tieleman. Thermodynamics of flip-flop and desorption for a systematic series of phosphatidylcholine lipids. *Soft Matter* **2009**, *5*, 3295–3302.

[288] J. S. Hub, B. L. de Groot, D. van der Spoel. g_whamA free weighted histogram analysis implementation including robust error and autocorrelation estimates. *J. Chem. Theory Comput.* **2010**, *6*, 3713–3720.

[289] B. Qiao, M. Olvera de la Cruz. Driving force for water permeation across lipid membranes. *J. Phys. Chem. Lett.* **2013**, *4*, 3233–3237.

[290] W. F. D. Bennett, N. Sapay, D. P. Tieleman. Atomistic simulations of pore formation and closure in lipid bilayers. *Biophys. J.* **2014**, *106*, 210–219.

[291] W. F. D. Bennett, J. L. MacCallum, M. J. Hinner, S. J. Marrink, D. P. Tieleman. Molecular view of cholesterol flip-flop and chemical potential in different membrane environments. *J. Am. Chem. Soc.* **2009**, *131*, 12714–12720.

[292] A. Choubey, R. Kalia, N. Malmstadt, A. Nakano, P. Vashishta. Cholesterol translocation in a phospholipid membrane. *Biophys. J.* **2013**, *104*, 2429–2436.

[293] M. A. J. Ferguson, A. F. Williams. Cell-surface anchoring of proteins via glycosylphosphatidylinositol structures. *Annu. Rev. Biochem.* **1988**, *57*, 285–320.

[294] D. Bonhenry, M. Tarek, F. Dehez. Effects of phospholipid composition on the transfer of a small cationic peptide across a model biological membrane. *J. Chem. Theory Comput.* **2013**, *9*, 5675–5684.

[295] I. Vorobyov, T. E. Olson, J. H. Kim, R. E. Koeppe, O. S. Andersen, T. W. Allen. Ion-induced defect permeation of lipid membranes. *Biophys. J.* **2014**, *106*, 586–597.

[296] Y. Hu, S. Ou, S. Patel. Free energetics of arginine permeation into model DMPC lipid bilayers: coupling of effective counterion concentration and lateral bilayer dimensions. *J. Phys. Chem. B* **2013**, *117*, 11641–11653.

[297] J. P. M. Jämbeck, A. P. Lyubartsev. Exploring the free energy landscape of solutes embedded in lipid bilayers. *J. Phys. Chem. Lett.* **2013**, *4*, 1781–1787.

[298] C. Neale, C. Madill, S. Rauscher, R. Pomès. Accelerating convergence in molecular dynamics simulations of solutes in lipid membranes by conducting a random walk along the bilayer normal. *J. Chem. Theory Comput.* **2013**, *9*, 3686–3703.

[299] L. B. Li, I. Vorobyov, T. W. Allen. The role of membrane thickness in charged proteinlipid interactions. *BBA-Biomembranes* **2012**, *1818*, 135–145.

[300] Y. Wang, D. Hu, D. Wei. Transmembrane permeation mechanism of charged methyl guanidine. *J. Chem. Theory Comput.* **2014**, *10*, 1717–1726.

[301] N. Sapay, W. F. D. Bennett, D. P. Tieleman. Molecular simulations of lipid flip-flop in the presence of model transmembrane helices. *Biochemistry* **2010**, *49*, 7665–7673.

[302] J. N. Israelachvili, *Intermolecular and Surface Forces*, Academic Press, **2010**.

[303] P. Bagchi. Theory of stabilization of spherical colloidal particles by nonionic polymers. *J. Colloid Interface Sci.* **1974**, *47*, 86–99.

[304] B. Vincent, J. Edwards, S. Emmett, A. Jones. Depletion flocculation in dispersions of sterically-stabilised particles ("soft spheres"). *Colloids Surf.* **1986**, *18*, 261–281.

[305] T. Kim, C.-H. Lee, S.-W. Joo, K. Lee. Kinetics of gold nanoparticle aggregation: Experiments and modeling. *J. Colloid Interface Sci.* **2008**, *318*, 238–243.

[306] K. I. Popov, R. J. Nap, I. Szleifer, M. O. de la Cruz. Interacting nanoparticles with functional surface groups. *J. Polym. Sci. Part B Polym. Phys.* **2012**, *50*, 852–862.

[307] G. I. Guerrero-García, P. González-Mozuelos, M. O. de la Cruz. Potential of mean force between identical charged nanoparticles immersed in a size-asymmetric monovalent electrolyte. *J. Chem. Phys.* **2011**, *135*, 164705–164705–10.

[308] X. Han, J. Goebl, Z. Lu, Y. Yin. Role of salt in the spontaneous assembly of charged gold nanoparticles in ethanol. *Langmuir* **2011**, *27*, 5282–5289.

[309] S. Lin, M. R. Wiesner. Paradox of stability of nanoparticles at very low ionic strength. *Langmuir* **2012**, *28*, 11032–11041.

[310] Y. S. Jho, S. A. Safran, M. In, P. A. Pincus. Effect of charge inhomogeneity and mobility on colloid aggregation. *Langmuir* **2012**, *28*, 8329–8336.

[311] T. Geyer, P. Born, T. Kraus. Switching between crystallization and amorphous agglomeration of alkyl thiol-coated gold nanoparticles. *Phys. Rev. Lett.* **2012**, *109*, 128302.

[312] M. R. Shirts, J. D. Chodera. Statistically optimal analysis of samples from multiple equilibrium states. *J. Chem. Phys.* **2008**, *129*, 124105–124105–10.

[313] S. Huißmann, C. N. Likos, R. Blaak. Explicit vs implicit water simulations of charged dendrimers. *Macromolecules* **2012**, *45*, 2562–2569.

[314] K. Klymko, A. Cacciuto. Free energy of multiple overlapping chains. *Phys. Rev. Lett.* **2011**, *107*, 278302.

[315] S. M. Mendoza, I. Arfaoui, S. Zanarini, F. Paolucci, P. Rudolf. Improvements in the characterization of the crystalline structure of acid-terminated alkanethiol self-assembled monolayers on Au(111). *Langmuir* **2007**, *23*, 582–588.

[316] M. K. Corbierre, N. S. Cameron, M. Sutton, K. Laaziri, R. B. Lennox. Gold nanoparticle/polymer nanocomposites: dispersion of nanoparticles as a function of capping agent molecular weight and grafting density. *Langmuir* **2005**, *21*, 6063–6072.

[317] D. N. Benoit, H. Zhu, M. H. Lilierose, R. A. Verm, N. Ali, A. N. Morrison, J. D. Fortner, C. Avendano, V. L. Colvin. Measuring the grafting density of nanoparticles in solution by analytical ultracentrifugation and total organic carbon analysis. *Anal. Chem.* **2012**, *84*, 9238–9245.

[318] A. Stradner, H. Sedgwick, F. Cardinaux, W. C. K. Poon, S. U. Egelhaaf, P. Schurtenberger. Equilibrium cluster formation in concentrated protein solutions and colloids. *Nature* **2004**, *432*, 492–495.

[319] A. I. Campbell, V. J. Anderson, J. S. van Duijneveldt, P. Bartlett. Dynamical arrest in attractive colloids: the effect of long-range repulsion. *Phys. Rev. Lett.* **2005**, *94*, 208301.

[320] F. Sciortino, P. Tartaglia, E. Zaccarelli. One-dimensional cluster growth and branching gels in colloidal systems with short-range depletion attraction and screened electrostatic repulsion. *J. Phys. Chem. B* **2005**, *109*, 21942–21953.

[321] M. Venturoli, B. Smit, M. M. Sperotto. Simulation studies of protein-induced bilayer deformations, and lipid-induced protein tilting, on a mesoscopic model for lipid bilayers with embedded proteins. *Biophys. J.* **2005**, *88*, 1778–1798.

[322] J. Yoo, Q. Cui. Three-dimensional stress field around a membrane protein: Atomistic and coarse-grained simulation analysis of gramicidin A. *Biophys. J.* **2013**, *104*, 117–127.

[323] T. Gil, J. H. Ipsen, Ole G, M. C. Sabra, M. M. Sperotto, M. J. Zuckermann. Theoretical analysis of protein organization in lipid membranes. *BBA-Biomembranes* **1998**, *1376*, 245–266.

[324] U. Schmidt, G. Guigas, M. Weiss. Cluster formation of transmembrane proteins due to hydrophobic mismatching. *Phys. Rev. Lett.* **2008**, *101*, 128104.

[325] D. L. Parton, J. W. Klingelhoefer, M. S. P. Sansom. Aggregation of model membrane proteins, modulated by hydrophobic mismatch, membrane curvature, and protein class. *Biophys. J.* **2011**, *101*, 691–699.

[326] J. A. Lundbaek, P. Birn, A. J. Hansen, R. Sogaard, C. Nielsen, J. Girshman, M. J. Bruno, S. E. Tape, J. Egebjerg, D. V. Greathouse, G. L. Mattice, R. E. Koeppe, O. S. Andersen. Regulation of sodium channel function by bilayer elasticity: the importance of hydrophobic coupling. effects of micelle-forming amphiphiles and cholesterol. *J. Gen. Physiol.* **2004**, *123*, 599–621.

[327] R. Phillips, T. Ursell, P. Wiggins, P. Sens. Emerging roles for lipids in shaping membrane-protein function. *Nature* **2009**, *459*, 379–385.

[328] J. A. Lundbaek, R. E. Koeppe, O. S. Andersen. Amphiphile regulation of ion channel function by changes in the bilayer spring constant. *Proc. Natl. Acad. Sci. USA* **2010**, *107*, 15427–15430.

[329] E. B. Watkins, C. E. Miller, J. Majewski, T. L. Kuhl. Membrane texture induced by specific protein binding and receptor clustering: active roles for lipids in cellular function. *Proc. Natl. Acad. Sci. USA* **2011**, *108*, 6975–6980.

[330] L. V. Chernomordik, M. M. Kozlov. Protein-lipid interplay in fusion and fission of biological membranes. *Annu. Rev. Biochem.* **2003**, *72*, 175–207.

[331] M. M. Kozlov, H. T. McMahon, L. V. Chernomordik. Protein-driven membrane stresses in fusion and fission. *Trends Biochem. Sci.* **2010**, *35*, 699–706.

[332] H. J. Risselada, H. Grubmüller. How SNARE molecules mediate membrane fusion: recent insights from molecular simulations. *Curr. Opin. Struct. Biol.* **2012**, *22*, 187–196.

[333] G. S. Ayton, E. Lyman, V. Krishna, R. D. Swenson, C. Mim, V. M. Unger, G. A. Voth. New insights into BAR domain-induced membrane remodeling. *Biophys. J.* **2009**, *97*, 1616–1625.

[334] M. Simunovic, A. Srivastava, G. A. Voth. Linear aggregation of proteins on the membrane as a prelude to membrane remodeling. *Proc. Natl. Acad. Sci. USA* **2013**, *110*, 20396–20401.

[335] J.-B. Fournier. Coupling between membrane tilt-difference and dilation: A new "ripple" instability and multiple crystalline inclusions phases. *Europhys. Lett.* **1998**, *43*, 725.

[336] R. A. Böckmann, A. Hac, T. Heimburg, H. Grubmüller. Effect of sodium chloride on a lipid bilayer. *Biophys. J.* **2003**, *85*, 1647–1655.

[337] T. A. Harroun, W. T. Heller, T. M. Weiss, L. Yang, H. W. Huang. Experimental evidence for hydrophobic matching and membrane-mediated interactions in lipid bilayers containing Gramicidin. *Biophys. J.* **1999**, *76*, 937–945.

[338] S. Kandasamy, R. Larson. Molecular dynamics simulations of model trans-membrane peptides in lipid bilayers: A systematic investigation of hydrophobic mismatch. *Biophys. J.* **2006**, *90*, 2326–2343.

[339] T. Kim, W. Im. Revisiting hydrophobic mismatch with free energy simulation studies of transmembrane helix tilt and rotation. *Biophys. J.* **2010**, *99*, 175–183.

[340] A. J. de Jesus, T. W. Allen. The determinants of hydrophobic mismatch response for transmembrane helices. *Biochim. Biophys. Acta* **2013**, *1828*, 851–863.

[341] T. Kim, K. I. Lee, P. Morris, R. W. Pastor, O. S. Andersen, W. Im. Influence of hydrophobic mismatch on structures and dynamics of gramicidin a and lipid bilayers. *Biophys. J.* **2012**, *102*, 1551–1560.

[342] H.-J. Kaiser, A. Orowski, T. Róg, T. K. M. Nyholm, W. Chai, T. Feizi, D. Lingwood, I. Vattulainen, K. Simons. Lateral sorting in model membranes by cholesterol-mediated hydrophobic matching. *Proc. Natl. Acad. Sci. USA* **2011**, *108*, 16628–16633.

[343] M. O. Jensen, O. G. Mouritsen. Lipids do influence protein function-the hydrophobic matching hypothesis revisited. *Biochim. Biophys. Acta* **2004**, *1666*, 205–226.

[344] J. F. Nagle, S. Tristram-Nagle. Structure of lipid bilayers. *Biochim. Biophys. Acta* **2000**, *1469*, 159–195.

[345] W. Shinoda, S. Okazaki. A Voronoi analysis of lipid area fluctuation in a bilayer. *J. Chem. Phys.* **1998**, *109*, 1517–1521.

[346] M. Alwarawrah, J. Dai, J. Huang. A molecular view of the cholesterol condensing effect in dopc lipid bilayers. *J. Phys. Chem. B* **2010**, *114*, 7516–7523.

[347] L. S. Vermeer, B. L. de Groot, V. Réat, A. Milon, J. Czaplicki. Acyl chain order parameter profiles in phospholipid bilayers: Computation from molecular dynamics simulations and comparison with 2H NMR experiments. *Eur. Biophys. J.* **2007**, *36*, 919–931.

[348] J.-P. Douliez, A. Ferrarini, E.-J. Dufourc. On the relationship between C-C and C-D order parameters and its use for studying the conformation of lipid acyl chains in biomembranes. *J. Chem. Phys.* **1998**, *109*, 2513–2518.

[349] D. Poger, W. F. Van Gunsteren, A. E. Mark. A new force field for simulating phosphatidylcholine bilayers. *J. Comput. Chem.* **2010**, *31*, 1117–1125.

[350] G. P. Moss. Basic terminology of stereochemistry. *Pure Appl. Chem.* **1996**, *68*, 2193.

[351] Y. Tu, M. Lv, P. Xiu, T. Huynh, M. Zhang, M. Castelli, Z. Liu, Q. Huang, C. Fan, H. Fang, R. Zhou. Destructive extraction of phospholipids from escherichia coli membranes by graphene nanosheets. *Nat. Nanotechnol.* **2013**, *8*, 594–601.

[352] S. Lev. Non-vesicular lipid transport by lipid-transfer proteins and beyond. *Nat. Rev. Mol. Cell. Biol.* **2010**, *11*, 739–750.

[353] P. D. Blood, G. A. Voth. Direct observation of Bin/amphiphysin/Rvs (BAR) domain-induced membrane curvature by means of molecular dynamics simulations. *Proc. Natl. Acad. Sci. USA* **2006**, *103*, 15068–15072.

[354] G. S. Ayton, P. D. Blood, G. A. Voth. Membrane remodeling from N-BAR domain interactions: insights from multi-scale simulation. *Biophys. J.* **2007**, *92*, 3595–3602.

[355] A. Šarić, A. Cacciuto. Fluid membranes can drive linear aggregation of adsorbed spherical nanoparticles. *Phys. Rev. Lett.* **2012**, *108*, 118101.

[356] A. Šarić, A. Cacciuto. Self-assembly of nanoparticles adsorbed on fluid and elastic membranes. *Soft Matter* **2013**, *9*, 6677.

[357] J. C. Stachowiak, C. C. Hayden, D. Y. Sasaki. Steric confinement of proteins on lipid membranes can drive curvature and tubulation. *Proc. Natl. Acad. Sci. USA* **2010**, *107*, 7781–7786.

[358] A. H. Bahrami, R. Lipowsky, T. R. Weikl. Tubulation and aggregation of spherical nanoparticles adsorbed on vesicles. *Phys. Rev. Lett.* **2012**, *109*, 188102.

[359] A. Šarić, A. Cacciuto. Mechanism of membrane tube formation induced by adhesive nanocomponents. *Phys. Rev. Lett.* **2012**, *109*, 188101.

[360] D. A. Walker, B. Kowalczyk, M. O. d. l. Cruz, B. A. Grzybowski. Electrostatics at the nanoscale. *Nanoscale* **2011**, *3*, 1316–1344.

[361] A. A. Gurtovenko, I. Vattulainen. Ion leakage through transient water pores in protein-free lipid membranes driven by transmembrane ionic charge imbalance. *Biophys. J.* **2007**, *92*, 1878–1890.

[362] E. H. Shin, Y. Li, U. Kumar, H. V. Sureka, X. Zhang, C. K. Payne. Membrane potential mediates the cellular binding of nanoparticles. *Nanoscale* **2013**, *5*, 5879–5886.

[363] L. V. Schäfer, D. H. d. Jong, A. Holt, A. J. Rzepiela, A. H. d. Vries, B. Poolman, J. A. Killian, S. J. Marrink. Lipid packing drives the segregation of transmembrane helices into disordered lipid domains in model membranes. *Proc. Natl. Acad. Sci. USA* **2011**, *108*, 1343–1348.

[364] G. van den Bogaart, K. Meyenberg, H. J. Risselada, H. Amin, K. I. Willig, B. E. Hubrich, M. Dier, S. W. Hell, H. Grubmüller, U. Diederichsen, R. Jahn. Membrane protein sequestering by ionic protein-lipid interactions. *Nature* **2011**, *479*, 552–555.

[365] R. H. Gensure, M. L. Zeidel, W. G. Hill. Lipid raft components cholesterol and sphingomyelin increase H+/OH permeability of phosphatidylcholine membranes. *Biochem. J.* **2006**, *398*, 485–495.

[366] P. Ionita, J. Wolowska, V. Chechik, A. Caragheorgheopol. Ligand dynamics in spin-labeled Au nanoparticles. *J. Phys. Chem. C* **2007**, *111*, 16717–16723.

[367] P. Ionita, A. Volkov, G. Jeschke, V. Chechik. Lateral diffusion of thiol ligands on the surface of au nanoparticles: an electron paramagnetic resonance study. *Anal. Chem.* **2008**, *80*, 95–106.

[368] A. A. Alabi, R. W. Tsien. Perspectives on kiss-and-run: role in exocytosis, endocytosis, and neurotransmission. *Annu. Rev. Physiol.* **2013**, *75*, 393–422.

[369] M. Bretou, C. Anne, F. Darchen. A fast mode of membrane fusion dependent on tight SNARE zippering. *J. Neurosci.* **2008**, *28*, 8470–8476.

[370] L. Shi, Q.-T. Shen, A. Kiel, J. Wang, H.-W. Wang, T. J. Melia, J. E. Rothman, F. Pincet. SNARE proteins: one to fuse and three to keep the nascent fusion pore open. *Science* **2012**, *335*, 1355–1359.

[371] X. Liu, D. Weaver, O. Shirihai, G. Hajnóczky. Mitochondrial 'kiss–and–run': interplay between mitochondrial motility and fusionfission dynamics. *EMBO J.* **2009**, *28*, 3074–3089.

[372] R. Hong, G. Han, J. M. Fernndez, B.-j. Kim, N. S. Forbes, V. M. Rotello. Glutathione-mediated delivery and release using monolayer protected nanoparticle carriers. *J. Am. Chem. Soc.* **2006**, *128*, 1078–1079.

[373] S. Dasgupta, T. Auth, G. Gompper. Shape and orientation matter for the cellular uptake of nonspherical particles. *Nano Lett.* **2014**, *14*, 687–693.

[374] J. Cruz, M. Mihailescu, G. Wiedman, K. Herman, P. C. Searson, W. C. Wimley, K. Hristova. A membrane-translocating peptide penetrates into bilayers without significant bilayer perturbations. *Biophys. J.* **2013**, *104*, 2419–2428.

[375] W. Kim, M. H. Hecht. Generic hydrophobic residues are sufficient to promote aggregation of the Alzheimer's A42 peptide. *Proc. Natl. Acad. Sci. USA* **2006**, *103*, 15824–15829.

[376] N. B. Last, D. E. Schlamadinger, A. D. Miranker. A common landscape for membrane-active peptides. *Protein Sci.* **2013**, *22*, 870–882.

[377] D. Frenkel, B. Smit, *Understanding Molecular Simulation: From Algorithms to Applications*, Academic Press, **2001**.

[378] D. van der Spoel, E. Lindahl, B. Hess, the GROMACS development team. GROMACS User Manual version 4.6.5. *www.gromacs.org* **2013**.

[379] M. P. Allen, D. J. Tildesley, *Computer Simulation Of Liquids*, Clarendon Press, **1987**.

[380] G. Bussi, D. Donadio, M. Parrinello. Canonical sampling through velocity rescaling. *J. Chem. Phys.* **2007**, *126*, 014101.

[381] H. J. C. Berendsen, J. P. M. Postma, W. F. v. Gunsteren, A. DiNola, J. R. Haak. Molecular dynamics with coupling to an external bath. *J. Chem. Phys.* **1984**, *81*, 3684–3690.

[382] B. Roux. The calculation of the potential of mean force using computer simulations. *Comput. Phys. Commun.* **1995**, *91*, 275–282.

[383] S. Kumar, J. M. Rosenberg, D. Bouzida, R. H. Swendsen, P. A. Kollman. The weighted histogram analysis method for free-energy calculations on biomolecules. I. The method. *J. Comput. Chem.* **1992**, *13*, 10111021.

[384] A. Halperin, M. Tirrell, T. P. Lodge. Tethered chains in polymer microstructures. *Adv. Polym. Sci.* **1992**, *100*, 31–71.

[385] S. Alexander. Polymer adsorption on small spheres - scaling approach. *Journal De Physique* **1977**, *38*, 977–981.

[386] P. G. de Gennes. Conformations of polymers attached to an interface. *Macromolecules* **1980**, *13*, 1069–1075.

[387] P.-G. de Gennes, *Scaling Concepts In Polymer Physics*, Cornell University Press, Ithaca, N.Y., **1979**.

[388] P. J. Flory, *Principles Of Polymer Chemistry*, Cornell University Press, **1953**.

[389] S. Komura, S. A. Safran. Scaling theory of mixed amphiphilic monolayers. *Eur. Phys. J. E Soft Matter* **2001**, *5*, 337–351.

[390] I. K. Voets, F. A. M. Leermakers. Self-consistent field theory for obligatory coassembly. *Phys. Rev. E.* **2008**, *78*, 061801.

[391] J. F. Marko, T. A. Witten. Phase-separation in a grafted polymer layer. *Phys. Rev. Lett.* **1991**, *66*, 1541–1544.

[392] S. Minko, M. Muller, D. Usov, A. Scholl, C. Froeck, M. Stamm. Lateral versus perpendicular segregation in mixed polymer brushes. *Phys. Rev. Lett.* **2002**, *88*, 035502.

[393] M. Muller. Phase diagram of a mixed polymer brush. *Phys. Rev. E.* **2002**, *65*, 030802.

[394] B. N. J. Persson, N. D. Lang. Electron-hole-pair quenching of excited states near a metal. *Phys. Rev. B* **1982**, *26*, 5409–5415.

[395] E. Dulkeith, M. Ringler, T. A. Klar, J. Feldmann, A. Muñoz Javier, W. J. Parak. Gold nanoparticles quench fluorescence by phase induced radiative rate suppression. *Nano Lett.* **2005**, *5*, 585–589.

[396] T. L. Jennings, M. P. Singh, G. F. Strouse. Fluorescent lifetime quenching near d = 1.5 nm gold nanoparticles: Probing NSET validity. *J. Am. Chem. Soc.* **2006**, *128*, 5462–5467.

[397] T. Pons, I. L. Medintz, K. E. Sapsford, S. Higashiya, A. F. Grimes, D. S. English, H. Mattoussi. On the quenching of semiconductor quantum dot photoluminescence by proximal gold nanoparticles. *Nano Lett.* **2007**, *7*, 3157–3164.

[398] G. P. Acuna, M. Bucher, I. H. Stein, C. Steinhauer, A. Kuzyk, P. Holzmeister, R. Schreiber, A. Moroz, F. D. Stefani, T. Liedl, F. C. Simmel, P. Tinnefeld. Distance dependence of single-fluorophore quenching by gold nanoparticles studied on DNA origami. *ACS Nano* **2012**, *6*, 3189–3195.

[399] J. A. Lemkul, W. J. Allen, D. R. Bevan. Practical considerations for building GROMOS-compatible small-molecule topologies. *J. Chem. Inf. Model.* **2010**, *50*, 2221–2235.

[400] A. W. Schttelkopf, D. M. F. van Aalten. PRODRG: A tool for high-throughput crystallography of protein-ligand complexes. *Acta Crystallogr. D Biol. Crystallogr.* **2004**, *60*, 1355–1363.

[401] K. C. Song, P. W. Livanec, J. B. Klauda, K. Kuczera, R. C. Dunn, W. Im. Orientation of fluorescent lipid analogue BODIPY-PC to probe lipid membrane properties: insights from molecular dynamics simulations. *J. Phys. Chem. B* **2011**, *115*, 6157–6165.

[402] M. R. R. de Planque, J. A. Killian. Protein-lipid interactions studied with designed transmembrane peptides: role of hydrophobic matching and interfacial anchoring. *Molec. Membrane Biol.* **2003**, *20*, 271–284.

[403] R. D. Kaiser, E. London. Determination of the depth of BODIPY probes in model membranes by parallax analysis of fluorescence quenching. *Biochim. Biophys. Acta* **1998**, *1375*, 13–22.

[404] R. Sachl, I. Boldyrev, L. B. A. Johansson. Localisation of BODIPY-labelled phosphatidylcholines in lipid bilayers. *Phys. Chem. Chem. Phys.* **2010**, *12*, 6027–6034.

[405] P. Anger, P. Bharadwaj, L. Novotny. Enhancement and quenching of single-molecule fluorescence. *Phys. Rev. Lett.* **2006**, *96*, 113002.

[406] P. Bharadwaj, P. Anger, L. Novotny. Nanoplasmonic enhancement of single-molecule fluorescence. *Nanotechnology* **2007**, *18*, 044017.

[407] T. J. Piggot, A. Piñeiro, S. Khalid. Molecular dynamics simulations of phosphatidylcholine membranes: a comparative force field study. *J. Chem. Theory Comput.* **2012**, *8*, 4593–4609.

[408] B. Hess. P-LINCS: a parallel linear constraint solver for molecular simulation. *J. Chem. Theory Comput.* **2008**, *4*, 116–122.

[409] W. F. Van Gunsteren, M. Karplus. Protein dynamics in solution and in a crystalline environment: a molecular dynamics study. *Biochemistry* **1982**, *21*, 2259–2274.

[410] S. Miyamoto, P. A. Kollman. SETTLE: An analytical version of the SHAKE and RATTLE algorithm for rigid water models. *J. Comput. Chem.* **1992**, *13*, 952–962.